AN EXPERIMENTAL STUDY INTO THE BEHAVIOUR OF TITANIUM-RICH AND CHROMIUM-RICH OXIDE MINERAL PHASES AT HIGH PRESSURES AND TEMPERATURES

by

Marcel Kamperman BSc. (Hons).

Submitted in fulfilment of the requirements
for the degree of Doctor of Philosophy (Geology)

University of Tasmania
Hobart
1996

To Karen,
Kirsten, Madeleine
and Quentin

"It is not for nothing that the scholar invented the Ph.D. thesis as his principle contribution to literary form. The Ph.D. thesis is the perfect image of his world. It is work done for the sake of doing work - perfectly conscientious, perfectly laborious, perfectly irresponsible."

Archibald MacLeish,
The Irresponsibles

DECLARATION

This thesis contains the results of research done in the Department of Geology, University of Tasmania, Hobart between 1991 and 1995.

This thesis contains no material which has been accepted or submitted for the award of any other higher degree or graduate diploma in any tertiary institution and to the best of the author's knowledge and belief, the thesis contains no material previously published or written by another person, except where due reference is made in the text of the thesis.

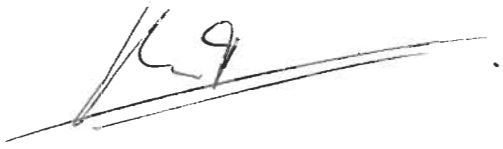

Marcel Kamperman
University of Tasmania
Hobart
(November, 1996)

AUTHORITY OF ACCESS

This thesis is not to be made available for loan or copying for one year following the date this statement was signed. Following that time the thesis may be made available for loan and limited copying in accordance with the Copyright Act 1968.

Marcel Kamperman
University of Tasmania
Hobart
(November, 1996)

ABSTRACT

AN EXPERIMENTAL STUDY INTO THE BEHAVIOUR OF TITANIUM-RICH AND CHROMIUM-RICH OXIDE MINERAL PHASES AT HIGH PRESSURES AND TEMPERATURES

The composition of fluid phases in the Earth's mantle are significantly affected by oxygen fugacity, and mantle fluids can be reasonably modelled by the C-H-O system. Using a broad generalization, under oxidized conditions (at ~FMQ) the fluid phase is dominated by CO_2-H_2O-rich fluids, under relatively reducing conditions (at ~FMQ-2-3 log units) by CH_4-H_2O-rich fluids, and under strongly reducing conditions (below IW) by CH_4 and H_2. Thus by controlling fluid speciation in the Earth's mantle, oxygen fugacity influences the P-T position of a mantle solidus and the composition of mantle-derived melts. Oxygen fugacity also constrains the oxidation state of elements and the stability of minerals. For example, natural diamonds and natural fluids approaching H_2O are at equilibrium in the mantle under reduced conditions at ~IW+1-2 log units. The $Fe^{3+}/\sum Fe$ ratios of mantle-derived oxide minerals, such as Cr-rich spinel and Mg-rich ilmenite, in equilibrium with silicates can be used to indicate the oxygen fugacity (fO_2) under which mantle derived mineral assemblages formed. The spinel-based oxygen geobarometer has received a significant amount of attention and appears to be experimentally well constrained for all but the most Cr-rich spinel assemblages. The ilmenite-based oxygen geobarometer, however, was formulated on the basis of existing thermodynamic data and has not been experimentally tested.

An important prerequisite that needs to be demonstrated when applying oxide mineral-based geothermometers and oxygen geobarometers to natural samples with confidence is mineral stoichiometry of the oxides and a knowledge of their ferric and ferrous iron contents. The availability of a synthetic multilayer crystal and accurately calibrated oxide and silicate standards make it possible to use the electron microprobe for precise oxygen analyses of spinels. A requirement of the oxygen measurement routine described is the use of repetitive statistical analyses of the oxygen standards and subsequent corrections and recalibration. A representative set of oxygen analyses for each spinel population studied is essential to obtain reliable data, and the danger of using single data is emphasized. Magnesium-rich kimberlitic ilmenites have been analysed for oxygen content and, within the accuracy of the technique (± 2 rel. %), are stoichiometric. Magnesiochromite spinels, having broad compositional similarities but different

petrogenetic and cooling histories, have been analysed for oxygen and their stoichiometry has been assessed. Diamond-indicator spinels from the Aries, Roberts Victor and Makganyene kimberlites and Argyle lamproite are stoichiometric. Spinel inclusions in olivine phenocrysts from low-Ti tholeiites from the Hunter Fraction Zone and high-Ca boninites from the Tonga Trench show a range of non-stoichiometry. Low $Fe^{3+}/\sum Fe$ values calculated assuming stoichiometry for such spinels are invalid. Spinels from metamorphosed volcanics from the Peak Hill-Glengarry Basin and the Heazlewood River Ultramafic Complex are also non-stoichoimetric, having significant $Fe_{8/3}O_4$ - $Cr_{8/3}O_4$ components. The results demonstrate that high-chromium spinel non-stoichiometry is a common feature. This has important implications when using ferric and ferrous iron concentrations to estimate the oxidation state or temperature of formation.

In the second section of this study, synthetic ilmenite-olivine-rutile±orthopyroxene assemblages were equilibrated between 900 and 1200 °C and 15 to 35 kbar, under controlled oxygen fugacity. Oxygen fugacity was controlled using the double capsule technique with inner sample capsules consisting of graphite, olivine, platinum or AgPd alloy. The outer capsule was Pt or AgPd alloy, and the oxygen buffers used in the experiments were WC-WO_2-graphite (WCWO), graphite-water/graphite-CO_2-CO (GW/GCO) , Ni-NiO (NNO), and Fe_2O_3-Fe_3O_4 (HM). Experiments were performed with a 0.5 inch piston-cylinder apparatus under fluid-excess conditions. Within the P-T-X range of the experiments, ilmenite compositions showed redox ratios, $Fe^{3+}/\sum Fe$, were a linear function of oxygen fugacity (0.03 at WCWO, 0.09 at GW/GCO, 0.20 at NNO and 0.73 at HM). The redox ratio of ilmenites at high oxidation conditions is found to be sensitive to temperature, and $Fe^{3+}/\sum Fe$ decreases with increasing temperature at HM buffer conditions. This temperature dependence is less noticeable under more reducing conditions. Similarly, rutile showed increasing iron contents with increasing oxygen fugacity. Investigations demonstrated that the major substitution was (Fe^{3+}O.OH) and iron contents (expressed as Fe_2O_3) varied linearly with oxygen fugacity from 1.6 wt.% at WCWO, 2.3 wt.% at GW/GCO, 3.9 wt.% at NNO and 6.7 wt.% at HM). The Fe_2O_3 content increases with increasing pressure, and to a lesser degree with temperature. Experimental results were applied to test existing ilmenite-based geothermometers. Both existing geothermometers progressively underestimated temperatures with an increasing ilmenite redox ratio. A least-squares fit to the experimental data, taking into account and correcting for the mole fraction of hematite in ilmenite, X_{hem}, determines Margules parameters defining the non-ideality terms and gives improved ilmenite-based geothermometers. Using the improved Margules parameters, a least-squares fit to the experimental data gives two ilmenite-based oxygen geobarometers: an improved olivine-orthopyroxene-ilmenite geobarometer and a new ilmenite-rutile geobarometer. The

barometers are applicable to a large spectrum of ilmenite compositions occurring in mantle rocks and gives reasonable results to temperatures as low as 900 °C.

Mg-rich ilmenites, often with elevated Cr_2O_3 contents and generally with low Fe^{3+} contents are often found in association with diamonds and diamond-bearing rocks, or assemblages that are believed to have originated in mantle source regions in close proximity to the diamond stability field. The ilmenite-based geothermometers and oxygen geobarometers described above ignore the effect of minor cations present in natural ilmenites, and the validity of their use with such natural mineral assemblages is untested. In the third part of this study, chromium bearing Mg-ilmenites are synthesized in the presence of olivine-orthopyroxene±spinel±rutile assemblages between 1050 and 1200 °C and 17 to 35 kbar, under controlled oxygen fugacity, using oxygen buffering techniques described above. Oxygen buffering was achieved with the use of Fe-FeO (IW), WC-WO_2-graphite (WCWO), Ni-NiO (NNO), and Fe_2O_3-Fe_3O_4 (HM) buffers under fluid-excess conditions. Within the P-T-X range of the experiments, ilmenite compositions showed increasing redox ratios and Cr_2O_3 contents as a linear function of oxygen fugacity. The Cr_2O_3 content of ilmenites at constant oxygen fugacities is strongly positively correlated with pressure. Experimental results were used to test existing geothermometers and oxygen geobarometers. A Monte Carlo fitting procedure to the experimental data, taking into account the Cr_2O_3 content of ilmenite, has modified previously determined Margules parameters expressing non-ideality in ilmenite solid solution and gives improved ilmenite-based geothermometers and oxygen geobarometers. Existing spinel-based geothermometers and geobarometers are also corrected using experimental data of high $Cr^{\#}$ spinel compositions. The revised oxygen geobarometers are applied to natural ilmenite and spinel upper mantle-derived xenocryst assemblages from kimberlites and lamproites from various regions. A consistent picture emerges from the ilmenite and spinel data which suggests that the oxygen fugacity of the lithospheric upper mantle is broadly bounded by the IW and FMQ buffers.

A further significant topic of this study relates to the incorporation of H^+ into nominally anhydrous mineral phases as a coupled substitution with trivalent elements such as Cr^{3+} and Fe^{3+}. The observations on iron and chromium substitution in rutile and their dependence on oxygen fugacity (for iron) led to the use of infra-red spectroscopy to confirm the presence of (OH) in both natural and synthetic rutiles. The presence of (OH) in rutile has previously been described. To investigate both the (CrOOH) and (FeOOH) solid solutions synthetic TiO_2, TiO_2-Cr_2O_3, TiO_2-Fe_2O_3, TiO_2-Fe_3O_4 and TiO_2-FeO mixes were run in H_2O-saturated conditions to determine maximum saturation of the

trivalent element in rutile. Attempts were also made to run TiO_2-Cr_2O_3 mixes under H^+-absent conditions in nominally anhydrous conditions.

In the TiO_2-Cr_2O_3 experiments there was little difference in Cr_2O_3 substitution into rutile between H_2O-saturated and 'anhydrous' experiments, and in both cases there is a positive correlation with pressure and temperature. Infrared spectroscopy showed a strong (OH) absorption peak around 3200 cm^{-1} in rutiles synthesized under H_2O-saturated conditions, but no absorption peaks for the 'anhydrous' experimental rutiles were detected over the mid-IR region.

The H_2O-saturated TiO_2-Cr_2O_3 experiments demonstrated that the incorporation of water in rutile is strongly controlled by pressure, temperature, and the redox state of the cations. At 1100 °C, H_2O contents of Cr-rich rutiles increased from 0.79 wt.% at 5 kbar to 1.08 wt.% at 20 kbar and similarly at 20 kbar, H_2O contents increased from 1.08 wt.% at 1100 °C to 1.65 wt.% at 1400 °C. The incorporation of H_2O into rutile is not favoured by the absence of trivalent cations. For example, rutiles synthesized in the presence of Fe_2O_3 at 20 kbars and 1100 °C contained 1.18 wt.% H_2O, whereas rutiles synthesized at the same physical conditions in the presence of Fe_3O_4 contained 0.46 wt.% H_2O. Also, rutiles synthesized under hydrous conditions at increasing oxygen fugacities from TiO_2-FeO compositions show increasing amounts of water and cation contents. Rutiles synthesized under hydrous conditions from TiO_2-only compositions did not contain any water. Also, rutiles synthesized from the TiO_2-FeO mix under varying oxygen fugacity conditions showed an increase in total iron content and water content with increasing fO_2.

These studies reveal a role for rutile in assessing both activity of water and oxidation state. They also show that rutile, an accessory mineral in eclogite, MARID and some peridotite samples from the upper mantle, provides a possible mechanism for recycling significant water contents from shallow to deep mantle conditions.

TABLE OF CONTENTS

Declaration i

Authority of Access ii

Abstract iii

Table of Contents vii

Acknowledgements xi

Chapter 1 An experimental study into the behaviour of titanium-rich and chromium-rich oxide mineral phases at high pressures and temperatures - perspectives and aims of this study 1

Chapter 2 Direct oxygen measurements of chromium-rich and titanium-rich mantle-derived oxides: implications for their stoichiometry and petrogenesis 7

2.1 Introduction 7

2.2 Analytical method 9
2.2.1 Design of analytical routine 9
2.2.2 Analytical procedure 11
2.2.3 Accuracy of oxygen measurements 14

2.3 Results 19
2.3.1 Diamond-indicator spinels 20
2.3.2 Spinel inclusions in olivine from primitive subduction related magmas 24
2.3.3 Spinels from metamorphosed volcanics 27
2.3.4 Magnesium-rich ilmenite xenocrysts from kimberlites 31

2.4 Conclusions 36

Chapter 3 An experimental study of the ilmenite-olivine-rutile±orthopyroxene mineral system with emphasis on geothermometry and oxygen barometry 39

3.1 Introduction 39

3.2 Experimental details 41
3.2.1 Selection and preparation of starting materials 41
3.2.2 Experimental technique 45
3.2.3 Analytical details 49

3.3 Treatment of analytical results 49
3.3.1 Calculation of ferric iron and problems of precision and accuracy 49
3.3.2 Attainment of phase equilibration 55

3.4 Experimental results 59
3.4.1 Silicate mineral chemistry 61
3.4.2 Oxide mineral chemistry 61

3.5 Testing of existing geothermometers and oxygen geobarometer 69
3.5.1 Fe-Mg exchange geothermometry 69
3.5.2 Oxygen geobarometry 71

3.6 Ilmenite-based Fe-Mg exchange thermometry and oxygen geobarometry 73
3.6.1 Olivine-ilmenite geothermometry 73
3.6.2 Olivine-orthopyroxene-ilmenite oxygen geobarometry 77
3.6.3 Rutile-ilmenite oxygen geobarometry 78
3.6.4 Orthopyroxene-ilmenite geothermometry 81

3.7 Conclusions 81

Chapter 4 An experimental study of the chromium-enriched ilmenite-olivine-orthopyroxene±spinel±rutile mineral system with emphasis on oxygen geobarometry: implications for the oxidation state of the upper mantle 83

4.1 Introduction 83

4.2 Experimental details 85
4.2.1 Selection and preparation of starting materials 85
4.2.2 Experimental technique 85
4.2.3 Analytical details 87

4.3 Treatment of analytical results 90
4.3.1 Calculation of ferric and ferrous iron 90
4.3.2 An experimental approach of an equilibrium position 90

4.4 Experimental results 96
4.4.1 Silicate mineral chemistry 100
4.4.2 Oxide mineral chemistry 103

4.5 Geothermometry and Oxygen Geobarometry 109
4.5.1 Spinel geothermometry and oxygen geobarometry 109
4.5.2 $FeFeO_3$-$FeTiO_3$-$MgTiO_3$-$CrCrO_3$ - $(A)(B)O_3$ formula 116
4.5.3 Ilmenite geothermometry 122
4.5.4 Ilmenite oxygen geobarometry 124

4.6 Results from the ilmenite- and spinel-based oxygen geobarometers and geothermometers 128

4.7 Conclusions 135

Chapter 5 An experimental study into the substitution of chromium, iron and water in rutile at high temperatures and pressures - implications for the role of rutile as an indicator of the water activity in the Earth's mantle ... 137

5.1 Introduction 137

5.2 Experimental details 139
5.2.1 Choice and preparation of starting materials 139
5.2.2 Experimental technique 139
5.2.3 Analytical details 140

5.3 Experimental results 142
5.3.1 Details of experimental results 142
5.3.2 Electron microprobe analyses 145

5.3.3 I.R. spectroscopy of synthetic rutiles 152
5.3.4 Determination of H_2O concentrations in rutile from I.R. measurements and elemental analyses 163

5.4 Discussion of results 165
5.4.1 Incorporation of H and cations into rutile 165
5.4.2 Rutile as a possible geohygrometer 169
5.4.3 A possible role for rutile in recycling water in the Earth's mantle 174

References Cited 177

Appendix A Experimental details A1

Appendix B Analytical details A9

Appendix C Electron probe microanalyses for oxygen A17

Appendix D Representative electron probe microanalyses of mineral phases from SiO_2-TiO_2-FeO-MgO experimental runs A30

Appendix E Representative electron probe microanalyses (EPMA) of mineral phases from SiO_2-TiO_2±Al_2O_3-Cr_2O_3-FeO-MgO-K_2O±NiO±ZnO experimental runs A45

Appendix F Silica activity version A68

ACKNOWLEDGEMENTS

Work on this thesis would not have been possible without the assistance and encouragement of those listed below.

I thank Professor David Headley Green (now at the Research School of Earth Sciences, ANU, Canberra) for bringing the topic to my attention, and his willingness to be my supervisor. I thank him for his help and supervision across the miles, his support, his sharp attention for detail and his keen interest in the progress of the research. His ability to connect parts of this work to a much broader scientific picture have greatly benefited my attitude towards fundamental and applied research.

Special thanks go to Keith Harris (Department of Geology) for his instructions in high pressure experimental work, for his efforts in preparing experimental capsules, starting mixes and assembly parts, for his interest in the project and the many useful discussions that we had.

Special thanks also go to Dr. Wayne Taylor (now at the Research School of Earth Sciences, ANU, Canberra) who took it upon himself to get me out of the high pressure experimental laboratory and into the diamond-related mineral research field, only to expose me to a large number of problems that still remain to be solved. His interest in the overall project right to the end was second to none, and I consider his guidance to be a major reason behind the completion of this work.

This project, by the very nature of the research arrangements and departmental changes over the last five years, has attracted many associate supervisors. I wish to thank Trevor Falloon, Wayne Taylor, Ron Berry and Tony Crawford of the Geology Department, and Roger Hamilton and Doug Haynes of Western Mining Corporation for accepting that role at various points in time.

Financial and logistic support came from Western Mining Corporation, Exploration Division. I am indebted to Mr. Roy Woodall whose initial interest sparked WMC's involvement in the project. Many thanks go to Roger Hamilton who introduced me to some 'real world' problems, and who was always happy to assist with providing samples, maps, literature and many very good ideas, most of which still require the due attention they deserve. Thanks also go to Jeff Foster, Bill Rose and Rob Waugh who provided many hours of stimulating discussions on any diamond-related topic, and all WMC personnel in the mineral dressing laboratory, Kalgoorlie. I also thank Doug Haynes for his constructive comments and support.

I also thank (in no particular order):

- Wieslaw Jablonski (Central Science Laboratory) for his instructions on the Cameca SX-50 electron microprobe, and his tireless efforts in getting 'Madame Cameca' to analyse the light elements of the periodic table in a reliable manner.

- Graham Rowbottom (Central Science Laboratory) for his invaluable technical assistance in FTIR spectroscopy and elemental analyses.
- Ron Berry (Department of Geology) for providing several challenging thermodynamic problems, and for his ability to bring to my attention much useful material to make these problems a little easier.
- Peter Cornish (Department of Geology) for making sure that money was no object, as long as my research account was in the black.
- Simon Stephens (Department of Geology) for his instructions on preparing probe mounts, and for his preparations of very high quality polished and doubly polished sections and olivine capsules.
- Tim St. Pierre (School of Mathematical and Physical Sciences, Murdoch University) for assisting with Mössbauer spectroscopy.
- Ralph Bottrill (Mineral Resources of Tasmania) for his help with X-ray diffraction work.
- Linda Tompkins (UWA, now at Ashton Mining) for assisting with analytical work.
- Hugh O'Neill (Research School of Earth Sciences, ANU, Canberra) for his valuable comments on several thermodynamic aspects of the project.
- Melissa Kirkley (Geochemistry Department, University of Cape Town) for supplying many oxide mineral assemblages from African kimberlites.
- Fellow members of the Petrology Research Group who were part of a most enjoyable scientific environment: Rick Varne, Andrew McNeil, Ingvar Sigurdsson, Ruth Lanyon, Alicia Verbeeten, Fernando Della Pasqua, Geoff Nichols, Greg Yaxley, Massimo Gasparon, Udi Hartonen, Chris Ballhaus, Russell Sweeney, Russell Fulton, John Sinton, Leonid Danyushevsky, Dimma Kamenetsky and Uri Babich, and any others who were inadvertently left off this list.
- Members of the Department of Geology and CODES who provided many happy hours of general discussion in the tea room.
- BHP Iron Ore Ltd. in Newman, W.A., for allowing me to use facilities to complete this thesis.

This project was undertaken while the author was a recipient of an Australian Postgraduate Research Award (Industry).

My utmost appreciation goes to my parents, Tony and Maria Kamperman, who helped Karen and myself cope with the challenging combination of parenthood and postgraduate studies. Their open-home 'policy' meant that there was always someone who would listen to us.

Finally, I wish to dedicate this work to my wonderful wife Karen, and our beautiful children Kirsten, Madeleine and Quentin. They were happy to believe and share in my dreams.

CHAPTER 1

AN EXPERIMENTAL STUDY INTO THE BEHAVIOUR OF TITANIUM-RICH AND CHROMIUM-RICH OXIDE MINERAL PHASES AT HIGH PRESSURES AND TEMPERATURES - PERSPECTIVES AND AIMS OF THIS STUDY

Major advances have been made in understanding the roles that oxide minerals play in assessing upper mantle and deep crustal petrogenetic processes. Experimental and mineral investigations using the techniques of crystallography, mineral chemistry, thermochemistry, and magnetic properties have been used over the past three decades to elucidate general relationships between oxide minerals and geological processes (e.g. Rumble, 1976; Lindsley, 1991a). The emphasis of this research has shifted gradually from focussing on the links between oxide mineral chemistry and host rock types, mineral assemblages, and the geological environment, to deriving quantitative estimates of intensive variables associated with igneous and metamorphic events from oxide-bearing mineral assemblages. The determination of variables such as temperature, pressure, oxygen fugacity (fO_2), and fluid composition from mineral assemblages will constrain petrological interpretations including partial melting, metamorphic P, T, t paths, and metasomatism. Despite occupying relatively small volumes (generally < 3 % by volume) in upper-mantle and lower crustal rocks, the oxide mineral group, with wide ranges in mineral compositions and mineral associations, has provided useful petrogenetic indicators (e.g. Haggerty, 1991; Sack and Ghiorso, 1991).

This thesis presents a series of experimental and natural studies relating mantle-derived Ti-rich minerals (e.g. ilmenite and rutile) and Cr-rich oxide minerals such as spinel. The research work has been aimed at extending the existing knowledge of these minerals, particularly with reference to the mantle processes that control their mineral chemistry, and their use as petrogenetic indicators pertaining to these processes. Specifically, emphasis for this work has been on oxide-bearing mantle mineral assemblages involving ilmenite and/or spinel most akin to those found in association with diamonds and diamond-bearing rocks, or assemblages that are believed to have originated in mantle source regions in close proximity to the diamond stability field. Such assemblages include, among other minerals, Mg-rich ilmenites, often with elevated Cr_2O_3 contents and generally with low Fe^{3+} contents, and magnesiochromite spinels, also with low Fe^{3+} contents (e.g. Gurney, 1989). In addition, Cr- and Fe-rich rutiles, have been documented

in association with diamonds and diamond-bearing assemblages and other mantle derived rocks (e.g. Haggerty, 1987). Of particular interest in this research have been the high Cr, Fe-rutiles associated with mica-amphibole-rutile-ilmenite-diopside (MARID) suite samples and the reaction relationships that they share with ilmenites in such assemblages (e.g. Dawson and Smith, 1977).

The redox state of the Earth's upper mantle has been a continuing topic of geological research and is widely recognized as being one of the most important physical variables in controlling a number of processes in the mantle. There is very little dispute that the oxygen fugacity, which defines the mantle redox state, is a heterogeneous variable in the mantle (e.g. Arculus, 1985; Haggerty and Tompkins, 1983; Haggerty, 1990; Green *et al.*, 1987; Taylor and Green, 1989; Ballhaus, 1993), and several authors have also inferred that the oxygen fugacity has changed during geological time (e.g. Arculus, 1985; Canil *et al.*, 1994). However, a number of differences on the spatial distribution, temporal variation and control of oxygen fugacity continue to exist. Of particular interest to geological research are the differences in oxygen fugacity between the mantle lithosphere ('cool' and chemically refractory part of the upper mantle) and the mantle asthenosphere ('hot' with temperatures inferred from magnetic temperatures and chemically fertile part of the upper mantle). A number of authors have indicated that the asthenosphere has a higher relative oxygen fugacity than the lithosphere, based on observations that asthenospherically-derived basaltic melts and their crystallization products are more oxidized than crystalline material from the lithospheric mantle (e.g. Arculus, 1985; Haggerty and Tompkins, 1983; Haggerty, 1990). The deep diamondiferous lithosphere displays features that may support evidence for a reduced regime, such as highly reduced indicator minerals and CH_4-rich fluids in diamond (Meyer, 1987). The removal of oxidized partial melts from a fertile asthenosphere can create a residue that is refractory and reduced (e.g. Menzies, 1990). Based on the spinel oxygen barometer of O'Neill and Wall (1987), the oxygen fugacity of the lithospheric mantle is believed to lie between the FMQ and IW buffers (see Appendix A for abbreviations of buffer equations).

Other researchers offer a contrasting model of oxygen zonation where the asthenosphere is more reduced than at least the upper part of the overlying lithosphere (e.g. Green *et al.*, 1987; Taylor and Green, 1989; Green *et al.*, 1990). These models propose a fluid-absent asthenosphere in which interstitial silicate melt may accommodate C as $(CO_3)^{2-}$ and H_2O as $(OH)^-$ with continuously variable fO_2 due to multivalent elements such at Ti, Fe, Cr and Mn. Beneath the asthenosphere a (CH_4 + H_2O) fluid may be present as CH_4 which does not partition into a known crystalline compound at high pressures, and CH_4 inhibits partial melting (in contrast to $(OH)^-$ and $(CO_3)^{2-}$). The subduction of oxidized crust and

lithosphere would create redox fronts against such reduced regions of the Upper Mantle and Transition Zone. Mantle melting may take place when the deep CH_4-rich fluids are oxidized to elemental carbon and water ('redox' melting) with a shift in the peridotite solidus as water activity (a_{H2O}) increases. The redox melting process is likely to occur in those parts of the mantle where sub-asthenospheric mantle and reduced asthenosphere can mix with remnants of oxidized recycled material.

Both models rely heavily on results from experiments involving oxide minerals done under upper mantle conditions. It has been shown that the $Fe^{3+}/\sum Fe$ value of oxide minerals such as spinel and ilmenite is a potential oxygen fugacity indicator, and the ratio forms the basis for a number of experimentally calibrated geobarometers (e.g. Eggler, 1983; O'Neill and Wall, 1987; Mattioli and Wood, 1988; Ballhaus *et al.*, 1991). The reliability of using the oxide geobarometers in calculating fO_2 values from mineral assemblages is strongly dependent on the assumption that the oxide minerals used in the calculations are stoichiometric. For example, for non-stoichiometric oxide minerals with lower Fe^{3+} contents than calculated from stoichiometry, corrected oxygen fugacities for mineral assemblages will be lower than those calculated when assuming oxide mineral stoichiometry. There are significant differences in opinion about oxide mineral stoichiometry based on Mössbauer spectroscopy (e.g. Virgo *et al.*, 1988; Lucas *et al.*, 1989; Wood and Virgo, 1989; Ballhaus *et al.*, 1990, 1991; Carmichael, 1991). Although a widely used technique for determining Fe^{3+} contents, Mössbauer spectroscopy has its drawbacks as it cannot be widely applied to small mineral grains because this technique requires a relatively large sample size. This thesis presents an analytical method for the determination of oxygen contents of small, individual oxide minerals grains using an electron microprobe (Chapter 2). The oxygen measurement technique, applied to spinels and ilmenites from several mantle-derived magmatic suites, allows an accurate assessment of stoichiometry and Fe^{3+} content calculation in individual grains.

Quantitative estimates of intensive variables formulated using experimental results can be tested for their accuracy against independent experimental data from multicomponent compositions (e.g. Carswell and Gibb, 1987). For example, Taylor and Green (1991) tested a number of existing mineral barometers and thermometers using an independent, internally consistent mineral chemistry data set of silicate phases from a fertile peridotite equilibrated in the presence of a reduced C-O-H fluid phase (IW+0.5 to IW+1.5 log units). They concluded that some geothermometers and geobarometers were accurate and precise, whereas others either overestimated or underestimated temperatures and pressures because: (i) they were applied to natural mineral assemblages with compositions outside the range of the internally constrained experimental compositions or, (ii) they failed to

adequately correct for non-ideality terms in relevant mineral solid solutions. Oxygen geobarometers, involving ilmenite-bearing or spinel-bearing peridotite assemblages, may be tested in a similar fashion. Taylor and Green (1991) also used their experimental data to test the ilmenite oxygen geobarometer of Eggler (1983) and considered that it overestimated fO_2 values by ~1.5 log units in their complex composition. The existing Eggler (1983) ilmenite oxygen geobarometer is based on experimental geothermometry studies by Andersen and Lindsley (1979, 1981) conducted under relatively reduced conditions (~FMQ to FMQ-2.0 log units). Discrepancies between experimental and calculated fO_2 values derived from the ilmenite oxygen geobarometer may be due to an inadequate correction for Fe^{3+} (expressed as hematite) in the ilmenite solid solution. This thesis presents the results of an experimental investigation in the ilmenite-bearing peridotite mineral system undertaken under mantle pressures and temperatures with oxygen fugacities ranging from ~FMQ-3.0 to FMQ+4.0 log units, and corrections for Fe^{3+} in the ilmenite solid solution are formulated and applied to the ilmenite oxygen geobarometer (Chapter 3). In addition, the data are used to test the existing ilmenite-olivine (Andersen and Lindsley, 1979, 1981) and ilmenite-orthopyroxene (Bishop, 1980) Fe-Mg exchange geothermometers and changes are proposed to these formulations. Also, a new oxygen geobarometer involving ilmenite and rutile is formulated here. It has been pointed out that ilmenite and rutile can coexist in the presence of hematite, which implies that the mineral equilibrium is controlled by an oxidation reaction (e.g. Rumble, 1976). However, to-date the value of the oxygen fugacity for the reaction involving ilmenite and rutile is not known, and the experimental work presented in Chapter 3 is used to derive the ilmenite-rutile oxygen geobarometer.

Ballhaus *et al.* (1991) tested the spinel-peridotite oxygen geobarometers of O'Neill and Wall (1987) and Mattioli and Wood (1988) and suggested that the former worked well for relatively reduced oxygen conditions (FMQ-2.0 to FMQ log units) with calculated fO_2 values generally within 0.5 log units of experimental values, but found that it broke down under oxidized conditions (FMQ+4.0 log units) and underestimated experimental fO_2 values by ~2.0 log units. In contrast the oxygen barometer of Mattioli and Wood (1988) did not fit the experimental data of Ballhaus *et al.* (1991) well and consistently overestimated the experimental fO_2 values. Taylor and Green (1991), using their independent mineral chemistry data set from a fertile peridotite equilibrated in the presence of a reduced C-O-H fluid phase, confirmed these results and concluded that the Mattioli and Wood (1988) oxygen geobarometer yielded erratic results, whereas the O'Neill and Wall (1987) and the Ballhaus *et al.* (1991) oxygen barometers calculated fO_2 values that compared well with the experimentally predicted values. The oxygen barometers, however, were found to be sensitive to bulk compositions. At high $Cr^{\#}$ values

for spinels (with $Cr^{\#}$ = Cr/Cr+Al ratios > 0.6) the Ballhaus *et al.* (1991) formulation tends to consistently overestimate the experimental fO_2 values by ~0.5-1.0 log units and the O'Neill and Wall (1987) formulation underestimates the fO_2 by a similar amount. Neither formulation considered experimentally constrained spinel compositions with high $Cr^{\#}$ values and the discrepancy between experimental and calculated fO_2 values may be due to: (i) an increased non-ideality component in high $Cr^{\#}$ spinels compared with the lower $Cr^{\#}$ spinels used in the existing oxygen geobarometers, or (ii) the presence of Cr^{2+} rather than Cr^{3+} in Cr-rich spinels formed under reduced conditions (IW to IW+1.0 log units) for which no correction has been made in the spinel solid solution models of the spinel oxygen geobarometers (e.g. Ballhaus, 1993).

Because Cr-rich spinels are potentially important indicators of oxygen fugacity in the diamond source region, a thorough examination of the existing oxygen geobarometers is warranted. In Chapter 4 experimental data are presented to test the existing spinel oxygen geobarometers using mineral assemblages with very high $Cr^{\#}$ spinels ($Cr^{\#}$ >0.9) synthesized under pressure-temperature conditions representative of the Earth's mantle with oxygen fugacities ranging from IW to HM conditions (~FMQ-4.0 to FMQ+4.0 log units), and the experimental work is used to reformulate the existing Ballhaus *et al.* (1991) oxygen geobarometer for high $Cr^{\#}$ spinel compositions. In addition, the Cr-rich experiments were aimed at synthesizing Cr-bearing Mg-ilmenites. The existing ilmenite-based oxygen geobarometer (Eggler, 1983) and (Andersen and Lindsley, 1981) olivine-ilmenite geothermometer does not adequately account for Cr_2O_3 in the ilmenite solid solution, and the data presented here are used to make appropriate corrections to the ilmenite solid soultion model.

The presence of H_2O or OH in mantle minerals is of importance because these components can have a major effect on petrogenetic processes such as melting, element partitioning and mineral phase transitions. Of the common mantle minerals, amphibole and phlogopite are most readily thought of as a repository for structurally bonded $(OH)^-$. However, with increasingly sophisticated analytical techniques available, fluids and volatiles such as H_2O, OH or H have been detected in mantle minerals that were previously believed to be free of such components. For example, the prediction that wadsleyite (β-Mg_2SiO_4), likely to be a major component of the transition zone, might be a significant host for OH was confirmed by spectroscopic measurements, and it has since been experimentally synthesized with H in its structure (e.g. Smyth, 1987; McMillan *et al.*, 1987, 1991). Aines and Rossman (1984) demonstrated that minor OH contents are commonly found in mantle-derived garnets. Rossman and Smyth (1990) documented hydroxyl contents of accessory minerals in mantle eclogites and related rocks. More

recently, a mechanism was proposed to recycle water from deep subducting slabs (> 300 km) back into the mantle using stishovite as a storage site for H_2O following the detection of significant amounts of H in stishovite using polarized Fourier transform infra-red spectroscopy (e.g Pawley *et al.*, 1993). Although oxide minerals with a significant hydrous component have been important in soil and surface environmental chemistry and geochemistry (e.g. goethite, manganite and boehmite), they have not featured highly in the discussion of upper mantle and lower crustal geological processes. Rutile, however, has a great affinity for water and it has been the subject of a number of investigations into the mechanisms of incorporating water into essentially anhydrous oxide minerals (e.g. Soffer, 1961; von Hippel *et al.*, 1962; Beran and Zemann, 1971; Hammer, 1988; Hammer and Beran, 1991; Vlassopoulos *et al.*, 1993). Research work established a possible correlation between increasing H_2O or OH concentrations in rutiles and the content of trivalent substitutional cations (e.g. Hammer and Beran, 1991; Vlassopoulos *et al.*, 1993). Also, Hammer and Beran (1991) suggested that the environment of formation played a role in determining the OH content of rutiles. However, the effect of varying pressure, temperature and oxygen fugacity on H_2O and minor element incorporation has not been experimentally studied. Here results are presented from high pressure-temperature experiments undertaken in the TiO_2-Cr_2O_3±H_2O, the TiO_2-Fe_2O_3-H_2O, the TiO_2-Fe_3O_4-H_2O, TiO_2-FeO±H_2O and TiO_2-H_2O systems (Chapter 5). In following with conclusions from previous studies of natural rutile-bearing assemblies, a strong link between the OH content of rutiles and cation contents as a function of pressure, temperature and oxygen fugacity is indicated.

CHAPTER 2

DIRECT OXYGEN MEASUREMENTS OF CHROMIUM-RICH AND TITANIUM-RICH MANTLE-DERIVED OXIDES: IMPLICATIONS FOR THEIR STOICHIOMETRY AND PETROGENESIS

2.1 Introduction

Experimental studies of spinel within the Fe-Ti-O ternary have demonstrated substantial non-stoichiometry which is a function of temperature, composition and oxygen fugacity (e.g. Aragon and McCallister, 1982), and the stoichiometry of natural Cr-Al-bearing spinels has also been a matter of recent debate (e.g. Wood and Virgo, 1989, Ballhaus et al., 1991, Carmichael, 1991). In addition, the stoichiometry of natural ilmenites too has been a focus of recent research (e.g. Virgo *et al.*, 1988; Lucas *et al.*, 1989). One important compositional parameter related to stoichiometry is the ferric iron/total iron ($Fe^{3+}/\sum Fe$) value. This value may be calculated from electron microprobe analytical data by assuming that the mineral structure has a perfect stoichiometry, for example with three cations per four anions for the spinel structure, or with two cations per three anions for the ilmenite structure. Stoichiometry calculations are based on the assumption of charge balance, with iron as the only cation with a variable valency state (e.g. Finger, 1972). It has been demonstrated that the $Fe^{3+}/\sum Fe$ value (or 'redox ratio') is a potential oxygen fugacity indicator, and a number of experimentally calibrated olivine-orthopyroxene-spinel oxygen geobarometers on this basis (e.g. O'Neill and Wall, 1987; Mattioli and Wood, 1988; Wood, 1990; Ballhaus *et al.*, 1991), an olivine-orthopyroxene-ilmenite oxygen geobarometer (e.g. Eggler, 1983; and herein Chapter 3), and an ilmenite-rutile oxygen geobarometer (herein Chapter 3) have been developed using the redox ratio of oxide minerals.

Ballhaus *et al.* (1990, 1991) and McGuire *et al.* (1989) demonstrated that for some spinels, Fe^{3+} calculated from electron microprobe analyses, assuming stoichiometry, agreed well with Fe^{3+} independently measured by Mössbauer spectroscopy. On the other hand, Wood and Virgo (1989) showed that certain electron microprobe analytical correction routines give systematic errors in calculated Fe^{3+} of spinels when compared to the results of Mössbauer spectroscopy. Virgo *et al.* (1988) showed that for ilmenite samples from four kimberlite localities the values of Fe^{3+} calculated from electron microprobe analyses assuming stoichiometry were consistently higher than those derived

from Mössbauer data. In contrast, Lucas *et al.* (1989) concluded that the Fe^{3+} content of kimberlitic ilmenites determined by Mössbauer spectroscopy compared well with Fe^{3+} values calculated from electron microprobe analyses assuming stoichiometry. However, a closer inspection of their data indicate that some of the documented ilmenites may have a significant non-stoichiometric component (cf. table 18.1b).

Since natural spinels and ilmenites often occur as small grains, inclusions or intergrowths in other minerals, Mössbauer spectroscopy cannot be widely applied, as it requires a relatively large sample size. To overcome this problem, an oxygen measurement technique using an electron microprobe has been developed, which allows an accurate assessment of stoichiometry and Fe^{3+} content calculation in individual spinel and ilmenite grains.

This chapter presents the results of oxygen analyses of chromium-rich spinels having broad compositional similarities from both high and low pressure-derived mantle-derived suites, and of mantle-derived magnesium-rich ilmenites from a number of kimberlites. Spinels are widely used as petrogenetic indicators. High chromium xenocrystic spinels found in kimberlites and lamproites (magnesiochromites with $Cr^{\#}=100*Cr/(Cr+Al)$ of 70-95, $Mg^{\#}=100*Mg/(Mg+Fe^{2+})$ of 50-80 and $Fe^{3+}/\sum Fe<0.3$) are often used as diamond-indicators (e.g. Haggerty, 1979; Ramsay, 1992; Kamperman *et al.*, 1993). A typical feature of many diamond-indicator spinels is that, when recalculated from metal-oxide analyses assuming stoichiometry, all Fe is present as Fe^{2+} and small amounts of Cr may also be present as Cr^{2+} (e.g. Haggerty, 1979). Such compositional features are believed to be consistent with their formation in the upper mantle at the high-pressure, reduced conditions of diamond stability (e.g. Haggerty, 1986).

High-chromium spinels from primitive subduction-related magmatic suites have $Fe^{3+}/\sum Fe$ values calculated according to stoichiometry that extend to very low values particularly in some boninitic suites (e.g. Sigurdsson *et al.*, 1993; Sobolev and Danyushevsky, 1994). If valid, the observed range would imply reduced crystallization conditions for many subduction-related suites in apparent contradiction of the generally accepted oxidized nature of magmas generated in subduction zones (e.g. Ballhaus *et al.*, 1991).

Magnesian ilmenites occur as xenocrysts and as phases within discrete xenoliths in kimberlites, and also as melt-derived crystallization products in kimberlites and olivine lamproites. The ilmenites are members of the hematite-ilmenite-geikielite mineral solid solution series. A typical characteristic of the kimberlitic ilmenites is the elevated MgO

content (>5 wt.%) and significant amounts of Cr_2O_3 may be present (>1 wt.%). Ferric iron in mantle-derived ilmenites is moderately low when calculated assuming stoichiometry (5-15 wt.% Fe_2O_3). Most mantle ilmenites are homogeneous in composition but several studies have indicated distinctive chemical trends. One of these trends, termed 'magmatic trend' (e.g. Haggerty *et al.*, 1979) or 'magnesium enrichment trend' (Mitchell, 1986), is one of increasing MgO and Cr_2O_3 content coupled with decreasing or constant Fe_2O_3. The majority (>90 %) of mantle ilmenite xenoliths from kimberlites belonging to the magmatic trend are relatively reduced and lie between approximately 25 and 60 mole % geikielite and, assuming stoichiometry, 10 and 20 mole % hematite (Haggerty, 1991). The mineral composition data have been employed to estimate an oxygen fugacity of the upper mantle between 10^{-6} and 10^{-7} bars at 30 kbar and 1230-1300 °C which is equivalent to WM-FMQ (Haggerty, 1990).

The oxygen measurement technique has been used here to demonstrate that non-stoichiometry is a common feature of oxide minerals, and the possibility of such mineral non-stoichiometry must be taken into account in petrological applications.

2.2 Analytical method

2.2.1 Design of analytical routine

The USNM 111989 gahnite from Brazil (e.g. Jarosewich *et al.*, 1980) was used as a natural mineral standard for the calibration of oxygen. This standard was analysed for oxygen by fast neutron activation analysis (FNAA, e.g. McGuire *et al.*, 1992), and O_{FNAA} of 35.20 wt.% (1σ 0.57) compares well with $O_{calculated}$ (from electron microprobe metal-oxide analyses with all iron as FeO) of 34.92 wt.%, suggesting that the spinel standard is stoichiometric (McGuire *et al.*, 1992). The average value of 35.06($\pm$0.15) wt.% has been accepted in this study as the gahnite oxygen content. The gahnite standard has a mean atomic number ($Z_{calculated}$ = 16.10) which is comparable to that of chromium-rich spinels (e.g. $Z_{calculated}$ = 16.29 for USNM 117075 chromite standard, Jarosewich *et al.*, 1980).

All oxygen analyses were performed at the University of Tasmania in Hobart on a Cameca SX-50 electron probe microanalyser (EPMA), equipped with one inclined and two vertical wavelength-dispersive spectrometers (WDS), with a total of eight analysing crystals. A PC1 W/Si (2d = 6 nm) multilayer crystal in the inclined spectrometer was used for measurements of oxygen. The remaining spectrometers were set with TAP and LiF analysing crystals. A multi-purpose analytical routine designed to analyse the oxygen content of minerals is described in Table 2.1.

Table 2.1: Details of the oxygen analytical label.

Element	Crystal	Mineral Standard
O K_α	PC1	USNM 111989 gahnite
Mg K_α	TAP	USNM 117075 chromite
Al K_α	TAP	USNM 111989 gahnite
Si K_α	TAP	USNM R17701 quartz
Ti K_α	LiF	Astimex MIMN 25-53 rutile
V, K_α	LiF	Vanadium metal
Cr K_α	LiF	USNM 117075 chromite
Mn K_α	LiF	Astimex MIMN 25-53 rhodonite
Fe K_α	LiF	USNM 96189 ilmenite
Ni K_α	LiF	Astimex MIMN 25-53 nickel silicide
Zn K_α	LiF	USNM 111989 gahnite

Table 2.2: Metal-oxide and oxygen analyses of standard USNM spinels.

	USNM 111989 gahnite			USNM 117075 chromite				
Oxides (wt.%)	Quoted values	Cameca SX-50 (Uni. Tas.) (n=18)		Quoted values	Cameca SX-50 (Uni. Tas.) (n=7)		Cameca SX-50 (Melb. Uni.) (n=9)	
SiO_2	-	dbl	(-)	0.00	dbl	(-)	0.02	(0.02)
TiO_2	-	dbl	(-)	0.00	0.12	(0.02)	0.09	(0.02)
Al_2O_3	55.32	55.10	(0.16)	9.92	9.69	(0.09)	9.64	(0.11)
Cr_2O_3	-	dbl	(-)	60.50	60.72	(0.25)	60.66	(0.60)
Fe_2O_3	0.66	0.54	(0.23)	3.45	3.58	(0.11)	3.34	(0.31)
FeO	1.38	1.43	(0.20)	9.93	9.69	(0.16)	10.01	(0.36)
FeO_{total}	1.97	1.91	(0.05)	13.04	12.91	(0.12)	13.02	(0.18)
MnO	0.37	0.42	(0.05)	0.11	0.17	(0.04)	0.08	(0.06)
MgO	-	0.03	(0.01)	15.20	15.31	(0.10)	15.15	(0.11)
NiO	-	dbl	(-)	0.00	0.18	(0.03)	na	(-)
ZnO	42.50	42.09	(0.33)	0.00	0.04	(0.04)	0.04	(0.03)
Total	100.16	99.55	(0.36)	98.77	99.14	(0.22)	98.68	(0.64)
$\Sigma_{cations}$	3.006	3.005	(0.003)	3.032	3.033	(0.001)	3.031	(0.003)
$O_{measured}$	35.20	34.79	(0.37)	na	33.03	(0.34)	na	(-)
$O_{calculated}$	34.99	34.80	(0.10)	33.08	33.13	(0.08)	33.01	(0.19)
O_{ratio}	1.006	1.000	(0.01)	-	0.997	(0.01)	-	(-)
$Fe^{3+}/\Sigma Fe$	0.299	0.253	(0.009)	0.238	0.250	(0.010)	0.231	(0.015)

Notes: Chromite major element data was obtained with the Cameca SX-50 electron microprobe at the University of Tasmania and Melbourne University. Quoted values are from Jarosewich et al. (1980). Values in parentheses represent standard deviations. bdl = below detection limit; na = not analysed; - and (-) = data not available. FeO_{total} is total measured iron; Fe_2O_3 and FeO values are determined assuming spinel stoichiometry. Totals are calculated for all iron as FeO_{total}; Σcations is total cation sum for four anions, calculated assuming all iron as FeO_{total}. $O_{measured}$ quoted for the gahnite standard was determined by FNAA with a standard deviation of 0.57 (McGuire et al., 1992). $O_{calculated}$ was calculated using Fe_2O_3 and FeO values. $O_{ratio} = O_{measured} \div O_{calculated}$. $Fe^{3+}/\Sigma Fe$ is calculated from cation data assuming stoichiometry. Chromite data for Cameca SX-50 at Melbourne University has 0.17 wt.% NiO assumed for oxygen and cation calculations.

Analyses were performed at 15 keV accelerating voltage, an electrical beam current of 20 nA, and a beam diameter varying from 1 to 10 μm at a 10,000x magnification. Oxygen was analysed at the beginning of each mineral analysis; counting time was 40 seconds on the peak and 20 seconds on the background measured on both sides of the analytical peak. Cations were analysed according to details described in Appendix B1. Concentrations were calculated from relative peak intensities using the PAP matrix correction procedure. Pouchou and Pichoir (1991) tested the PAP matrix correction model against the ZAF matrix correction model in quantitative microanalysis, and concluded that the PAP correction method is more suitable for the treatment of low energy X-ray intensities. On the natural gahnite standard containing 35.06 wt.% oxygen, the analytical conditions yielded a peak to background ratio for O of 93, comparable to that of Al (82) and better than Zn (62).

Probe mounts of mineral grain composites under investigation were made using cold-set epoxy. Care was taken to obtain a high quality polish, using various grades of diamond polishing paste. A probe mount, including the gahnite and other oxygen standards (McGuire *et al.*, 1992), was prepared in a similar fashion. The average standard grain was 1-2 mm in diameter. Sample probe mounts and the standard probe mount were coated at the same time with a thin film of ultra high-purity carbon, ensuring uniformity of coating of standards and samples.

2.2.2 Analytical procedure

The oxygen standards were recalibrated at the beginning of each analytical session. The gahnite oxygen standard was checked at regular intervals (after each 5 to 10 analyses) during every analytical session, and crystal reverifications or recalibrations were made when the value of $O_{analysed}$: $O_{accepted}$ (i.e. the oxygen ratio) was <0.98 or >1.02. Each analysis quoted represents an average of two or three analytical points, always taken at the same area of the standard grain to avoid any possibility of incorporating standard nonhomogeneity. The unknown grains were analysed over very small areas (generally ~10 μm separated) and did not involve core to rim analyses, thus avoiding the possibility of grain nonhomogeneity. Analytical values quoted for unknown grains also represent an average of two or three analyses, and for oxygen and the major cations these values demonstrate a precision better than 2 rel.%. Table 2.2 illustrates the average metal-oxide and oxygen analyses of the USNM 111989 gahnite and the USNM 117075 chromite using the oxygen analytical routine. Values are shown together with quoted analytical values for the oxide standards.

Figure 2.1: (A) and (B) Correction method used for adjusting oxygen analytical results where a systematic standard shift occurred upward (A) or downward (B) during an analytical session. Oxygen data for a session were adjusted by an average correction factor calculated from the ratio (= oxygen ratio) of the measured oxygen content to the accepted oxygen content of 35.06 wt.% for the gahnite standard. (C) Correction method used for adjusting oxygen analytical results where standard drift occurred during an analytical session. The variable correction factor is shown for illustrative purposes. Oxygen data for a session was adjusted by a variable correction factor calculated from the oxygen ratio. The oxygen ratio between 0.98 and 1.02 indicates the range of acceptable measured oxygen values from the gahnite standard. See text for recalibration and reverification procedure where the ratio was less than 0.98 or greater than 1.02.

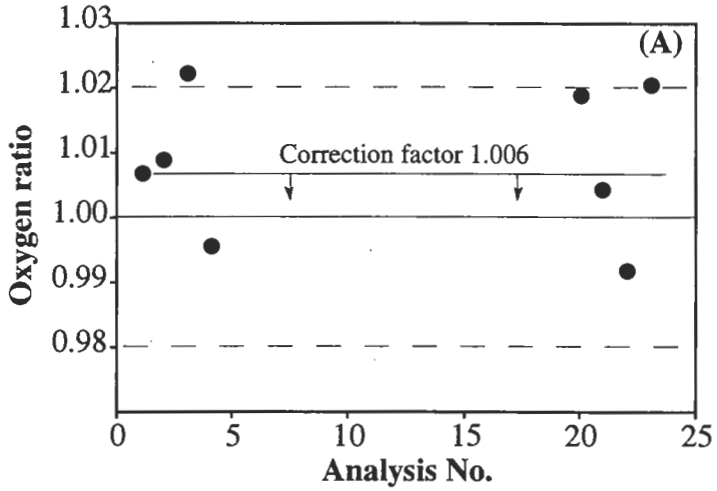
(A)
Oxygen ratio
1.03
1.02
1.01
1.00
0.99
0.98
Correction factor 1.006
0
5
10
15
20
25
Analysis No.

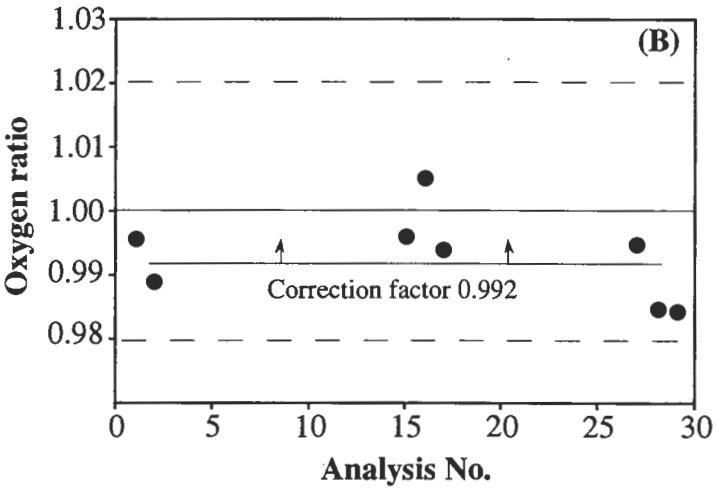
(B)
Oxygen ratio
1.03
1.02
1.01
1.00
0.99
0.98
Correction factor 0.992
0
5
10
15
20
25
30
Analysis No.

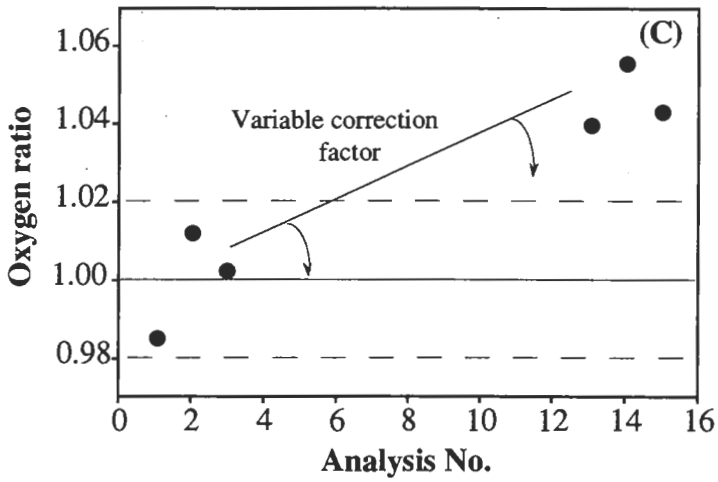
(C)
Oxygen ratio
1.06
1.04
1.02
1.00
0.98
Variable correction factor
0
2
4
6
8
10
12
14
16
Analysis No.

Oxygen data corrections (in terms of oxygen by wt.%) were made by adjusting the analytical results when a systematic shift of the oxygen ratio (Figure 2.1A and 2.1B) or consistent regular drift of the oxygen ratio occurred (Figure 2.1C) between two adjacent sets of standard analyses. To check that the corrected data obtained during intervals when drift occurred were reliable, analyses of some grains were repeated after verification, and compared with the corrected value. Table 2.3 illustrates the results of this procedure from analyses on the same spinel grain (an inclusion in olivine from a Tongan boninite) during an analytical session before and after verification. The results demonstrate an accuracy better than 2 rel.%.

The cation standards were checked at the beginning of each analytical session, and recalibrations were made when the value of $cation_{analysed}$: $cation_{standard}$ was <0.98 or >1.02. The USNM 117075 chromite standard was checked at the beginning and the end of each analytical session, and for the duration of a given analytical session cation drift did not exceed 1 rel.%. Only analyses with totals (which equals the sum of cations plus $O_{measured}$) between 98.5 and 101.0 wt.% were accepted. Analyses beyond this range were excluded for reasons of poor quality, which, when recalculated to cation analyses, would affect any conclusions on mineral non-stoichiometry. All of the excluded analyses came from spinel inclusions in olivine (refer to section 2.3.2). Although the reasons for occasionally obtaining poor totals from such spinel analyses have not been given a proper consideration here, there are two plausible explanations. It is suggested that it may be caused by (i) a poor contact between the inclusions and the host crystals (which can occur during grinding and polishing of samples as a result of different physical properties of inclusions and hosts minerals), or (ii) a poor contact between the host crystal and epoxy which can occur in instances where a probe mount contains many small mineral grains.

2.2.3 Accuracy of oxygen measurements

Repetitive analyses of the same grain performed during one analytical session (Figure 2.2) show deviations less than 2 rel.%. To enable comparison of the data analysed during different analytical sessions, several grains were analysed during different sessions. For example, two analyses for sample 5-28/OL5-SPA yielded 31.02 wt.% O and 31.16 wt.% O. An average of 31.09 wt.% was accepted as the O content. Similarly, for sample 5-28/OL8-SPB, oxygen contents determined were 32.62 wt.% O and 32.82 wt.% O, and an average O content of 32.72 wt.% was accepted. Finally, analyses of secondary standards with known oxygen content, ranging from 41.25 to 53.05 wt.% O, analysed by FNAA (Table 2.4 and Figure 2.3) all imply that there is no systematic error in the analytical routine introduced by PAP matrix corrections, and that the accuracy is 2 rel.%.

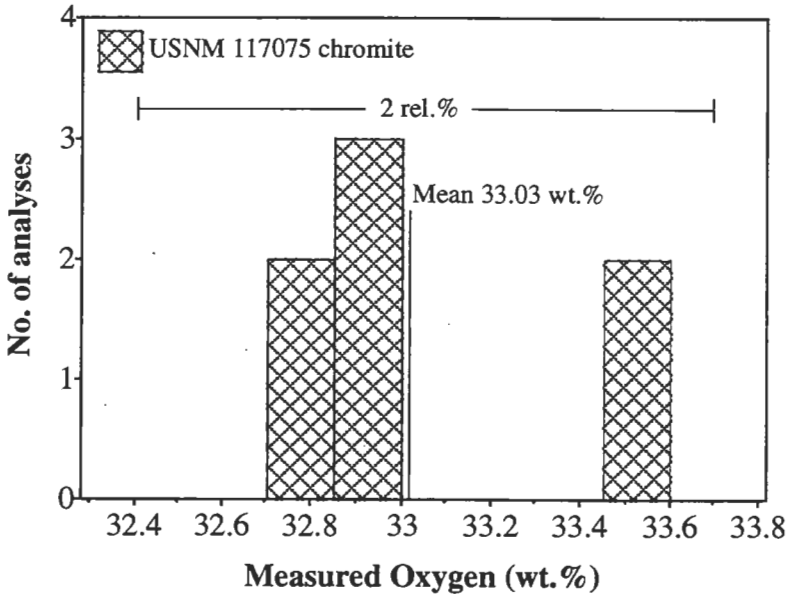

Figure 2.2: Frequency histogram of repetitive oxygen analyses (wt.%) of the USNM 117075 chromite during an analytical session. The chromite has an average oxygen content of 33.03 wt%. The error bar indicates 2 rel.% of the mean.

Table 2.3: Procedure for correcting oxygen data following standard drift during an analytical session.

No.	1	2	3	4	5	6	7
Analyses	1-3	11-12	13-15		16-18	19-20	21
Sample	Gahnite	5-28/OL10-SP	Gahnite	5-28/OL10-SP (corrected)	Gahnite (recalibrated)	5-28/OL10-SP (new)	Gahnite
O (wt%)	34.99 (0.39)	33.02 (0.08)	36.62 (0.25)	31.61	34.98 (0.27)	31.53 (0.26)	34.96
O_{ratio}	0.9980		1.0445		0.9977		0.9971

Notes: The oxygen analyses were obtained in one continuous session. The row 'Analyses' indicates the order of samples analysed during the session. Data shown are average values of corresponding points with data in parentheses representing standard deviations. O_{ratio} values are obtained by $O_{measured}/O_{accepted}$ for the gahnite standard of McGuire et al. (1992). See text for discussion.

Table 2.4: Chemical analyses of secondary silicate standards.

Sample	Quartz	Kaersutite	Albite	Olivine	Almandine
USNM no.	122838	131928	131705	131929	112140
O_{EPMA}	53.05	43.22	49.95	44.93	41.25
	(0.31)	(0.14)	(0.16)	(0.27)	(0.08)
O_{FNAA}	53.55	42.87	49.83	44.8	41.94
	(0.07)	(0.83)	(0.87)	(0.30)	(0.39)
O_{calc}	53.25	43.05	48.65	43.98	41.87
Si	46.74	18.51	31.82	19.58	17.95
Al		7.82	10.47		11.91
Fe^{2+}		0.56		6.86	19.78
Fe^{3+}		8.63	0.06		0.83
Mg		7.49		29.76	5.03
Mn		0.09		0.10	1.69
Ti		3.11			0.03
Cr					0.03
Ca		7.45	0.17	0.02	1.24
Na		2.09	8.49	0.01	0.09
K		1.19	0.22		
Ni				0.34	
Zn					
H		0.01			

Notes: O_{EPMA} values determined in this work using a Cameca SX-50 electron microprobe analyser. O_{FNAA} values determined by McGuire et al.(1992) using Fast Neutron Activation. O_{calc} values calculated by McGuire et al.(1992) assuming perfect charge balance and using measured H contents and $Fe^{3+}/\Sigma Fe$ values where applicable. Values in parentheses represent standard deviations.

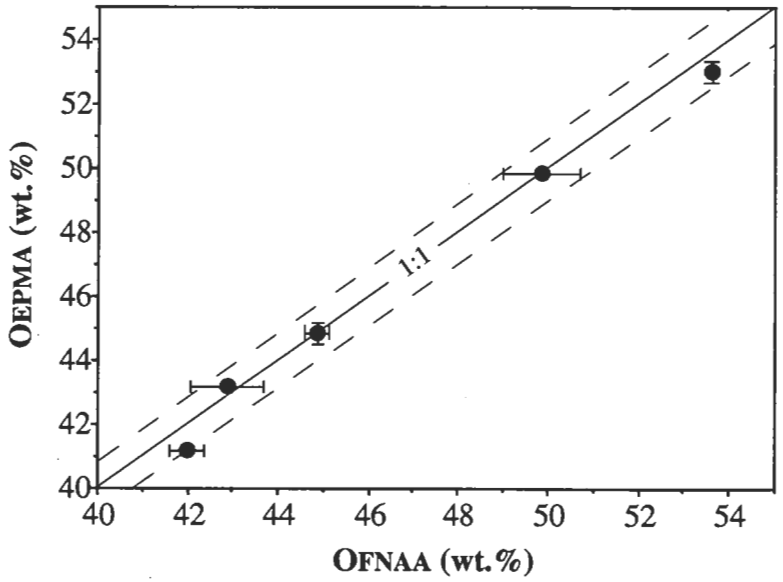

Figure 2.3: Comparison of oxygen (wt.%) of secondary standards (see Table 2.4 for details) measured by the Cameca SX-50 (O_{EPMA}), vs. oxygen (wt.%) measured using the fast neutron activation technique (O_{FNAA}, McGuire et al., 1992). The dashed lines indicate 2 rel.% of the mean. Error bars (included where larger than the size of the symbol) indicate one standard deviation.

2.3 Results

The following parameters are used in the presentation of the analytical results:
(a) $\Sigma_{cations}$ is the sum of cations calculated on the basis of 4 oxygens for spinels, and 3 oxygens for ilmenites, assuming that all Fe is present as Fe^{2+} and all Cr is present as Cr^{3+}.
(b) $Fe^{3+}/\sum Fe$ (st) is the redox ratio of oxide minerals, determined from ferric and ferrous iron contents calculated from metal-oxide compositions assuming stoichiometry.
(c) $O_{calculated}$ is wt.% O calculated from metal-oxide compositions assuming stoichiometry.
(d) $\Delta O = (O_{measured}-O_{calculated})$. This variable is the deviation from stoichiometry; a negative value for ΔO indicates that less trivalent cations are present than calculated from stoichiometry, that oxygen vacancies are present, or that there are more divalent cations present than calculated from stoichiometry. In contrast, a positive value for ΔO indicates that more trivalent cations are present than calculated from stoichiometry and that a divalent cation deficiency exists in the mineral structure. In some tables and illustrations, the term O_{ratio} ($=O_{measured}\div O_{calculated}$) has been used as an alternative parameter to illustrate analytical results. Where used, a value for O_{ratio} greater than unity indicates that more trivalent cations are present than calculated from stoichiometry and that a divalent cation deficiency exists in the mineral structure. On the other hand, a value of O_{ratio} less than unity indicates that less trivalent cations are present than calculated from mineral stoichiometry, that oxygen vacancies are present, or that there are more divalent cations present than calculated from stoichiometry.
(e) O_{max} is the calculated oxygen content assuming that all Fe is present as Fe^{3+}, all Cr as Cr^{3+}, all Mn as Mn^{2+}; O_{min} is the calculated oxygen content assuming all Fe is present as Fe^{2+}.

When Cr^{2+} is not present, $O_{measured}$ is expected to be between O_{max} and O_{min}; where $O_{measured}$ is less than O_{min}, this may indicate that, for example, Cr^{2+} is present in spinel. Assuming that no other elements but Fe and Cr can be present in variable oxidation states (+2 or +3), $O_{measured}$ is not expected to be larger than O_{max}.

Because oxygen has a low atomic number compared with Fe, the established 2 rel.% accuracy of the oxygen analyses corresponds to very large differences in calculated Fe^{2+} and Fe^{3+}. For example, 2 rel.% oxygen for a typical high-chromium spinel is ~0.65 wt.%, which corresponds to 2.92 wt.% FeO or 2.16 wt.% Fe_2O_3. This demonstrates the danger of using individual oxygen analyses for estimations of real $Fe^{3+}/\sum Fe$ values and for the need to assess the possibility of non-stoichiometry. For these reasons, a statistical approach to the oxygen data obtained from mineral populations has been employed. The

average ΔO for a population is calculated when the difference between individual ΔO values does not exceed 2 rel.% of $O_{measured}$, and either (i): analysed spinels show similar cation contents (within the range of microprobe accuracy), or (ii): no correlation exists within a population between ΔO and cation concentrations. Where a good correlation exists between ΔO and cation concentrations (standard deviations less than 2 rel.% of oxygen concentrations), a line of best fit has been chosen to represent a sample population, rather than an average composition or selection of individual analyses.

Results are presented in full in Appendix C and are summarized in the following sections.

2.3.1 Diamond-indicator spinels

Five spinel grains from the Middle Proterozoic diamond-bearing Argyle olivine lamproite diatreme in the East Kimberley region of Western Australia were analysed (Jaques *et al.*, 1986). These spinels occur as ~1 mm xenocrysts in the lamproite matrix, and have been derived from depleted mantle harzburgites or dunites. The spinels are characterised by a very constant composition including oxygen, and the average of the analyses is shown in Table 2.5 (No. 1). According to the cation analyses, these spinels are stoichiometric with all Fe present as Fe^{2+}. Oxygen contents (in terms of ΔO) of the individual spinels are shown on Figure 2.4A. Variations between individual analyses are well inside the accuracy and an average of 31.83 wt.%. has been accepted as the O content of these spinels. Thus, the results lead to a ΔO value of +0.13 wt.%. Although this may indicate a low degree of non-stoichiometry with some Fe present as Fe^{3+}, it is suggested that the existing data are insufficient for such a conclusion, and rather, show a good agreement between cation and oxygen data. Both indicate that Argyle spinels are stoichiometric, with all iron present as Fe^{2+}.

It is also concluded that spinels from the Lower Proterozoic diamond-bearing Aries kimberlite diatreme in the Kimberley region, Western Australia (e.g. Edwards *et al.*, 1992) are stoichiometric, based on analyses of eight grains from a spinel concentrate. Like the Argyle spinels, these spinels also occur as ~1 mm xenocrysts in the kimberlite matrix, and are also interpreted as having been derived from depleted mantle assemblages and collected from the wall rocks during kimberlite ascent. Despite the fact that they are characterised by some significant variations in cation contents (Table 2.5, No. 2-6), the cation data indicate that, within error, all Fe is present as Fe^{2+} and the average spinel has ΔO of +0.05 wt.% (Figure 2.4A).

Table 2.5: Representative analyses of diamond indicator spinels.

No.	1		2	3	4	5	6
Locality	Argyle		Aries	Aries	Aries	Aries	Aries
Grain No.			No.13	No.8	No.12	No.11	No.5
Type	Lmp		Kmb	Kmb	Kmb	Kmb	Kmb
Si	0.04	(0.01)	0.02	0.02	0.05	0.02	0.02
Ti	0.02	(0.00)	0.03	0.00	0.14	0.23	0.02
Al	2.15	(0.47)	5.81	4.89	3.41	5.99	6.17
Cr	47.01	(0.87)	42.20	43.74	45.71	40.65	41.75
V	0.09	(0.01)	0.12	0.10	0.16	0.12	0.12
Fe	10.61	(0.21)	10.63	10.94	9.77	11.52	10.42
Mg	7.37	(0.04)	7.63	7.25	7.25	7.29	7.78
Mn	0.22	(0.04)	0.22	0.20	0.22	0.26	0.22
Ni	0.05	(0.02)	0.06	0.08	0.04	0.06	0.07
Zn	0.05	(0.04)	0.10	0.11	0.09	0.07	0.11
O	31.83	(0.35)	32.59	32.53	31.94	32.77	33.44
Total	99.43	(0.56)	99.40	99.86	98.77	98.98	100.12
$O_{calculated}$	31.70	(0.12)	32.91	32.62	32.02	32.53	33.06
ΔO	0.13	(0.21)	-0.32	-0.09	-0.08	0.24	0.38
$\Sigma_{cations}$	3.001		2.997	2.994	2.983	3.000	2.997
O_{min}	31.69		32.91	32.62	32.02	32.53	33.06
O_{max}	33.21		34.44	34.19	33.42	34.18	34.55
FeO (corr)	13.65		13.68	14.08	12.57	14.82	13.41
Fe_2O_3 (corr)	0		0	0	0	0	0

Notes: Kmb = kimberlite, Lmp = lamproite. Analysis No.1 is an average of five analyses of individual grains; numbers in brackets show the range of individual analyses. See the beginning of the Results section for the definition of parameters of spinel compositions used in this table. FeO (corr) = wt.% of FeO in spinels, calculated on the basis of oxygen measurements. Fe_2O_3 (corr) = wt.% of Fe_2O_3 in spinels, calculated on the basis of oxygen measurements.

Table 2.5 continued: Representative analyses of diamond indicator spinels.

Locality	Roberts Victor				Makanyene			
Type	Kmb				Kmb			
No.	7	8	9	10	11	12	13	14
Grain No.	303	402	406	410	307	004	006	105
Si	0.01	0.05	0.03	0.04	0.01	0.03	0.05	0.03
Ti	0.14	0.18	0.11	0.16	0.19	0.27	0.13	0.22
Al	5.07	3.14	4.38	3.96	4.87	3.82	4.01	4.51
Cr	42.37	43.69	44.15	44.05	41.43	42.27	41.90	42.61
V	0.12	0.07	0.20	0.12	0.17	0.10	0.10	0.10
Fe	11.86	12.69	10.54	10.35	13.43	12.90	12.44	10.78
Mg	7.92	7.90	7.93	8.39	7.18	7.69	8.09	8.45
Mn	0.28	0.28	0.24	0.11	0.18	0.22	0.21	0.18
Ni	0.05	0.13	0.06	0.06	0.05	0.07	0.08	0.10
Zn	0.07	0.05	0.04	0.11	0.10	0.08	0.05	0.04
O	32.36	32.28	32.79	33.27	32.29	32.13	32.57	33.33
Total	100.26	100.48	100.47	100.62	99.91	99.58	99.63	100.35
$O_{calculated}$	33.14	32.51	32.85	32.77	32.56	32.36	32.48	32.86
ΔO	-0.78	-0.23	-0.06	0.50	-0.27	-0.23	0.09	0.47
$\Sigma_{cations}$	3.018	3.035	3.004	3.014	3.021	3.031	3.037	3.020
O_{min}	32.95	32.14	32.81	32.62	32.33	32.03	32.08	32.64
O_{max}	34.65	33.96	34.32	34.11	34.26	33.88	33.87	34.19
FeO (corr)	13.5	12.97	13.22	11.99	15.24	13.61	12.44	11.9
Fe_2O_3 (corr)	1.95	3.74	0.38	1.47	2.27	3.32	3.96	2.18

Notes: Kmb = kimberlite. See the beginning of the Results section for the definition of parameters of spinel compositions used in this table. FeO(real) = wt.% of FeO actually present in spinels. Fe_2O_3(real) = wt.% of Fe_2O_3 actually present in spinels.

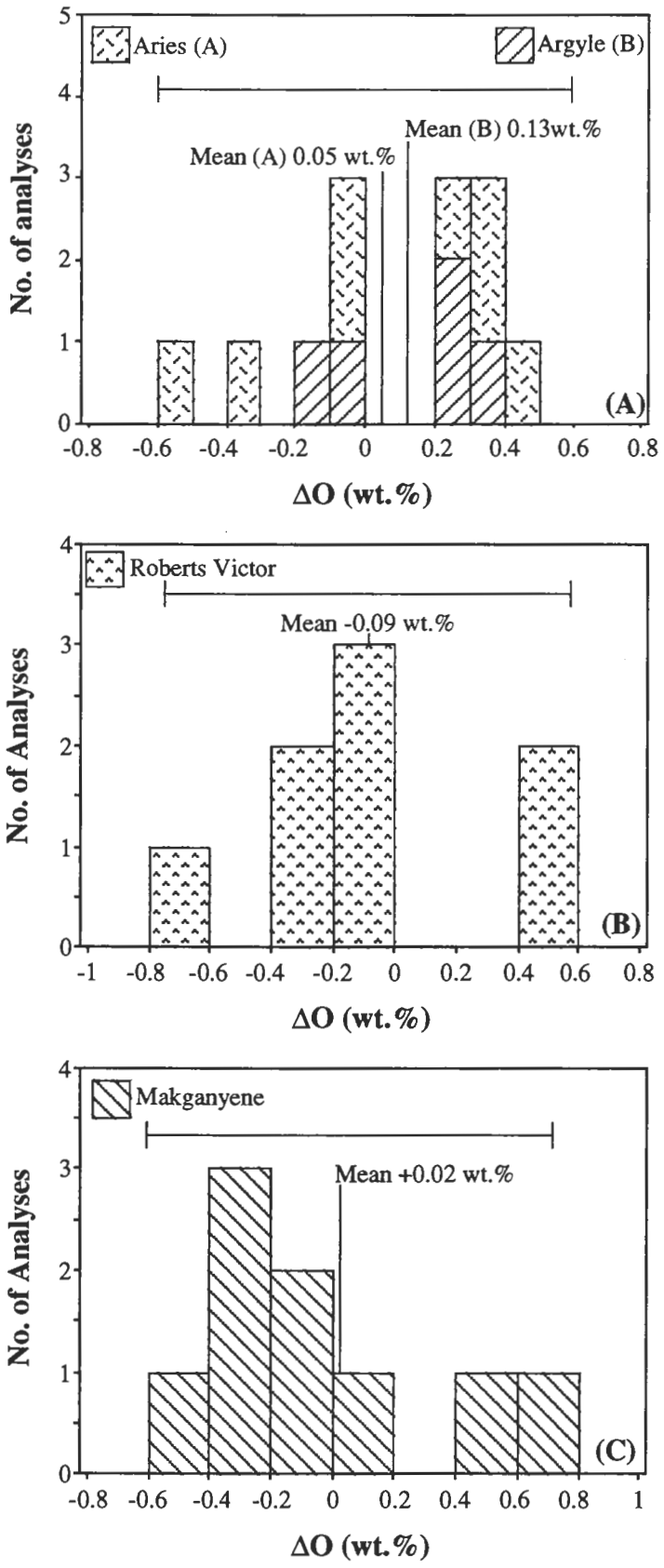

Figure 2.4: Frequency histogram of ΔO (wt.%) for spinels from (A) the Aries kimberlite and Argyle lamproite, (B) the Roberts Victor kimberlite and (C) the Makganyene kimberlite. The error bars indicate 2 rel.% of the mean.

Spinels from the Cretaceous diamond-bearing Roberts Victor and Makganyene kimberlite diatremes from the Kalahari craton in southern Africa (e.g. Gurney *et al.*, 1991) are also stoichiometric, based on analyses of eight grains from a spinel concentrate from each diatreme. Like the diamond-indicator spinels described above, the spinels from the diamond-bearing kimberlite diatremes occur as small xenocrysts in a kimberlite matrix, and their origin is also believed to be a depleted mantle source. The spinels are characterised by total cation contents >3 (per 4 oxygens) with Fe present as Fe^{2+} and Fe^{3+} (Table 2.5, No. 7-10 and 11-14 respectively). Although these spinels display some significant variations in cation contents and show a range of ΔO, no correlation between ΔO and spinel composition can be shown. Rather, the cation data show that, within error, the average spinel for the Roberts Victor kimberlite spinels has ΔO of -0.09 wt.% (Figure 2.4B), and the average spinel for the Makganyene kimberlite has ΔO of +0.02 wt.% (Figure 2.4C).

2.3.2 Spinel inclusions in olivine from primitive subduction related magmas

Chromium-rich spinels are common liquidus minerals in primitive subduction-related suites. Usually they are found as inclusions (up to 50 μm in diameter) in olivine phenocrysts. Two suites described here, low-Ti tholeiites from the Hunter Fracture Zone, North Fiji Basin (e.g. Sigurdsson *et al.*, 1993) (Table 2.6, No. 1-5), and Tongan high-Ca boninites (e.g. Sobolev and Danyushevsky, 1994) (Table 2.6, No. 6-10), are characterised by a large range of olivine compositions and subsequent variations in the compositions of spinel inclusions (Table 2.6, Figure 2.5). All analysed spinels have $\Sigma_{cations}$ >3 implying the presence of Fe^{3+} if these spinels are stoichiometric. Both suites show a negative correlation between $Cr^{\#}$ and $Fe^{3+}/\Sigma Fe$ values calculated assuming stoichiometry (Figure 2.5A). Spinels from the Hunter Fracture Zone show a range of $Fe^{3+}/\Sigma Fe$ (st) values from 0.27-0.37, and spinels from Tongan boninites show a range from 0.16-0.34.

Unlike the diamond-indicator spinels, oxygen data for spinel inclusions in olivine phenocrysts from subduction-related suites show wide deviations from mineral stoichiometry ($-1.0<\Delta O<+1.9$), deviations which are real with respect to the accuracy of the technique. Also unlike the diamond-indicator spinels, these spinels show a good correlation between non-stoichiometry and spinel composition (Figure 2.5B and 2.5C). Spinel $Fe^{3+}/\Sigma Fe$ values calculated according to stoichiometry correlate with ΔO. This leads to corrected (i.e. actual) $Fe^{3+}/\Sigma Fe$ values that are significantly higher for spinels with low calculated $Fe^{3+}/\Sigma Fe$ (st) (i.e. apparently reduced).

Table 2.6: Representative analyses of spinel inclusions in olivine phenocrysts from primitive subduction-related magmas.

No.	1	2	3	4	5	6	7	8	9	10
Grain No.	115-4/H1 OL80-SP	115-4/H1 OL15E-SP	115-4/H1 OL88-SP	115-4/H1 OL77A-SP	115-4/H1 OL19-SPA	5-24/ OL3-SP	5-24/ OL3A-SPC	5-24/ OL27-SP	5-24/ OL4-SPA	5-24/ OL4-SPB
Type	Thol	Thol	Thol	Thol	Thol	Bon	Bon	Bon	Bon	Bon
Si	0.04	0.05	0.05	0.04	0.03	0.03	0.03	0.03	0.04	0.05
Ti	0.13	0.07	0.05	0.06	0.10	0.07	0.06	0.02	0.05	0.04
Al	6.57	5.20	5.21	5.22	5.57	3.29	3.45	3.47	3.28	3.23
Cr	34.59	38.29	36.78	37.07	36.89	41.97	41.24	40.94	44.21	43.03
Fe	18.14	15.97	17.26	16.86	16.57	15.44	15.54	16.01	10.72	11.13
Mg	6.98	7.35	6.80	6.98	7.04	7.07	7.07	6.88	8.43	8.25
Mn	0.22	0.28	0.21	0.22	0.20	0.20	0.23	0.24	0.16	0.17
Ni	0.07	0.09	0.05	0.06	0.08	0.06	0.06	0.06	0.04	0.09
Zn	0.09	0.03	0.06	0.02	0.05	0.06	0.03	0.08	0.09	0.04
O	32.67	32.62	32.64	32.85	33.14	32.06	32.08	32.20	33.15	32.71
Total	99.49	99.96	99.10	99.37	99.68	100.26	99.79	99.93	100.17	98.73
$O_{calculated}$	32.72	32.65	32.00	32.12	32.29	32.16	32.01	31.91	32.43	31.91
ΔO	-0.05	-0.03	0.64	0.73	0.85	-0.10	0.07	0.29	0.72	0.80
$\Sigma_{cations}$	3.079	3.062	3.071	3.070	3.065	3.053	3.056	3.059	3.027	3.033
O_{min}	31.88	31.98	31.26	31.40	31.61	31.60	31.42	31.30	32.15	31.56
O_{max}	34.48	34.27	33.73	33.81	33.98	33.81	33.65	33.59	33.68	33.15
FeO (st)	15.85	14.60	15.57	15.18	15.20	14.80	14.75	15.07	11.25	11.16
Fe_2O_3 (st)	8.32	6.61	7.38	7.23	6.80	5.63	5.83	6.14	2.83	3.51
$Fe^{3+}/\Sigma Fe$ (st)	0.321	0.289	0.299	0.300	0.287	0.255	0.262	0.268	0.185	0.221
FeO (corr)	16.26	14.83	9.78	8.61	7.56	15.70	14.08	12.49	4.79	3.98
Fe_2O_3 (corr)	7.87	6.36	13.82	14.53	15.29	4.63	6.57	9.01	10.01	11.49
$Fe^{3+}/\Sigma Fe$ (corr)	0.303	0.278	0.560	0.603	0.645	0.210	0.296	0.394	0.653	0.722
Fo	88.00	89.44	88.21	88.55	89.04	88.70	88.70	88.62	93.26	93.26

Notes: Thol = tholeiite, Bon = boninite. Analysis No.1-5 = spinel inclusions from low-Ti tholeiites from the Hunter Fracture Zone. Analysis 6-10 = spinel inclusion from high-Ca boninites from the northern Tonga Trench. See the beginning of the Results section for the definition of parameters of spinel compositions used in this table. (st) stands for values calculated assuming stoichiometry from cation analyses. (corr) stands for values calculated on the basis of oxygen data. During cation analyses of these spinels, vanadium was not included in the analytical label. A value of 0.15 wt% for V_2O_3 is assumed in all recalculations. This assumption is based on results obtained by Sobolev and Danyushevsky (1994) and Danyushevsky (unpubl.) who analysed a large number of spinel inclusions from the same samples. Results indicated a value for V_2O_3 of 0.15±0.07 wt.%, with no correlation to other element concentrations. Fo indicates the composition of the olivine host mineral.

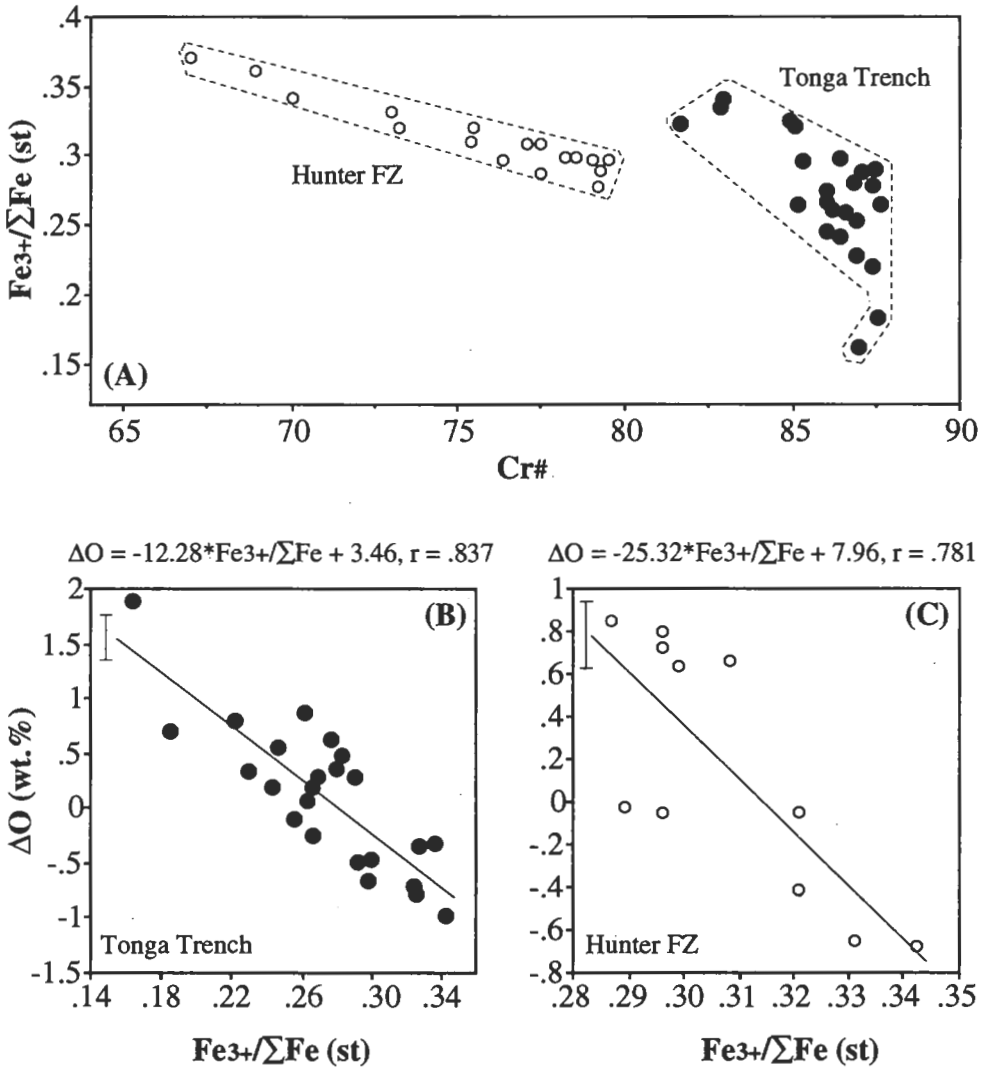

Figure 2.5: (A) $Fe^{3+}/\sum Fe$ (st) vs. $Cr^{\#}$ for spinel inclusions in olivine from low-Ti tholeiites from the Hunter Fracture Zone and Tongan high-Ca boninites. $Fe^{3+}/\sum Fe$ (st) is calculated assuming spinel stoichiometry. (B) and (C) ΔO (wt.%) vs. $Fe^{3+}/\sum Fe$ (st) for spinel inclusions from the Tongan boninites and the Hunter Fracture Zone tholeiites respectively. The equations for ΔO as a function of $Fe^{3+}/\sum Fe$ (st) represents lines of best fit. The error bars indicate 2 rel.% of the mean.

Results obtained are of particular importance for estimating MgO contents and, as a result, liquidus temperatures of primitive subduction-related melts which were in equilibrium with chromium-rich spinels and their olivine hosts. Indeed, the $Mg^{\#}$ of such melts can be inferred using well-known parameters of olivine-melt equilibria (e.g. Ford et al., 1983). Thus MgO contents are a function of Fe^{2+} concentrations which in turn are dependent on oxygen fugacity (e.g. Kress and Carmichael, 1988). The low $Fe^{3+}/\sum Fe$ values calculated in the most primitive chromium-rich spinels according to stoichiometry will lead to erroneously low fO_2 values when calculated using a spinel oxygen geosensor. This in turn will lead to erroneously high Fe^{2+} and, as a result, high MgO in primitive subduction-related melts.

The analytical results indicate that oxygen fugacity cannot be correctly estimated assuming spinel stoichiometry and the use of cation compositions of chromium-rich spinels from primitive subduction-related magmas. Accurate determinations of fO_2 for these suites remain a problem, as even correctly known cation compositions of non-stoichiometric spinels are not sufficient for fO_2 calculation, because the effect of cation deficiency (or excess) on the activity of elements in chromium-rich spinels is unknown.

2.3.3 Spinels from metamorphosed volcanics

Two populations of chromium-rich spinel from old volcanic complexes of boninitic affinity, the Middle Proterozoic greywackes and volcanics from the greenschist facies Glengarry Group in the Peak Hill area, central Western Australia (e.g. Hynes and Gee, 1986), and the weakly metamorphosed Upper-Middle Cambrian Heazlewood River Ultramafic Complex, Western Tasmania (e.g. Peck, 1990), were also analysed. Although a magmatic origin has been suggested for both spinel populations, these spinels have undergone metamorphic re-equilibration, and in this respect differ from those described in the previous sections.

Eight spinels were investigated from a spinel concentrate from the Peak Hill area. These spinels are characterised by very high Cr_2O_3 contents (61 to 71 wt.%), variably high Mn and Zn and low Fe contents (Table 2.7, No. 1-8) compared to the previously discussed spinels. According to cation analyses with $\Sigma_{cations} < 3$ they have all Fe present as Fe^{2+}. Unlike diamond- indicator and boninitic spinels, these spinels have very high positive ΔO (+1.8 to +3.0 wt.%) assuming spinel stoichiometry, and a good correlation exists between ΔO and Zn, Fe and Cr content (Figure 2.6, Table 2.7). With the exception of one spinel grain (Table 2.7, Sample No. 405), the $O_{measured}$ is significantly higher than O_{max}, which requires that all Mn is present as Mn^{3+} and that some Cr is present as Cr^{4+} in order to achieve charge neutrality.

Table 2.7: Representative analyses of spinels from metamorphosed volcanics

No.	1	2	3	4	5	6	7	8	9	
Locality	Peak Hill	Peak Hill	Peak Hill	Peak Hill	Peak Hill	Peak Hill	Peak Hill	Peak Hill	Heazlewood	
Grain No.	507	405	202	304	204	806	708	203	n=8	
Si	0.04	0.01	0.03	0.02	0.03	0.03	0.04	0.03	0.03	(0.01)
Ti	0.01	0.09	0.07	0.01	0.02	0.01	0.05	0.02	0.02	(0.00)
Al	1.46	2.76	1.69	1.67	1.54	1.46	1.79	1.85	3.20	(0.26)
Cr	48.31	42.00	47.73	47.40	46.76	47.39	44.72	45.89	42.56	(0.67)
V	0.01	0.01	0.01	0.01	0.01	0.01	0.01	0.01	0.04	(0.00)
Fe	9.39	19.20	8.16	9.87	11.49	10.67	14.91	12.29	17.28	(1.11)
Mg	7.08	2.05	7.52	6.50	5.66	5.52	3.46	5.20	5.26	(0.23)
Mn	0.53	1.41	0.90	0.99	0.81	1.04	0.83	0.60	0.24	(0.05)
Ni	0.12	0.01	0.10	0.06	0.05	0.10	0.05	0.00	0.04	(0.04)
Zn	0.06	0.56	0.43	0.27	0.36	0.77	0.95	1.37	0.07	(0.03)
O	33.04	31.33	33.37	33.06	32.76	32.88	32.07	33.33	31.88	(0.62)
Total	100.04	99.42	99.99	99.84	99.48	99.87	98.87	100.57	100.61	(0.68)
$O_{calculated}$	31.25	29.36	31.34	30.91	30.40	30.47	29.39	30.37	31.38	(0.28)
ΔO	1.79	1.97	2.03	2.15	2.36	2.41	2.68	2.96	0.50	(0.65)
$\Sigma_{cations}$	2.988	3.002	2.992	2.989	2.989	2.982	2.985	2.994	3.030	
O_{min}	31.25	29.36	31.34	30.91	30.40	30.47	29.39	30.37	31.06	
O_{max}	32.59	32.11	32.50	32.33	32.04	32.00	31.53	32.13	33.53	
FeO (st)	12.08	24.57	10.50	12.69	14.78	13.73	19.19	15.81	19.34	
Fe_2O_3 (st)	-	-	-	-	-	-	-	-	3.21	
$Fe^{3+}/\Sigma Fe$ (st)		-							0.130	
FeO (corr)	-	7.00	-	-	-	-	-	-	14.89	
Fe_2O_3 (corr)	13.43	19.67	11.66	14.11	16.42	15.26	21.32	17.57	8.16	
$Fe^{3+}/\Sigma Fe$ (corr)	-	0.717	-	-	-	-	-	-	0.330	

Notes: Analysis No. 9 is an average of eight analyses of individual grains; numbers in brackets show the range of individual analyses. See the beginning of the Results section for the definition of parameters of spinel compositions used in this table. (st) stands for values calculated assuming stoichiometry from cation analyses. (corr) stands for values calculated on the basis of oxygen data.

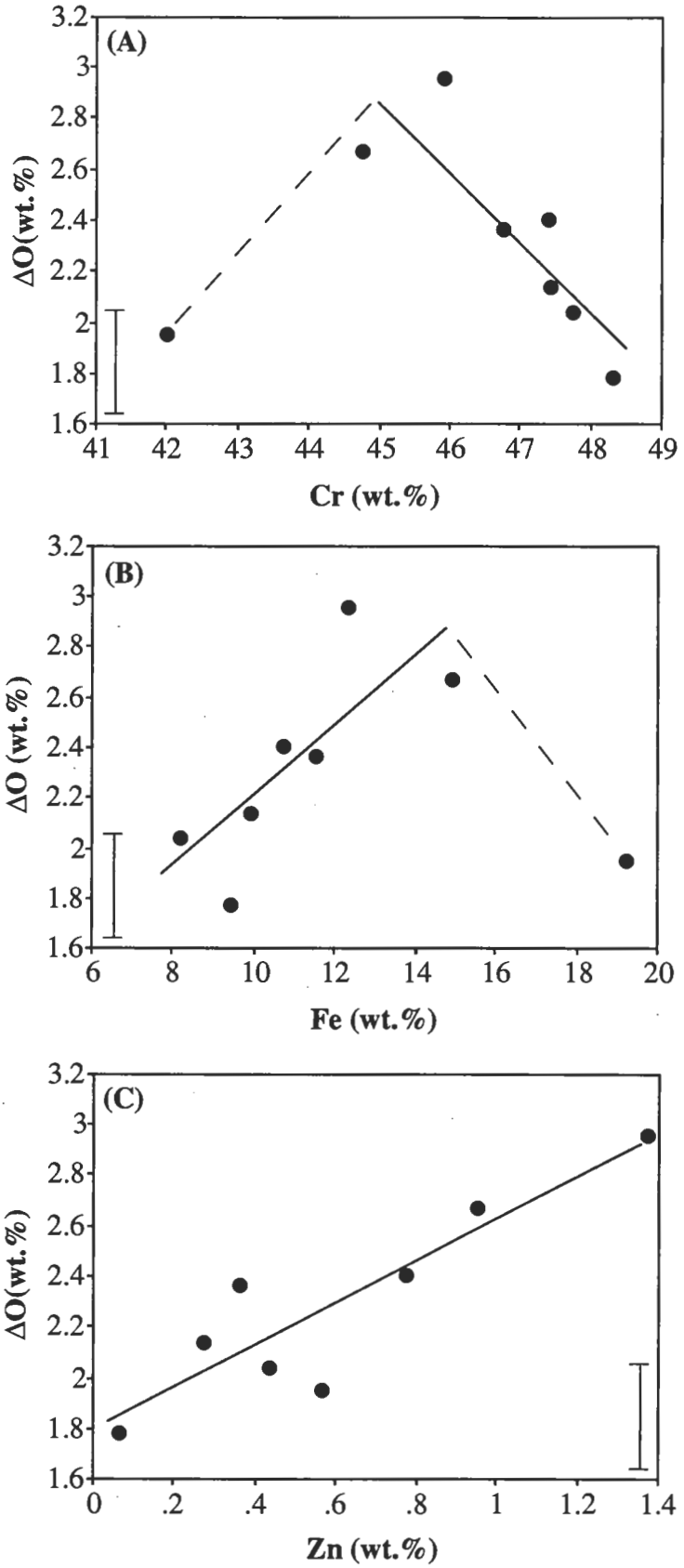

Figure 2.6: (A) ΔO (wt.%) vs. Cr (wt.%), (B) ΔO (wt.%) vs. Fe (wt.%) and (C) ΔO (wt.%) vs. Zn (wt.%) for Peak Hill spinels. The error bars indicate 2 rel.% of the mean.

Table 2.8: Peak Hill spinel recalculated in terms of endmembers.

Grain No.	507	708	304	204	202	806	203
$R^{2+}(R^{4+}R^{2+})O_4$	0.0032	0.0050	0.0018	0.0030	0.0050	0.0025	0.0030
$R^{2+}(R^{3+})_2O_4$	0.5708	0.3094	0.5343	0.4707	0.6137	0.4745	0.4612
$\square_{0.33}(R^{3+})_{2.67}O_4$	0.4260	0.6856	0.4639	0.5263	0.3813	0.5230	0.5358
$O_{calculated}$ (wt.%)	32.63	31.61	32.43	32.12	32.60	32.11	32.18
$O_{measured}$ (wt.%)	33.04	32.07	33.06	32.76	33.37	32.88	33.33
ΔO	+0.41	+0.46	+0.63	+0.64	+0.77	+0.77	+1.15
% maghemite	52.4	79.6	61.7	68.3	57.2	71.3	81.8
$Cr^{4+}/\sum Cr$	0.050	0.062	0.080	0.084	0.100	0.100	0.157

Notes: $R^{2+}(R^{4+}R^{2+})O_4$ is the ulvospinel-type endmember, $R^{2+}(R^{3+})_2O_4$ is the ordinary spinel endmember and $\square_{0.33}(R^{3+})_{2.67}O_4$ is the maghemite-type endmember, where $\square$ indicates a site vacancy. In all cases R^{2+} represents the divalent cations (i.e. Mg, Zn and Ni), R^{3+} represents the trivalent cations (i.e. Al, Cr, V, Fe and Mn), and R^{4+} represents the tetravalent cations (i.e. Si and Ti). It is assumed that all Fe is present as Fe^{3+} and Mn is present as Mn^{3+}. $O_{calculated}$ values are determined on the basis of the spinel endmembers shown in this table. % maghemite indicates the '$\square_{0.33}(R^{3+})_{2.67}O_4$ in structure' as calculated from the oxygen data, and takes into account Mn as Mn^{3+} and some Cr as Cr^{4+}. $Cr^{4+}/\sum Cr$ indicates the ratio of Cr cations in the tetravalent oxidation state to the total Cr cation content, as calculated from the oxygen data.

The recalculation of the Peak Hill spinels in terms of a maghemite-type endmember component, and the assumption that all Mn is present as Mn^{3+}, still indicates excess oxygen (positive ΔO), suggesting that Cr may indeed be present in a higher oxidation state (Table 2.8). Although the presence of Cr^{4+} implies a very high oxidation state, minor amounts of Cr^{4+} have been reported in other minerals (e.g. rutile, Ishida *et al.*, 1990). The relationships between oxygen and cations indicate that these spinels deviate greatly from spinel stoichiometry, and have compositions that lie between the Me_3O_4 and $\square_{0.33}Fe_{2.67}O_4$ - $\square_{0.33}Cr_{2.67}O_4$ (maghemite or cubic γ-Fe_2O_3, and the Cr-bearing equivalent of maghemite) endmembers. To estimate this degree of non-stoichiometry of each analysis, 'the percent of $\square_{0.33}Me^{III}_{2.67}O_4$' (where $\square$ represents a site vacancy, and Me^{III} represent trivalent cations) has been re-calculated on the basis of the actual oxygen analyses, and has been found to vary between approximately 50 and 80 mol % (Table 2.8, Figure 2.7).

Spinels from the Heazlewood Complex most likely occurred originally as inclusions in mafic silicate phenocrysts in boninitic lavas. Eight analysed grains have very similar cation compositions and an average of the analyses is shown in Table 2.7 (No. 9). Oxygen data show variations inside 2 rel.% of $O_{measured}$, with a mean of ΔO = +0.5 wt.% (Figure 2.8), and as no correlation was observed between cation compositions and ΔO variations, an average of 31.88 wt.% O has been accepted as the oxygen content of these spinels. The oxygen data indicate that Heazlewood spinels are significantly non-stoichiometric having an excess of 4.95 wt.% $\square_{0.33}Fe_{2.67}O_4$ compared to stoichiometry.

2.3.4 Magnesium-rich ilmenite xenocrysts from kimberlites

Magnesium-rich ilmenites are commonly found as xenocrysts in kimberlites (e.g Mitchell, 1986). They typically occur as rounded to ellipsoidal nodules, and the grains studied here were up to 5 mm in diameter. Four populations from the Cretaceous Monastery, Nouzees, Orapa and Rietfontein kimberlite diatremes in southern Africa were analysed for oxygen. The Monastery and Orapa kimberlites are located on the Kaapvaal craton and in the Limpopo Belt of the Kalahari craton respectively, whereas the Nouzees kimberlite is located off-craton in the Namaqua-Natal Mobile Belt to the south-west of the Kalahari craton, and the Rietfontein kimberlite is located off-craton in the Kheis-Magondi Mobile Belt to the west of the Kalahari craton (e.g. Nixon, 1987).

The ilmenites are characterised by a large range of compositions (Table 2.9). They show a negative correlation between $Mg^{\#}$ and $Fe^{3+}/\Sigma Fe$ (st) values calculated assuming stoichiometry, with stoichiometric redox ratios ranging from 0.14-0.60 (Figure 2.9).

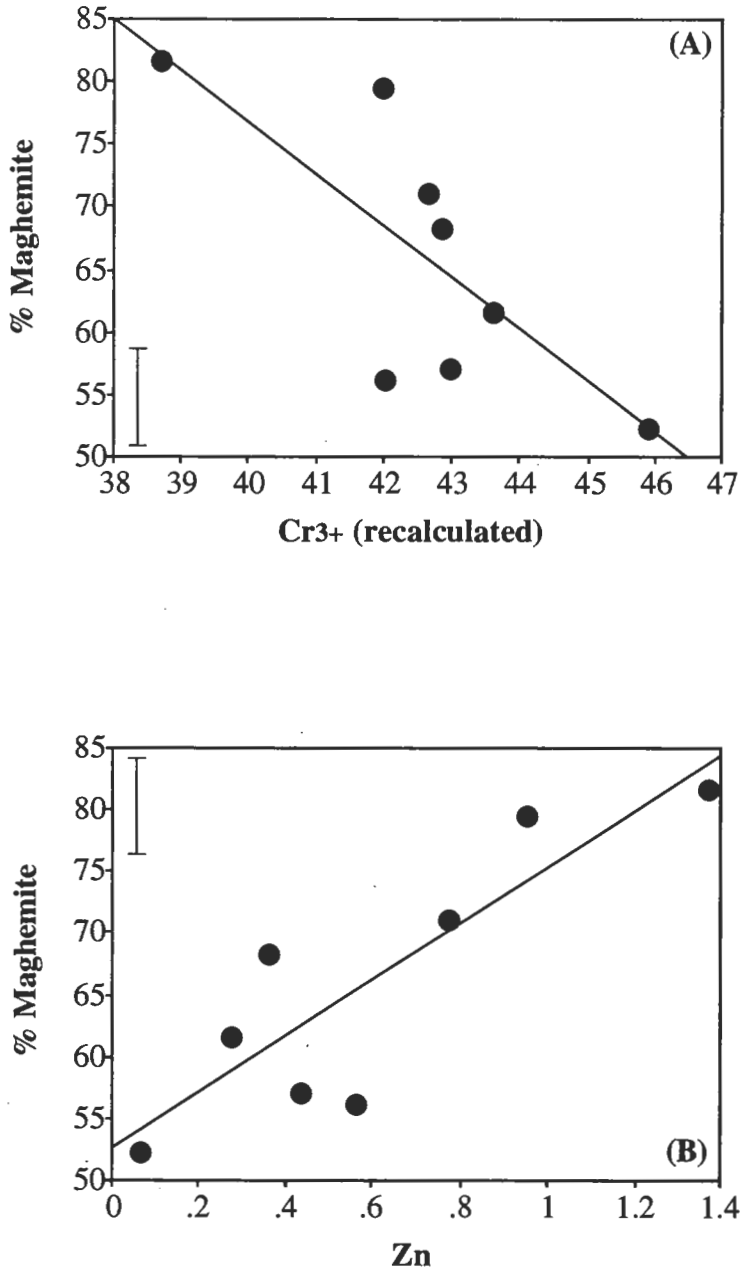

Figure 2.7: (A) % Maghemite vs. $Cr^{3+}_{recalculated}$ (wt.%) and (B) % Maghemite vs. Zn (wt.%) for spinels from the Peak Hill area. % Maghemite represents the amount of $\square_{1/3}Me_{8/3}O_4$ in spinel, and is calculated from the oxygen data. $Cr^{3+}_{recalculated}$ is calculated from the oxygen data assuming all Fe as Fe^{3+}, all Mn as Mn^{3+}, and some Cr as Cr^{4+} to achieve electric neutrality. The error bars indicate 2 rel.% of the mean.

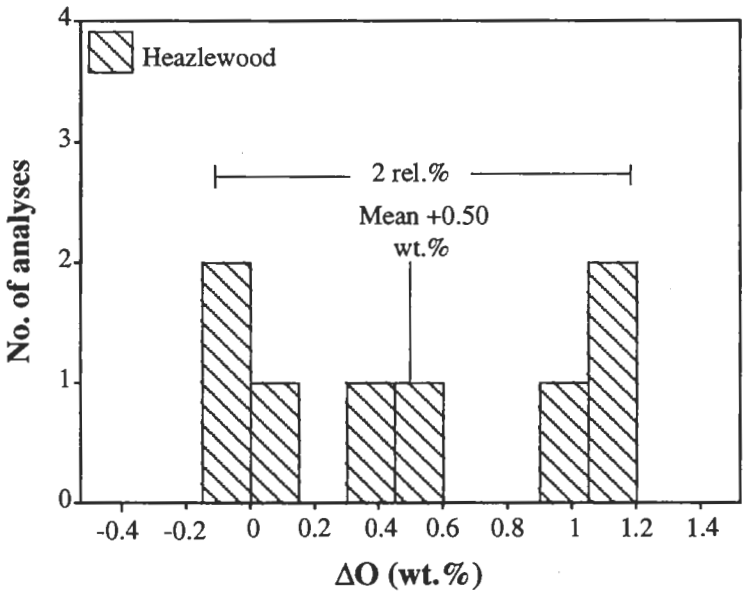

Figure 2.8: Frequency histogram of ΔO (wt.%) for spinels from the Heazlewood River Ultramafic Complex. The error bar indicates 2 rel.% of the mean.

Table 2.9: Representative analyses of Mg-rich ilmenites.

Locality	Monastery		Nouzees		Orapa		Rietfontein	
No.	1	2	3	4	5	6	7	8
Grain No.	201	202	409	410	602	609	807	809
Si	0.05	0.00	0.01	0.00	0.03	0.01	0.00	0.00
Ti	29.82	32.32	32.17	32.22	30.51	28.79	32.10	19.62
Al	0.41	0.10	0.01	0.02	0.32	0.00	0.01	0.02
Cr	0.24	0.52	0.77	1.13	0.07	1.81	2.06	1.63
Fe	29.00	24.52	24.61	24.47	26.80	30.62	23.06	44.68
Mg	6.13	7.24	7.17	7.27	7.03	4.44	7.42	1.87
Mn	0.18	0.20	0.30	0.25	0.22	0.24	0.30	0.07
Ni	0.14	0.06	0.10	0.09	0.03	0.08	0.19	0.08
Zn	0.04	0.03	0.00	0.04	0.04	0.00	0.01	0.10
O	33.53	34.34	33.96	34.49	33.67	32.93	34.23	31.69
Total	99.54	99.33	99.08	99.97	98.72	98.92	99.40	99.75
$O_{calculated}$	34.12	34.33	34.31	34.53	34.20	32.95	34.50	31.74
ΔO	-0.59	0.01	-0.35	-0.04	-0.53	-0.02	-0.27	-0.05
$Fe^{3+}/\sum Fe$ (st)	0.295	0.153	0.161	0.163	0.284	0.247	0.138	0.589
$Fe^{3+}/\sum Fe$ (corr)	0.153	0.156	0.060	0.150	0.144	0.243	0.059	0.581
	(0.161)	(0.196)	(0.193)	(0.197)	(0.175)	(0.150)	(0.206)	(0.098)
$Mg^{\#}$	40.80	44.48	44.37	44.91	45.69	30.66	46.16	18.97

Notes: See the beginning of the Results section for the definition of parameters used in this table. $Fe^{3+}/\sum Fe$ (st) is calculated from cation analyses assuming stoichiometry. $Fe^{3+}/\sum Fe$ (corr) is calculated from oxygen analyses. Values in brackets represent the 2 rel.% range of oxygen analyses.

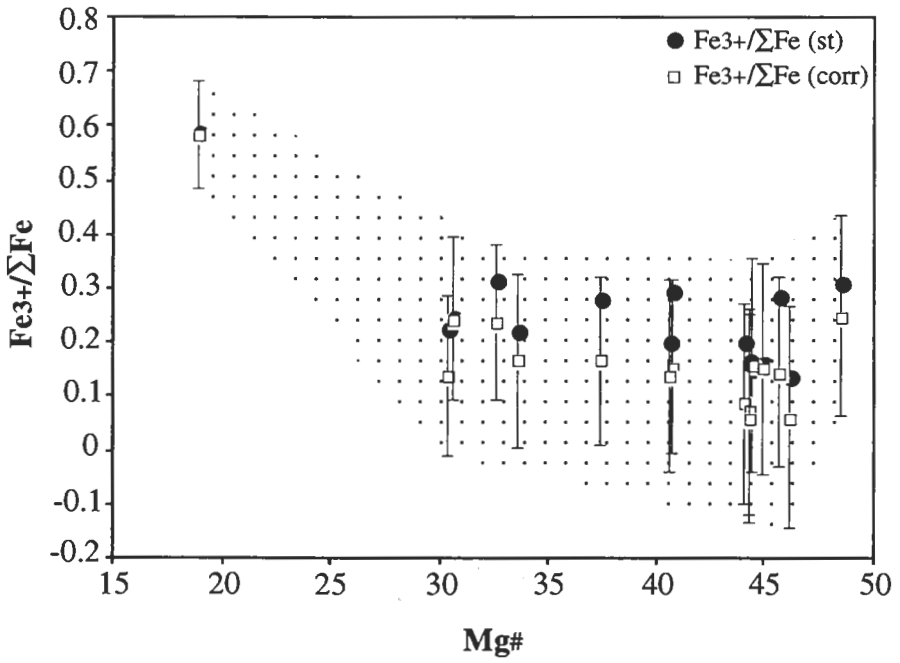

Figure 2.9: $Fe^{3+}/\sum Fe$ vs. $Mg^{\#}$ for Mg-rich ilmenite xenocrysts from kimberlites. $Fe^{3+}/\sum Fe$ (st) (solid symbols) is calculated assuming ilmenite stoichiometry. $Fe^{3+}/\sum Fe$ (corr) is calculated from oxygen analyses. The error bars represent an accuracy of 2 rel.%. The stippled field represent the area of stoichiometry within the range of accuracy.

Oxygen analyses for the magnesium-rich ilmenites show a variation in ΔO value ($-0.59 < \Delta O < +0.01$) which, unlike the oxygen data for the different spinel groups discussed above, can neither be correlated with cation compositions, nor be accounted for by the accuracy of the analytical technique. Such negative ΔO values could indicate a degree of non-stoichiometry, with some ilmenites having either excess divalent cations, an oxygen deficiency, or Ti^{3+} coexisting with Fe^{3+} (e.g. Virgo *et al.* 1988). Although these possibilities cannot be eliminated on the basis of the probe analyses, it is important to note that for ilmenites with different cation compositions the $Fe^{3+}/\sum Fe$ ratios calculated from stoichiometry fall well within 2 rel.% of the redox ratio calculated from the oxygen analyses (Figure 2.9). Thus, in the absence of any other evidence, it is tentatively suggested that the magnesium-rich mantle ilmenites analysed are, like the high pressure mantle-derived spinels, stoichiometric with Fe present as Fe^{2+} and Fe^{3+} according to the stoichiometric recalculations.

2.4 Conclusions

The results have demonstrated that the electron microprobe can be used for precise oxygen analyses of spinels. Unlike common analytical routines for other major elements, an essential part of the oxygen measurement routine developed is the use of repetitive statistical analyses of a standard and subsequent corrections and recalibration.

Chromium-rich spinels with different petrogenesis and cooling histories show a different stoichiometry (Figure 2.10). Diamond-indicator spinels from kimberlite and lamproite matrices are close to stoichiometric composition with very low Fe^{3+} contents. These spinels are mantle xenocrysts originating from high pressure domains. They are interpreted as having undergone long annealing times in the mantle under high pressure-temperature conditions that will favour stoichiometry. Spinel inclusions in olivine phenocrysts show a range of non-stoichiometry which correlates with the composition of spinels. The data show that low $Fe^{3+}/\sum Fe$ values calculated for such spinels assuming Me_3O_4 stoichiometry are invalid. Chromium-rich spinels from thick lava sequences and from low pressure-temperature metamorphic terranes can be significantly non-stoichiometric, with significant divalent cation deficiencies which result in high positive ΔO values. Where unusually oxidized conditions have prevailed, oxygen analyses can indicate the presence of elements in elevated oxidation states, e.g. Mn as Mn^{3+} and Cr as Cr^{4+}.

The analytical results have indicated that spinel non-stoichiometry may be a common occurrence in chromium-rich spinels. This has serious consequences when using ferric iron in spinels to calculate the oxygen fugacity from heterogeneous mineral redox equilibria, or ferrous iron to calculate the temperature of formation from mineral exchange reactions.

Magnesium-rich mantle-derived ilmenites appear stoichiometric. Like chromium-rich diamond-indicator spinels, they are xenocrysts that originated from high pressure-temperature regimes in the mantle where relatively long residence times have ensured mineral stoichiometry.

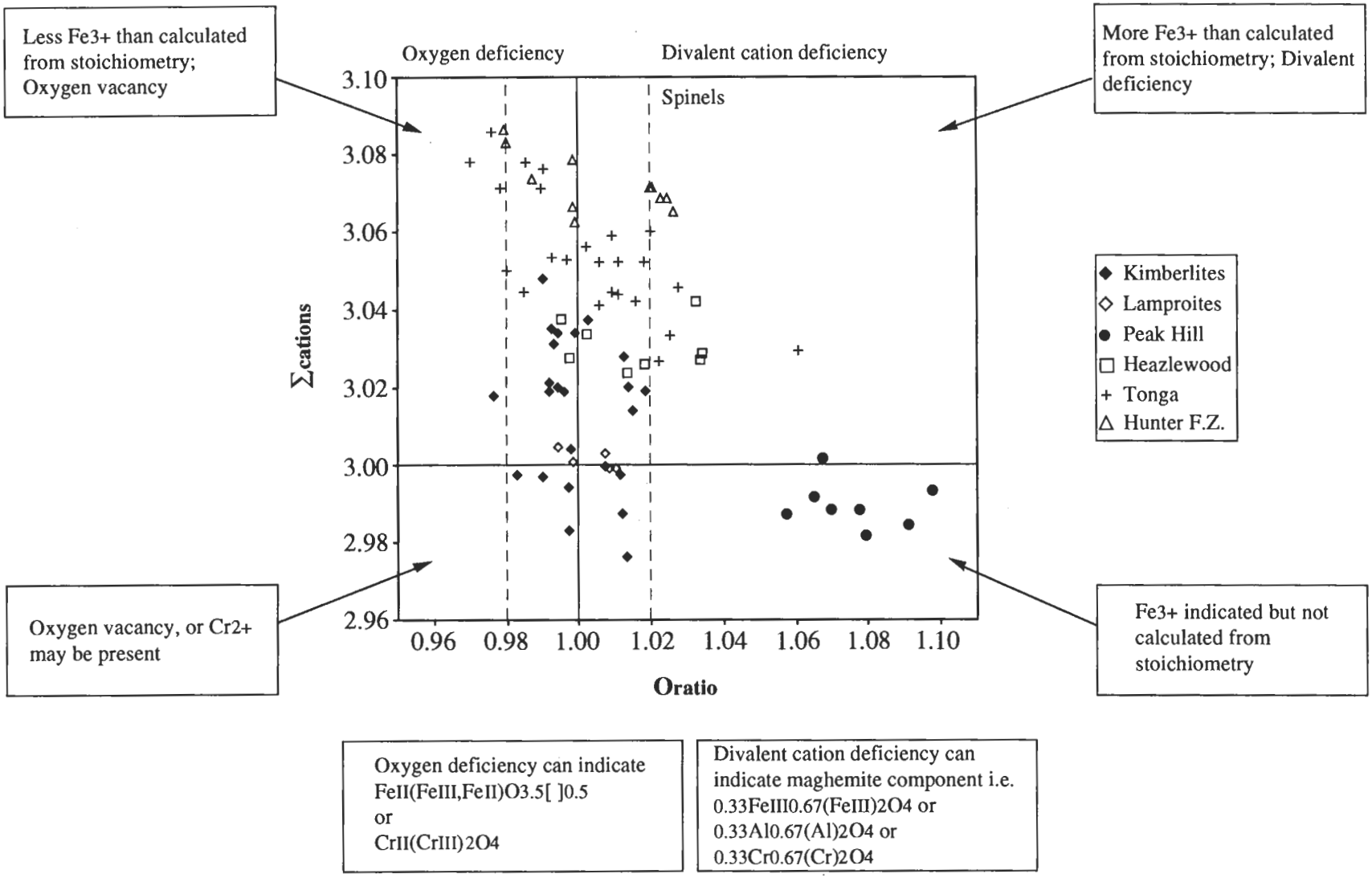

Figure 2.10: Plot against O_{ratio} of $\Sigma_{cations}$ of spinel oxygen analyses. O_{ratio} represents O_{meas} divided by O_{calc}, and $\Sigma_{cations}$ represent the total number of cations calculated on the basis of 4 oxygens for spinels, assuming that all Fe is present as Fe^{2+} and all Cr is present as Cr^{3+}. The diagram is divided into four major fields, corresponding to oxygen deficiency, divalent cation deficiency, ferric iron calculated and no ferric iron calculated. The dashed lines indicate 2 rel.% accuracy of the analytical technique. See text for explanation.

CHAPTER 3

AN EXPERIMENTAL STUDY OF THE ILMENITE-OLIVINE-RUTILE±ORTHOPYROXENE MINERAL SYSTEM WITH EMPHASIS ON GEOTHERMOMETRY AND OXYGEN BAROMETRY

3.1 Introduction

Minerals belonging to the ilmenite mineral group are a widespread accessory mineral, occurring throughout the Earth's upper mantle and crust, in lunar basalts (e.g. El Goresy *et al.*, 1974) and in some meteorites (e.g. Bunch and Keil, 1971). Mg-rich ilmenite is considered to be a characteristic minerals of kimberlites (e.g. Moore, 1987) and has been used extensively as an indicator mineral in diamond exploration (e.g. Atkinson, 1989). The ilmenite mineral group (hereafter referred to as 'ilmenite') can be described in terms of its ilmenite ($FeTiO_3$), geikielite ($MgTiO_3$), pyrophanite ($MnTiO_3$), hematite (Fe_2O_3) and eskolaite (Cr_2O_3) endmembers.

Although ilmenites, like other oxide minerals such as spinels, generally form only a minor component in upper mantle-derived rock assemblages (<3 % by volume), their wide ranging mineral compositions allow them to be used as petrogenetic indicators. The mineral chemistry of ilmenites is dependent on bulk-rock composition and associated mineral assemblage, the geological environment and petrogenetic processes (e.g. Mitchell, 1986 and references therein; Haggerty, 1989, 1991). Many on-going petrological investigations have focussed on establishing general relationships between the ilmenite mineral chemistry, the host rock types and geological processes that formed ilmenite-bearing mineral assemblages (e.g. Boyd, 1971; Mitchell, 1973, 1977; Pasteris, 1980; Leblanc *et al.*, 1982; Haggerty *et al.*, 1985; Moore, 1987; Pearce, 1990; Cawthorn and Biggar, 1993). In contrast to this approach, many recent studies have placed an increasing emphasis on deriving quantitative estimates of intensive variables associated with petrologic events from the mineral chemistry of ilmenite-bearing assemblages. Such investigations have included Fe-Mg exchange geothermometry involving ilmenite and common ferromagnesian silicate mineral solutions such as olivine (e.g. Andersen and Lindsley, 1979, 1981; Bishop, 1979) and pyroxene (e.g. Bishop, 1977, 1980), and oxygen geobarometry involving hematite solid solution in ilmenite from olivine-orthopyroxene-ilmenite mineral assemblages (e.g. Eggler, 1983). The success in applying results obtained from such investigations to calculating intensive variables as recorded by natural

ilmenite-bearing assemblies depends critically on having adequately constrained relationships between physical conditions, the stability of minerals and mineral compositions.

The Fe-Mg exchange geothermometers involving ilmenite-olivine (Andersen and Lindsley, 1979, 1981) and ilmenite-orthopyroxene (Bishop, 1979) were experimentally calibrated as a function of pressure and temperature only, and the olivine-orthopyroxene-ilmenite oxygen geobarometer (Eggler, 1983) was formulated using ilmenite solid solution thermodynamic parameters of the Andersen and Lindsley (1981) ilmenite-olivine geothermometer. However, experimental work to-date has not systematically tested the effect of oxygen fugacity (fO_2) on the ilmenite-bearing mineral equilibria as an intensive variable.

The amount of ferric iron in ilmenite (often expressed as the hematite component in ilmenite) is dependent on the oxygen fugacity at which the ilmenite is formed. Provided that the activity-composition relations of the mineral solid solution are well understood, the ferric iron content of ilmenites may be used to calculate fO_2 from a heterogeneous mineral system involving olivine, orthopyroxene and ilmenite according to the equilibrium reaction: 8 $Fe_{0.5}SiO_2$ (fa) + O_2 (fluid) = 2 Fe_2O_3 (hem) + 2 $Fe_2Si_2O_6$ (fs). A similar discussion involving the magnetite solid solution in spinel has been used to derive an olivine-orthopyroxene-spinel oxygen geobarometer (e.g. O'Neill and Wall, 1987; Mattioli and Wood, 1988; Wood, 1990; Ballhaus *et al.*, 1991). Since experimental work to-date has not taken into account the effect of oxygen fugacity as an intensive variable, its calculation from ilmenite-bearing mineral equilibria remains restricted by uncertainties in the activity-composition of the hematite component in ilmenite.

Two contrasting solution models are currently available in the international literature to assess the activity-composition relations in ilmenite solid solutions. The essential difference between the models lies in the treatment of hematite substitution in ilmenite. The Andersen and Lindsley (1979, 1981, 1988) model is based on the assumption that the ilmenite solid solution remains fully ordered over the temperature-composition range of interest, and temperature-dependent symmetric and asymmetric regular solution parameters are used to describe the excess Gibbs energy. On the other hand, Ghiorso (1990) and Ghiorso and Sack (1991) have suggested a complex solution model which takes into account cation ordering, and the excess Gibbs energy is described in terms of composition-ordering parameters. Neither model can be used below ~550 °C because they do not account for the effects of low temperature, second-order magnetic phase transitions.

In an attempt to test the effect of oxygen fugacity as an intensive variable on the ilmenite solid solution, a series of high pressure-temperature experiments were performed at controlled fO_2 with the use of oxygen buffer components. The purpose of this chapter is: (i) to present new experimental data of peridotite assemblages involving Mg-rich ilmenite, synthesized under P-T-fO_2 conditions representative of the Earth's upper mantle; (ii) to apply the experimental data to the existing Fe-Mg exchange ilmenite-based geothermometers; (iii) to test and revise the existing olivine-orthopyroxene-ilmenite oxygen geobarometer, using a fully ordered ilmenite solid solution model; and (iv) to introduce an oxygen geobarometer involving rutile-ilmenite assemblages, using a fully ordered ilmenite solid solution model.

[Note: One of the starting mixes described here (YVB-1) represents a composition used by Dr. Y. Babich (Institute for Mineralogy and Petrology, Siberian Branch, Academy of Sciences, Russia) for controlled oxygen fugacity experiments to test the olivine-orthopyroxene-ilmenite oxygen geobarometer of Eggler (1983). This experimental work was undertaken under supervision of Professor D.H. Green at the Geology Department of the University of Tasmania during 1990-1991 and some of the conclusions of this work are presented in Babich *et al.* (1992). This chapter presents independently derived mineral analyses of products of selected YVB-1 experiments which are believed to be more accurate than those presented by Babich *et al.* (1992) due to improved analytical techniques and the use of more appropriate mineral standards (see section 3.3.2). The work by the author on selected YVB-1 experiments commenced during the middle of 1991, and consisted of the preparation of new probe mounts from remnants of experimental run products, visual microscope inspections and full analyses of all mineral phases in each available run product. No data presented here have been taken from Babich *et al.* (1992). This work was undertaken as part of a larger program with the aim to extend the work on ilmenite mineral geochemistry as a function of composition and intensive variables such as temperature, pressure and oxygen fugacity].

3.2 Experimental details

3.2.1 Selection and preparation of starting materials

Full details of the starting mix preparation and the experimental technique are described in Appendix A. The starting compositions used in this experimental study are a TiO_2-rich harzburgite (YVB-1) with a bulk $Mg^{\#} = 100*Mg/(Mg+Fe^{2+})$ of 80, and a TiO_2-rich dunite (MAK-2) with a bulk $Mg^{\#}$ of 90.9 (Table 3.1).

Table 3.1: Starting compositions.

	YVB-1[a]	MAK-2[b]	MAK-1[c]
SiO_2	34.0 (31.4)	34.1 (28.9)	35.4 (31.4)
TiO_2	20.0 (13.9)	12.2 (7.8)	20.8 (13.9)
FeO	14.2 (11.0)	8.1 (5.7)	5.5 (4.9)
MgO	31.8 (43.8)	45.6 (57.6)	38.3 (50.6)
$Mg^{\#}$	80.0	90.9	92.5
Normative compositions (wt%)			
Olivine	25	75	35
Orthopyroxene	41	4	34
Ilmenite[d]	34	21	25
Rutile	-	-	6

Notes: Major element analyses are shown in wt.%; values in parentheses indicate analyses in mol %.
[a] YVB-1 is a Ti-enriched harzburgite from Babich et al. (1992), [b] MAK-2 is a Ti-enriched dunite, [c] MAK-1 is a Ti-enriched harzburgite (presented here for purposes of comparison). [d] Ilmenite compositions in normative calculations are assumed to contain MgO: for YVB-1 ilmenite with $Mg^{\#}$ 47; for MAK-2 ilmenite with $Mg^{\#}$ 55 and for MAK-1 ilmenite with $Mg^{\#}$ 60.

Table 3.2: Equilibrium equations for calculation of log fO_2 values for some common oxygen buffers from pressure and temperature data.

Buffer	Equilibrium Equation	Reference
WCWO	14.33 - 29105/T - 1.56logT + 66P/T	Taylor and Foley, 1989
FMQ	82.75 + 0.00484T - 30681/T - 24.45logT +94P/T - 0.002P	O'Neill, 1987a
NNO	12.78 - 25073/T - 1.1logT + 45P/T + 0.0025P	O'Neill, 1987b
MH	14.91 - 26184/T + 20P/T - 0.005P	Hemingway, 1990

Notes: Calculations involve pressures in kbars and temperatures in °K. Pressure corrections are from standard molar volume and thermal expansion data. The Hemmingway (1990) equilibrium equation for the HM oxygen buffer requires a correction for unit activity of magnetite (e.g. O'Neill, 1988; O'Neill, pers. comm.).

All mix compositions were prepared from spectroscopically pure oxides, enriched in ilmenite components to promote the growth of large oxide grains under sub-solidus experimental conditions. In the preparation of the starting mixes, mineral data from the literature were taken into account to derive representative compositions. For example, Green and Sobolev (1975) report an ilmenite-bearing garnet-lherzolite from the Wesselton kimberlite, South Africa, with an ilmenite $Mg^{\#}$ value of 47. In the normative calculation of the YVB-1 mix reported here, ilmenite is assumed to have a composition of $Mg^{\#}$ 47 also, whereas in the preparation of the MAK-2 mix ilmenite is assumed to have an $Mg^{\#}$ value of 55. Such high $Mg^{\#}$ ilmenites have been reported widely, for example as a groundmass phase or as inclusions in olivine phenocrysts from the Wesselton kimberlite, South Africa (Shee, 1984) or as megacrysts from the Frank Smith and Premier kimberlites, South Africa (e.g. Mitchell, 1977).

Mineral assemblages observed in the YVB-1 experiments consisted of olivine-orthopyroxene-ilmenite-rutile (Figure 3.1). Initial experiments which aimed at synthesizing an olivine-orthopyroxene-ilmenite assemblage with high $Mg^{\#}$ ilmenites were undertaken with a starting composition differing from the YVB-1 mix in $Mg^{\#}$ only (MAK-1 with $Mg^{\#}$ 92.5, Table 3.1). However, ilmenite was not a stable mineral phase and mineral assemblages consisted of olivine-orthopyroxene-rutile (Figure 3.1). The alternative composition (MAK-2), differing from the MAK-1 starting composition in having a lower SiO_2 content and a slightly lower $Mg^{\#}$, produced olivine-ilmenite-rutile mineral assemblages (Figure 3.1). Thus, it can be seen that under the physical limitations of the experimental technique available in this study, the YVB-1 mix represents a starting composition close to the maximum extent of the mineral assemblage olivine-orthopyroxene-ilmenite-rutile.

The stability field for olivine-orthopyroxene-ilmenite-rutile under the experimental conditions employed in this study is limited to somewhat iron rich compositions. For example, using a multi-variable phase diagram (e.g. Connolly, 1990) for the experimental compositions used in this study, and the Holland and Powell (1990) thermodynamic data set, it can be seen that the olivine-orthopyroxene-ilmenite-rutile field at 20 kbar is constrained by olivine compositions of Fo_{72} and orthopyroxenes with $Mg^{\#}$ 81 (Figure 3.2). The silicates become more magnesian with increasing pressure, and at 60 kbar olivine compositions in the four phase field are projected at Fo_{82}, and orthopyroxene compositions have compositions with $Mg^{\#}$ 91. Although these projections are limited to pure $FeTiO_3$ at one of the apices, and thus do not take into account MgO and Fe_2O_3 substitution in ilmenite, or Fe_2O_3 substitution into rutile, the pressure effect on the stability field for olivine-orthopyroxene-ilmenite-rutile with respect to $Mg^{\#}$, is well shown.

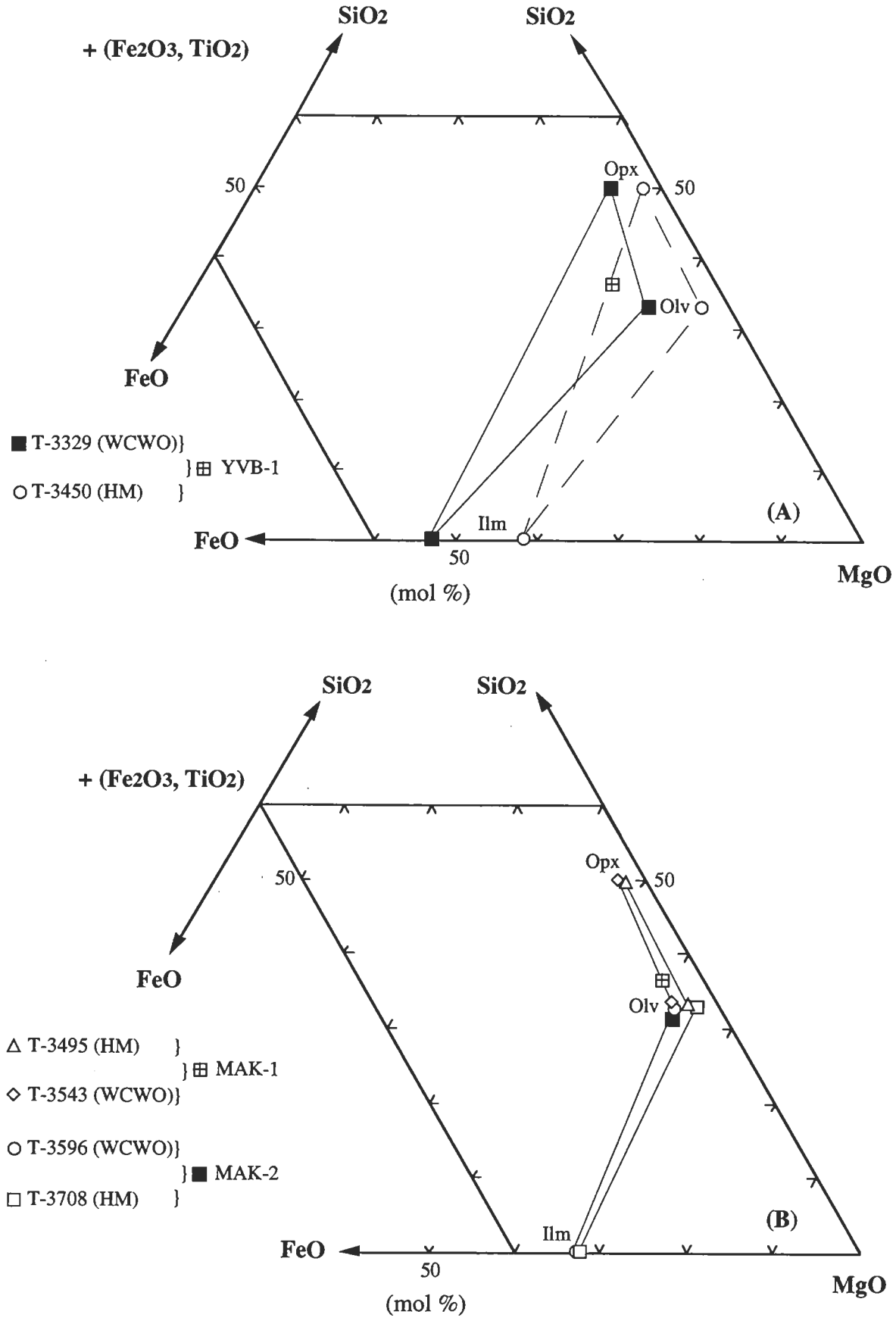

Figure 3.1: SiO_2-FeO-MgO plane projected from (TiO_2+Fe_2O_3) illustrating the mineral stability fields for the YVB-1 (A), and MAK-1 and MAK-2 (B) experimental starting mixes. Details of the experimental runs shown are given in Table 3.5 and Appendix D.

Furthermore, it can also be demonstrated that the effect of temperature is less pronounced on the extent of the four phase stability field than the pressure effect (Figure 3.2).

3.2.2 Experimental technique

All experiments were performed with a 0.5 inch (1.27 cm) piston-cylinder apparatus (e.g. Boyd and England, 1960) using techniques similar to those described by Green and Ringwood (1967). Run conditions varied from 900 to 1200 °C and 15 to 35 kbar. Experimental assemblages used outer sleeves of NaCl, NaCl-pyrex, talc or talc-pyrex as pressure media. A pressure correction of -10 % of the nominal load pressure was applied to experimental runs using talc sleeves. Pressures with NaCl-sleeved assemblages in the 10-35 kbar range were estimated to have an accuracy of ±(1 % + 0.5) kbar (Mirwald *et al.*, 1975). Temperatures were monitored with $Pt/Pt_{90}Rh_{10}$ thermocouples, and controlled to within ±10 °C of the desired values. Experiments were run for durations between 20 and 176 hours, with the run time depending on the temperature of the experiment and the buffering capacity of the oxygen buffer components. Typical run products are shown in Figure 3.3.

The controlled oxygen fugacity experiments used the double-capsule technique of Huebner (1971) with oxygen buffering being achieved through both welded and open inner sample capsules. The oxygen buffers used in these experiments were WC-WO_2-graphite (WCWO), Ni-NiO (NNO), and Fe_2O_3-Fe_3O_4 (HM). The equations for calculating oxygen fugacity values (fO_2) for experimental conditions at known pressures and temperatures are given in Table 3.2. Where values for fO_2 in this chapter are reported with reference to the fayalite-magnetite-quartz (FMQ) buffer, they are quoted as $\Delta \log fO_2$ (FMQ) log units.

The requirements of oxygen buffering are: (i) the capsule material does not react with the buffer components or the sample mix; (ii) the buffer components do not infiltrate the sample mix as a result of high element mobility under fluid rich conditions, and (iii) iron loss from the sample mix is avoided. The following paragraphs summarise the oxygen buffering technique employed here to achieve these requirements. A more detailed description of the experimental buffering technique is given in Appendix A3.

Experiments with the WCWO buffer used a technique modified from that described by Taylor and Foley (1989). The sample was contained in an inner graphite capsule and sealed in a welded outer $Ag_{50}Pd_{50}$ or Pt capsule. The inner capsule was isolated from the buffer mix by graphite protective lids.
(figure 3.2)

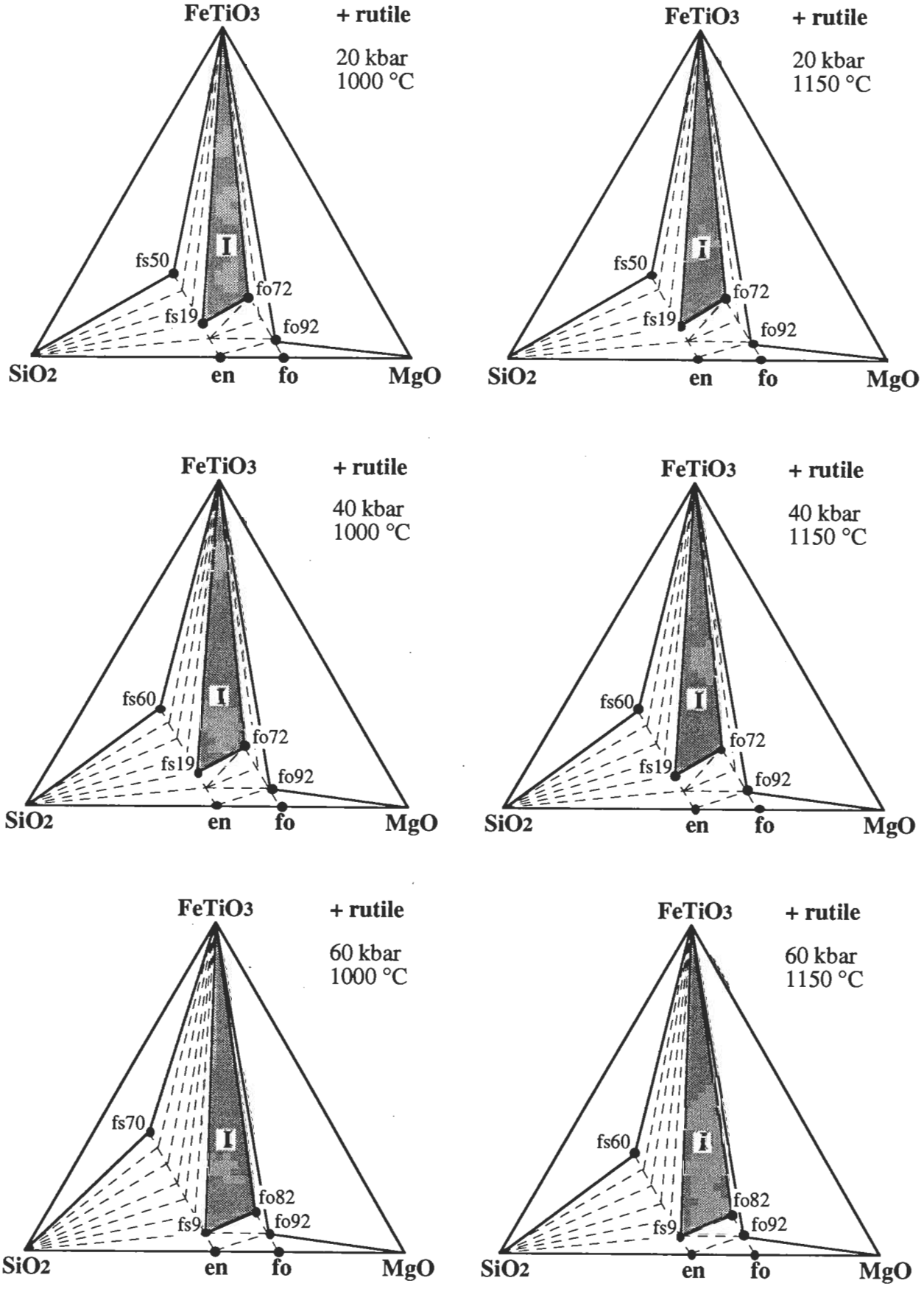

Figure 3.2: $FeTiO_3$-SiO_2-MgO plane projected from rutile, and illustrating the stability field for olivine-orthopyroxene-ilmenite-rutile assemblages (I) derived from the YVB-1 experimental composition described in this study. The projections are made using a multi-variable phase diagram projection program (Connolly, 1990), and silicate endmember compositions at different P-T conditions are calculated using the Holland and Powell (1990) thermodynamic data set.

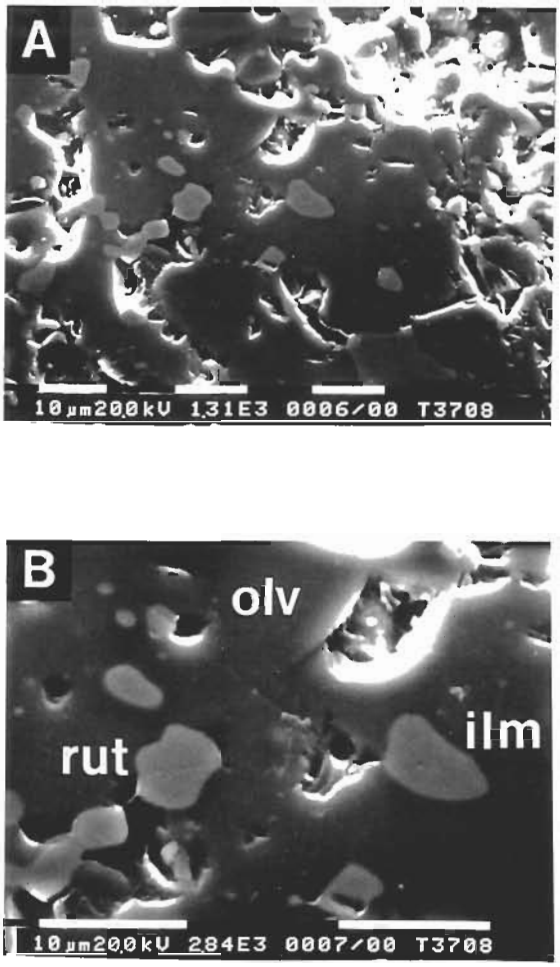

Figure 3.3: Back-scattered electron images of experimental products of MAK-2 starting composition. (A) is experiment T-3708 (20 kbar, 1050 °C, HM buffer) showing abundant oxide minerals (ilmenite + rutile) in a silicate (olivine) matrix. (B) is a magnified image of the central area in (A). Dark grey grains are ilmenite (ilm), and light gray grains are rutile (rut); olv = olivine. The white scale bar in both illustrations indicates 10 µm.

The buffer consisted of a mix of W-WO_3-C made up in a 29:1:70 mole ratio. Stearic acid (~3-5 wt.%) was added to the buffer material and the equilibrium fluid generated under WCWO conditions was H_2O-CH_4 (Taylor and Green, 1987).

Oxygen fugacity conditions around FMQ are generated by the use of the NNO buffer. At these buffer conditions, graphite capsules are no longer stable and, with low $Fe^{3+}/\sum Fe$ ratios, the use of metal capsules with accompanying iron loss is considered less than ideal. Instead, experiments are carried out in capsules made of San Carlos Olivine (Fo_{90}). The sample mix is contained in olivine capsule cylinders covered by olivine powder and an olivine lid. This inner capsule assembly is sealed in an outer Pt or $Ag_{50}Pd_{50}$ capsule. The buffer mix consists of Ni-NiO made up in a 1:5 mole ratio. The fluid is pure H_2O which is added to the buffer (~1 µl) and sample (~0.5 µl). The use of olivine capsules in this buffer assembly has some advantages over more conventional double capsule techniques in that: (i) redox equilibria are achieved very rapidly because the fluid equilibrates directly with the buffer and the sample, and (ii) iron loss to the capsule has been eliminated.

The highest oxygen fugacities were generated with the use of the HM buffer. The sample mix was contained in a $Ag_{50}Pd_{50}$ or $Ag_{75}Pd_{25}$ welded inner metal capsule together with ~3 wt.% H_2O. This inner assembly was placed in a $Ag_{50}Pd_{50}$ or Pt outer capsule and surrounded by a mechanical mix of hematite:magnetite (made up in a 9:1 mole ratio) containing ~2 wt.% H_2O, and the outer capsule was sealed. Oxygen buffering was achieved by the thermal decomposition of H_2O and the exchange of H_2 between buffer and sample through the inner semi-permeable metal capsule walls.

A number of experiments were conducted under graphite-water (GW) or graphite-CO_2-CO (GCO) conditions through the use of graphite in the presence of a fluid source. These 'furnace-buffers' do not act like an oxygen buffer sensu stricto but rather define a fixed point on the system C-O-H-graphite saturation curve in P-T-fO_2 space (Taylor, 1985). For these buffer experiments the sample mix and a fluid source (~0.5-1.5 µl H_2O) were contained in an inner graphite enclosed in a welded Pt or $Ag_{50}Pd_{50}$ capsule. Graphite powder was used to surround the inner graphite capsule and a small amount of H_2O (~0.5 µl) was added to provide part of the volatile component. Following the experiment, the capsule was pierced and the composition of the resultant fluid was determined by mass spectroscopy (e.g. Taylor, 1985; Taylor and Foley, 1989). The oxygen fugacity of the experiment was determined using the fluid composition data, the physical parameters of the experiment and knowledge of the C-O-H-graphite saturation curve in P-T-fO_2 space (Taylor, 1985). This approach has been described in more detail in Appendix B7.

3.2.3 Analytical details

Run products and residual buffer material were optically examined under an immersion oil of accurately known refractive index (RI) to identify mineral phases and to ensure that buffer exhaustion had not occurred. Probe mounts of experimental run material were made using cold-set epoxy, and a high grade polish of the probe mounts was accomplished using successively finer grades of diamond polishing paste.

All mineral phases in the experimental runs were analysed at the University of Tasmania with a Cameca SX-50 electron probe microanalyser which was calibrated using natural mineral standards. Concentrations were calculated from relative peak intensities using a PAP matrix correction procedure. Analytical conditions were 15 kV accelerating voltage, and a 20 nA beam current. A TAP crystal was used for analysing Mg, Al and Si. A PET crystal was used for analysed Ti and Cr. Mn, Fe, Ni and Zn were analysed on an LiF crystal. All elements were analysed at 20 seconds on the peak and 10 seconds on each side of the peak. A detailed description of analytical procedures is given in Appendix B1.

3.3 Treatment of analytical results

3.3.1 Calculation of ferric iron and problems of precision and accuracy

Electron microprobe analyses do not distinguish between the valence states of iron, and the determination of the ratio of FeO and Fe_2O_3 must therefore involve some assumptions. The ferric iron content of ilmenite can be calculated from electron microprobe analyses assuming that the sole constraint on the mineral composition is perfect stoichiometry, with two cations per three anions. Stoichiometry calculations are based on the assumption of charge balance, with iron as the only cation with a variable valency state (e.g. Finger, 1972). The recalculation procedure determines an equivalent number of oxygens for the cations present, and any deviation from the ideal of number of oxygens in the mineral formula is assumed to be due to the presence of Fe^{3+} (e.g. Chapter 2 herein). In the ensuing discussion, "precision" is regarded as the measure of scatter expected in the analytical data, whereas "accuracy" concerns the absolute deviation of the analyses from the true value. Precision, as expected, contributes to accuracy.

Wood and Virgo (1989) presented a method, modified from Finger (1972), to estimate the precision of ferric iron contents in spinels from electron microprobe analyses assuming mineral stoichiometry. In this study, the Wood and Virgo (1989) method has been modified by considering a mineral structure with two cations and three anions, rather than three cations and four anions, in order to determine the precision of ferric iron in ilmenite,

and results are presented in Table 3.3. Electron microprobe analyses were performed in a routine manner (see Appendix B1) and, generally, the calculated standard deviation for major oxide elements is less than 2 rel.% (Table 3.3). For the most reduced experimental run in this study with the lowest ferric iron contents in ilmenites (T-3329) the calculated $Fe^{3+}/\sum Fe$ ratio is 0.009 with a calculated precision of 0.005 (2σ). Thus, with proper care the electron microprobe is capable to obtain a precision better than ±0.002 mol % Fe_2O_3, which corresponds to an uncertainty of about ±0.4 log units in fO_2 (calculated using the ilmenite oxygen geobarometer from Eggler, 1983).

Although the electron microprobe method is potentially precise enough, the main problem in determining ferric iron contents is lack of accuracy, which, as will be demonstrated below, is much worse than precision. Two important contributing factors to this lack of accuracy are uncertainties in electron microprobe matrix correction procedures (e.g. Wood and Virgo, 1989) and large concentrations of light elements, for example Mg in ilmenite, for which the uncertainties are greatest (e.g. Wood, 1991).

Systematic errors introduced by large concentrations of light elements have been investigated using synthetic ilmenites from the YVB-1 experimental oxide mix. The ilmenites were initially analysed by Babich *et al.* (1992) using a Cameca SX-50 electron probe microanalyser with a 15 kv accelerating voltage and a 20 nA beam current, and with concentrations calculated using a PAP matrix correction procedure. The standards used were as follows: Mg - olivine (Fo_{90}); Si - quartz; Fe - fayalite; Ti - ilmenite, synthetic rutile or pure titanium. The ilmenites were reanalysed for this work using the same analytical conditions as those of Babich *et al.* (1992) but with different standards specifically selected for oxide analyses : Mg - chromite; Si - quartz; Fe - ilmenite; Ti - rutile. A comparison of the data shows that there are significant differences between the two analytical approaches (Table 3.4). The ilmenite analyses of Babich *et al.* (1992) consistently indicate more TiO_2 and less MgO and, in all but one analysis, more FeO than those presented in this work. These analytical differences result in considerably lower calculated ferric iron contents for ilmenites in Babich *et al.* (1992) than in this work. The effect on calculated oxygen fugacities is in some cases quite substantial: for experiment T-3410 the higher value of Fe^{3+} give an fO_2 about 0.4 log units above FMQ whereas the lower value gives an fO_2 about 1.4 log units below FMQ (using Eggler, 1983). For the most reduced experiment (T-3329) the higher value of Fe^{3+} calculates a value for fO_2 about 3.0 log units below FMQ whereas the analysis of Babich *et al.* (1992) does not allow an estimate for fO_2 because no ferric iron was calculated from ilmenite stoichiometry. The differences in calculated fO_2's between the higher and lower Fe^{3+} values become insignificant under oxidized conditions greater than NNO (e.g. T-3366).

Table 3.3: Precision of ferric iron in ilmenite as determined by electron microprobe.

Experiment: T-3377 (n=6)	wt%	(a) St. Dev.	(b) N(ΣN=2)	(c) $2\sigma_N$
SiO_2	0.05	23.32	0.0011	0.0005
TiO_2	54.24	0.53	0.9377	0.0073
FeO_{total}	27.69	0.75	0.4100	0.0067
MgO	15.43	0.65	0.5288	0.0061
Total	97.41			
Fe_2O_3 (calc)	7.08		$N_{Fe^{3+}}$ (d)	0.1224
FeO (calc)	21.32		$2\sigma_{Fe^{3+}}$ (e)	0.0145

Notes: The standard deviation of the measured oxides (a) is calculated from electron probe analyses as rel.%. N indicates the number of calculated cations in the ilmenite structure (b). The precision is given as 2 standard deviations, i.e. with a 95% confidence level (c). The number of ferric iron cations is calculated from the total number of oxygens associated with 2 cations, taking all Fe as FeO and 'forcing' the formula unit to have 3 oxygens (d). The uncertainty in ferric iron content is calculated using the method of Wood and Virgo (1989) but corrected for ilmenite stoichiometry rather than spinel stoichiometry (e). The ferric iron content for each of the six individual ilmenites of sample T-3377 was calculated and the actual standard deviation of stoichiometrically calculated Fe^{3+} ($2\sigma_{Fe3+}$ 0.0126) is in good agreement with that calculated here using the revised method of Wood and Virgo (1989).

Table 3.4: Comparison of the effects of different mineral standards on ilmenite compositions, all experiments at 1100 °C.

Experiment	T-3329	T-3329	T-3350	T-3350	T-3410	T-3410	T-3366	T-3366
Method	this work	YVB	this work	YVB	this work	YVB	this work	YVB
SiO_2	0.10	NA	0.06	NA	0.15	NA	0.08	NA
TiO_2	57.42	59.28	55.96	57.24	54.77	57.16	34.83	36.22
Fe_2O_3	0.30	-	3.06	1.58	5.35	0.80	39.16	37.63
FeO	27.40	28.06	25.17	27.44	24.13	27.33	12.75	14.58
FeO_{total}	27.67	28.06	27.92	28.86	28.94	28.05	47.99	48.44
MgO	13.66	13.21	14.15	13.49	14.19	13.51	10.47	10.10
$Mg^{\#}$	47.1	45.6	50.1	46.7	51.2	46.8	59.4	55.3
Si	0.002	0.000	0.001	0.000	0.003	0.000	0.002	0.000
Ti	0.995	1.011	0.972	0.986	0.950	0.993	0.639	0.658
Fe^{3+}	0.005	-	0.053	0.027	0.093	0.014	0.719	0.684
Fe^{2+}	0.528	0.532	0.486	0.526	0.466	0.528	0.260	0.294
Mg	0.469	0.447	0.487	0.461	0.488	0.465	0.381	0.364
Sum	2.000	1.989	2.000	2.000	2.000	2.000	2.000	2.000
$Fe^{3+}/\sum Fe$	0.009	-	0.098	0.049	0.166	0.026	0.734	0.699
$Mg^{\#}$ (olv)	85.1	85.1	87.8	87.2	87.1	86.4	94.8	94.7
T_{calc} (°C)	1170	1112	996	952	985	946	506	499
$\Delta \log fO_2$ $(FMQ)_{calc}$	-3.09	-	-0.72	-1.36	0.37	-1.39	3.81	3.72
$\Delta \log fO_2$ $(FMQ)_{buffer}$	-2.65	-2.65	-1.07	-1.07	0.27	0.27	3.90	3.90

Notes: Experimental details are given in Table 3.6. The row entitled 'method' refers to the mineral standards used in the analytical work: YVB (Babich et al., 1992) used the following mineral standards: Mg - olivine (Fo_{90}); Si - quartz; Fe - fayalite; Ti - ilmenite, synthetic rutile or pure titanium. In comparison, this work used the following mineral standards: Mg - chromite; Si - quartz; Fe - ilmenite; Ti - rutile. The Fe_2O_3 and FeO contents are calculated from FeO_{total} assuming mineral stoichiometry. T_{calc} is the calculated temperature using the olivine-ilmenite Fe-Mg exchange geothermometer of Anderson and Lindsley (1981); $\Delta \log fO_2$ $(FMQ)_{calc}$ is the calculated oxygen fugacity, compared to FMQ, using the ilmenite oxygen geothermometer of Eggler (1983), and $\Delta \log fO_2$ $(FMQ)_{buffer}$ is the calculated oxygen fugacity of the experiment, compared to FMQ, using relevant buffer equations described in Table 3.2.

Variations in temperature calculations, though less pronounced than the fO_2's, also result from the analytical differences. For reduced experiments with FMQ-2.5 log units to FMQ (T-3329, T-3350 and T-3410) temperatures calculated using the ilmenite-olivine Fe-Mg exchange geothermometer (Andersen and Lindsley, 1981) are between 40-60 °C higher for ilmenite analyses from this work than for ilmenite analyses of the same experiment from Babich *et al.* (1992). However, for the more oxidized experiment at FMQ+4.0 log units (T-3366) there is little difference in the calculated temperature for the two data sets.

Because of the sensitivity of the recalculation procedure many authors have pointed out that a careful selection of mineral standards and, in some cases, the matrix correction program used for microprobe analyses will minimize systematic errors and improve the accuracy of the microprobe method for determining the ferric iron content (e.g. O'Neill and Wall, 1987; Wood and Virgo, 1989; Ballhaus *et al.*, 1991). However, Wood (1991) emphasizes that most oxide analyses in the literature are not made with oxygen geobarometry in mind so that systematic errors in calculated fO_2 of around 2.0 log units are still quite likely. Clearly, there is a need to demonstrate accuracy and reproducibility of ferric iron in studies aimed at oxygen geobarometry, and Wood and Virgo (1989) and Bryndzia and Wood (1990) suggested that this could be adequately achieved by checking the microprobe calibration against a secondary oxide mineral standard analysed for ferric iron by Mössbauer spectroscopy. Ballhaus *et al.* (1991) disagreed with this approach on grounds of additional introduced errors related to the Mössbauer analytical technique, particularly where a small single grain may not be representative of a bulk $Fe^{3+}/\Sigma Fe$ ratio. Nonetheless, it is argued here that there is support for the use of a secondary standard, provided it can be shown that the mineral is: (i) homogeneous in composition and large enough to provide individual samples for the different analytical techniques, and: (ii) the interpretation of the Mössbauer spectra is unambiguous.

In this work, analyses of experimental ilmenites were routinely checked against a chemically homogeneous, Mg-rich ilmenite megacryst from the Monastery kimberlite, South Africa (~1 cm in diameter), analysed by Mössbauer spectroscopy and electron microprobe (including WDS and EDS; see Appendix B1, Table B2). At room temperature, the ^{57}Fe Mössbauer spectrum of the Monastery ilmenite consists of two overlapping doublets due to Fe^{2+} and Fe^{3+}, and the high velocity component of the Fe^{3+} doublet is not resolved (Figure 3.4). To obtain meaningful fits of the data, the spectrum was fitted by constraining the intensities and the widths of the component peaks of each doublet to be equal (e.g. Virgo *et al.*, 1988).

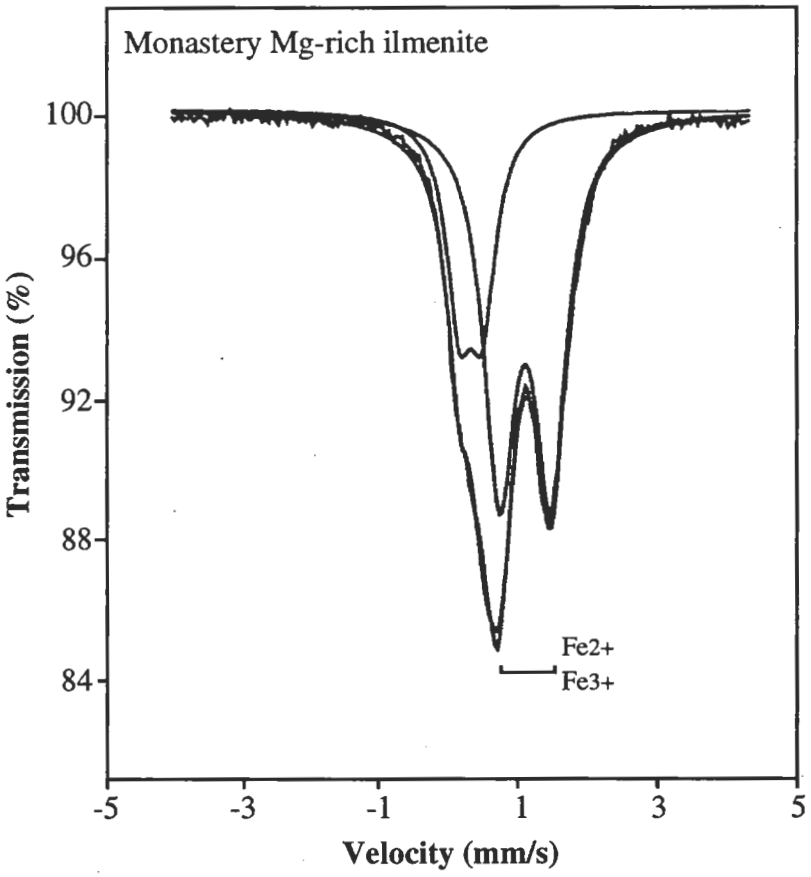

Figure 3.4: ^{57}Fe Mössbauer spectrum of the Monastery Mg-rich ilmenite megacryst.

This procedure suggests that 30±5 % of total iron is in the trivalent state, and spectral parameters of the Fe^{3+} component are found to be consistent with those reported by Murad and Johnston (1987) (Dr. T. G. St. Pierre, pers. comm.). In comparison, electron microprobe analyses (both WDS and EDS) of the ilmenite indicate 28±3 % of total iron in the trivalent state when assuming stoichiometry. The good agreement between the Mössbauer and the electron microprobe data suggests that the Monastery ilmenite is stoichiometric, and that the electron microprobe correction procedures are accurate. Thus, it is tentatively concluded that the quality of the analytical data and the homogeneous nature of the ilmenite can be used in establishing reproducibility and accuracy of ferric iron in ilmenites of unknown composition.

For the treatment of rutile analyses it is assumed that all the iron is trivalent because this poses less crystal-chemical problems than the substitution of divalent cations for quadrivalent titanium (e.g. Dawson and Smith, 1977).

3.3.2 Attainment of phase equilibration

A requirement in applying results from experimental studies of short duration to geological mineral assemblages which were formed over much longer periods of time is a demonstration that phase equilibration has been reached. Oxide mixes such as those used in this study are often more reactive than natural minerals and may produce metastable phase assemblages and mineral compositions. Equilibration of experimental reactions in this study appears to have been achieved as shown by the following tests. Firstly, analytical work showed homogeneity among mineral grains across each experimental charge with $Mg^{\#}$ ranges for olivine and ilmenite of ≤5 % for the entire range of P-T conditions. Secondly, chemical zoning in large olivine grains within each experimental charge was not observed, suggesting equilibration and a minimum iron loss to metal sample capsules. However, it should be noted that these two tests can only be used 'qualitatively' in demonstrating phase equilibration.

A more definitive method in demonstrating equilibrium attainment involves the use of experimental run products as starting mixes in experiments which attempt to approach an equilibrium position from experimentally and compositionally opposite directions. Such a reversal (meaning apparent compositional convergence) experiment was undertaken as part of this study. The starting material for the reversal experiment was a MAK-2 assemblage with olivine, ilmenite and rutile from run number T-3596 synthesized at 1150 °C, 32 kbar and FMQ-2.59 log units (WCWO buffer). The run product (T-3596 'initial') was reground under acetone to grain sizes between 5-10 μm and loaded in a $Ag_{50}Pd_{50}$ capsule. Some MAK-2 oxide mix was loaded as a discrete layer on top of the reground

run product and the entire assembly was re-equilibrated (T-3948) under water saturated, sub-solidus conditions at 1050 °C, 20 kbar and FMQ+4.58 log units (HM buffer) for four days. The run products of this reversal experiment are denoted as T-3596 'reversed' and T-3948 'oxide mix' respectively (Table 3.5). The reground run product in the reversal run was fine grained (<10 μm in diameter), whereas the oxide mix was coarser grained (10-20 μm in diameter).

It appears that the HM buffer may have become exhausted during the experimental run, as observed by a lower than expected Fe^{3+} contents in the oxide mix ilmenites (Table 3.5). A close examination of the final buffer product revealed magnetite, with no visible hematite detected. Although other reasons, such as mineral non-stoichiometry (e.g. Lindsley, 1976; Ballhaus *et al.*, 1991) or iron loss to the metal capsule, can not be excluded, buffer component exhaustion, due to a relatively long run time of four days, remains the most likely explanation (e.g. Huebner, 1971). Nevertheless, despite the apparent buffer failure, there is evidence that compositional convergence was approached. Firstly, the $K_D^{olv\text{-}ilm}{}_{Fe\text{-}Mg}$ was reset to the new experimental temperature, and the $Fe^{3+}/\Sigma Fe$ ratio in ilmenites from the oxide mix and reground run product showed higher values than ilmenites from the original run in a response to a higher oxygen fugacity of the reversal experiment. Perhaps most significantly, olivine, ilmenite and rutile compositions from the oxide mix and the reground run product in the 'reversed' experiments are similar, and noticeably different from the original mineral compositions, suggesting that an equilibrium position, albeit poorly controlled in terms of the oxygen buffer, was achieved from opposite directions.

Reversibility, or compositional bracketing, of experimental results remains difficult to demonstrate due to different rates of reaction for sintered oxide mixes and reground, crystalline run products, the potential presence of metastable phases and possible loss of reagent components. Also, a true compositional bracket can only be obtained with confidence if a single compositional parameter (e.g. Fe-Mg exchange) is isolated and a continuous diffusionally controlled compositionally gradient from the starting to the final composition can be established (e.g. Pattison, 1994). Unless this can be done, the terms "reversal" and "compositional bracket" used to describe apparent convergence experiments that equilibrated by a solution and precipitation mechanism, especially those involving variations in more than one compositional parameter, should at best be be used with utmost care, if not abandoned altogether. Rather, Pattison (1994) suggests the use of terms such as "consistency experiment" or "redundancy experiment" to indicate an increased degree of confidence in an experimental result when it is achieved using different starting materials or starting compositions.

Table 3.5: Analytical details of a consistency experiment involving the MAK-2 oxide mix.

Experiment	T-3596 initial		T-3948 oxide mix		T-3596 reversed	
T (°C)	1150		1050		1050	
P (kbar)	32		20		20	
Buffer	WCWO		HM		HM	
logfO_2	-9.56		-4.83		-4.83	
ΔlogfO_2 (FMQ)	-2.59		4.15		4.15	
Run time (hrs)	30		96		96	
	Olivine (n=5)		Olivine (n=3)		Olivine (n=3)	
SiO_2	40.26		41.48		41.54	
TiO_2	0.32		0.36		0.40	
FeO	7.67		7.10		7.48	
MgO	51.06		52.14		52.14	
Total	99.32		101.07		101.56	
Mg#	92.2		92.9		92.6	
Cations (4 oxygens)						
Si	0.985	(0.012)	0.993	(0.005)	0.991	(0.007)
Ti	0.006	(0.005)	0.006	(0.003)	0.007	(0.001)
Fe	0.157	(0.012)	0.142	(0.005)	0.149	(0.002)
Mg	1.862	(0.015)	1.860	(0.006)	1.854	(0.007)
Sum	3.009		3.001		3.002	
	Ilmenite (n=4)		Ilmenite (n=3)		Ilmenite (n=3)	
SiO_2	0.15		0.14		0.21	
TiO_2	59.65		58.23		58.17	
Fe_2O_3	1.08		2.19		2.45	
FeO	17.73		17.86		18.26	
MgO	20.25		19.45		19.25	
Total	98.86		97.87		98.35	
Mg#	67.1		66.0		65.3	
Cations (3 oxygens)						
Si	0.003	(0.001)	0.003	(0.005)	0.005	(0.004)
Ti	0.988	(0.013)	0.978	(0.009)	0.975	(0.005)
Fe^{3+}	0.018	(0.027)	0.037	(0.021)	0.041	(0.014)
Fe^{2+}	0.326	(0.018)	0.334	(0.010)	0.340	(0.004)
Mg	0.665	(0.012)	0.648	(0.009)	0.639	(0.006)
Sum	2.000		2.000		2.000	
$Fe^{3+}/\Sigma Fe$	0.052		0.099		0.108	
$K_D^{olv\text{-}ilm}{}_{Mg\text{-}Fe}$	5.8		6.7		6.6	

Table 3.5: continued.

Experiment	T-3596 initial		T-3948 oxide mix		T-3596 reversed	
	Rutile (n=8)		Rutile (n=4)		Rutile (n=3)	
SiO_2	0.13		0.07		0.09	
TiO_2	95.18		97.33		97.36	
FeO	1.71		1.02		1.02	
MgO	0.69		0.05		0.05	
Total	97.72		98.46		98.51	
Cations (2 oxygens)						
Si	0.002	(0.001)	0.001	(0.000)	0.001	(0.000)
Ti	0.981	(0.004)	0.993	(0.001)	0.993	(0.000)
Fe	0.020	(0.002)	0.012	(0.001)	0.012	(0.000)
Mg	0.014	(0.004)	0.001	(0.000)	0.001	(0.000)
Sum	1.017		1.006		1.006	

Notes: Experimental details are given in Table 3.6. T-3596 'initial' represents the original experimental run; T-3948 'oxide mix' and T-3596 'reversed' represent the consistency experimental runs, with the 'oxide mix' being the MAK-2 starting mix, and T-3596 'reversed' being the run product of the original experiment. Values in parentheses represent standard deviations. See text for explanation.

The work described here is an example of such a consistency experiment. Oxide mixes are known to be more reactive than crystalline materials and often produce metastable phase assemblages and phase compositions. On the other hand, Pattison (1994) documented a number of unreversed solid solution experiments, using crystalline starting materials, which yielded consistent compositional trends as a function of pressure, temperature and other intensive parameters, which were necessary, if not sufficient, indications that a chemical equilibrium was closely approached. The reversal experiment (*sensu stricto*) documented in this study demonstrates apparent multi-parameter convergence for oxide and crystalline mix compositions, and suggests a close approach to chemical equilibrium.

3.4 Experimental results

Details of experimental run conditions, and phases detected in these runs are presented in Table 3.6. Representative electron probe microanalyses are shown in Appendix D1.1 to D2.4.

The experimental runs were performed at sub-solidus conditions. A typical run product consisted of large (with a diameter up to ~15–20 μm) equant, subhedral olivine grains and, in case of YVB-1, subordinate, poikiolitic orthopyroxene grains. Orthopyroxene was absent from some YVB-1 experiments (T-3377 and T-3410) conducted under NNO oxygen buffer conditions. This confirms the difficulty in controlling the orthopyroxene stability (and the silica activity, a_{SiO2}), particularly in olivine capsules, which can create a potential problem in oxygen geobarometry studies. For example, Ballhaus *et al.* (1991) noted that the a_{SiO2} in the melt and a_{mt} in spinel were inversely related through the FMQ equilibrium and, provided that all other variables were kept constant, a drop in a_{SiO2} caused an increase in ferric iron in spinel. Although ferric iron in ilmenite will show a similar response to changes in a_{SiO2}, results from a number of experiments under NNO oxygen buffer conditions where orthopyroxene was detected did not give different redox ratios in ilmenite. The oxide phases were interstitial, anhedral to subhedral ilmenite grains, and subhedral to euhedral lath-shaped rutile grains included in the silicate matrix. Ilmenite and rutile were generally present in similar proportions. However, rutile was occasionally the dominant Ti-bearing oxide phase (e.g. T-3445 where only one ilmenite grain was detected).

Table 3.6: Summary of experimental run conditions in the SiO_2-TiO_2-FeO-MgO system, and phases detected.

Run Number	Composition	P (kbar)	T (°C)	Run time (hrs)	Buffer	logfO_2	ΔlogfO_2 (FMQ)	Phases
T-3329	YVB-1	30	1100	48	WCWO	-10.32	-2.65	Olv+Opx+Ilm+Rut±Arm
T-3350	YVB-1	30	1100	48	GW/GCO	-8.74	-1.07	Olv+Opx+Ilm+Rut
T-3357	YVB-1	25	1100	48	GW/GCO	-9.04	-1.03	Olv+Opx+Ilm+Rut
T-3366	YVB-1	25	1100	48	HM	-4.11	3.90	Olv+Opx+Ilm+Rut
T-3377	YVB-1	15	1100	48	NNO	-8.40	0.27	Olv+Ilm+Rut
T-3386	YVB-1	25	1000	119	HM	-5.51	3.80	Olv+Opx+Ilm+Rut
T-3398	YVB-1	35	1200	20	NNO	-6.57	-0.32	Olv+Opx+Ilm+Rut±Gl(?)
T-3399	YVB-1	25	900	176	HM	-7.15	3.67	Olv+Opx+Ilm+Rut
T-3409	YVB-1	25	1050	50	NNO	-8.69	-0.06	Olv+Opx+Ilm+Rut
T-3410	YVB-1	15	1100	30	NNO	-8.40	0.27	Olv+Ilm+Rut
T-3412	YVB-1	35	1100	48	HM	-4.01	3.33	Olv+Opx+Ilm+Rut
T-3419	YVB-1	35	1000	120	HM	-5.40	3.19	Olv+Opx+Ilm+Rut
T-3431	YVB-1	25	1000	98	NNO	-9.39	-0.08	Olv+Opx+Ilm+Rut
T-3436	YVB-1	35	1100	49	GW/GCO	-8.64	-1.30	Olv+Opx+Ilm+Rut
T-3437	YVB-1	25	1000	96	GW/GCO	-11.57	-2.26	Olv+Opx+Ilm+Rut
T-3445	YVB-1	30	1050	84	GW/GCO	-9.23	-0.94	Olv+Opx+Rut±Ilm
T-3450	YVB-1	15	1000	79	HM	-5.61	4.41	Olv+Opx+Ilm+Rut
T-3495	MAK-1	25	1100	41	HM	-3.67	4.33	Olv+Opx+Rut
T-3543	MAK-1	35	1150	28	WCWO	-9.42	-2.64	Olv+Opx+Rut
T-3525	MAK-2	25	1150	26	NNO	-7.46	-0.04	Olv+Opx+Rut
T-3535	MAK-2	28	1125	39	WCWO	-10.07	-2.56	Olv+Opx+Rut±Arm
T-3547	MAK-2	35	1150	24	WCWO	-9.42	-2.64	Olv+Opx+Rut
T-3596	MAK-2	32	1150	30	WCWO	-9.56	-2.59	Olv+Opx+Rut±Arm
T-3665	MAK-2	30	1100	48	HM	-2.87	3.69	Olv+Opx+Rut
T-3705	MAK-2	20	1050	48	NNO	-8.88	0.10	Olv+Opx+Rut
T-3708	MAK-2	20	1050	71	HM	-4.83	4.15	Olv+Opx+Rut

Notes: Abbreviations: Olv = olivine, Opx = orthopyroxene, Ilm = ilmenite, Rut = rutile, Arm = armalcolite, Gl = glass, ± indicates that a phase was present in trace quantities.

A powder X-ray diffraction (XRD) analysis was made of one of the run products synthesized under oxidized conditions (T-3665) to ascertain the nature of the mineral phases, particularly ilmenite. Details of the analytical technique are given in Appendix B4. Results of the XRD are given in Figure 3.5 and Table 3.7. The diffraction pattern of sample T-3665 shows that the experimental run product contains olivine, rutile and an ilmenite phase. This ilmenite phase has cell dimensions of a_0 = 5.053 (±0.010) Å and c_0 = 13.906 (±0.015) Å. The lattice size is compatible with a composition intermediate between hematite and ilmenite-geikielite, which is consistent with electron microprobe analyses.

3.4.1 Silicate mineral chemistry

Olivine compositions (Appendices D1.1 and D2.1) range from $Fo_{85.1\text{-}95.0}$ (YVB-1) and $Fo_{92.2\text{-}96.3}$ (MAK-2). The Fo content systematically increases with increasing oxygen fugacity which is consistent with an increase in the activity of Fe^{3+} and a decrease in Fe^{2+} under increasing oxidation conditions at constant total Fe (Figure 3.6A).

Orthopyroxene compositions for the YVB-1 composition (Appendices D1.2) range from $Mg^{\#}$ 87.4–95.2. Similarly to the Fo value of olivines, the $Mg^{\#}$ of the orthopyroxenes increases linearly with increasing oxygen fugacity (Figure 3.6B). Pyroxene $Mg^{\#}$ values are slightly higher than Fo contents in co-existing olivines under reduced conditions, but similar under oxidized conditions (Figure 3.6C).

3.4.2 Oxide mineral chemistry

Ilmenite compositions show a strong dependence on the oxygen fugacity conditions in these experiments (Appendices D1.3 and D2.2). The $Fe^{3+}/\sum Fe$ ratio (redox ratio) in ilmenite is a suitable parameter to describe the compositional response to fO_2 and within the P-T-fO_2-composition range of the experimental work, the ratio displays a simple near-linear relationship with $\Delta \log fO_2$ (FMQ), with a correlation coefficient of 0.980 (Figure 3.7A).

The redox ratio of ilmenites at high oxidation conditions is found to be slightly sensitive to temperature, and $Fe^{3+}/\sum Fe$ decreases with increasing temperature at HM (Figure 3.7B). However, under more reducing conditions this temperature effect becomes less evident. The redox ratio also shows a slight pressure dependence in the most oxidized experiments, and for both starting compositions $Fe^{3+}/\sum Fe$ in ilmenite decreases with increasing pressure at HM (Figure 3.7C). Again, within the analytical error, this effect cannot be detected under more reducing conditions. The pressure dependence of the redox ratio, which has also been documented for spinel (e.g. Ballhaus *et al.*, 1991) appears to be consistent with a

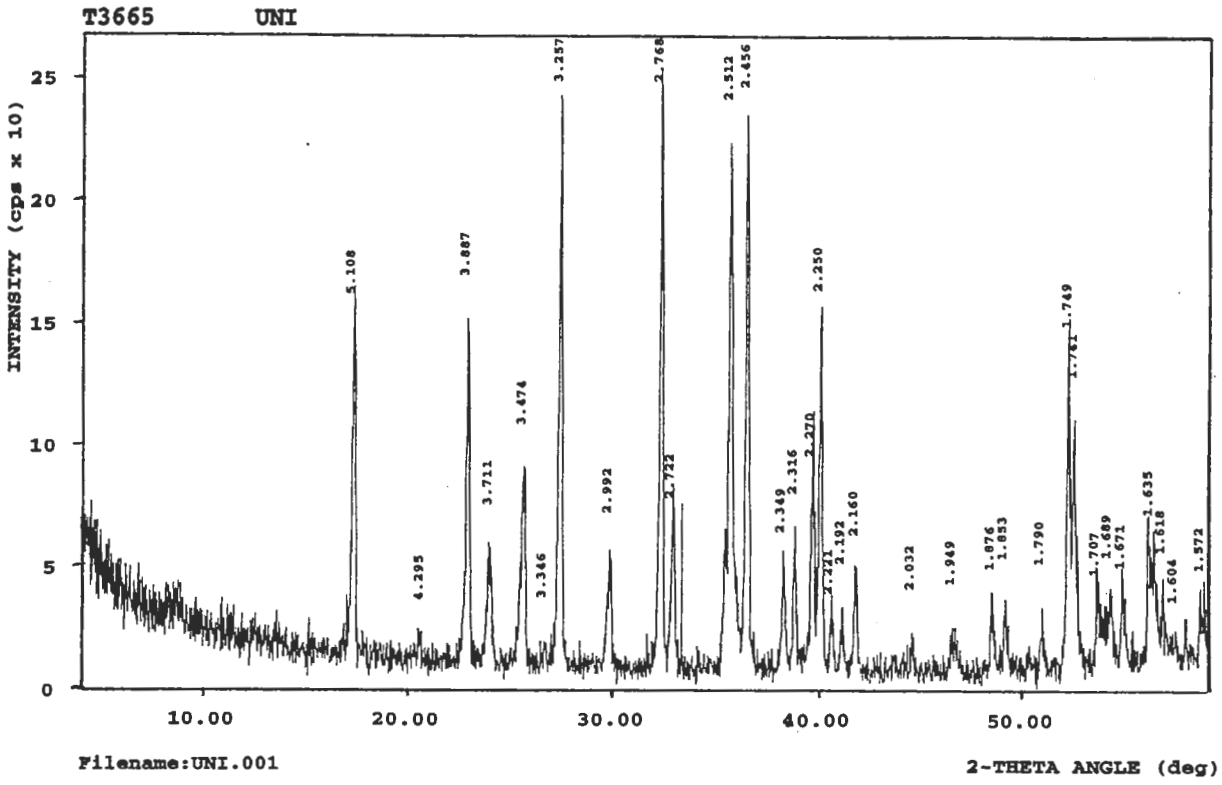

Figure 3.5: X-ray diffraction pattern of MAK-2 experiment T-3665 run product (30 kbar, 1100 °C). See Table 3.7 for an explanation of the peak positions.

Table 3.7: X-ray diffraction data of experiment T-3665.

Mineral	d Å	Intensity (I/I_1)
Olivine	2.76	100
	2.45	70
	2.51	65
	5.09	40
Ilmenite	2.72	20
	1.851	10
	1.705	10
	4.62	2
Rutile	3.25	60
	1.618	15
	2.19	10
	3.35	60

Notes: For each mineral the strongest three peaks are given, as well as the peak with the greatest d-spacing. Intensities are given as ratios with respect to the strongest peak (I_1) of the entire diffraction pattern.

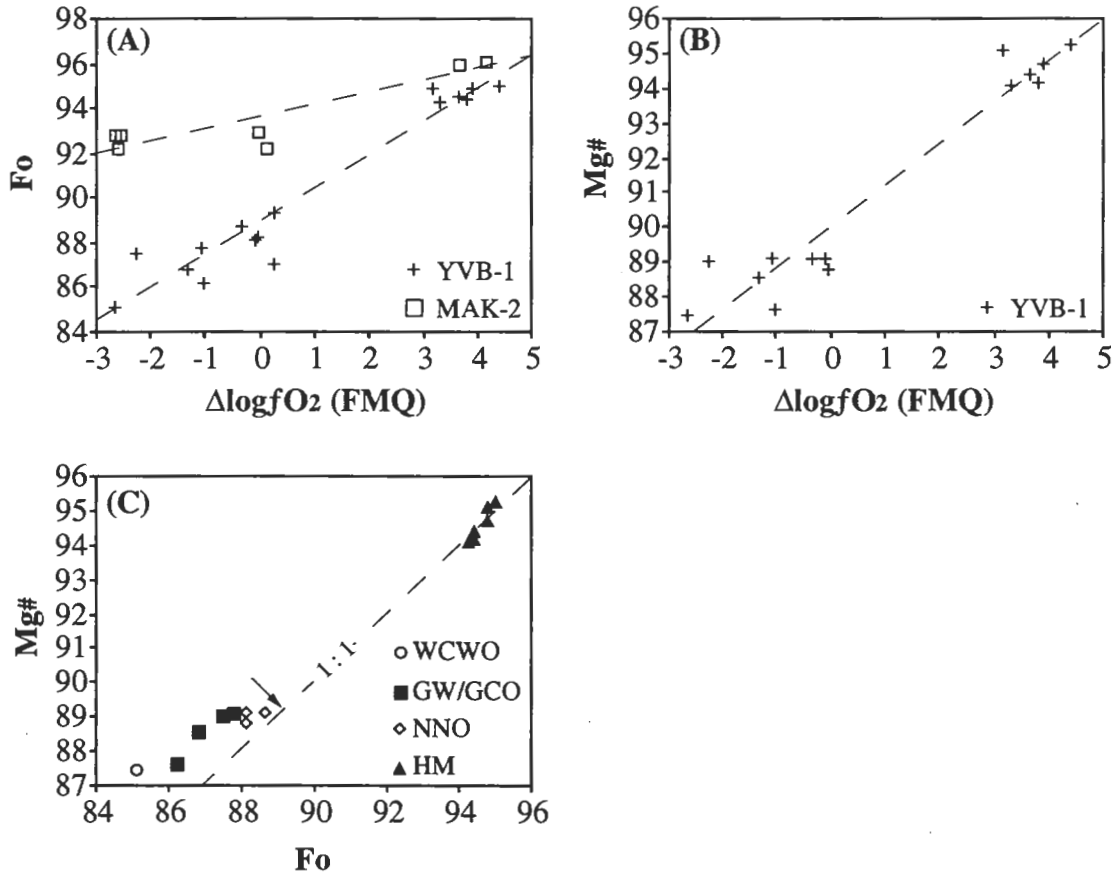

Figure 3.6: Chemical variation of silicate minerals in experimental runs involving YVB-1 and MAK-2 oxide mixes. (A) Plot against $\Delta \log fO_2$ (FMQ) of forsterite content of olivine (Fo). (B) Plot against $\Delta \log fO_2$ (FMQ) of $Mg^{\#}$ for orthopyroxene. The dashed lines in (A) and (B) represent lines of best fit. (C) Plot against Fo of $Mg^{\#}$ for orthopyroxene as a function of oxygen buffers used. Arrow indicates increasing experimental temperatures for NNO experiments.

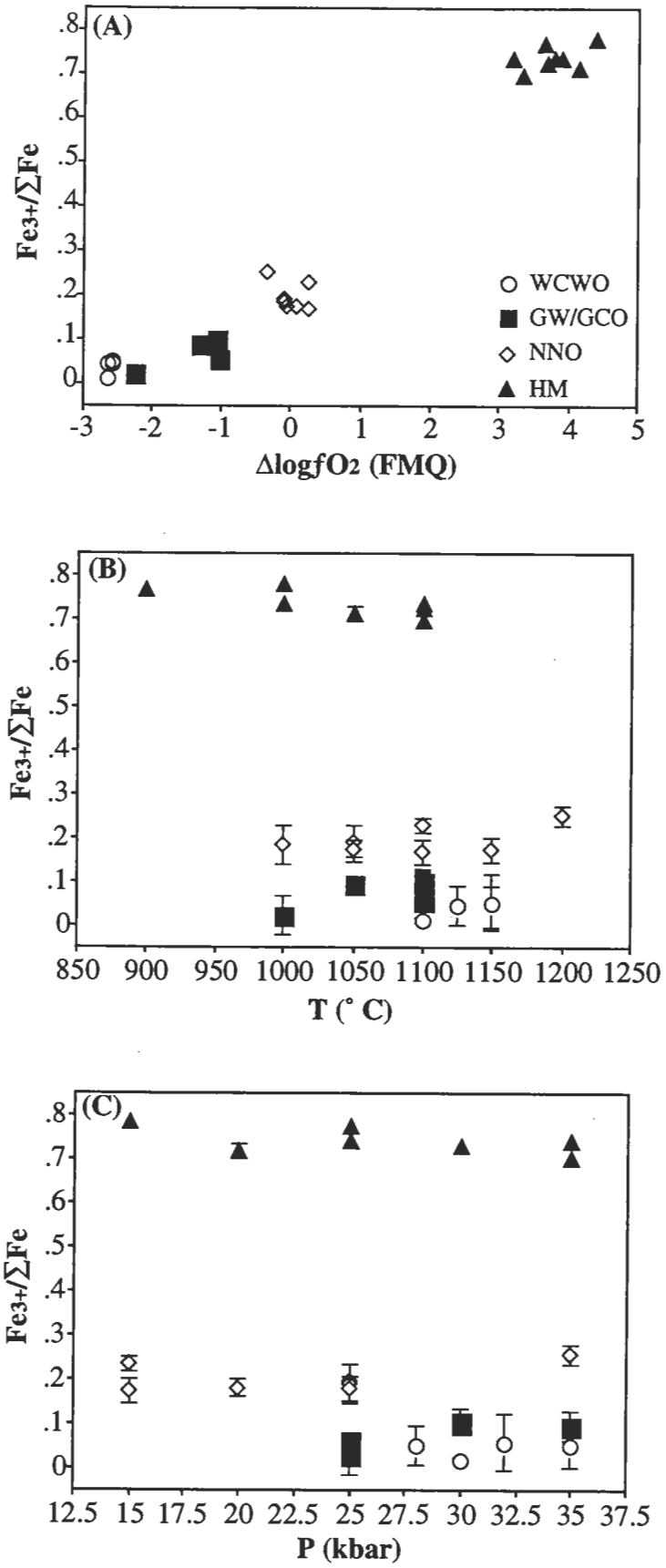

Figure 3.7: The $Fe^{3+}/\Sigma Fe$ ratio in ilmenite as a function of (A) experimental oxygen fugacity, expressed as $\Delta \log fO_2$ (FMQ), (B) experimental run temperature and (C) experimental run pressure. Error bars (included only where larger than the size of the symbol) are two standard deviations.

standard pressure correction based on molar volume changes. The P-T dependence of the ilmenite redox ratio for the most oxidized conditions (HM) supports the necessity expressed earlier for a closer investigation of the substitution of ferric iron in ilmenite, and any related hematite non-ideality terms.

Experimental ilmenite compositions can be illustrated in terms of the ilmenite ternary, recalculated as the ilmenite, geikielite and hematite solid solution endmembers (Figure 3.8). This illustration confirms the increasing hematite component with an increasing oxygen fugacity of the experiment, reflecting an increase in the $Fe^{3+}/\sum Fe$ ratio of the ilmenites. A significant feature of the illustration is the apparent lack of evidence for the existence of the large, low pressure (originally established at 1 atm), immiscibility gap between the hematite and geikielite endmembers extending towards the ilmenite join, as described by Woermann *et al.* (1970). These authors state that ..."extensive miscibility is present in the ternary at ~6 kbar and 1300 °C." Haggerty and Tompkins (1984) correctly pointed out that the extent of immiscibility and the influence of fO_2 at high pressures were unknown. In response to these early observations, the absence of a two phase spinel-pseudobrookite oxide assemblage in experiments from this study shows that ilmenites, synthesized under high P-T, oxidized conditions (HM) are stable and have an ilmenite structure (e.g. XRD results, Table 3.7). Thus, it is concluded that the immiscibility gap either does not exist under the P-T-fO_2-composition conditions of these experiments, or is smaller than suggested in the earlier studies.

Rutiles, like ilmenites, have compositions that are strongly dependent on the oxygen fugacity conditions of the experiments (Appendices D1.4 and D2.3). The iron content of rutiles, expressed as Fe_2O_3, increases with increasing oxygen fugacity from 1.6 wt.% (WCWO) to 6.7 wt.% (HM), and a near-linear relationship exists between the Fe_2O_3 content and $\Delta \log fO_2$ (FMQ) with a correlation coefficient of 0.94 (Figure 3.9A). Within the range of oxygen fugacity values for each oxygen buffer, the iron content of rutiles is sensitive to pressure, and Fe_2O_3 increases with increasing pressure (Figure 3.9B). The Fe_2O_3 content also increases with increasing temperature (Figure 3.9C). The MgO content of rutiles is elevated ranging from 0.12–0.82 wt.%, and there is a broad positive correlation between temperature and the magnesium content (Figure 3.9D).

Armalcolite was observed as a rare accessory mineral phase only in some experiments conducted under the most reduced conditions (WCWO; T-3329, T-3535 and T-3596). Armalcolite analyses are given in Appendices D1.5 and D2.4. All analyses from the experiments recalculate as armalcolite using the scheme of Bowles (1989).

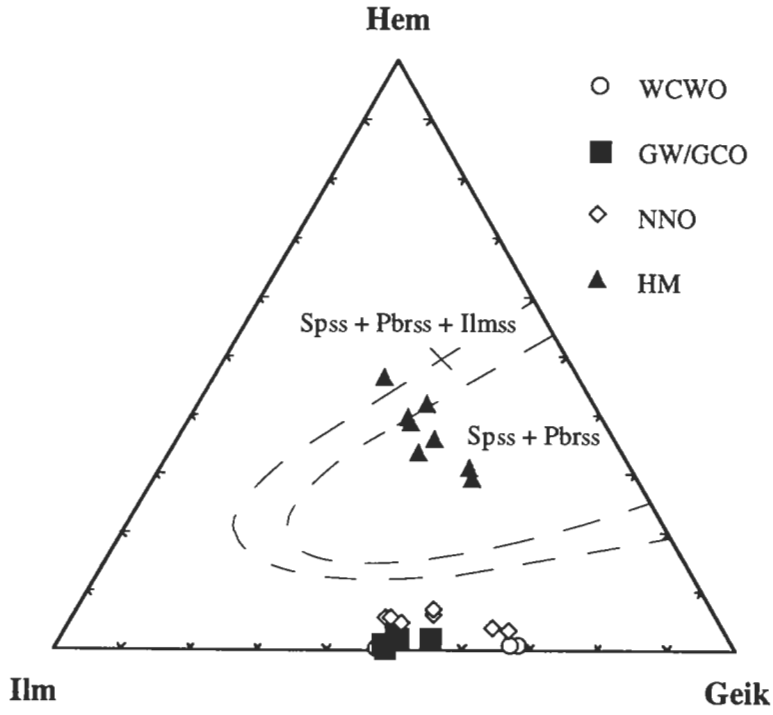

Figure 3.8: Experimental ilmenite compositions expressed in terms of ilmenite solid solution endmembers (Ilm = mol % ilmenite, Geik = mol % geikielite, Hem = mol % hematite). Decomposition loops at 1300 °C and 1 atm are from Woermann *et al.* (1970) (Sp_{ss} = spinel and Pbr_{ss} = pseudobrookite solid solution members, respectively).

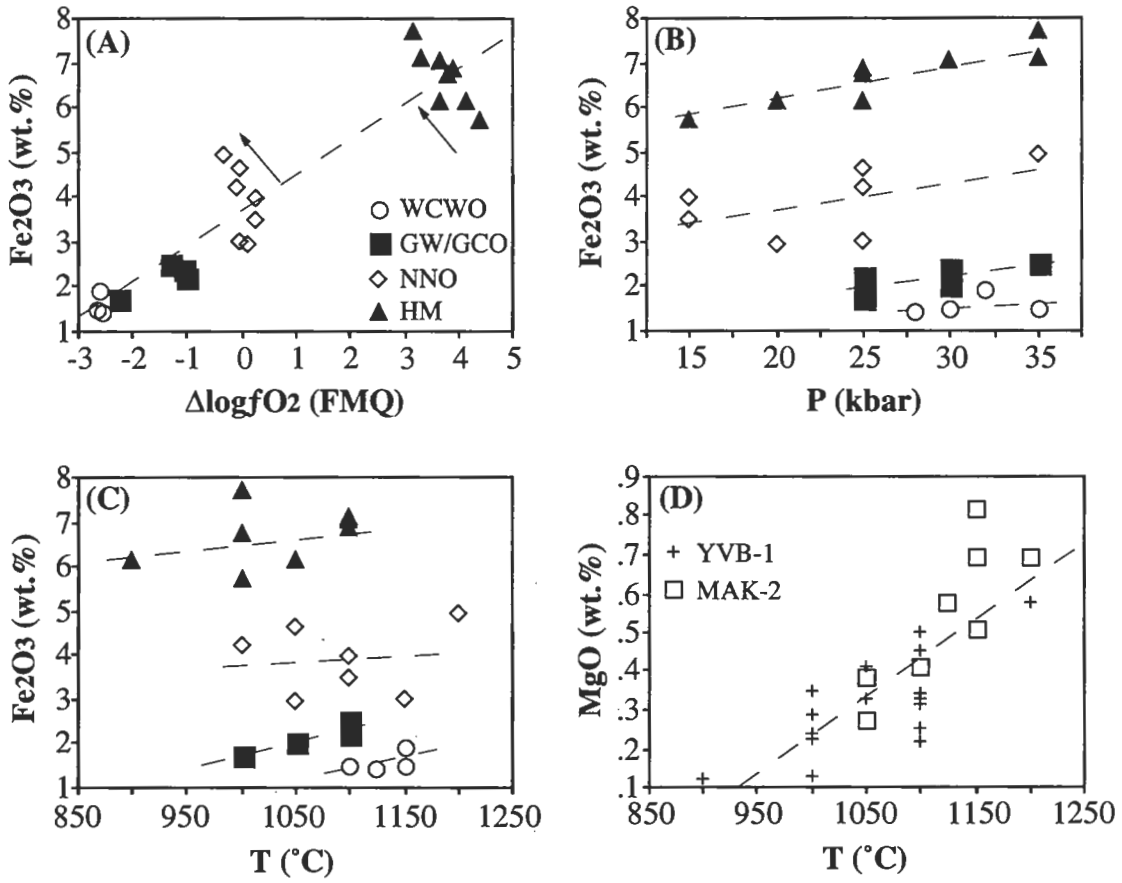

Figure 3.9: Chemical variation of rutile in experimental runs involving YVB-1 and MAK-2 oxide mixes. (A) Plot against $\Delta \log fO_2$ (FMQ) of Fe_2O_3. Arrows indicate trend associated with increasing pressure. (B) Plot against pressure of Fe_2O_3 as a function of oxygen buffers used. The legend for the buffers is shown in (A). (C) Plot against temperature of Fe_2O_3 as a function of oxygen buffers used. The legend for the buffers is shown in (A). (D) Plot against temperature of MgO. The dashed lines represent lines of best fit.

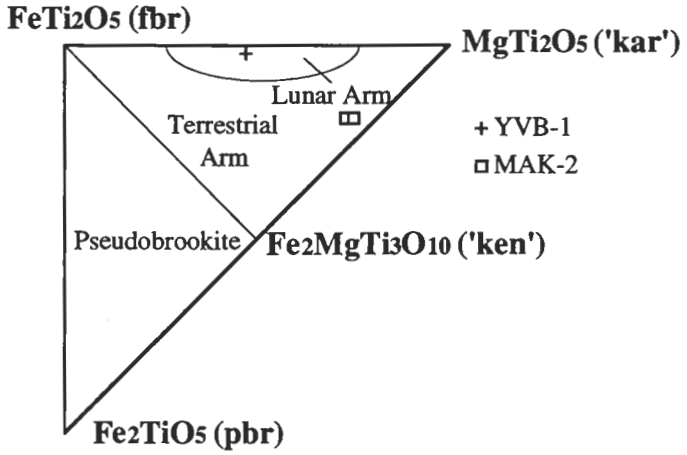

Figure 3.10: Experimental armalcolite compositions recalculated using the scheme of Bowles (1988), where fbr = ferropseudobrookite, pbr = pseudobrookite, 'ken' = 'kennedyite' and 'kar' = karrooite.

The armalcolite from YVB-1 (T-3329) can best be described as having a composition similar to lunar armalcolites with little ferric iron (e.g. Wechsler, 1977), whereas the armalcolite compositions from MAK-2 (T-3535 and T-3596) are more akin to 'karrooite' with some ferric iron (Figure 3.10). Armalcolite grains analysed were fine grained (<5-10 μm), and analyses documented here may represent a chemical overlap with surrounding mineral grains. Alternatively, the analyses could represent fine grained rutile-ilmenite intergrowths, although scanning electron microscopy could not resolve such textures. Also, the presence of armalcolite as a metastable phase can not be ruled out. It should therefore be noted that as the stability of armalcolite is not the focus of this study, and it only occurred in three experiments at very low fO_2 conditions, its occurrence will not be considered further.

3.5 Testing of existing geothermometers and oxygen geobarometer

The Andersen and Lindsley (1981) olivine-ilmenite Fe-Mg exchange geothermometer, the Bishop (1980) orthopyroxene-ilmenite Fe-Mg exchange geothermometer and the Eggler (1983) ilmenite oxygen geobarometer will hereafter be referred to as AL81, B80 and E83 respectively.

3.5.1 Fe-Mg exchange geothermometry

Andersen and Lindley (1979, 1981) calibrated the olivine-ilmenite Fe-Mg exchange geothermometer between 700-980 °C at 1 kbar and 800-900 °C at 13 kbar by equilibrating synthetic $(Fe,Mg)_2SiO_4$ - $(Fe,Mg)TiO_3$ solid solutions under oxygen fugacity conditions at approximately FMQ-1.0 log units. The geothermometer was derived by fitting an asymmetric ternary ilmenite solid solution and a symmetric solution model for olivine to the experimental data using a least squares analysis. The AL81 geothermometer gives a poor fit to the experimental data of this study. The thermometer is sensitive to the redox ratio of ilmenite and can not be used with confidence for ilmenites with $Fe^{3+}/\Sigma Fe$ ratios below 0.05 or above 0.15 (Figure 3.11). Below FMQ-2.0 log units the thermometer systematically overestimates temperatures by 60-100 °C, whereas at FMQ it underestimates temperatures by 90-150 °C. Increasing oxidation conditions render the thermometer unreliable with temperatures being underestimated by as much as 600 °C for olivine-ilmenite mineral pairs synthesized under HM conditions.

The orthopyroxene-ilmenite Fe-Mg exchange geothermometer of Bishop (1980) was experimentally calibrated between 800-1515 °C at 13 kbar and 1000-1360 °C at 36 kbar using synthetic $(Fe,Mg)SiO_3$ - $(Fe,Mg)TiO_3$ solid solutions.

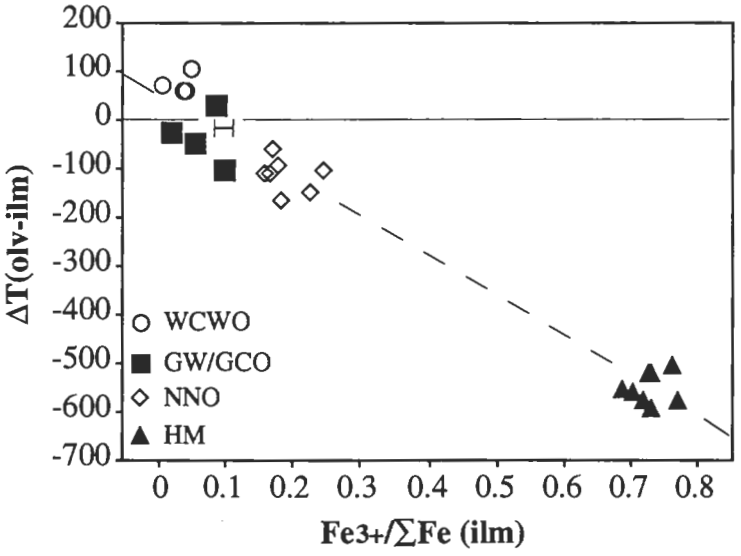

Figure 3.11: Calculated temperatures, using the Anderson and Lindsley (1981) Fe-Mg exchange geothermometer, for experimental olivine-ilmenite mineral pairs against the $Fe^{3+}/\sum Fe$ ratio of ilmenites, as a function of oxygen buffers used. ΔT(olv-ilm) denotes the difference between experimental and calculated temperatures (in °C). The bar denotes the compositional range of experimental ilmenites investigated by Anderson and Lindsley (1981).

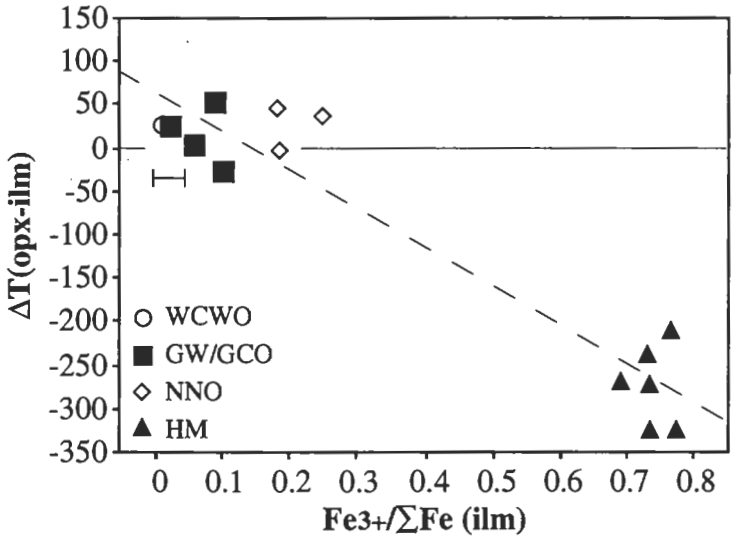

Figure 3.12: Calculated temperatures, using the Bishop (1980) Fe-Mg exchange geothermometer, for experimental orthopyroxene-ilmenite mineral pairs against the $Fe^{3+}/\sum Fe$ ratio of ilmenites, as a function of oxygen buffers used. ΔT(opx-ilm) denotes the difference between experimental and calculated temperatures (in °C). The bar denotes the compositional range of experimental ilmenites investigated by Bishop (1980).

The oxygen fugacity was not experimentally controlled by oxygen buffers, but the use of iron and graphite capsules under anhydrous conditions ensured a reducing environment, and the Fe_2O_3 component in ilmenite was in all cases kept below 10 mol %. Bishop (1980) formulated the geothermometer by fitting a regular ilmenite solution model and an ideal solution model for orthopyroxene to the activity data. The B80 thermometer is sensitive to the $Fe^{3+}/\sum Fe$ value of ilmenites but it gives a better fit than the AL81 geothermometer for oxygen fugacity conditions equivalent to ~FMQ-2.0 log units to FMQ (Figure 3.12). Experimental temperatures calculated from mineral chemistry data over this fO_2 range are within 50 °C of actual temperatures. However, at highly oxidized conditions (HM) the B80 formulation breaks down and underestimates temperatures from orthopyroxene-ilmenite mineral pairs by as much as 300 °C.

These results indicate that neither temperature formulation makes appropriate corrections for the ferric iron content of ilmenites, although the orthopyroxene-ilmenite geothermometer appears to be more reliable under relatively reduced, mantle oxygen fugacity conditions. A reasonable explanation for the discrepancy between actual and calculated temperatures as a function of fO_2 is that the ilmenite-based thermometers were only calibrated for temperature over a narrow range of oxygen fugacity. The effect of oxygen fugacity on the $Fe^{3+}/\sum Fe$ ratio in ilmenite was not investigated and, as a consequence, its influence on the respective ilmenite-silicate K_D's was not established.

3.5.2 Oxygen geobarometry

The olivine-orthopyroxene-ilmenite oxygen geobarometer of Eggler (1983), defined by the equilibrium 8 $Fe_{0.5}SiO_2$ (fa) + O_2 (fluid) = 2 Fe_2O_3 (hem) + 2 $Fe_2Si_2O_6$ (fs) was formulated using existing ΔG^o data from calibrated equilibrium reactions involving fayalite, ferrosilite and hematite (e.g. Bohlen and Boettcher, 1981; Chou, 1978; Eugster and Wones, 1962). The E83 oxygen geobarometer was presented using two sets of olivine-orthopyroxene activity-composition relations and accompanying ilmenite solution models: model A represented a regular symmetric solution fit to both olivine and orthopyroxene activities, whereas model B represented a regular asymmetric solution fit to olivine activities and a regular symmetric solution fit to orthopyroxene activities. The ilmenite solution model for the oxygen geobarometer was adopted directly from AL81. The E83 oxygen geobarometer gives a good fit to the experimental results from this study. Model A gives $\Delta \log fO_2$ (FMQ) results ±0.5 log units of the experimental values for all but the most reduced experiment where the calculated value is ~1.0 log unit lower than the experimental value (WCWO, T-3329) (Figure 3.13). Model B is also gives a good fit with calculated $\Delta \log fO_2$ (FMQ) values slightly lower than model A (Figure 3.13).

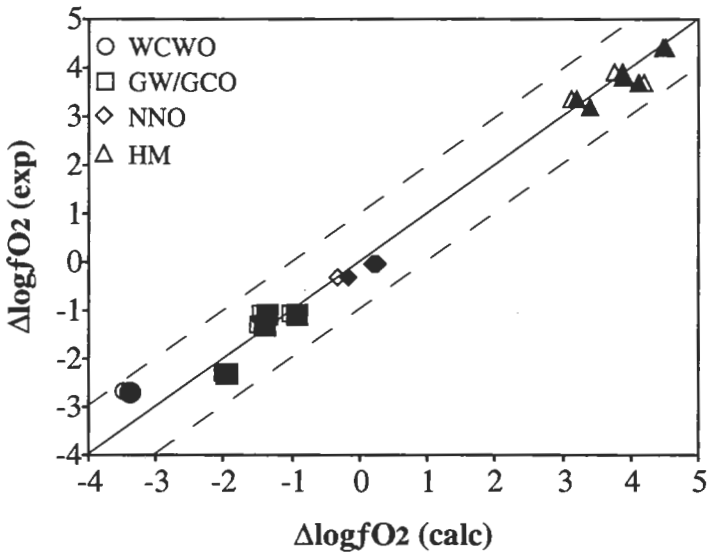

Figure 3.13: The Eggler (1983) olivine-orthopyroxene-ilmenite oxygen geobarometer applied to experimental data from this study, where $\Delta \log fO_2$ (calc) denotes calculated oxygen fugacities with reference to the fayalite-magnetite-quartz oxygen buffer, and $\Delta \log fO_2$ (exp) denotes the experimental oxygen fugacity conditions. Closed and open symbols denote oxygen fugacity values calculated using model (A) and (B) of Eggler (1983), respectively. The dashed lines indicate ± 1.0 log unit.

It is important to note, however, that the E83 model is potentially flawed because it employs an ilmenite solution model based on the AL81 olivine-ilmenite Fe-Mg exchange reaction which is shown to be unreliable under oxidized conditions (e.g. Figure 3.11). The AL81 formulation was based on reduced experiments with low X_{hem} (<6 mol %), and the Margules terms involving hematite (W_G^{hem}) were evaluated from independent experimental mineral data consisting of coexisting magnesian magnetite and ilmenite (Pickney and Lindsley, 1976; Lindsley, 1978). Using the W_G^{hem} terms, a $W_G^{ilm\text{-}gk}$ term (where W_G indicates the Margules parameter for excess free-energy, G^{xs}, and the superscript indicates for which part of the solid solution the W_G term applies, in this case ilmenite-geikielite) was determined from the Fe-Mg exchange experimental results. However, it can be shown that for the Andersen and Lindsley (1981) experiments, conducted under reduced conditions, the determination of $W_G^{ilm\text{-}gk}$ is essentially independent of any W_G^{hem} terms. For example, equation (8) of Andersen and Lindsley (1981) becomes $RT\ln\gamma^{ilm}_{FeTiO3} \approx W_G^{ilm\text{-}gk}(X^2_{gk})$ at low X_{hem}, and similarly, their equation (9) can be written as $RT\ln\gamma^{ilm}_{MgTiO3} \approx W_G^{ilm\text{-}gk}(X^2_{ilm})$. This independence of W_G^{hem} terms at reduced experimental conditions is illustrated in figure 1a. of Andersen and Lindsley (1981) where, within the P-T range of the authors' experiments, ΔG_{exch} calculated for three different solution models are essentially the same. On the other hand, the E83 oxygen geobarometer is critically dependent on X_{hem} and W_G^{hem} terms, as well as W_G terms involving ilmenite and geikielite (cf. Eggler, 1983, equation 3). Thus, with the AL81 geothermometer having been shown to be increasingly unreliable under increasing oxygen fugacities (e.g. Figure 3.11), the use of poorly constrained AL81 W_G^{hem} terms in formulating the E83 oxygen geobarometer is considered invalid and requires correction.

3.6 Ilmenite-based Fe-Mg exchange thermometry and oxygen geobarometry

3.6.1 Olivine-ilmenite geothermometry

Experimental data from this study have been used to formulate a new olivine-ilmenite Fe-Mg exchange geothermometer. The exchange reaction:

$$MgTiO_3\ (gk) + Fe_{0.5}SiO_2\ (fa) = FeTiO_3\ (ilm) + Mg_{0.5}SiO_2\ (fo) \qquad (3.1)$$

can be expressed as:

$$\Delta G_{exch} = \Delta H_{exch} - T\Delta S_{exch} + P\Delta V_{exch} - 2\,RT\ln(a^{ilm}_{MgTiO3}) - RT\ln(a^{olv}_{Fe2SiO4}) + 2\,RT\ln(a^{ilm}_{FeTiO3}) + RT\ln(a^{olv}_{Mg2SiO4}) \qquad (3.2)$$

where the gas constant, R = 8.314 J K^{-1} mol^{-1}, T is in °K, P is in bar, and ΔV_{exch} = -0.047 J bar^{-1} (Fischer and Medaris, 1969; Lindsley, 1976b).

Olivine activities, according to a regular solution model, can be expressed as:

$$RT\ln a^{olv}_{Fe0.5SiO2} = RT\ln X^{olv}_{Fe} + W^{olv}_{Fe\text{-}Mg}(X^{olv}_{Mg})^2 \quad (3.3)$$

and $$RT\ln a^{olv}_{Mg0.5SiO2} = RT\ln X^{olv}_{Mg} + W^{olv}_{Fe\text{-}Mg}(1 - X^{olv}_{Mg})^2 \quad (3.4)$$

where X^{olv}_{Fe} = [Fe/(Mg+Fe)]^{olv} and $W^{olv}_{Fe\text{-}Mg}$ is the Margules term for the non-ideality of olivine (O'Neill and Wall, 1987). A number of experimental studies have been undertaken to ascertain the magnitude of the olivine non-ideality term (e.g. Matsui and Nishizawa, 1974; O'Neill and Wood, 1979; Jamieson and Roeder, 1984; Wiser and Wood, 1991). Following a detailed discussion of published data, von Seckendorff and O'Neill (1993) adopted the two-site regular model for olivine of Wiser and Wood (1991) with $W^{olv}_{Fe\text{-}Mg}$ = (3700 + 0.0108P) J mol^{-1}, which has also been used for this study.

The AL81 model is based on an ilmenite solid solution that remains fully ordered over the temperature-composition range of interest, and Andersen and Lindsley (1981) obtained expressions for the non-ideal ilmenite and geikielite components using the assumption that the ilmenite-geikielite and geikielite-hematite binaries were symmetric, and the ilmenite-hematite binary was asymmetric. However, the experimental ilmenite data presented in this study, ranging from $0.003<X_{hem}<0.465$, does not extend far enough across the binary to allow the accurate calculation of an asymmetric model. Thus, for the purpose of this model it has been assumed that the ilmenite-hematite binary is symmetric. It should be noted that Wood *et al.* (1990) obtained acceptable results for hematite activity assuming the hematite-ilmenite binary is symmetric. Thus the AL81 non-ideality equations (8) and (9) for ilmenite and geikielite respectively become:

$$RT\ln\gamma^{ilm}_{FeTiO3} = W^{ilm\text{-}gk}_{G}(X^{2}_{gk} + X_{gk}X_{hem}) - W^{gk\text{-}hem}_{G}X_{gk}X_{hem} + W^{ilm\text{-}hem}_{G}(X^{2}_{hem} + X_{gk}X_{hem}) \quad (3.5)$$

$$RT\ln\gamma^{ilm}_{MgTiO3} = W^{ilm\text{-}gk}_{G}(X^{2}_{ilm} + X_{ilm}X_{hem}) + W^{gk\text{-}hem}_{G}(X^{2}_{hem} + X_{ilm}X_{hem}) - W^{ilm\text{-}hem}_{G}X_{ilm}X_{hem} \quad (3.6)$$

respectively, where $X_{ilm} = [Fe^{2+}/(Fe^{2+} + Mg + (Fe^{3+}/2))]^{ilm}$, $X_{gk} = [Mg/(Fe^{2+} + Mg + (Fe^{3+}/2))]^{ilm}$ and $X_{hem} = [(Fe^{3+}/2)/(Fe^{2+} + Mg + (Fe^{3+}/2))]^{ilm}$. Using the non-ideality terms described above, and the AL81 expression for $W_G^{ilm\text{-}gk} = 5767 - 3.09T + 0.011P$, equation (3.2) can be expressed as:

$$\Delta G_{exch} = \Delta H_{exch} - T\Delta S_{exch} - 0.047P + RT\ln K_{id}$$
$$+ (3700 + 0.0108P)(2X_{Fe}^{olv} - 1)$$
$$+ (5767 - 3.09T + 0.011P)(X_{gk} - X_{ilm})$$
$$+ (W_G^{ilm\text{-}hem} - W_G^{gk\text{-}hem})(X_{hem}) \qquad (3.7)$$

where $K_{id} = [(X_{Fe}^{ilm})(X_{Mg}^{olv})] / [(X_{Mg}^{ilm})(X_{Fe}^{olv})]$, and $X_{Fe}^{ilm} = Fe^{2+}/(Fe^{2+} + Mg)$. Equation (3.7) was solved for ΔH_{exch}, ΔS_{exch} and the $(W_G^{gk\text{-}hem} - W_G^{ilm\text{-}hem})$ non-ideality term using a least-squares fit through the experimental data to give the olivine-ilmenite Fe-Mg exchange geothermometer:

$$T\,(^{\circ}C) = -273 + \{-8389 + P[-0.047 + 0.0108(2X_{Fe}^{olv} - 1) + 0.011(X_{gk} - X_{ilm})]$$
$$+ 3700(2X_{Fe}^{olv} - 1) + 5676(X_{gk} - X_{ilm}) - 20375X_{hem}\}$$
$$/ [3.09(X_{gk} - X_{ilm}) - 8.314\ln K_{id} + 6.09] \qquad (3.8)$$

where ΔH_{exch} = -8.39 (3.9) $kJmol^{-1}$, ΔS_{exch} = 6.09 (2.8) $Jmol^{-1}K^{-1}$, and the $(W_G^{ilm\text{-}hem} - W_G^{gk\text{-}hem})$ non-ideality term equals -20375 (1119) $Jmol^{-1}$, values in brackets represent standard errors, calculated by the least-squares method. Andersen and Lindsley (1981) data resolved W_G^{hem} terms into a W_H and a temperature-dependent W_S component. However, it is noted that the experimental data set presented in this study, which was conducted over a smaller temperature range than the Andersen and Lindsley (1981) experiments, cannot accurately resolve the W_H and W_S terms. The $\Delta G^0_{exch,\,298}$ value calculated by the model is -10.2 $kJmol^{-1}$, which compares well with the AL81 $\Delta G^0_{exch,\,298}$ values of -8.3–10.0 $kJmol^{-1}$ (depending on the solution models used, Andersen and Lindsley, 1981). Also, Bishop (1979) computes a $\Delta G^0_{exch,\,298}$ value of -7.9 $kJmol^{-1}$ which is within the range calculated from the model presented here and the AL81 values. Finally, in estimating the temperatures of equilibration of the coexisting experimental olivine-ilmenite assemblages, the geothermometer in equation (3.8) gives calculated temperatures that no longer deviate from experimental temperatures as a function of the ilmenite redox ratio (Figure 3.14).

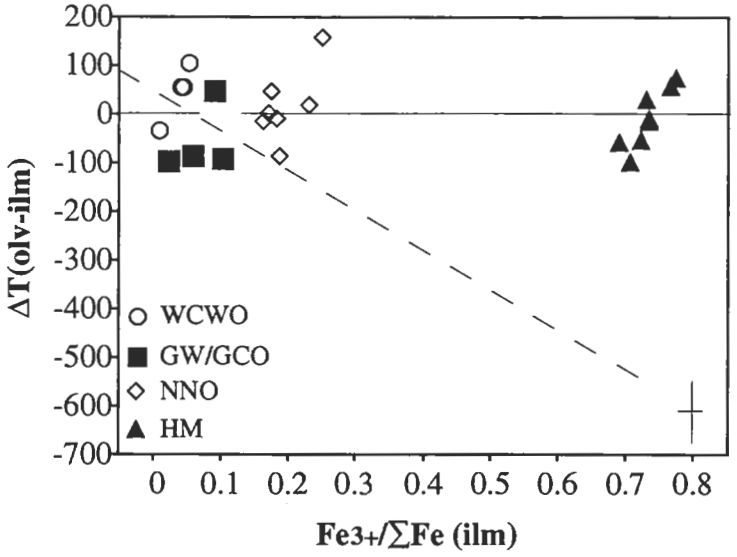

Figure 3.14: Calculated temperatures, using the Fe-Mg exchange geothermometer presented in this study, for experimental olivine-ilmenite mineral pairs against the $Fe^{3+}/\sum Fe$ ratio of ilmenites, as a function of oxygen buffers used. ΔT(olv-ilm) denotes the difference between experimental and calculated temperatures (in °C). The error bar denotes one standard deviation. The dashed line shows the trend of corresponding ΔT values calculated using the Anderson and Lindsley (1981) thermometer (see Figure 3.11).

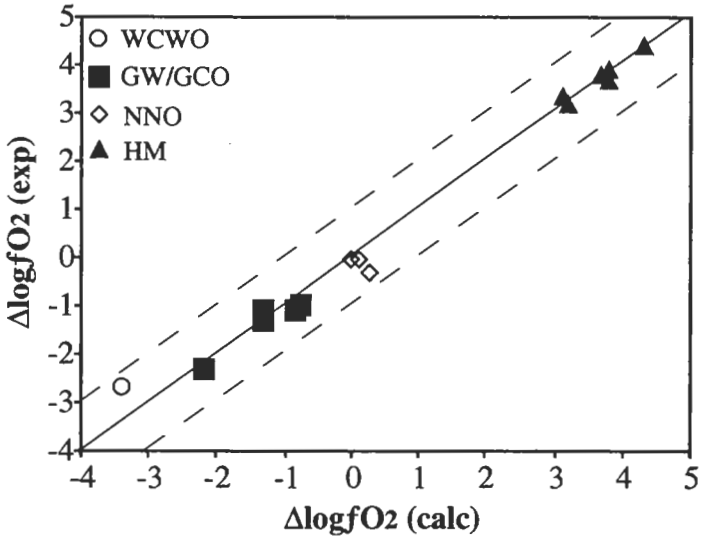

Figure 3.15: Experimental oxygen fugacities (with reference to the fayalite-magnetite-quartz oxygen buffer) against calculated oxygen fugacities, using the olivine-orthopyroxene-ilmenite oxygen geobarometer presented in this study, for experimental mineral pairs. The dashed lines indicate ± 1.0 log unit.

3.6.2 Olivine-orthopyroxene-ilmenite oxygen geobarometry

The olivine-orthopyroxene-ilmenite redox equilibrium can be used to calculate the oxygen fugacity:

$$8\ Fe_{0.5}SiO_2\ (fa) + O_2\ (fluid) = 2\ Fe_2O_3\ (hem) + 2\ Fe_2Si_2O_6\ (fs) \qquad (3.9)$$

(abbreviated FFH reaction) and the equilibrium reaction can be expressed as:

$$\Delta G = \Delta H - T\Delta S + P\Delta V_s - 4\ RT\ln(a^{olv}_{Fe2SiO4}) - RT\ln(a_{O2})$$
$$+ 2\ RT\ln(a^{ilm}_{Fe2O3}) + 2\ RT\ln(a^{opx}_{Fe2Si2O6}) \qquad (3.10)$$

Adopting the earlier argument regarding the symmetric nature of the ilmenite-hematite binary (see section 3.6.1), equation (3) of Eggler (1983) becomes:

$$RT\ln\gamma^{ilm}_{Fe2O3} = W_G^{ilm\text{-}hem}(X^2_{ilm} + X_{ilm}X_{gk}) + W_G^{gk\text{-}hem}(X^2_{gk} + X_{ilm}X_{gk})$$
$$- W_G^{ilm\text{-}gk}(X_{ilm}X_{gk}) \qquad (3.11)$$

Thus, using equation (3.3) to describe a two-site regular model for olivine and assuming an ideal solid solution for orthopyroxene (e.g. O'Neill and Wall, 1987; Mattioli and Wood, 1988; Ballhaus *et al.*, 1991; von Seckendorff and O'Neill, 1993), equation (3.10) can be written as:

$$\log fO_2\ (FFH) = \Delta S/(2.303R) - \Delta H/(2.303RT) + 0.0375P/T$$
$$+ 2\log(X^{ilm}_{Fe3+}) + 2\log(a^{opx}_{Fe}) - 8\log(X^{olv}_{Fe})$$
$$- 8\ W^{olv}_{Fe\text{-}Mg}(X^{olv}_{Mg})^2/(2.303RT) - W_G^{ilm\text{-}gk}(X_{ilm}X_{gk})\ /(2.303RT)$$
$$+ W_G^{ilm\text{-}hem}(X^2_{ilm} + X_{ilm}X_{gk})\ /(2.303RT)$$
$$+ W_G^{gk\text{-}hem}(X^2_{gk} + X_{ilm}X_{gk})\ /(2.303RT) \qquad (3.12)$$

where $X^{olv}_{Fe} = [Fe/(Mg+Fe)]^{olv}$, $X^{ilm}_{Fe3+} = [(Fe^{3+}/2)/(Fe^{2+}+Mg+(Fe^{3+}/2))]^{ilm}$, a^{opx}_{Fe} equals the activity of ferrosilite in orthopyroxene, and $\Delta V_s = 0.718\ Jbar^{-1}$ (Holland and Powell, 1990). The non-ideality terms $W^{olv}_{Fe\text{-}Mg}$ and $W_G^{ilm\text{-}gk}$ are described above, and a value for the combined ($W_G^{ilm\text{-}hem} - W_G^{gk\text{-}hem}$) non-ideality term of -20375 $Jmol^{-1}$ was adopted from the olivine-ilmenite Fe-Mg exchange geothermometer (see section 3.6.1).

Using a least-squares fit through the experimental data, equation (3.12) can be solved for ΔS and ΔH to give the oxygen geobarometer:

$$\log fO_2\,(\mathrm{FFH}) = 8.905 - \frac{22840}{T} + \frac{0.0375P}{T}$$
$$+ 2\log(X^{ilm}_{Fe3+}) + 2\log(a^{opx}_{Fe}) - 8\log(X^{olv}_{Fe})$$
$$-\{(1546 + 0.005P)((X^{olv}_{Mg})^2) + (602 - 0.323T + 0.001P)(X_{ilm}X_{gk})$$
$$+ 272(X^2_{gk} + X_{ilm}X_{gk}) + 2401(X^2_{ilm} + X_{ilm}X_{gk})\} / T \qquad (3.13)$$

where P is in bar, T in °K and mole fractions of olivine and ilmenite endmembers have been described in section 3.6.1. For the reaction (3.9) ΔH = -437.56 (42.1) kJmol^{-1} and ΔS = -170.48 (34.0) Jmol^{-1}K^{-1} (where values in brackets represent standard errors), and $\Delta G^0_{1,\,298}$ equals -386.8 kJmol^{-1}. In contrast with the standard Gibbs free energy calculated here from the experimental data, Eggler (1983), using a series of independently documented phase equilibrium experiments, obtained a $\Delta G^0_{1,\,298}$ value of -412.3 kJmol^{-1}. The least-squares procedure resolved the combined ($W_G^{gk\text{-}hem}$ - $W_G^{ilm\text{-}hem}$) term into $W_G^{ilm\text{-}hem}$ = -22852 Jmol^{-1} (4111), and $W_G^{gk\text{-}hem}$ = -2477 (467) J mol^{-1} (where values in brackets represent standard errors).

The oxygen geobarometer in equation (3.13) gives an average calculated fO_2 deviation of -0.01 log units (with a 1σ of 0.30 log units) over the experimentally calibrated P-T-X range (Figure 3.15). In its practical application, the oxygen geobarometer is considered reliable to ±0.3 log units if temperatures are accurately known. However, temperatures are normally also estimated from the mineral assemblages. The olivine-ilmenite thermometer (equation 3.8) can be used to calculate equilibration temperatures with a reasonable reliability, and the average deviation in calculated fO_2 values using olivine-ilmenite temperatures is 0.10 log units (with a σ of 1.10 log units). The increased standard deviation probably reflects the limited range of calibrated temperatures, and some care needs to be exercised in evaluating equilibration temperatures. Results indicate that the oxygen geobarometer is reliable to ±1.0 log unit for temperatures as low as 900 °C.

3.6.3 Rutile-ilmenite oxygen geobarometry

Rutile-ilmenite mineral pairs are potential oxygen fugacity indicators through the oxidation equilibrium:

$$4\,FeTiO_3\,(ilm) + O_2\,(fluid) = 4\,TiO_2\,(rut) + 2\,Fe_2O_3\,(hem) \qquad (3.14)$$

(abbreviated RIO reaction) which can be expressed as:

$$\Delta G = \Delta H - T\Delta S + P\Delta V_s - 4\,RT\ln(a^{ilm}_{FeTiO3}) - RT\ln(a_{O2}) + 4\,RT\ln(a^{rut}_{TiO2}) + 2\,RT\ln(a^{ilm}_{Fe2O3}) \quad (3.15)$$

Using equations (3.5) and (3.11) for the ilmenite and hematite non-ideality terms respectively, and assuming ideal site mixing in rutile, equation (3.15) can be written as:

$$\begin{aligned}\log fO_2 &= \Delta S/(2.303R) - \Delta H/(2.303RT) + 0.0473P/T \\ &+ 4\log(X^{rut}_{TiO2}) + 2\log(X^{ilm}_{Fe3+}) - 4\log(X^{ilm}_{Fe2+}) \\ &+ W_G^{gk\text{-}ilm}(2X_{ilm}X_{gk} - 4X_{gk}) \ /(2.303RT) \\ &+ W_G^{gk\text{-}hem}(2X_{gk}X_{hem} + 2X_{gk}) \ /(2.303RT) \\ &+ W_G^{ilm\text{-}hem}(2X_{ilm} + 2X_{hem}X_{ilm} - 4X_{hem}) \ /(2.303RT)\end{aligned} \quad (3.16)$$

where $X^{ilm}_{Fe2+} = [(Fe^{2+})/(Fe^{2+} + Mg + (Fe^{3+}/_2))]^{ilm}$, $X^{ilm}_{Fe3+} = [(Fe^{3+}/_2)/(Fe^{2+} + Mg + (Fe^{3+}/_2))]^{ilm}$, $(W_G^{ilm\text{-}hem} - W_G^{gk\text{-}hem})$ equals -20375 Jmol^{-1} (see section 3.6.1) and ΔV_s = 0.906 Jbar^{-1} (Holland and Powell, 1990). Adopting the AL81 expression for $W_G^{ilm\text{-}gk}$ as described in section 3.6.1, equation (3.16) can be solved from the experimental data set using a least-squares fit to give the following oxygen geobarometer:

$$\begin{aligned}\log fO_2\,(RIO) &= 18.618 - \frac{34090}{T} + \frac{0.0473P}{T} \\ &+ 4\log(X^{rut}_{TiO2}) + 2\log(X^{ilm}_{Fe3+}) - 4\log(X^{ilm}_{Fe2+}) \\ &+ \{(602 - 0.323T + 0.001P)(X_{ilm}X_{gk} - 2X_{gk}) \\ &+ (23036 - 17.9T)(X_{gk}X_{hem} + X_{gk})) \\ &+ (20908 - 17.9T)(X_{ilm} + X_{ilm}X_{hem} - 2X_{hem})\} / T\end{aligned} \quad (3.17)$$

where P is in bar, T is in °K and mole fractions for ilmenite endmembers are described in section 3.6.1. The calculated value for ΔH for the oxidation reaction equals -652.74 (91.0) kJmol^{-1} and ΔS = -356.49 (71.0) Jmol^{-1}K^{-1} (with values in brackets representing standard errors), and $\Delta G^0_{1,\,298}$ equals -546.5 kJmol^{-1}. For the oxidation equilibrium involving ilmenite and rutile, the regression coefficient to the least-squares fit of the experimental data was improved by the introduction of a temperature-dependent non-ideality Margules term (i.e. $W_G = W_H - TW_S$), and the combined $(W_G^{gk\text{-}hem} - W_G^{ilm\text{-}hem})$ non-ideality term was resolved into $W_G^{ilm\text{-}hem}$ = 200200 - 171.2T Jmol^{-1}, and $W_G^{gk\text{-}hem}$ = 220500 - 171.2T Jmol^{-1}, where the standard errors for the W_H and W_S terms are 63000 Jmol^{-1} and 48 JK^{-1}mol^{-1} respectively.

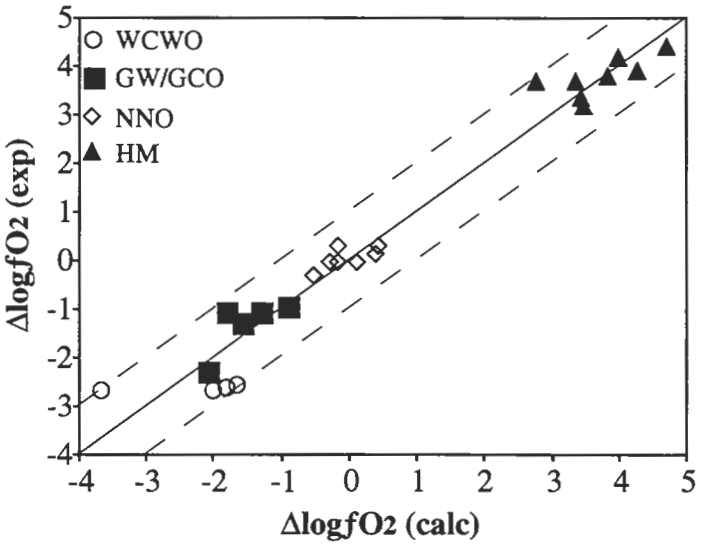

Figure 3.16: Experimental oxygen fugacities (with reference to the fayalite-magnetite-quartz oxygen buffer) against calculated oxygen fugacities, using the rutile-ilmenite oxygen geobarometer presented in this study, for experimental mineral pairs. The dashed lines indicate ± 1.0 log units.

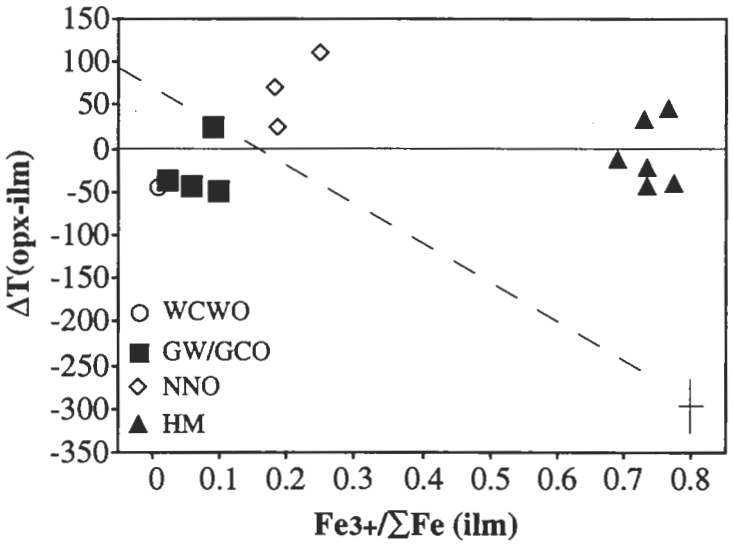

Figure 3.17: Calculated temperatures, using the Fe-Mg exchange geothermometer presented in this study, for experimental orthopyroxene-ilmenite mineral pairs against the $Fe^{3+}/\sum Fe$ ratio of ilmenites, as a function of oxygen buffers used. ΔT(opx-ilm) denotes the difference between experimental and calculated temperatures (in °C). The error bar denotes one standard deviation. The dashed line shows the trend of corresponding ΔT values calculated using the Bishop (1980) thermometer (see Figure 3.12).

Within the P-T-X calibration range the rutile-ilmenite oxygen geobarometer gives an average calculated fO_2 deviation of -0.01 log units (with a 1σ of 0.50 log units) (Figure 3.16).

3.6.4 Orthopyroxene-ilmenite geothermometry

The orthopyroxene-ilmenite Fe-Mg exchange geothermometer is represented by the following equilibrium reaction:

$$FeTiO_3\ (ilm) + MgSiO_3\ (en) = MgTiO_3\ (gk) + FeSiO_3\ (fs) \qquad (3.18)$$

(Bishop, 1980). From experimental data obtained under reducing conditions (equivalent to ~FMQ-2.0 log units), Bishop (1980) determined a ΔV_{exch} for the reaction of -0.103 $Jbar^{-1}$ and a $\Delta G^0_{r,\,1300}$ of 20.5 $kJmol^{-1}$. Combining the B80 geothermometer and the ΔT - $Fe^{3+}/\sum Fe_{ilm}$ best-fit relationship (c.f. Figure 3.12) the following modified orthopyroxene-ilmenite geothermometer is formulated:

$$T\,(^\circ C) = \frac{1484 + 1634\,[Fe^{2+}/(Fe^{2+} + Mg)]^{ilm} + 1185\,[Fe^{3+}/(Fe^{3+} + Fe^{2+})]^{ilm} + 0.0124\,P}{\ln K_D} - 273 \qquad (3.19)$$

where $K_D = (Mg/Fe)^{opx} / (Mg/Fe)^{ilm}$ and P is in bar. The revised ilmenite-orthopyroxene geothermometer no longer gives calculated temperatures that deviate from experimental temperatures at high ilmenite redox ratios over the range of P-T-X conditions (Figure 3.17). However, for oxygen fugacity conditions equivalent to ~FMQ-2.0 log units to FMQ, calculated temperatures have not significantly improved to warrant the use of equation (3.19). It is important therefore to consider the $Fe^{3+}/\sum Fe$ ratio in ilmenite before selecting the appropriate geothermometer, and the B80 geothermometer is recommended for mineral assemblages with $Fe^{3+}/\sum Fe_{ilm}$ ratios <~0.3, whereas equation (3.19) should be used for assemblages with ilmenite redox ratios >~0.3.

3.7 Conclusions

Experimental results published in this chapter have shown that ilmenite is a mineral phase which can be used in association with other silicate and oxide mineral phases to calculate a number of intensive variables, such as temperature of formation and oxygen fugacity. Mg-rich ilmenites were synthesized in the Ti-enriched peridotite system under mantle P-T conditions (900-1200 °C and 15-35 kbar) and over a wide range in fO_2 (FMQ±4.0 log units). Existing ilmenite-based Fe-Mg olivine-ilmenite (e.g. Andersen and

Lindsley, 1981) and orthopyroxene-ilmenite (Bishop, 1980) exchange geothermometers were tested with the experimental mineral data. Although these thermometers worked reasonably well under reduced conditions (~FMQ-1.5 log units), they were found to become increasingly unreliable with increasing fO_2, especially under conditions higher than FMQ. It is therefore reasonable to expect significant errors when deriving quantitative equations describing intensive variables by extrapolation over the range of fO_2 documented here. The experimental data in this study were used to formulate new exchange thermometers with improved corrections for the hematite component in ilmenite.

The olivine-orthopyroxene-ilmenite oxygen geobarometer (Eggler, 1983) was also corrected using the improved thermodynamic treatment of hematite in the ilmenite solid solution. Although the existing Eggler (1983) oxygen geobarometer appears to be in good agreement with the experimental data, it has been emphasized that this barometer was originally derived from poorly constrained ilmenite thermodynamic formulations involving hematite, and as such warranted revision.

A new oxygen geobarometer, based on ilmenite-rutile mineral assemblages, has also been formulated from the experimental data. The reader is referred to Chapter 4 for, among other topics, a more detailed discussion of the application of ilmenite-based oxygen barometers developed in this study.

Experimental results in this study have also indicated that the substitution of iron (expressed as ferric iron) in rutile is dependent on experimental P-T-fO_2 conditions. The iron content of experimentally synthesized rutiles strongly increases with increasing oxygen fugacities. Because a link exists between the oxygen fugacity and the water activity of the experimental buffer technique employed in this study, it is suggested here that the substitution of iron in rutile may be coupled to the water content of rutile (e.g. Hammer and Beran, 1991), and that, if correct, rutile may be considered as a potential indicator of the water activity under which rutile-bearing assemblages formed. Although no further work has been done in this chapter to establish quantitative relationships between the intensive variables (e.g. pressure, temperature, oxygen fugacity and water activity) and the cation content of rutile, the reader is referred to Chapter 5 for a more detailed experimental study and discussion.

CHAPTER 4

AN EXPERIMENTAL STUDY OF THE CHROMIUM-ENRICHED ILMENITE-OLIVINE-ORTHOPYROXENE±SPINEL±RUTILE MINERAL SYSTEM WITH EMPHASIS ON ILMENITE AND SPINEL GEOTHERMOMETRY AND OXYGEN GEOBAROMETRY

4.1 Introduction

Chromium constitutes an an important chemical component in the upper mantle, and is present as a major element in spinel (e.g. Sack and Ghiorso, 1991), or as a minor element in many mantle-derived silicates and oxides such as garnet (e.g. Dawson and Stephens, 1975), clinopyroxene (e.g. Eggler and McCallum, 1976), orthopyroxene (e.g. Eggler *et al.*, 1979), olivine (e.g. Eggler *et al.*, 1979) and ilmenite (e.g. Haggerty, 1975). Sobolev (1977) used natural mineral compositions to demonstrate that, in general, with increasing pressure, chromium is redistributed from spinels into silicates, and the highest levels of Cr_2O_3 in mantle-derived silicates are found in those minerals which occur as inclusions in, or as intergrowths with diamond. In contrast, the behaviour of Cr in ilmenite is more complex, and appears to be a function of several factors including oxygen fugacity, pressure, temperature, crystallization history and petrological environment. For example, Sobolev (1977) suggested a link between oxidizing conditions and the solubility of chromium in megacryst ilmenite ('megacryst' terminology as defined by Harte, 1977) with low Cr_2O_3 contents detected in ilmenites formed in reduced environments. However, Sobolev (1977) also described low Cr ilmenites with elevated Fe_2O_3 contents, where a possible paragenesis for these ilmenites exists with low-Cr garnets. Some ilmenites documented as intergrowths with, or inclusions in diamond are among those with the lowest Cr contents among mantle-derived ilmenites (e.g. Meyer and Svisero, 1975; Sobolev, 1977), although diamond-inclusion ilmenites with elevated Cr_2O_3 contents have also been documented (e.g. Meyer and McCallum, 1986). Haggerty (1975) drew attention to a parabolic MgO-Cr_2O_3 relationship for several megacryst ilmenite populations from kimberlites in west Africa and South Africa. Here Cr_2O_3 contents sharply decrease at essentially constant MgO, followed by decreasing MgO at constant, low Cr_2O_3 concentration, until the most MgO-depleted compositions where there may be enrichment in Cr_2O_3 at relatively constant MgO. However, Mitchell (1986) and Moore (1987), among others, found that this compositional pattern was not necessarily fully duplicated in megacryst ilmenite populations from different locations, but rather different locations

defined sections of the MgO-Cr_2O_3 parabola, and the latter author reports a suggestion that the two limbs of the Haggerty parabola may represent grains derived from different kimberlite sources (Haggerty, pers. comm. to Moore, 1984). Both Gurney *et al.* (1979) and Schulze (1984) noted that the Cr_2O_3 content of megacryst ilmenites may be linked with their crystallization history. Ilmenites with essentially constant, low Cr_2O_3 contents from the Monastery kimberlite discrete nodule suite were interpreted as a late-forming phase, following the earlier crystallization of garnet, orthopyroxene, clinopyroxene and olivine (Gurney *et al.*, 1979), whereas megacryst ilmenites from the Hamilton Branch kimberlite, displaying variable Cr_2O_3 contents as a parabolic function of MgO, were interpreted to have been present throughout the period of crystallization of the associated silicate megacryst suite (Schulze, 1984).

Ilmenite occurs as small (<10 μm-0.05 mm) groundmass minerals in some kimberlites, or enclosed in euhedral olivine crystals, and these ilmenites generally appear to be distinctly more Cr_2O_3 rich than to those associated with the megacryst suite (e.g. Boyd and Nixon, 1973; Shee, 1984; Mitchell, 1986). Ilmenites are also characteristic mineral phases in the MARID suite of rocks and in metasomatized mantle peridotites (e.g. Dawson and Smith, 1977; Jones *et al.*, 1982). These ilmenites are generally enriched in Cr_2O_3 and MgO and, unlike many ilmenite megacrysts populations, display a wide, though apparently non-systematic, compositional variation (e.g. Dawson and Smith, 1977).

Megacryst magnesian ilmenites are reported in ultramafic lamprophyres, melilitites, alnöites, alkali basalts and basanites (e.g. Rock, 1989; Haggerty *et al.*, 1985; Nixon and Boyd, 1979; Parfenoff, 1982; Leblanc *et al.*, 1982). Compositionally these ilmenites overlap the Mg-poor portion of the kimberlitic ilmenite field, but in general they have distinctly lower Cr_2O_3 contents (e.g. Mitchell, 1986). Ilmenites are also described in carbonatites (e.g. Gaspar and Wyllie, 1983), but they are typically poor in MgO and Cr_2O_3 when compared with kimberlitic ilmenites (e.g. Mitchell, 1986).

From the above summary it becomes evident that the behaviour of chromium in Ti-rich systems, and more specifically the substitution of Cr_2O_3 in mantle-derived ilmenite, is diverse and deserving of further study. Of particular interest here is the comment by Sobolev (1977) that "it is necessary to arrange experimental investigations of systems with titanium and chromium at high pressures and temperatures and varying P_{O2}". Consistent with that suggestion, the aims of this chapter are: (i) to extend the experimental data presented in Chapter 3 of peridotite assemblages involving Mg-rich ilmenite, synthesized under subsolidus P-T-fO_2 conditions, into the Cr-rich compositional field; (ii) to document these Ti- and Cr-rich systems as a function of the experimental P-T-fO_2

conditions; and (iii) to test and, where necessary, suggest revisions to the ilmenite-based geothermometers and oxygen geobarometers taking into account the effects of Cr substitution. In addition, existing spinel-based geothermometers and oxygen geobarometers are tested and, where necessary, revised taking into account experimental compositions published in this study.

4.2 Experimental details

4.2.1 Selection and preparation of starting materials

Full details of the starting mix preparation and the experimental technique are described in Appendix A. The starting compositions used in this experimental study are a TiO_2-Cr_2O_3 enriched harzburgite (modified from YVB-1, see Chapter 3 herein) with a bulk $Mg^{\#}$ = 100*Mg/(Mg+Fe^{2+}) of ~80, and a variable $Cr^{\#}$ = 100*Cr/(Cr+Al) of 100 (MAK-6), ~90 (MAK-7) and ~81 (MAK-8) (Table 4.1). All mix compositions were prepared from spectroscopically pure oxides, and were enriched in ilmenite and spinel components to facilitate the growth of oxide grains under sub-solidus experimental conditions. The high chromium contents of the starting mixes were chosen not only to study Cr incorporation into ilmenite, but also to encourage crystallization of high $Cr^{\#}$ spinels, and test existing spinel-based oxygen geobarometers (e.g. O'Neill and Wall, 1987; Wood, 1990; Ballhaus *et al.*, 1991). An 'artificial' melt component was generated in the experiments by addition of ~1 wt% K_2O to the starting mixes to enhance mineral growth. Other metal-oxide contents were corrected to take into account the possible partitioning of their components into a K_2O-rich melt. In general however, partitioning of other oxide components into such a melt can be considered a relatively insignificant factor as the calculated modal melt component is low (<2 %). Small amounts of nickel (0.3 wt.% NiO) and zinc (0.3 wt.% ZnO) were added to the MAK-6 starting mix following suggestions that these components partition into mantle-derived spinels as a function of temperature (e.g. Griffin *et al.*, 1992). However, no detailed analytical work has been undertaken to-date to establish any relationship between temperature of formation and the Ni-Zn content of spinels.

4.2.2 Experimental technique

All experiments were performed with a 0.5 inch (1.27 cm) piston-cylinder apparatus (e.g. Boyd and England, 1960) using techniques similar to those described by Green and Ringwood (1967). Run conditions varied from 1025 to 1200 °C and 17 to 35 kbar. Outer sleeves of NaCl, NaCl-pyrex, talc or talc-pyrex were used as pressure media in the experimental assemblages. A pressure correction of -10 % of the nominal load pressure was applied to experimental runs using talc sleeves.

Table 4.1: Starting compositions.

	MAK-6	MAK-7	MAK-8
SiO_2	42.6 (39.7)	38.2 (35.7)	38.4 (35.6)
TiO_2	4.4 (3.1)	6.2 (4.3)	6.1 (4.3)
Al_2O_3	-	0.5 (0.3)	1.0 (0.5)
Cr_2O_3	6.8 (2.5)	6.7 (2.5)	6.1 (2.2)
FeO	13.8 (10.7)	15.1 (11.8)	14.8 (11.5)
MgO	31.1 (43.2)	32.3 (44.9)	32.6 (45.2)
K_2O	0.7 (0.4)	1.0 (0.6)	1.0 (0.6)
NiO	0.3 (0.2)	-	-
ZnO	0.3 (0.2)	-	-
$Mg^{\#}$	80.1	79.2	79.7
$Cr^{\#}$	100.0	89.3	81.5
Normative compositions (wt%)			
Olivine	24	37	37
Orthopyroxene	58	40	40
Ilmenite[a]	8	11	11
Spinel[b]	9	10	10
Melt[c]	1	2	2

Notes: Major element analyses are shown in wt.%; values in parentheses indicate analyses in mol %.
[a] Ilmenite compositions in normative calculations are assumed to contain MgO: for all starting compositions ilmenite is assumed with $Mg^{\#}$ 45. [b] Spinel compositions in normative calculations are assumed to contain MgO and to have variable $Cr^{\#}$: for MAK-6, spinels have $Mg^{\#}$ 45 and $Cr^{\#}$ 100, for MAK-7, spinels have $Mg^{\#}$ 45 and $Cr^{\#}$ 90, and for MAK-8, spinels have $Mg^{\#}$ 45 and $Cr^{\#}$ 80. [c] Normative melt compositions are calculated to include K_2O.

Pressures with NaCl-sleeved assemblages in the 10-35 kbar range were estimated to have an accuracy of ±(1 % + 0.5) kbar (Mirwald *et al.*, 1975). Temperatures were monitored with $Pt/Pt_{90}Rh_{10}$ thermocouples, and controlled to within ±10 °C of the desired values. Experimental run times ranged from 24 to 96 hours, depending on the temperature of the experiment and the buffering capacity of the oxygen buffer components. Typical run products are shown in Figure 4.1.

The controlled oxygen fugacity experiments used the double-capsule technique of Huebner (1971) with oxygen buffering being achieved through both welded and open inner sample capsules. The oxygen buffers used in these experiments were iron-wüstite (IW), WC-WO_2-graphite (WCWO), Ni-NiO (NNO), and Fe_2O_3-Fe_3O_4 (HM). The equations for calculating oxygen fugacity values (fO_2) for experimental conditions at known pressures and temperatures are given in Appendix A3 (Table A2). Where values for fO_2 in this chapter are reported with reference to the fayalite-magnetite-quartz (FMQ) buffer, they are quoted as $\Delta \log fO_2$ (FMQ) log units.

4.2.3 Analytical details

Run products and residual buffer material were optically examined under an immersion oil of accurately known refractive index (RI) to identify mineral phases and to ensure that buffer exhaustion had not occurred. Probe mounts of experimental run material were made using cold-set epoxy, and a high grade polish of the probe mounts was accomplished using successively finer grades of diamond polishing paste.

All mineral phases in the experimental runs were analysed at the University of Tasmania with a Cameca SX-50 electron probe microanalyser which was calibrated using natural mineral standards. Concentrations were calculated from relative peak intensities using a PAP matrix correction procedure. Analytical conditions were 15 kV accelerating voltage, and a 20 nA beam current. A TAP crystal was used for analysing Mg, Al and Si, a PET crystal was used for analysed Ti and Cr, and Mn, Fe, Ni and Zn were analysed on an LiF crystal. All elements were analysed at 20 seconds on the peak and 10 seconds on the background. A detailed description of analytical procedures is given in Appendix B.

Figure 4.1: Back-scattered electron images of experimental products of the Cr_2O_3-bearing peridotite system. (A) is experiment T-3864 (22 kbar, 1050 °C, NNO buffer, MAK-6 starting composition) showing abundant oxide minerals (ilmenite + spinel) in a silicate (olivine + orthopyroxene) matrix. Ilmenites are large (10-20 μm), dark grey grains, whereas spinels are small (<5 μm), light grey minerals. Spinels are often found as clusters of 5-10 individual grains. (B) is experiment T-3858 (20 kbar, 1050 °C, IW buffer, MAK-7 starting composition) showing dark grey ilmenite grains (ilm) and light grey spinel grains (spi) in a silicate (olivine + orthopyroxene) matrix. (C) is also experiment T-3858 showing a large (~10 μm) poikilitic orthopyroxene (opx) containing very fine grained oxide minerals, and small (<5 μm), light grey, rounded spinels (spi). The lathlike grain in the upper central section of the image is phlogopite. The white scale bar in (A) indicates 0.1 mm, and in (B) and (C) indicates 10 μm.

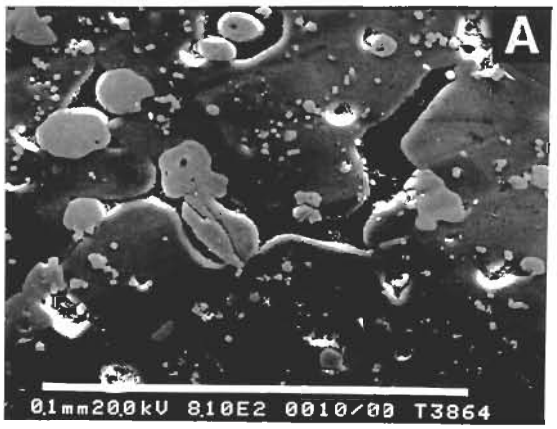
A
0.1mm20.0kV 8.10E2 0010/00 T3864

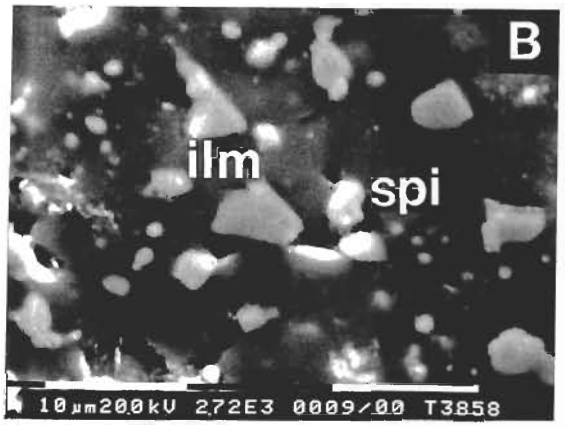
B
ilm
spi
10µm20.0kV 2.72E3 0009/00 T3858

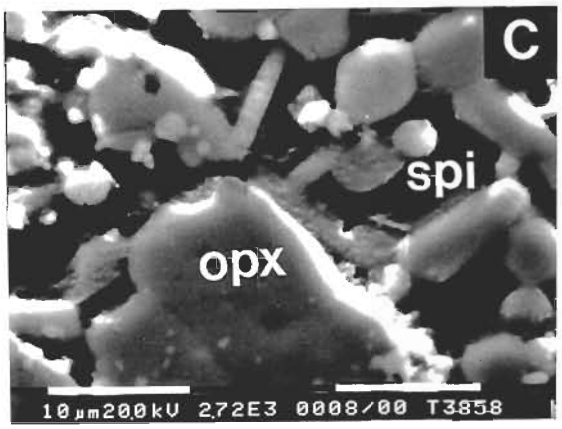
C
spi
opx
10µm20.0kV 2.72E3 0008/00 T3858

4.3 Treatment of analytical results

4.3.1 Calculation of ferric and ferrous iron

Electron microprobe analyses only give values for total iron. A common procedure to estimate the amount of ferric iron in minerals such as ilmenite and spinel involves the assumption of mineral stoichiometry, where iron is the only cation with a variable valence state (e.g. Finger, 1972; Mattioli *et al.*, 1989; Chapter 2 herein). Wood and Virgo (1989) described the difficulties in obtaining precise contents for ferric iron from relatively inaccurate microprobe data using the stoichiometry recalculation procedure, and presented a method for estimating the uncertainty in ferric iron contents in spinels. Similar problems with precision have been shown to exist for recalculation methods involving ilmenite (see Chapter 3 herein). In this chapter experimental ilmenite and spinel compositions were recalculated for ferric and ferrous iron following the methods described in Chapter 3, and by Wood and Virgo (1989) respectively, and analytical data are presented in relevant tables in terms of a calculated precision of 2σ.

4.3.2 An experimental approach of an equilibrium position

As pointed out in the previous chapter (refer to section 3.2.2), it is desirable that equilibrium compositions be approached from different conditions and compositional directions in experimental studies of relatively short duration before results can be used with any confidence to interpret geological processes which take place over much longer periods of time. Beside the 'qualitative' observations that compositional homogeneity exists among silicate and oxide phases in the individual run products, and that chemical zoning in large silicate and oxide grains is not observed, a consistency experiment (e.g. Pattison, 1994) was also undertaken for the Cr-rich compositions. Experimental details and mineral compositions are shown in Table 4.2. The starting materials for this experiment were a MAK-8 assemblage with olivine, orthopyroxene and hematite from run numbers T-3910 and T-3911, synthesized at 1075 °C, 22 kbar, FMQ+4.5 log units (HM buffer), and 1175 °C, 32 kbar, FMQ+4.0 log units (HM buffer) respectively. The experimental run products were reground separately under acetone to grain sizes between 5-10 μm, and T-3910 mix was loaded in a graphite capsule. Using a 'sandwich' technique, some MAK-8 starting mix was loaded as a discrete layer on top of the T-3910 mix, followed by a discrete layer of T-3911 mix. The entire assembly was re-equilibrated under sub-solidus conditions at 1125 °C, 25 kbar and FMQ-2.5 log units (WCWO buffer) for three days. The three run products are described in Table 4.2 as T-3910 'reversed', T-3946 'oxide mix' and T-3911 'reversed', respectively. The reground run products in the reversal run were fine grained (<10 μm in diameter), whereas the oxide mix was coarser grained (10-20 μm in diameter).

Table 4.2: Analytical details of a consistency experiment involving the MAK-8 oxide mix.

Experiment	T-3910 initial		T-3911 initial		T-3910 reversed		T-3946 oxide mix		T-3911 reversed	
T (°C)	1075		1175		1125		1125		1125	
P (kbar)	22		32		25		25		25	
Buffer	HM		HM		WCWO		WCWO		WCWO	
logfO_2	-4.47		-3.13		-10.22		-10.22		-10.22	
ΔlogfO_2 (FMQ)	4.05		3.56		-2.51		-2.51		-2.51	
Run time (hrs)	48		24		72		72		72	
	Olivine (n=6)		Olivine (n=4)		Olivine (n=3)		Olivine (n=3)		Olivine (n=3)	
SiO_2	41.13		40.72		38.98		39.23		39.35	
TiO_2	0.32		0.14		0.30		0.30		0.38	
Cr_2O_3	0.37		0.23		0.42		0.43		0.49	
FeO	4.73		5.07		15.30		15.28		15.57	
MgO	53.56		53.60		44.42		44.85		44.19	
Total	100.11		99.78		99.42		100.08		99.99	
$Mg^{\#}$	95.3		95.0		83.8		84.0		83.5	
Cations (4 oxygens)										
Si	0.985	(0.024)	0.981	(0.010)	0.987	(0.015)	0.987	(0.005)	0.992	(0.018)
Ti	0.006	(0.004)	0.003	(0.000)	0.006	(0.001)	0.006	(0.002)	0.007	(0.009)
Cr	0.007	(0.004)	0.004	(0.001)	0.008	(0.002)	0.008	(0.001)	0.010	(0.005)
Fe	0.095	(0.008)	0.102	(0.002)	0.324	(0.005)	0.321	(0.005)	0.328	(0.009)
Mg	1.912	(0.025)	1.924	(0.009)	1.677	(0.015)	1.681	(0.007)	1.660	(0.018)
Sum	3.005		3.014		3.003		3.003		2.996	

Notes: T-3910 'initial' and T-3911 'initial' represent the original experimental runs; T-3946 'oxide mix', and T-3910 'reversed' and T-3911 'reversed' represent the consistency experimental runs, with the 'oxide mix' being the MAK-8 starting mix, and T-3910 'reversed' and T-3911 'reversed' being the run products of the original experiment. Values in parentheses represent standard deviations. See text for explanation.

Table 4.2: continued.

Experiment	T-3910 initial		T-3911 initial		T-3910 reversed		T-3946 oxide mix		T-3911 reversed	
T (°C)	1075		1175		1125		1125		1125	
P (kbar)	22		32		25		25		25	
Buffer	HM		HM		WCWO		WCWO		WCWO	
$\log fO_2$	-4.47		-3.13		-10.22		-10.22		-10.22	
$\Delta \log fO_2$ (FMQ)	4.05		3.56		-2.51		-2.51		-2.51	
	Orthopyroxene (n=5)		Orthopyroxene (n=5)		Orthopyroxene (n=3)		Orthopyroxene (n=3)		Orthopyroxene (n=3)	
SiO_2	56.90		56.60		56.08		56.23		39.35	
TiO_2	0.38		0.41		0.51		0.63		0.38	
Al_2O_3	0.59		0.74		0.40		0.31			
Cr_2O_3	0.59		0.63		0.57		0.60		0.49	
FeO	3.57		3.84		9.10		9.21		15.57	
MgO	37.58		37.35		33.10		33.27		44.19	
Total	99.61		99.56		99.77		100.24		99.99	
$Mg^{\#}$	95.0		94.6		86.6		86.5		86.8	
Cations (6 oxygens)										
Si	1.950	(0.026)	1.943	(0.019)	1.965	(0.028)	1.962	(0.004)	1.957	(0.005)
Ti	0.010	(0.002)	0.010	(0.006)	0.013	(0.003)	0.016	(0.001)	0.012	(0.001)
Al	0.024	(0.013)	0.030	(0.007)	0.017	(0.004)	0.013	(0.000)	0.023	(0.004)
Cr	0.016	(0.004)	0.017	(0.003)	0.016	(0.002)	0.016	(0.001)	0.018	(0.001)
Fe	0.102	(0.008)	0.110	(0.010)	0.267	(0.008)	0.269	(0.001)	0.265	(0.003)
Mg	1.919	(0.024)	1.911	(0.020)	1.728	(0.027)	1.730	(0.005)	1.735	(0.007)
Sum	4.021		4.023		4.006		4.007		4.010	

Table 4.2: continued.

Experiment	T-3910 initial		T-3911 initial		T-3910 reversed		T-3946 oxide mix		T-3911 reversed	
T (°C)	1075		1175		1125		1125		1125	
P (kbar)	22		32		25		25		25	
Buffer	HM		HM		WCWO		WCWO		WCWO	
$\log fO_2$	-4.47		-3.13		-10.22		-10.22		-10.22	
$\Delta \log fO_2$ (FMQ)	4.05		3.56		-2.51		-2.51		-2.51	
	Hematite (n=5)		Hematite (n=5)		Ilmenite (n=3)		Ilmenite (n=3)		Ilmenite (n=3)	
SiO_2	0.07		0.07		0.20		0.10		0.39	
TiO_2	21.37		21.70		38.08		51.30		35.31	
Al_2O_3	0.80		1.12		1.51		0.27		1.52	
Cr_2O_3	21.48		22.26		21.01		8.84		22.62	
Fe_2O_3	39.95		39.12		12.20		0.54		15.05	
FeO	6.68		6.75		15.11		25.62		12.90	
MgO	7.08		7.21		10.87		11.58		10.84	
Total	97.43		98.22		98.97		98.25		98.62	
$Mg^{\#}$	65.4		65.6		56.1		44.6		60.0	
Cations (3 oxygens)										
Si	0.002	(0.001)	0.002	(0.001)	0.005	(0.002)	0.002	(0.003)	0.009	(0.012)
Ti	0.401	(0.004)	0.402	(0.009)	0.672	(0.025)	0.907	(0.006)	0.626	(0.021)
Al	0.023	(0.001)	0.032	(0.001)	0.042	(0.002)	0.007	(0.001)	0.042	(0.014)
Cr	0.423	(0.005)	0.434	(0.016)	0.390	(0.010)	0.164	(0.001)	0.421	(0.038)
Fe^{3+}	0.749	(0.010)	0.725	(0.024)	0.215	(0.051)	0.010	(0.014)	0.267	(0.063)
Fe^{2+}	0.139	(0.006)	0.139	(0.012)	0.297	(0.012)	0.504	(0.004)	0.254	(0.016)
Mg	0.263	(0.009)	0.265	(0.007)	0.380	(0.014)	0.406	(0.006)	0.381	(0.017)
Sum	2.000		2.000		2.000		2.000		2.000	
$Fe^{3+}/\sum Fe$	0.843		0.839		0.420		0.019		0.512	

Table 4.2: continued.

Experiment	T-3910 initial	T-3911 initial	T-3910 reversed	T-3946 oxide mix	T-3911 reversed
T (°C)	1075	1175	1125	1125	1125
P (kbar)	22	32	25	25	25
Buffer	HM	HM	WCWO	WCWO	WCWO
$\log fO_2$	-4.47	-3.13	-10.22	-10.22	-10.22
$\Delta \log fO_2$ (FMQ)	4.05	3.56	-2.51	-2.51	-2.51
			Spinel (n=3)	Spinel (n=3)	Spinel (n=3)
SiO_2			0.20	0.55	0.62
TiO_2	spinels	spinels	17.99	8.92	19.88
Al_2O_3			3.33	4.03	3.25
Cr_2O_3	not	not	39.55	46.19	35.75
Fe_2O_3			0.00	2.36	0.00
FeO	detected	detected	26.27	23.92	26.30
MgO			10.44	10.75	10.94
Total			97.79	96.71	96.74
$Mg^{\#}$			41.5	44.5	42.6
Cations (4 oxygens)					
Si			0.007 (0.006)	0.019 (0.012)	0.021 (0.003)
Ti			0.460 (0.075)	0.233 (0.007)	0.509 (0.051)
Al			0.133 (0.008)	0.165 (0.005)	0.130 (0.033)
Cr			1.062 (0.051)	1.269 (0.030)	0.962 (0.053)
Fe^{3+}			0.000 (0.000)	0.062 (0.044)	0.000 (0.000)
Fe^{2+}			0.746 (0.028)	0.695 (0.020)	0.748 (0.030)
Mg			0.529 (0.025)	0.557 (0.055)	0.555 (0.053)
Sum			2.936	3.000	2.924
$Fe^{3+}/\sum Fe$			0.000	0.082	0.000
$Cr^{\#}$			88.9	88.5	88.1

There is good evidence that the consistency experiment approached an equilibrium position. Firstly, olivine and orthopyroxene compositions from the reground mixes and the oxide mix in the 'reversed' run product are similar, and the silicates from the reground mixes have lower $Mg^{\#}$ than the original silicates in response to more reduced oxygen activity conditions. Secondly, spinel is observed in the 'reversed' run products but is absent in the original, high oxidation, experiments. As will be shown later, spinel is present in all but the most oxidized experiments (HM conditions), where Cr-rich hematite is the only oxide phase present. The presence of a spinel phase in the reduced consistency experiment indicates that an oxidation equilibrium was approached from the oxidized starting mixes. Spinel grains in the 'reversed' mixes were very fine grained (<5 μm) and difficult to analyse, and low spinel cation totals for these spinels (Table 4.2) indicate poor oxide analyses rather than non-stoichiometry or an absence of ferric iron. Furthermore, spinel compositions from the 'reversed' mixes show higher TiO_2 and FeO (or 'ilmenite' components) contents, and lower Cr_2O_3 and Al_2O_3 (or 'spinel' components) contents than the oxide mix spinels, whereas the MgO contents are approximately similar. A further demonstration that an equilibrium position was approached is indicated by the observation that Ti-rich phases in the consistency experiment show a distinct chemical response to the lower oxidation conditions imposed by the WCWO oxygen buffer. All spinels show similar $Mg^{\#}$ and $Cr^{\#}$ values. The Ti-rich oxide in the HM experimental run is a Cr-bearing hematite, whereas the Ti-rich oxide in the reduced 'reversal' experiment is a Cr-bearing ilmenite with significantly more TiO_2 (Table 4.2). Ferric iron in the 'reversed' ilmenites is significantly lower, and FeO has increased, resulting in a lower redox ratio, $Fe^{3+}/\sum Fe$ of 0.42–0.51 compared with ~0.84 for the Cr-rich hematite. The chromium content of the 'reversed' ilmenites does not differ markedly from the original oxides, but MgO has increased. Unlike the spinels, the 'reversed' ilmenites differ from the 'oxide mix' ilmenites in having lower TiO_2 and FeO contents (or 'ilmenite' components), and higher Al_2O_3 and Cr_2O_3 contents (or 'spinel' components). The 'oxide mix' ilmenites have a lower redox ratio ($Fe^{3+}/\sum Fe$ ~0.02) which is similar to values reported in ilmenites from other reduced, WCWO oxygen buffer, experiments. Thus, although the 'reversed' ilmenites differ significantly from the original Ti-rich oxides and approach the composition of oxide mix ilmenites synthesized under the same conditions, the 'reversal' is incomplete indicating sluggishness of the reaction for the Ti-rich oxide phase (hematite-ilmenite solid solution).

From the phase relations and chemical compositions it can be seen that a multi-parameter convergence for both oxide and crystalline mix compositions has been approached in the experiment described, but complete equilibrium is not demonstrated. The 'case' for equilibrium being reached in the 'forward' experiments thus relies on the

consistency of the data obtained, the absence of compositional zoning and the partial 'reversal' described above.

4.4 Experimental results

Table 4.3 contains details of experimental run conditions, and phases detected in these runs. Representative electron probe microanalyses are shown in Appendix D1.1 to D2.4.

The experimental runs were performed under conditions of incipient melting, i.e. a minor (~2-3%) K-rich siliceous melt was present but there was no major melting of the olivine, orthopyroxene and oxide assemblage. A typical run product consisted of large (with a diameter up to ~15-20 μm) equant, subhedral olivine grains and poikilitic orthopyroxene grains. The oxide phases were interstitial, anhedral to subhedral, evenly distributed ilmenite grains, and subhedral to euhedral spinel grains which were present in small clusters within the silicate matrix. Rutile was detected in several high temperature (>1100 °C) NNO experimental runs. In those experiments where rutile is observed, its occurrence appears to be at the expense of the modal amount of ilmenite in comparison with experiments of similar P-T conditions conducted using different oxygen buffers.

A powder X-ray diffraction (XRD) analysis was made of one of the run products synthesized under oxidized conditions (T-3770) to ascertain the nature of the mineral phases, particularly the Ti-rich oxide. Details of the analytical technique are given in Appendix B4. Results of the XRD are given in Figure 4.2 and Table 4.4. The diffraction pattern of sample T-3770 shows that the experimental run product contains orthopyroxene, olivine and a oxide phase with a d-spacing close to those of hematite. The hematite phase has cell dimensions of a_0 = 5.038 (±0.010) Å and c_0 = 13.734 (±0.015) Å. The small c_0 value, compared to pure hematite, indicates substitution of a smaller cation (e.g. Cr or Mg).

The observation that, under oxidized conditions, the oxide present in the chemical systems used in this study is Cr-rich hematite, appears to be consistent with Katsura and Muan (1964). These authors have shown extensive solid solution between Cr_2O_3 and Fe_2O_3 end-members, present only at high values of fO_2 (~10^{-2}-10^{-4} atm), in the FeO-Fe_2O_3-Cr_2O_3 system at 1300 °C and 1 atm total pressure, which is unlikely to be important in natural chromites. At lower fO_2, Katsura and Muan (1964) described a two-phase field consisting of spinel + R_2O_3 (analogous with the spinel-ilmenite two-phase field observed in experiments undertaken in this study at redox conditions below HM),

Table 4.3: Summary of experimental run conditions in the SiO_2-TiO_2-Cr_2O_3±Al_2O_3-FeO-MgO±NiO±ZnO±K2O system, and phases detected.

Run Number	Composition	P (kbar)	T (°C)	Run time (hrs)	Buffer	logfO_2	ΔlogfO_2 (FMQ)	Phases
T-3740	MAK-6	30	1150	48	WCWO	-9.65	-2.55	Opx+Olv+Ilm+Spi
T-3743	MAK-6	20	1050	72	WCWO	-11.54	-2.56	Opx+Olv+Ilm+Spi
T-3770	MAK-6	35	1200	25	HM	-2.83	3.42	Opx+Olv+Hem
T-3808	MAK-6	30	1200	73	WCWO	-9.03	-2.47	Opx+Olv+Ilm+Spi
T-3813	MAK-6	25	1100	72	NNO	-8.05	-0.05	Opx+Olv+Spi+Ilm+Rut
T-3834	MAK-6	30	1100	69	HM	-4.06	3.61	Opx+Olv+Hem
T-3840	MAK-6	35	1200	46	IW	-10.57	-4.32	Opx+Olv+Ilm+Spi
T-3841	MAK-6	25	1100	73	IW	-12.26	-4.25	Opx+Olv+Ilm+Spi
T-3855	MAK-7	20	1050	93	NNO	-8.88	0.10	Olv+Opx+Ilm+Spi
T-3858	MAK-7	20	1050	72	IW	-13.19	-4.22	Olv+Opx+Ilm+Spi+Phl
T-3862	MAK-7	25	1100	72	WCWO	-10.56	-2.56	Olv+Opx+Ilm+Spi
T-3863	MAK-7	30	1150	64	IW	-11.38	-4.29	Olv+Opx+Ilm+Spi
T-3864	MAK-6	22	1050	95	NNO	-8.80	0.04	Opx+Olv+Ilm+Spi
T-3872	MAK-7	35	1200	48	HM	-2.83	3.42	Olv+Opx+Hem
T-3879	MAK-7	32	1175	26	WCWO	-9.24	-2.54	Olv+Opx+Ilm+Spi
T-3880	MAK-8	22	1075	76	WCWO	-11.07	-2.55	Olv+Opx+Ilm+Spi
T-3897	MAK-8	32	1175	27	WCWO	-9.24	-2.54	Olv+Opx+Ilm+Spi
T-3901	MAK-8	17	1025	96	IW	-13.71	-4.18	Olv+Opx+Ilm+Spi+Phl
T-3903	MAK-8	27	1125	46	NNO	-7.68	-0.10	Olv+Opx+Spi+Ilm+Rut
T-3909	MAK-8	25	1125	48	NNO	-7.75	-0.04	Olv+Opx+Spi+Ilm+Rut
T-3910	MAK-8	22	1075	48	HM	-4.47	4.05	Olv+Opx+Hem
T-3911	MAK-8	32	1175	24	HM	-3.13	3.56	Olv+Opx+Hem
T-3912	MAK-8	25	1145	50	IW	-11.65	-4.17	Olv+Opx+Ilm+Spi
T-3913	MAK-7	25	1100	50	HM	-4.11	3.90	Olv+Opx+Hem
T-3937	MAK-6	28	1100	45	NNO	-7.95	-0.14	Opx+Olv+Ilm+Spi
T-3944	MAK-7	26	1125	44	NNO	-7.71	-0.07	Olv+Opx+Spi+Ilm+Rut

Notes: Abbreviations: Olv = olivine, Opx = orthopyroxene, Ilm = ilmenite, Hem = hematite, Spi = spinel, Rut = rutile, Phl = phlogopite. The order of phases listed approximates the modal proportion of the relevant minerals observed in the experimental run products.

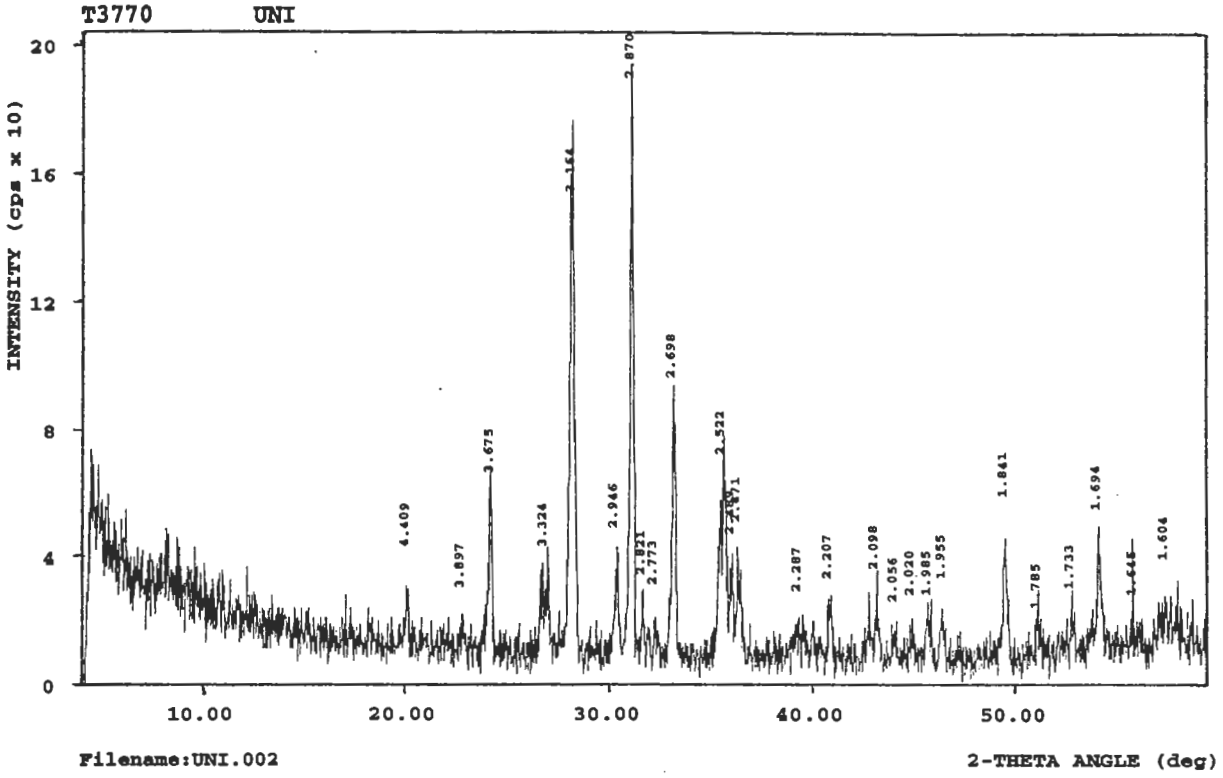

Figure 4.2: X-ray diffraction pattern of MAK-6 experiment T-3770 run product (35 kbar, 1200 °C). See Table 4.4 for an explanation of the peak positions.

Table 4.4: X-ray diffraction data of experiment T-3770.

Mineral	d Å	Intensity (I/I_1)
Olivine	2.76	5
	2.47	20
	2.25	5
	5.10	2
Orthopyroxene	3.16	90
	2.87	100
	2.53	50
	4.40	10
Hematite	3.68	35
	2.70	60
	1.84	30
	3.68	35

Notes: For each mineral the strongest three peaks are given, as well as the peak with the greatest d-spacing. Intensities are given as ratios with respect to the strongest peak (I_1) of the entire diffraction pattern.

followed by, firstly, a chromite-magnetite solid solution, and then a spinel-wüstite two-phase field at increasingly reducing conditions. The introduction of TiO_2+MgO in the experiments of this study results in a enlargement of the Katsura and Muan (1964) spinel + R_2O_3 two phase field, and Ti-bearing Mg-spinel coexisting with Cr-bearing Mg-ilmenite is now reported at oxygen buffer conditions as low as IW.

Experimental ilmenite compositions are also illustrated in terms of the ilmenite ternary, recalculated as the ilmenite, geikielite and hematite solid solution endmembers (Figure 4.3). This illustration confirms the increasing hematite component with an increasing oxygen fugacity of the experiment, reflecting an increase in the $Fe^{3+}/\sum Fe$ ratio of the Ti-oxide phase. In following with the Cr-free ilmenites (see Chapter 3 herein), there is a lack of evidence in these high pressure experiments for the existence of an immiscibility gap between the hematite and geikielite endmembers extending towards the ilmenite join as observed at low pressure (originally established at 1 atm, e.g. Woermann *et al.*, 1970). Rather, in the absence of a three phase spinel-pseudobrookite-ilmenite oxide assemblage in experiments from this study, the Cr-rich Ti-oxides, synthesized under high P-T, oxidized conditions (HM) are stable and have an hematite structure (e.g. XRD results, Table 4.4).

4.4.1 Silicate mineral chemistry

Olivine compositions (Appendices E1.1, E2.1 and E3.1) range from $Fo_{82.5-95.3}$, and like experimental olivine composition described in Chapter 3, the Fo content systematically increases with increasing oxygen fugacity (Figure 4.4A). Chromium contents of experimental olivines broadly appear to be decreasing with increasing experimental oxygen fugacity conditions (Figure 4.4B). In the reduced experiments, the presence of small amounts of Cr^{2+} in olivine (e.g. Haggerty *et al.*, 1970) is difficult to test but cannot be ruled out.

Orthopyroxene compositions (Appendices E1.2, E2.2 and E3.2) range from $Mg^{\#}$ 84.6-95.0. As for olivine, the $Mg^{\#}$ of the orthopyroxenes increases linearly with increasing oxygen fugacity, and, as already observed in Chapter 3, orthopyroxene $Mg^{\#}$ values are slightly higher than Fo contents in co-existing olivines under the most reduced conditions (below NNO), but become similar under oxidation conditions above NNO (Figure 4.4A). Like co-existing olivine, experimental orthopyroxene also shows a decrease in Cr contents with increasing oxygen fugacity (Figure 4.4C). Within the P-T-X-fO_2 range covered by the experimental study, Cr substitution in orthopyroxene is independent on either pressure or temperature.

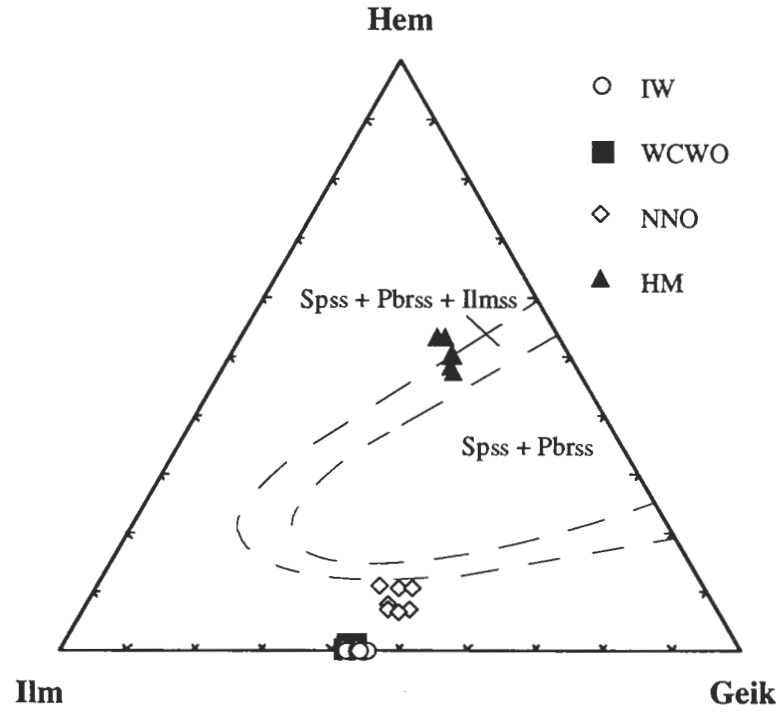

Figure 4.3: Experimental ilmenite compositions expressed in terms of ilmenite solid solution endmembers (Ilm = mol % ilmenite, Geik = mol % geikielite, Hem = mol % hematite). Decomposition loops at 1300 °C and 1 atm are from Woermann *et al.* (1970) (Sp_{ss} = spinel and Pbr_{ss} = pseudobrookite solid solution members, respectively).

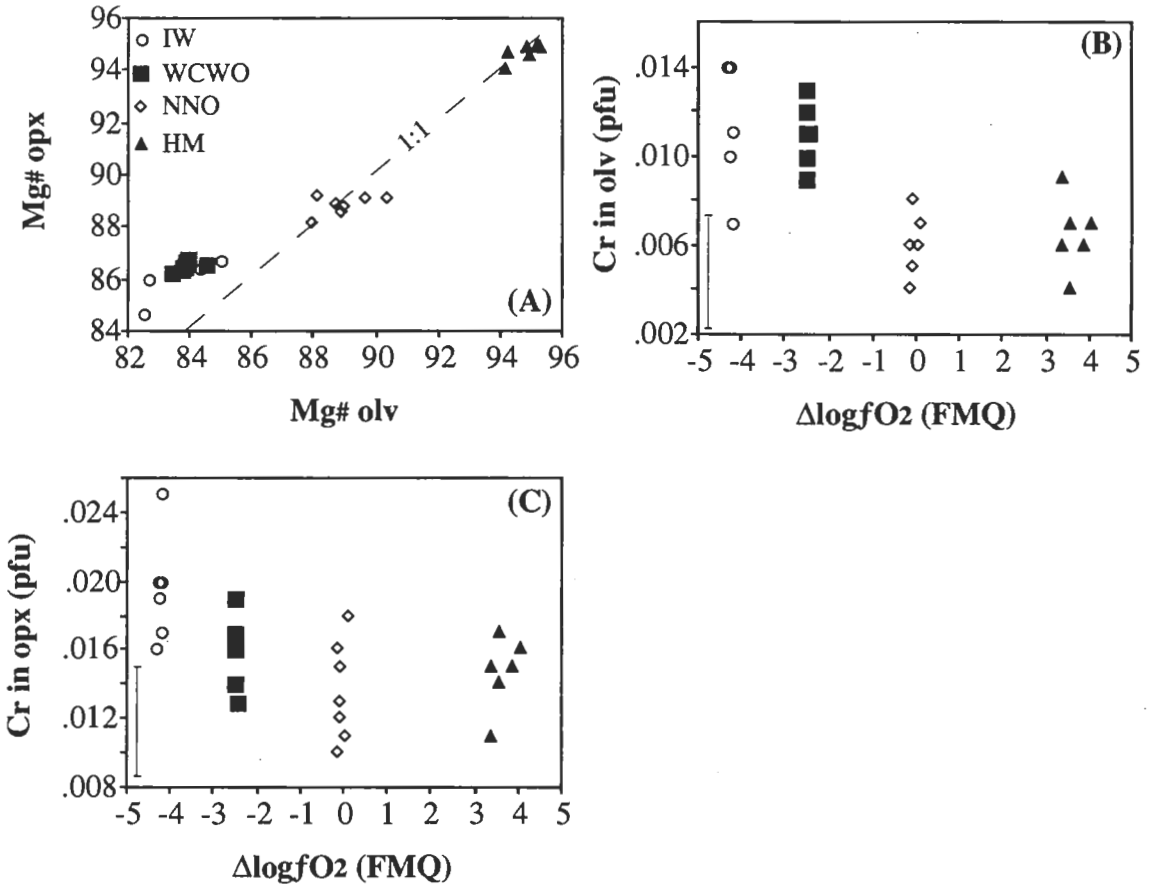

Figure 4.4: Chemical variation of silicate minerals in experimental runs involving Cr-rich MAK-6, MAK-7 and MAK-8 oxide mixes. (A) Plot against Fo of $Mg^{\#}$ for orthopyroxene as a function of oxygen buffers used. (B) Plot against $\Delta \log fO_2$ (FMQ) of the Cr content (per formula unit, pfu) of olivine. (C) Plot against $\Delta \log fO_2$ (FMQ) of the Cr content (pfu) of orthopyroxene. Error bars in (B) and (C) indicate one standard deviation.

Phlogopite is observed as an accessory mineral phase in two low temperature experiments (1050 °C and 1025 °C) under reduced conditions (IW; T-3858 and T-3901 respectively), and mineral analyses are given in Appendices E2.6 and E3.6. The phlogopites are broadly similar in composition to kimberlitic phlogopites (e.g. Mitchell, 1986), and they contain significant amounts of TiO_2 (5.84 and 4.42 wt.% respectively) and Cr_2O_3 (1.97 and 1.58 wt.% respectively). The presence of phlogopite is attributed to subsolidus conditions by pressure, temperature and a_{H2O} (e.g. Sweeney *et al.*, 1993). The two experiments where phlogopite was observed in the run product were performed at relatively low pressures (20 and 17 kbar respectively), and inferred low a_{H2O} conditions. Phlogopite was not observed in experimental run products at IW conditions with pressures >20 kbar, or in low pressure, oxidized (>IW) run products where the experimental a_{H2O} is higher. As the stability of phlogopite is not the focus of this study, and the mineral phase is only observed in two experiments at very low fO_2 conditions, its occurrence will not be considered further.

4.4.2 Oxide mineral chemistry

Ilmenite compositions show a strong dependence on the oxygen fugacity conditions of the experiments (Appendices E1.3, E2.3 and E3.3). Within the P-T-X range of the experimental work, the ilmenite redox ratio, $Fe^{3+}/\sum Fe$, displays a near-linear relationship with $\Delta \log fO_2$ (FMQ) for experiments between WCWO and HM conditions (Figure 4.5). Ilmenites synthesized under IW conditions contain no Fe^{3+} according to stoichiometry. The redox ratio of the ilmenites in this study does not show a marked pressure or temperature dependence over the range of oxygen fugacity conditions of the experiments.

The chromium content of ilmenites is found to be sensitive to oxygen fugacity conditions (Figure 4.6A). Ilmenites synthesized under IW conditions contain ~0.10-0.20 pfu Cr, whereas ilmenites synthesized under NNO conditions contain ~0.15-0.25 pfu Cr. The effect of oxygen fugacity is more noticeable under oxidation conditions above NNO, and the resultant hematite oxide phase synthesized under HM conditions contains ~0.40-0.50 pfu Cr. The substitution of chromium into the ilmenite structure is found to be sensitive to both pressure and temperature of formation over the range of the experimental oxidation conditions (Figure 4.6B and 4.6C). For oxygen fugacity conditions between IW and NNO, the Cr content of ilmenite increases from ~0.10 pfu at 1025 °C to ~0.20 pfu at 1200 °C. Likewise, the Cr content increases from ~0.10 pfu at 17 kbar to ~0.20 pfu at 35 kbar. The substitution of Cr in the hematite phase synthesized under HM buffer conditions follows a similar pattern to that in ilmenite, and with increasing pressure and temperature conditions, the Cr content increases in a linear fashion (Figure 4.6B and 4.6C).

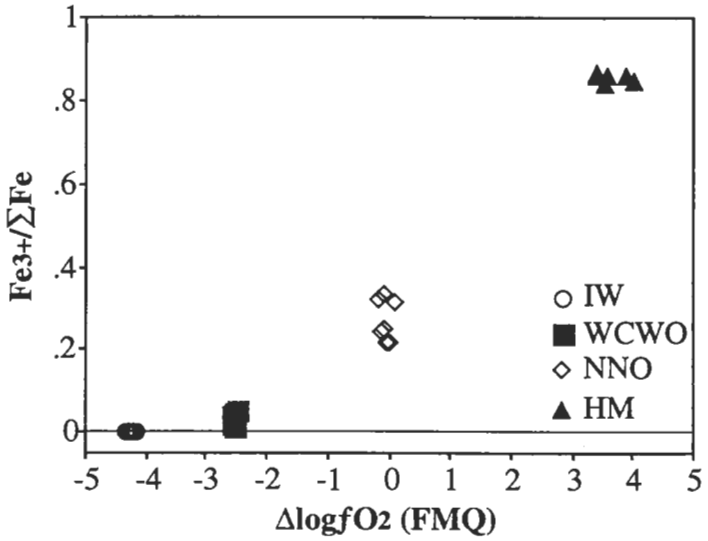

Figure 4.5: The $Fe^{3+}/\Sigma Fe$ ratio in chromium-rich ilmenite as a function of experimental oxygen fugacity, expressed as $\Delta \log fO_2$ (FMQ).

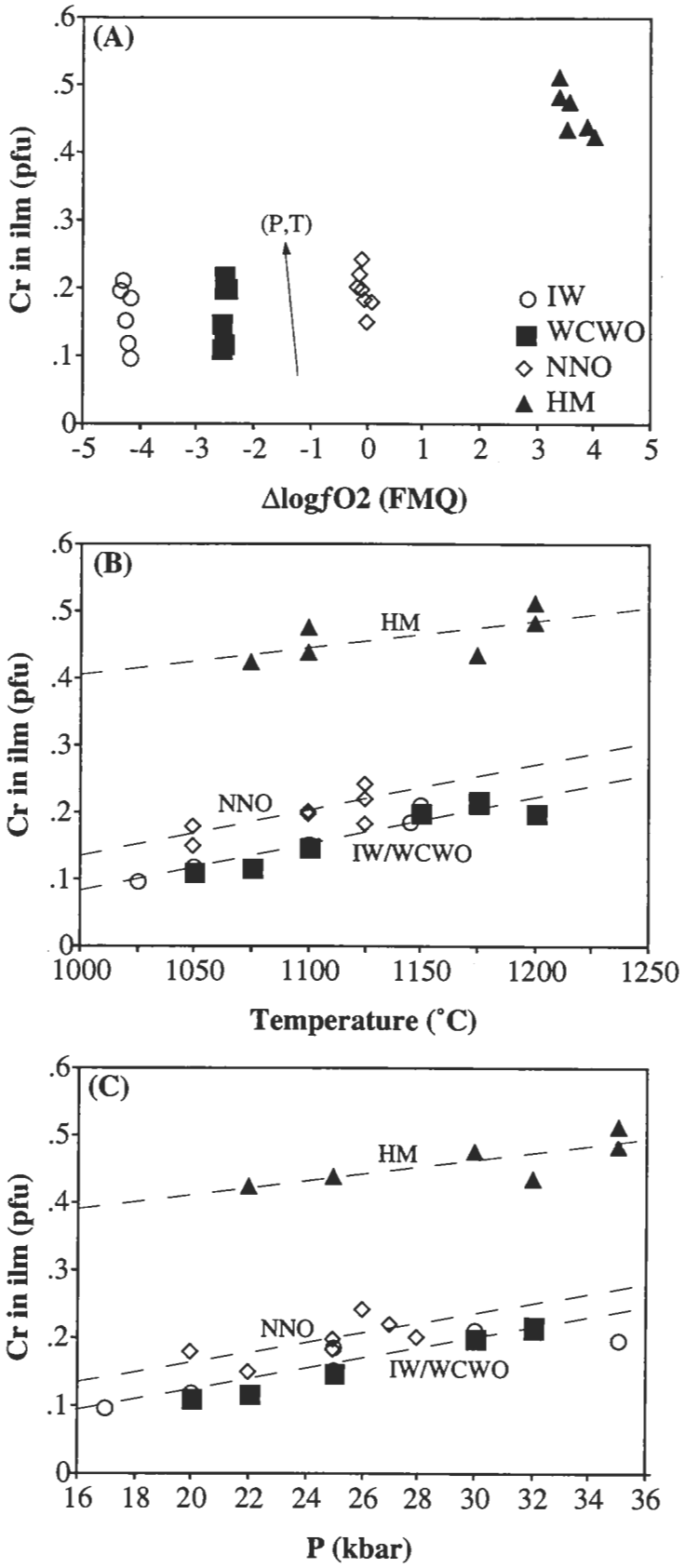

Figure 4.6: The Cr content of ilmenite (per formula unit, pfu) as a function of (A) experimental oxygen fugacity, expressed as $\Delta \log fO_2$ (FMQ), (B) experimental run temperature and (C) experimental run pressure. The arrow in (A) shows increasing Cr content with increasing P,T conditions for each oxygen buffer. The dashed lines in (B) and (C) are lines of best fit.

Consistent with observations from previous spinel-based oxygen geobarometer studies (e.g. O'Neill and Wall, 1987; Mattioli and Wood, 1988; Wood, 1990; Ballhaus *et al.*, 1991), spinel compositions, in terms of $Fe^{3+}/\sum Fe$, reflect a strong dependence on the oxygen fugacity conditions of the experiments. The redox ratio of the Cr-rich ($Cr^{\#}>90$) experimental spinels in this study increases linearly with an increasing $\Delta \log fO_2$ (FMQ) for experiments between WCWO and NNO, which can be extrapolated to a pure Fe_3O_4 spinel endmember redox ratio of 0.667 (Figure 4.7). The redox ratio of 0.667 is considered a limiting minimum value, as hematite is stable under HM conditions in these experiments rather than a spinel phase. Within the P-T-X-fO_2 range covered by the experimental study, the redox ratio of the spinels is found to be insensitive to both temperature and pressure.

The titanium content of spinels is sensitive to oxygen fugacity conditions (Figure 4.8A). Spinels synthesized under IW conditions contain ~0.20-0.30 pfu Ti, whereas spinels synthesized under NNO conditions contain ~0.10-0.15 pfu Ti. At constant oxygen fugacity conditions, the substitution of Ti into the spinel structure increases with increasing temperature (Figure 4.8B) and pressure (Figure 4.8C) for the IW and WCWO experiments. However, under NNO conditions the Ti content of spinel decreases slightly with increasing pressure (Figure 4.8C), and shows itself to be independent of temperature (Figure 4.8B). The effect of temperature and pressure on the titanium content of spinel is greatest under the most reducing conditions (IW), and decreases with increasing oxygen fugacity.

Rutile is observed in varying modal amounts in four experiments conducted under NNO buffer conditions (T-3813, T-3903, T-3909 and T-3944; refer to Appendices E1.5, E2.5 and E3.5 for mineral analyses), and the rutiles contain significant amounts of chromium (6.99-7.87 wt.% Cr_2O_3) and iron (2.10-2.60 wt.% expressed as Fe_2O_3). In a separate part of this study, it has been shown that rutile contains Cr(O,OH) and Fe^{3+}(O,OH) solid solution, and its occurrence may reflect a_{H2O} variations as well as P,T, fO_2 and bulk composition controls. Rutile is absent from the lower temperature and pressure experiments (<25 kbar) and also from the 28 kbar, 1100 °C experiment (T-3937).

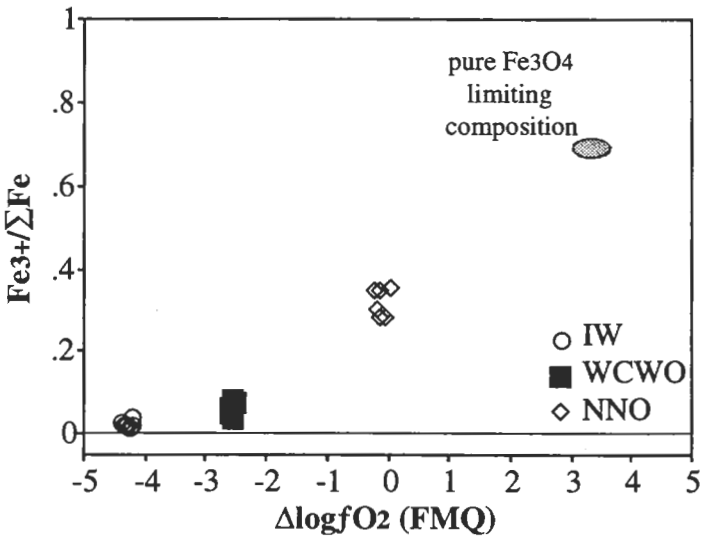

Figure 4.7: The $Fe^{3+}/\Sigma Fe$ ratio in spinels as a function of experimental oxygen fugacity, expressed as $\Delta \log fO_2$ (FMQ). Pure Fe_3O_4 with $Fe^{3+}/\Sigma Fe$ of 0.667 is shown as a limiting factor for spinel compositions.

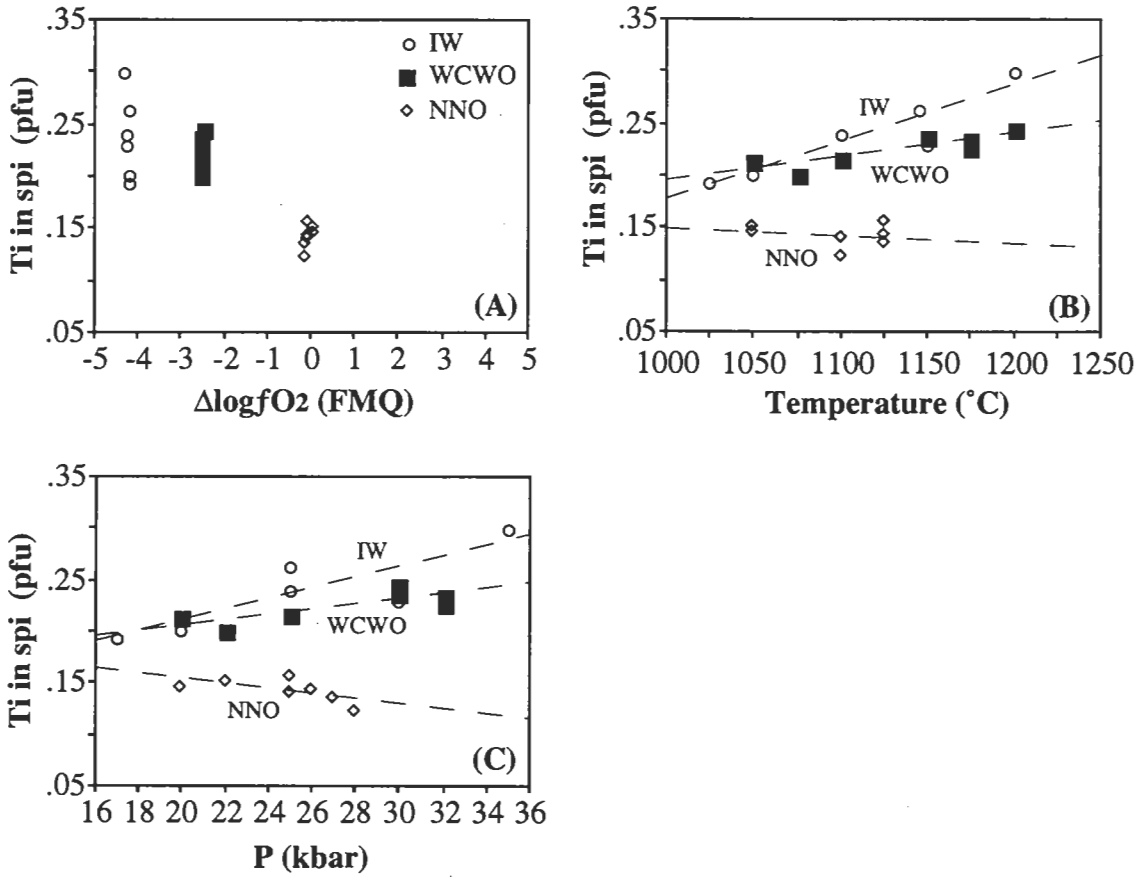

Figure 4.8: The Ti content of spinel (per formula unit, pfu) as a function of (A) experimental oxygen fugacity, expressed as $\Delta \log fO_2$ (FMQ), (B) experimental run temperature and (C) experimental run pressure. The dashed lines indicate a line of best fit.

4.5 Geothermometry and Oxygen Geobarometry

The experimental data in this study provide newly published high precision oxide-silicate geochemical relations in a compositional and oxygen fugacity range where experiments are scarce, and offer the opportunity to test existing exchange geothermometers and oxygen geobarometers and, where necessary, improve the existing equations.

4.5.1 Spinel geothermometry and oxygen geobarometry

Chromium-rich spinels are widely used as petrogenetic indicators, and such spinels found in kimberlites and lamproites (magnesiochromites with $Cr^{\#}$ of 70-95, $Mg^{\#}$ of 50-80 and $Fe^{3+}/\sum Fe<0.3$) are often used as potential diamond-indicators (e.g. Haggerty, 1979; Ramsay, 1992; Kamperman *et al.*, 1993, and Chapter 2 herein). In contrast with the high $Cr^{\#}$ compositions of diamond-indicator spinels, the existing olivine-orthopyroxene-spinel oxygen geobarometers of Mattioli and Wood (1988), O'Neill and Wall (1987), Wood (1990) and Ballhaus *et al.* (1991) were formulated on the basis of spinel compositions with $Cr^{\#}$ generally not exceeding ~70. The experimental data obtained in this study therefore present an opportunity to test the various oxygen geobarometers for their reliability when applied to spinel compositions with high $Cr^{\#}$ (e.g. $Cr^{\#}>80$-90).

The four above-mentioned spinel oxygen geobarometers tested in this study were originally formulated using a different experimental and/or theoretical approach. Mattioli and Wood (1988) calibrated Fe_3O_4 activities in $MgAl_2O_4$ spinels by electrochemically determining the fO_2's recorded by mixtures of hematite and spinel solid solution between 800 and 1000 °C. In contrast to this experimental work, O'Neill and Wall (1987) entirely used a thermodynamic model to calculate the magnetite activity from the O'Neill-Navrotsky (1984) cation distribution model, taking into account order-disorder between octahedral and tetrahedral sites and available experimental data on macroscopic properties, such as interphase partitioning and miscibility gaps. Nell and Wood (1991) presented an updated O'Neill-Wall approach, incorporating the Mattioli and Wood (1988) results and new measurements on order-disorder in spinel. Wood (1990), on the other hand, experimentally equilibrated olivine, orthopyroxene and spinel at known fO_2, 1 atm and 1200 °C to test the Nell and Wood (1991) approach. Finally, Ballhaus *et al.* (1991) made an empirical recalibration of the oxygen geobarometer described by O'Neill and Wall (1987).

Oxygen fugacity values calculated from the existing oxygen geobarometers for spinel-bearing assemblages from this study are presented in Figure 4.9.

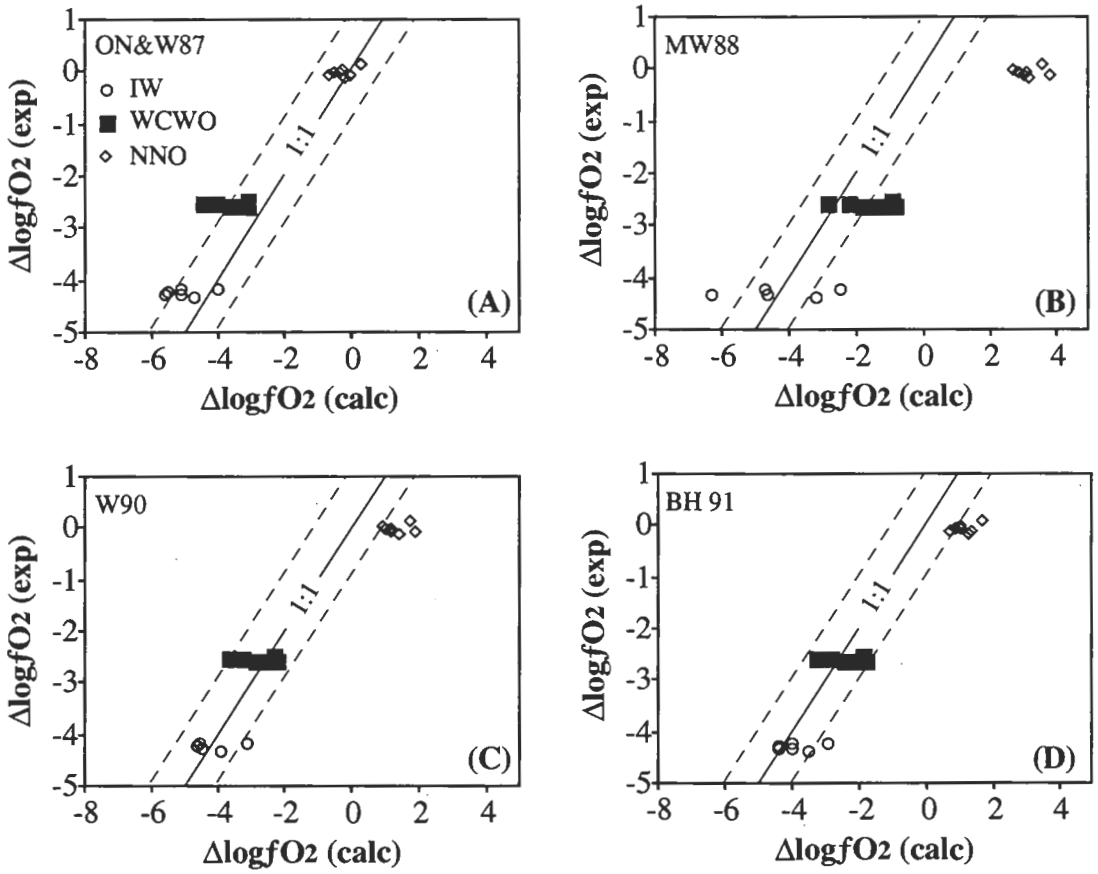

Figure 4.9: The olivine-orthopyroxene-spinel oxygen geobarometer versions of (A) O'Neill and Wall (1987), (B) Mattioli and Wood (1988), (C) Wood (1990) and Ballhaus *et al.* (1991) applied to the experimental data of this study. The dashed lines indicate ± 1.0 log units.

The O'Neill and Wall (1987) spinel oxygen geobarometer (ON&W87) gives a very good fit to the experimental data of this study at NNO (approximately equal to FMQ; Figure 4.9A). However, under more reduced conditions (<FMQ) the ON&W87 geobarometer consistently underestimates experimental oxygen fugacity values by as much as two log units. The Mattioli and Wood (1988) oxygen geobarometer (MW88) gives a relatively poor model fit to the experimental data over the entire fO_2 range (Figure 4.9B). It presents a wide spread of predicted oxygen fugacity values in the reduced region (~FMQ-4.0 log units), and at FMQ the MW88 geobarometer systematically overestimates experimental values by as much as four log units. At ~FMQ-2.5 log units, the MW88 geobarometer overestimates oxygen fugacity values by up to two log units. The Wood (1990) and Ballhaus *et al.* (1991) spinel oxygen geobarometers (abbreviated as W90 and BH91 respectively) give a very similar fit to the experimental data, and may be considered more reliable than the ON&W87 and MW88 geobarometers under reduced (<FMQ) conditions (Figure 4.9C and 4.9D). Both geobarometers give a fit to the experimental data within one log unit for conditions at ~FMQ-4.0 and ~FMQ-2.5 log units, although the BH91 geobarometer has a tendency to slightly overestimate experimental fO_2 values at the more reduced conditions. However, at FMQ, both models break down and overestimate fO_2 by about two log units. Thus, for reduced mantle conditions (<FMQ), the Wood (1990) model and the Ballhaus *et al.* (1991) model, appear to be the most reliable oxygen geobarometers for mineral assemblages with high $Cr^{\#}$ spinels. For conditions around FMQ however, the O'Neill and Wall (1987) model is the preferred oxygen geobarometer, whereas the Mattioli and Wood (1988) model is not recommended for the entire range of fO_2 values used in this study.

The experimental data from this study, with the high $Cr^{\#}$, Ti-rich spinel compositions, are combined with the Ballhaus *et al.* (1991) and Wood (1990) experimental data to re-formulate the Ballhaus *et al.* (1991) oxygen geobarometer equation, using a Monte Carlo fitting routine and introducing a Ti correction, for the fayalite-ferrosilite-magnetite (FFM) buffer:

$$6\,Fe_2SiO_4\,(fa) + O_2\,(fluid) = 2\,Fe_3O_4\,(mt) + 3\,Fe_2Si_2O_6\,(fs) \qquad (4.1)$$

to give the oxygen fugacity relative to FMQ as:

$$\Delta\log fO_2\,(FMQ) = 3.659 - \frac{2076}{T} - \frac{0.04P}{T} - 6\log(X_{Fe}^{olv}) - \left(\frac{4239}{T}\right)(1 - X_{Fe}^{olv})^2$$
$$+ 2\log(X_{Fe2+}^{spi}) + 4\log(X_{Fe3+}^{spi}) + \left(\frac{4820}{T}\right)(X_{Al}^{spi})^2 + \left(\frac{4626}{T}\right)(X_{Ti}^{spi})^2 \qquad (4.2)$$

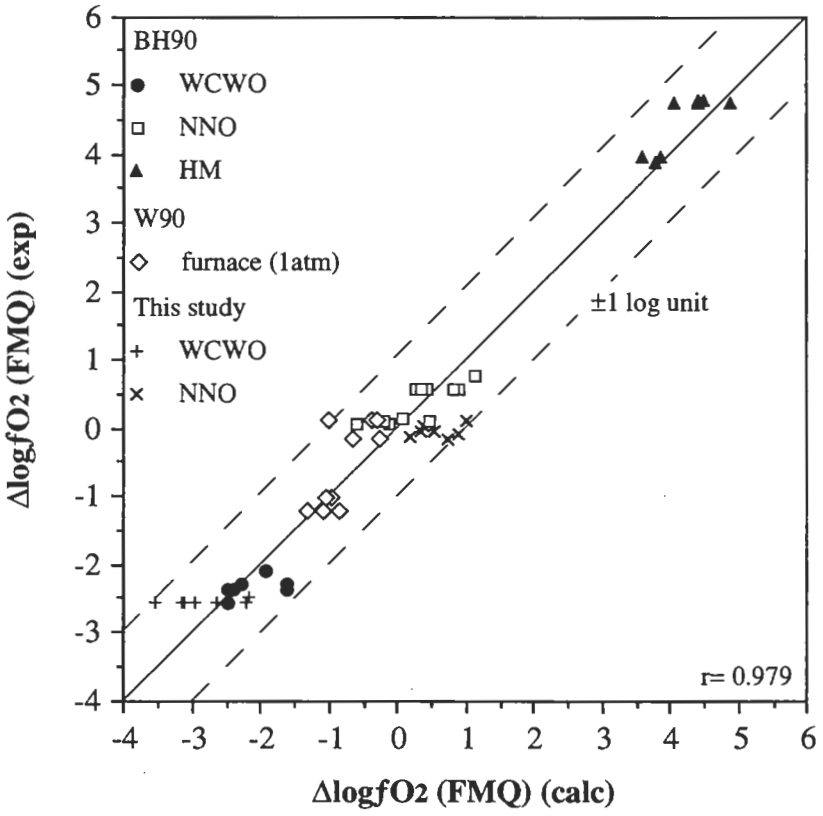

Figure 4.10: Experimental oxygen fugacities (with reference to the fayalite-magnetite-quartz oxygen buffer) against calculated oxygen fugacities, using the revised olivine-orthopyroxene-spinel oxygen geobarometer presented in this study, for experimental mineral pairs. The dashed lines indicate ± 1.0 log units. BH91 and W90 symbols indicate Ballhaus *et al.* (1991) and Wood (1990) experimental data respectively. The regression coefficient, r, equals 0.979 for the data set.

where T is in °K, P is in bar, X_{Fe}^{olv} is the $Fe^{2+}/(Fe^{2+} + Mg)$ ratio in olivine, X_{Fe2+}^{spi} is the $Fe^{2+}/(Fe^{2+} + Mg)$ ratio in spinel, X_{Fe3+}^{spi} equals $Fe^{3+}/(Al + Cr + Fe^{3+} + 2Ti)$ in spinel, X_{Al}^{spi} equals $Al/(Al + Cr + Fe^{3+} + 2Ti)$ in spinel and X_{Ti}^{spi} is the $2Ti/(Al + Cr + Fe^{3+} + 2Ti)$ ratio in spinel. Within the experimental P-T-X calibration range the revised spinel oxygen geobarometer gives a better fit than the existing Ballhaus *et al.* (1991) oxygen geobarometer, particularly at $\Delta \log fO_2 \sim$ FMQ (Figure 4.10 and Figure 4.11).

A variation to the FFM oxygen geobarometer is obtained by the introduction of a silica activity term (e.g. O'Neill and Wall, 1987; Wood, 1991):

$$2\ MgSi_{0.5}O_2\ (fo) + SiO_2\ (qtz) = Mg_2Si_2O_6\ (en) \qquad (4.3)$$

and writing equation (4.1) relative to the quartz standard state gives:

$$6\ FeSi_{0.5}O_2\ (fa) + O_2\ (fluid) = 2\ Fe_3O_4\ (mt) + 3\ SiO_2\ (qtz) \qquad (4.4)$$

Using the silica activity for orthopyroxene-undersaturated assemblages (see Appendix F for the calculation of a_{SiO2}), the experimental data from this study and the Ballhaus *et al.* (1991) and Wood (1990) data are used to give the oxygen fugacity relative to FMQ as:

$$\begin{aligned}\Delta \log fO_2\ (FMQ) = {} & 4.426 - \frac{1895}{T} - \frac{0.037P}{T} + 3\log(a_{SiO2}) \\ & - 6\log(X_{Fe}^{olv}) - \left(\frac{4239}{T}\right)(1 - X_{Fe}^{olv})^2 + 2\log(X_{Fe2+}^{spi}) + 4\log(X_{Fe3+}^{spi}) \\ & + \left(\frac{4270}{T}\right)(X_{Al}^{spi})^2 + \left(\frac{4626}{T}\right)(X_{Ti}^{spi})^2 \end{aligned} \qquad (4.5)$$

where the individual components are described above. The olivine-spinel + silica activity oxygen geobarometer is illustrated in Figure 4.12. The introduction of the a_{SiO2} term diminishes the need to determine the activity of the $Fe_2Si_2O_6$ component, which is small in mantle-derived orthopyroxenes. However, it should be noted that Wood (1991) argues that the potential error related to estimating the ferrosilite activity in orthopyroxene is insignificant. Rather, Wood (1991) suggests that uncertainties from Fe_3O_4 activity calculations are potentially much larger, and prefers an approach which estimates the magnetite component in spinel as accurately as possible.

The Ballhaus *et al.* (1991) olivine-spinel Fe-Mg exchange geothermometer can be revised, using a Monte Carlo fitting routine, from the high $Cr^{\#}$, Ti-rich spinel experimental data presented in this study, and the earlier published experimental data of Ballhaus *et al.* (1991) and Wood (1990), to give:

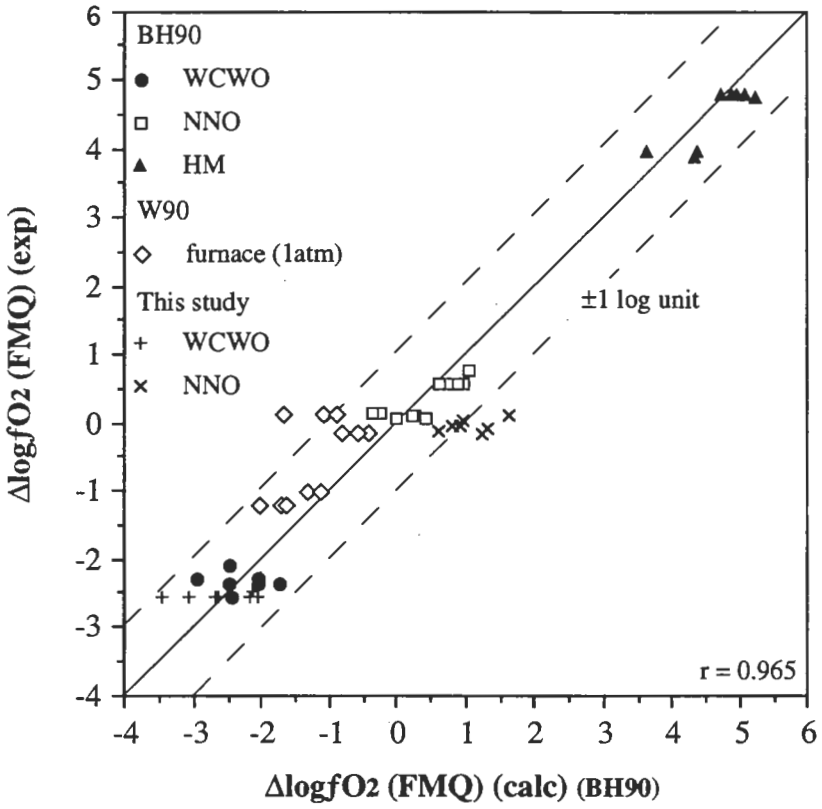

Figure 4.11: Experimental oxygen fugacities (with reference to the fayalite-magnetite-quartz oxygen buffer) against calculated oxygen fugacities, using the Ballhaus *et al.* (1991) olivine-orthopyroxene-spinel oxygen geobarometer, for experimental mineral pairs. The dashed lines indicate ± 1.0 log units. BH91 and W90 symbols indicate Ballhaus *et al.* (1991) and Wood (1990) experimental data respectively. The regression coefficient, r, equals 0.965 for the data set.

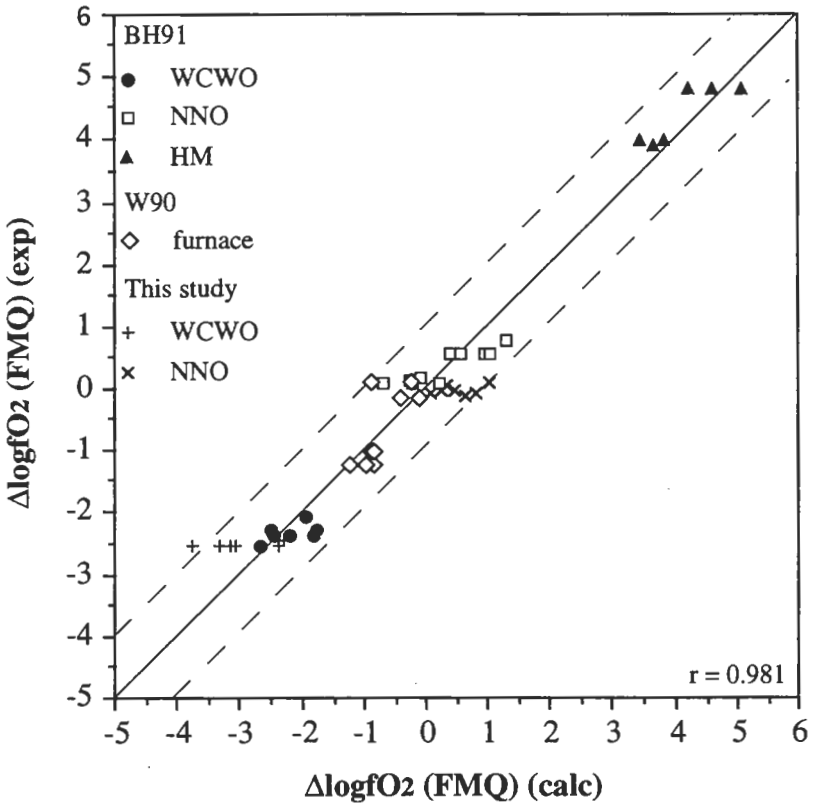

Figure 4.12: Experimental oxygen fugacities (with reference to the fayalite-magnetite-quartz oxygen buffer) against calculated oxygen fugacities, using the revised olivine-spinel + silica activity oxygen geobarometer presented in this study, for experimental mineral pairs. The dashed lines indicate ± 1.0 log units. BH91 and W90 symbols indicate Ballhaus *et al.* (1991) and Wood (1990) experimental data respectively. The regression coefficient, r, equals 0.981 for the data set.

$$T\,(^{\circ}C) = -273 + \{15180 + 0.022P + [(7000 + 0.011P)(1 - 2X_{Fe}^{olv})]$$
$$- 2515(X_{Mg}^{sp} - X_{Fe2+}^{sp}) + 15550X_{Cr}^{sp} + 20390(X_{Fe3+}^{sp} + X_{Ti}^{sp})\}$$
$$/\,[8.314\ln K_{id} + 9.953] \qquad (4.6)$$

where $K_{id} = [(X_{Fe2+}^{spi})(X_{Mg}^{olv})] / [(X_{Mg}^{spi})(X_{Fe}^{olv})]$ and other individual components are described above. The revised olivine-spinel geothermometer presented in this study is shown to give a better fit to the experimental data, with a regression coefficient of 0.804 (Figure 4.13), than the Ballhaus *et al.* (1991) geothermometer, with a regression coefficient of 0.687 (Figure 4.14).

4.5.2 $FeFeO_3$-$FeTiO_3$-$MgTiO_3$-$CrCrO_3$ - $(A)(B)O_3$ formula

For the purposes of a four-component ilmenite model it is assumed that Ti is confined to the B-site, i.e. (Fe^{2+}, Mg) and Ti are fully ordered over the A and B octahedral sites respectively. The ilmenite solid solution in its simplest form can then be represented as a four-component mix of the endmember "molecules". It should be noted that this assumption will not be valid for hematite-rich solid solutions at high temperatures (e.g. Ghiorso & Sack, 1991, Wood *et al.*, 1991), however, it is possible that the model will be able to predict hematite activities in Fe_2O_3-Cr_2O_3 rich solid solutions well enough for the oxygen sensor formulation.

The Andersen and Lindsley (1981) model for $FeTiO_3$-$MgTiO_3$-Fe_2O_3 assumed the ilmenite-geikielite and hematite-geikielite binaries were symmetric and the hematite-ilmenite binary was asymmetric. Wood *et al.* (1991) on the other hand obtained acceptable results for the hematite activity assuming the hematite-ilmenite binary was symmetric. For the purpose of this model, and because the experimental ilmenite data presented in this study do not extend far enough across the binary to allow the accurate calculation of an asymmetric model, it has been assumed that the ilmenite-hematite binary is symmetric with all ternary interaction parameters set to 0.

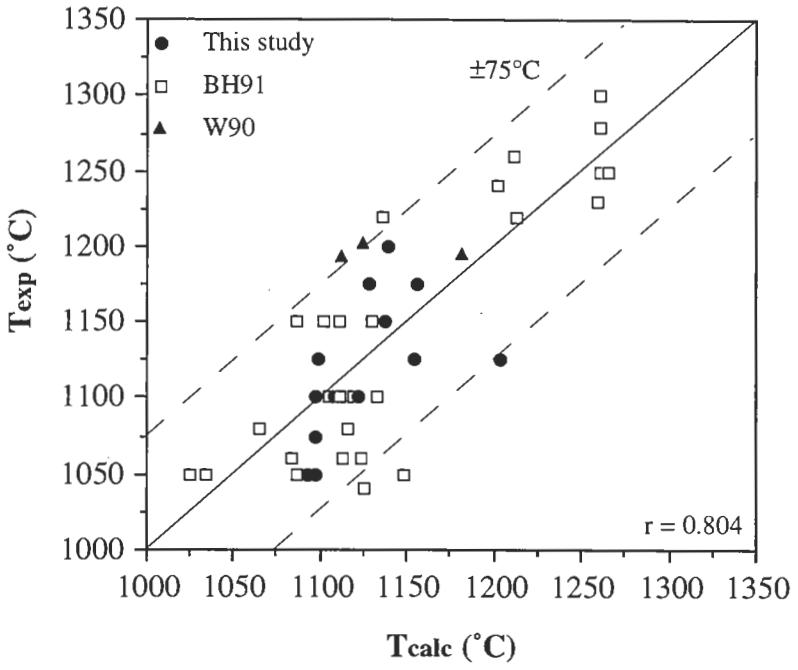

Figure 4.13: Experimental temperatures against calculated temperatures, using the olivine-spinel geothermometer presented in this study, for experimental mineral pairs. The dashed lines indicate ± 75 °C. BH91 and W90 symbols indicate Ballhaus *et al.* (1991) and Wood (1990) experimental data respectively. The regression coefficient, r, equals 0.804 for the data set.

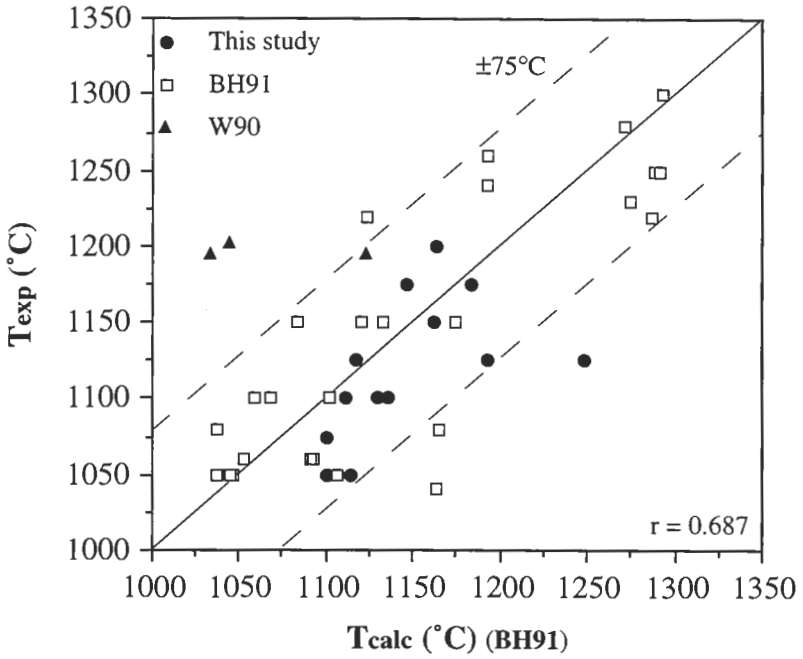

Figure 4.14: Experimental temperatures against calculated temperatures, using the Ballhaus *et al.* (1991) olivine-spinel geothermometer, for experimental mineral pairs. The dashed lines indicate ± 75 °C. BH91 and W90 symbols indicate Ballhaus *et al.* (1991) and Wood (1990) experimental data respectively. The regression coefficient, r, equals 0.687 for the data set.

From the generalized 1-site mixing model equation (e.g. Spear, 1993), the following expression for a quaternary asymmetric solution (component "1") can be derived:

$$\begin{aligned} RT\ln\gamma_1 &= W_{21}(2X_1X_2 - 2X_1^2X_2) + W_{12}(X_2^2 - 2X_1X_2^2) \\ &+ W_{31}(2X_1X_3 - 2X_1^2X_3) + W_{13}(X_3^2 - 2X_1X_3^2) \\ &+ W_{41}(2X_1X_4 - 2X_1^2X_4) + W_{14}(X_4^2 - 2X_1X_4^2) \\ &+ W_{32}(-2X_2^2X_3) + W_{23}(-2X_2X_3^2) \\ &+ W_{42}(-2X_2^2X_4) + W_{24}(-2X_2X_4^2) \\ &+ W_{43}(-2X_3^2X_4) + W_{34}(-2X_3X_4^2) \\ &+ W_{123}(X_2X_3 - 2X_1X_2X_3) + W_{124}(X_2X_4 - 2X_1X_2X_4) \\ &+ W_{134}(X_3X_4 - 2X_1X_3X_4) + W_{234}(-2X_2X_3X_4) \end{aligned}$$

To convert this expression to a symmetric model the following is set:

$W_{21} = W_{12}$, $W_{31} = W_{13}$, $W_{41} = W_{14}$, $W_{32} = W_{23}$, $W_{42} = W_{24}$, and $W_{43} = W_{34}$.

Hence it follows that:

$$\begin{aligned} RT\ln\gamma_1 &= 2W_{12}(X_1X_2X_3) + 2W_{12}(X_1X_2X_4) + W_{12}(X_2^2) \\ &+ 2W_{13}(X_1X_2X_3) + 2W_{13}(X_1X_3X_4) + W_{13}(X_3^2) \\ &+ 2W_{14}(X_1X_2X_4) + 2W_{14}(X_1X_3X_4) + W_{14}(X_4^2) \\ &+ 2W_{23}(X_1X_2X_3) + 2W_{23}(X_2X_3X_4) - 2W_{23}(X_2X_3) \\ &+ 2W_{24}(X_1X_2X_4) + 2W_{24}(X_2X_3X_4) - 2W_{24}(X_2X_4) \\ &+ 2W_{34}(X_1X_3X_4) + 2W_{34}(X_2X_3X_4) - 2W_{34}(X_3X_4) \\ &+ W_{123}(X_2X_3) - 2W_{123}(X_1X_2X_3) + W_{124}(X_2X_4) - 2W_{124}(X_1X_2X_4) \\ &+ W_{134}(X_3X_4) - 2W_{134}(X_1X_3X_4) - 2W_{234}(X_2X_3X_4) \end{aligned}$$

Gathering all ternary terms and noting that $C_{ijk} = W_{ij} + W_{ik} + W_{jk} - W_{ijk}$, where C_{ijk} is the ternary interaction parameter which is independent of any of the binary terms, i.e. it can be set to zero without affecting the binary terms, the following terms can be derived:

$$X_1X_2X_3(2W_{12} + 2W_{13} + 2W_{23} - 2W_{123}) = X_1X_2X_3(2C_{123}) = 0$$

$$X_1X_2X_4(2W_{12} + 2W_{14} + 2W_{24} - 2W_{124}) = X_1X_2X_4(2C_{124}) = 0$$

$$X_1X_3X_4(2W_{13} + 2W_{14} + 2W_{34} - 2W_{134}) = X_1X_3X_4(2C_{134}) = 0$$

$$X_2X_3X_4(2W_{23} + 2W_{24} + 2W_{34} - 2W_{234}) = X_2X_3X_4(2C_{234}) = 0$$

which leaves:

$$RT\ln\gamma_1 = W_{12}(X_2^2) + W_{13}(X_3^2) + W_{14}(X_4^2) - 2W_{23}(X_2X_3) - 2W_{24}(X_2X_4) - 2W_{34}(X_3X_4) + W_{123}(X_2X_3) + W_{124}(X_2X_4) + W_{134}(X_3X_4)$$

Because C_{ijk} has been set at zero, the following holds:

$$W_{123} = W_{12} + W_{13} + W_{23}$$

$$W_{124} = W_{12} + W_{14} + W_{24}$$

$$W_{134} = W_{13} + W_{14} + W_{34}$$

and:

$$RT\ln\gamma_1 = W_{12}X_2(X_2 + X_3 + X_4) + W_{13}X_3(X_3 + X_2 + X_4) + W_{14}X_4(X_4 + X_2 + X_3) - W_{23}(X_2X_3) - W_{24}(X_2X_4) - W_{34}(X_3X_4)$$

which can also be written as:

$$RT\ln\gamma_1 = W_{12}X_2(1-X_1) + W_{13}X_3(1-X_1) + W_{14}X_4(1-X_1) - W_{23}(X_2X_3) - W_{24}(X_2X_4) - W_{34}(X_3X_4)$$

Let 1 = H (hematite), 2 = I (ilmenite), 3 = G (geikielite), 4 = E (eskolaite):

and $X_1 = X_{hem}$, $X_2 = X_{ilm}$, $X_3 = X_{gk}$, $X_4 = X_{esk}$, which leads to:

$$RT\ln\gamma_{hem} = W_{HI}X_{ilm}(1-X_{hem}) + W_{HG}X_{gk}(1-X_{hem}) + W_{HE}X_{esk}(1-X_{hem}) - W_{IG}(X_{ilm}X_{gk}) - W_{IE}(X_{ilm}X_{esk}) - W_{GE}(X_{gk}X_{esk})$$

$$RT\ln\gamma_{ilm} = W_{HI}X_{hem}(1-X_{ilm}) + W_{IG}X_{gk}(1-X_{ilm}) + W_{IE}X_{esk}(1-X_{ilm}) - W_{HG}(X_{hem}X_{esk}) - W_{HE}(X_{hem}X_{esk}) - W_{GE}(X_{gk}X_{esk})$$

$$RT\ln\gamma_{gk} = W_{HG}X_{hem}(1-X_{gk}) + W_{IG}X_{ilm}(1-X_{gk}) + W_{GE}X_{esk}(1-X_{gk}) - W_{HI}(X_{hem}X_{ilm}) - W_{HE}(X_{hem}X_{esk}) - W_{IE}(X_{ilm}X_{esk})$$

For the four-component molecular mixing ilmenite model the activity of hematite component can be written as:

$$RT\ln(a_{hem}) = RT\ln[X_{hem}] + RT\ln[\gamma_{hem}]$$

where X_{hem} is the mole fraction of the hematite component.

As Cr-Fe^{3+} ordering in $(A)(B)O_3$ ilmenite solid solution is not explicitly considered in this study, the final expression for the activity of hematite component can be written as:

$$\ln(a_{hem}) = \ln[X_{hem}] + (W_{HI}/RT)X_{ilm}(1-X_{hem}) + (W_{HG}/RT)X_{gk}(1-X_{hem}) + (W_{HE}/RT)X_{esk}(1-X_{hem}) - (W_{IG}/RT)(X_{ilm}X_{gk}) - (W_{IE}/RT)(X_{ilm}X_{esk}) - (W_{GE}/RT)(X_{gk}X_{esk})$$

where: $X_{hem} = (Fe^{3+}/2)/(Mg+Fe^{2+}+(Fe^{3+}/2)+(Cr/2))$

$X_{esk} = (Cr/2)/(Mg+Fe^{2+}+(Fe^{3+}/2)+(Cr/2))$

$X_{gk} = Mg/(Mg+Fe^{2+}+(Fe^{3+}/2)+(Cr/2))$

$X_{ilm} = Fe^{2+}/(Mg+Fe^{2+}+(Fe^{3+}/2)+(Cr/2))$

$\Sigma(X_i) = 1.0$

and W_{HI} is the hematite-ilmenite Margules parameter

W_{HG} is the hematite-geikielite Margules parameter

W_{HE} is the hematite-eskolaite Margules parameter

W_{IG} is the ilmenite-geikielite Margules parameter

W_{IE} is the ilmenite-eskolaite Margules parameter

W_{GE} is the geikielite-eskolaite Margules parameter

with unknown Margules parameters W_{HI}, W_{HG}, W_{HE}, W_{IG}, W_{IE}, W_{GE} which require solving from the experimental data.

4.5.3 Ilmenite geothermometry

The olivine-ilmenite Fe-Mg exchange geothermometer formulated in Chapter 3 (section 3.6.1, equation 3.8) underestimates experimental run temperatures for chromium-rich ilmenite bearing assemblages, synthesized under oxygen buffer conditions below NNO, by as much as 200 °C, whereas it overestimates experimental run temperatures for chromium-rich hematite bearing assemblages, synthesized at HM oxygen buffer conditions by up to 400 °C (Figure 4.15). Experimental data from this study, in combination with the experimental data from Chapter 3 and Andersen and Lindsley (1981), have been used to formulate a revised olivine-ilmenite Fe-Mg exchange geothermometer which takes into account the effects of Cr substitution in ilmenite.

The olivine-ilmenite temperature dependent exchange reaction is written as:

$$MgTiO_3\ (gk) + Fe_{0.5}SiO_2\ (fa) = FeTiO_3\ (ilm) + Mg_{0.5}SiO_2\ (fo) \qquad (4.7)$$

which can be expressed as:

$$\Delta G_{exch} = \Delta H_{exch} - T\Delta S_{exch} + P\Delta V_{exch} - 2\,RT\ln(a^{ilm}_{MgTiO3}) - RT\ln(a^{olv}_{Fe2SiO4}) + 2\,RT\ln(a^{ilm}_{FeTiO3}) + RT\ln(a^{olv}_{Mg2SiO4}) \qquad (4.8)$$

where the gas constant, R = 8.314 J K^{-1} mol^{-1}, T is in °K, P is in bar, and ΔV_{exch} = -0.047 J bar^{-1} (Fischer and Medaris, 1969; Lindsley, 1976b).

Using olivine activities previously described in Chapter 3 herein (equations 3.3 and 3.4), and the non-ideality terms for the ilmenite and geikielite solid solution components described above (section 4.5.2), equation (4.8) can be written as:

$$\Delta G_{exch} = \Delta H_{exch} - T\Delta S_{exch} - 0.047P + RT\ln K_{id} + W^{olv}_{Fe\text{-}Mg}(2X^{olv}_{Fe} - 1) + W^{ilm\text{-}gk}_{G}(X_{gk} - X_{ilm}) + (W^{ilm\text{-}hem}_{G} - W^{gk\text{-}hem}_{G})X_{hem} + (W^{ilm\text{-}esk}_{G} - W^{gk\text{-}esk}_{G})X_{esk} \qquad (4.9)$$

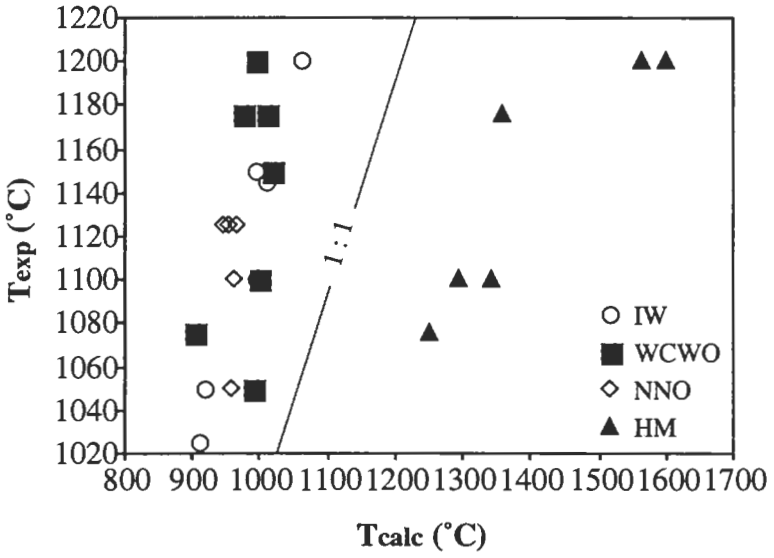

Figure 4.15: Experimental temperatures against calculated temperatures, using the olivine-ilmenite geothermometer presented in Chapter 3 herein, for experimental Cr-rich ilmenite bearing mineral assemblages.

where $K_{id} = [(X^{ilm}_{Fe2+})(X^{olv}_{Mg})] / [(X^{ilm}_{Mg})(X^{olv}_{Fe})]$, and $X^{ilm}_{Fe} = Fe^{2+}/(Fe^{2+} + Mg)$.

Equation (4.9) was solved using a Monte Carlo fitting routine through the experimental data of this study and the Andersen and Lindsley (1981) data, to give the following revised olivine-ilmenite Fe-Mg exchange geothermometer:

$$T\,(^{\circ}C) = -273 + \{-13715 + P[-0.047 + 0.015(2X^{olv}_{Fe} - 1) + 0.011(X_{gk} - X_{ilm})] + 3785(2X^{olv}_{Fe} - 1) + 2830(X_{gk} - X_{ilm}) - 19560X_{hem} - 7840X_{esk} + 45122X_{hem}X_{esk}\} / [2.231 - 8.314\ln K_{id}] \quad (4.10)$$

where $W^{olv}_{Fe\text{-}Mg} = (3785 + 0.015P)$ Jmol^{-1}, $W^{ilm\text{-}gk}_{G} = (2830 + 0.011P)$ Jmol^{-1}, $(W^{ilm\text{-}hem}_{G} - W^{gk\text{-}hem}_{G}) = -19560$ Jmol^{-1} and $(W^{ilm\text{-}esk}_{G} - W^{gk\text{-}esk}_{G}) = -7840$ Jmol^{-1}. The value for W^{olv}_{G} obtained here is in excellent agreement with $W^{olv}_{Fe\text{-}Mg} = (3700 + 0.0108P)$ Jmol^{-1} (e.g. von Seckendorff and O'Neill, 1993), which has been used in earlier studies (e.g. see Chapter 3 herein). Also, the value for the $(W^{ilm\text{-}hem}_{G} - W^{gk\text{-}hem}_{G})$ non-ideality term compares very well with that obtained previously for Cr-free experiments (-20375 Jmol^{-1}, see section 3.6.1). With the exception of two Andersen and Lindsley (1981) high temperature data points, the revised olivine-ilmenite geothermometer reproduces experimental temperatures to better than ±100 °C, and in most cases better than ±70 °C (Figure 4.16). Also, the calibration of the revised olivine-ilmenite geothermometer presented in this study is not significantly dependent on the Cr content of ilmenite (Figure 4.17). The non-ideality terms obtained here have been further used in the ilmenite-based oxygen geobarometer equation.

4.5.4 Ilmenite oxygen geobarometry

The olivine-orthopyroxene-ilmenite redox equilibrium (abbreviated FFH reaction) can, as shown previously in Chapter 3 (see section 3.6.2), be used to calculate the oxygen fugacity:

$$8\,Fe_{0.5}SiO_2\,(fa) + O_2\,(fluid) = 2\,Fe_2O_3\,(hem) + 2\,Fe_2Si_2O_6\,(fs) \quad (4.11)$$

and the equilibrium reaction can be expressed as:

$$\Delta G = \Delta H - T\Delta S + P\Delta V_s - 4\,RT\ln(a^{olv}_{Fe2SiO4}) - RT\ln(a_{O2}) + 2\,RT\ln(a^{ilm}_{Fe2O3}) + 2\,RT\ln(a^{opx}_{Fe2Si2O6}) \quad (4.12)$$

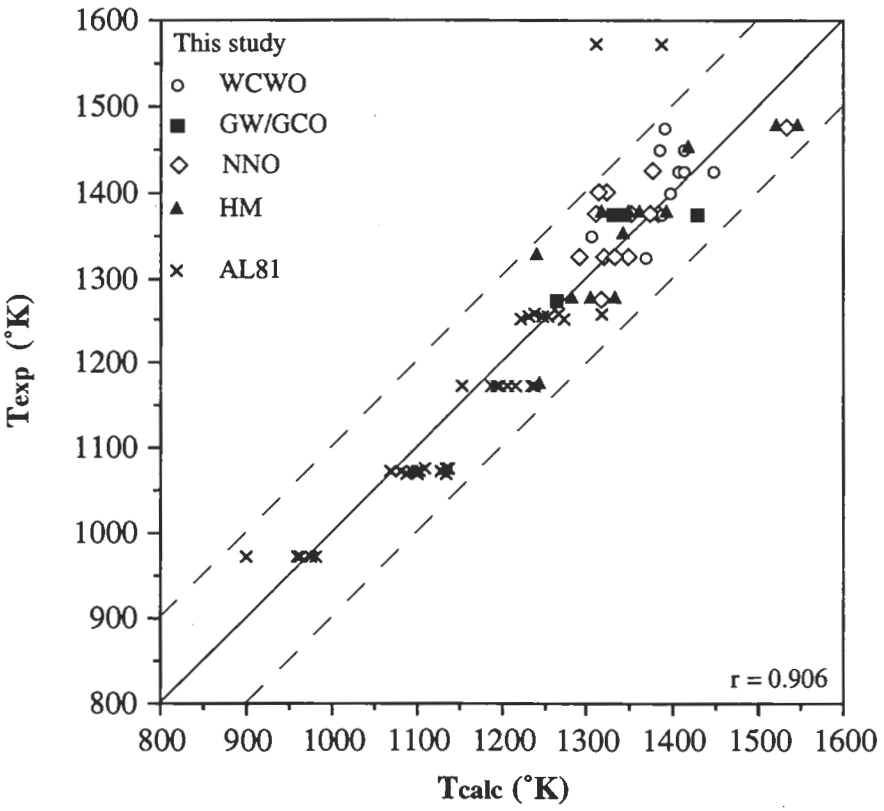

Figure 4.16: Experimental temperatures against calculated temperatures, using the olivine-ilmenite geothermometer presented in this study, for experimental mineral pairs. The dashed lines indicate ± 100 °C. AL81 symbols indicate Andersen and Lindsley (1981) experimental data. The regression coefficient, r, equals 0.906 for the data set.

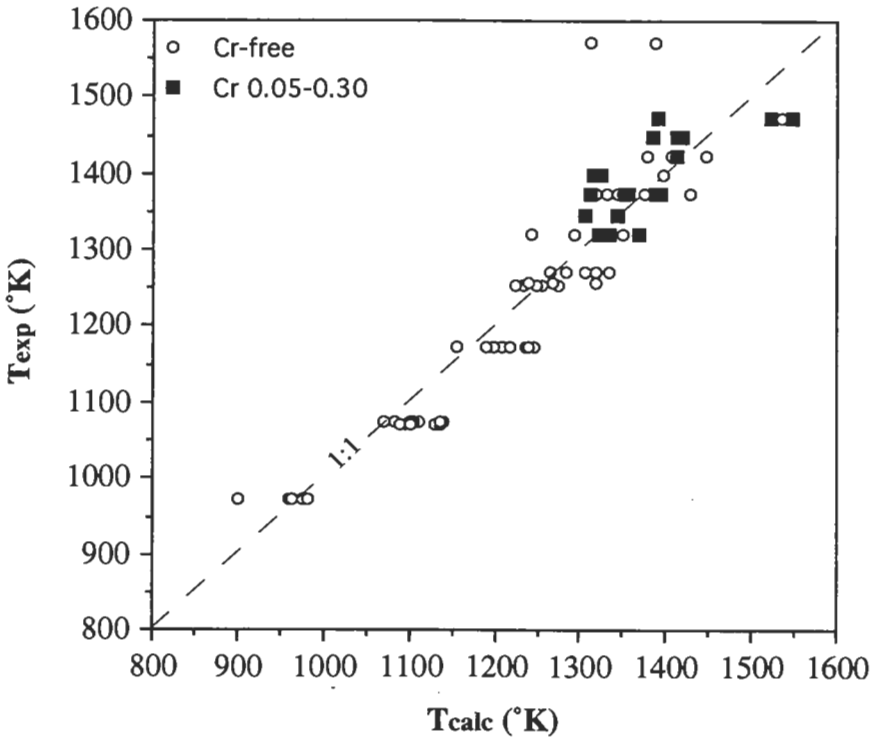

Figure 4.17: Experimental temperatures against calculated temperatures, using the revised olivine-ilmenite geothermometer presented here, for experimental mineral pairs, with particular emphasis on Cr-free and Cr-bearing ilmenites.

Using the hematite end-member non-ideality term described above (section 4.5.2) and a two-site regular solution model for olivine, and assuming an ideal solid solution for orthopyroxene (e.g. O'Neill and Wall, 1987; Mattioli and Wood, 1988; Ballhaus *et al.*, 1991; von Seckendorff and O'Neill, 1993), equation (4.12) can be written as:

$$\begin{aligned}
&\log fO_2\,(\mathrm{FFH}) = \Delta S/(2.303R) - \Delta H/(2.303RT) + 0.0375P/T \\
&+ 2\log(X^{ilm}_{Fe3+}) + 2\log(a^{opx}_{Fe}) - 8\log(X^{olv}_{Fe}) \\
&- 8W^{olv}_{Fe\text{-}Mg}(X^{olv}_{Mg})^2/(2.303RT) + 2W^{hem\text{-}ilm}_{G}X_{ilm}(1 - X_{hem})\ /(2.303RT) \\
&+ 2W^{hem\text{-}gk}_{G}X_{gk}(1 - X_{hem})\ /(2.303RT) \\
&+ 2W^{hem\text{-}esk}_{G}X_{esk}(1 - X_{hem})\ /(2.303RT) \\
&- 2W^{ilm\text{-}gk}_{G}(X_{ilm}X_{gk})\ /(2.303RT) - 2W^{ilm\text{-}esk}_{G}(X_{ilm}X_{esk})\ /(2.303RT) \\
&- 2W^{gk\text{-}esk}_{G}(X_{gk}X_{esk})\ /(2.303RT) \qquad (4.13)
\end{aligned}$$

where $X^{olv}_{Fe} = [Fe/(Mg+Fe)]^{olv}$, $X^{ilm}_{Fe3+} = [(Fe^{3+}/2)/(Fe^{2+}+Mg+(Fe^{3+}/2))]^{ilm}$, a^{opx}_{Fe} is the activity of ferrosilite in orthopyroxene, and $\Delta V_s = 0.718$ Jbar^{-1} (Holland and Powell, 1990).

Using a Monte Carlo fitting routine through the experimental data of this study and the Andersen and Lindsley (1979) data (with orthopyroxene-saturated olivine-ilmenite experiments, and assuming that in these experiments oxalic acid "buffers" near graphite-water, W.R. Taylor, pers. comm.), equation (4.13) can be solved to give the revised olivine-orthopyroxene-ilmenite oxygen geobarometer:

$$\begin{aligned}
&\log fO_2\,(\mathrm{FFH}) = 5.257 - \frac{18253}{T} + \frac{0.0375P}{T} \\
&+ 2\log(X^{ilm}_{Fe3+}) + 2\log(a^{opx}_{Fe}) - 8\log(X^{olv}_{Fe}) \\
&-\{(1581 + 0.006P)((X^{olv}_{Mg})^2) + (295 + 0.001P)(X_{ilm}X_{gk}) \\
&- 275X_{esk}(1 - X_{hem}) + 1923X_{ilm}(1 - X_{hem}) \\
&- 119X_{gk}(1 - X_{hem}) + 2282X_{ilm}X_{esk}) + 3101X_{gk}X_{esk}\}\ /\ T \qquad (4.14)
\end{aligned}$$

where P is in bar, T in °K and mole fractions of olivine and ilmenite endmembers have been described above. The fitting routine resolved the following Margules parameters: $W_{IG} = (2824 + 0.010P)$ Jmol^{-1}, $W_{HE} = 2633$ Jmol^{-1}, $W_{HI} = -18410$ Jmol^{-1}, $W_{HG} = 1140$ Jmol^{-1}, $W_{IE} = 21847$ Jmol^{-1}, $W_{GE} = 29688$ Jmol^{-1}. The revised olivine-orthopyroxene-ilmenite oxygen geobarometer is illustrated in Figure 4.18A and 4.18B, which shows that

for the experimental data set the regression coefficient equals 0.994, and that calculated oxygen fugacities can be determined within one log unit of the experimental oxygen fugacities (Figure 4.18B).

A variation to the FFH oxygen geobarometer can be obtained in a similar manner to that discussed above with the spinel oxygen geobarometer, by the introduction of a silica activity term which, when writing equation (4.11) relative to the quartz standard state, gives:

$$4\ FeSi_{0.5}O_2\ (fa) + O_2\ (fluid) = 2\ Fe_2O_3\ (hem) + 2\ SiO_2\ (qtz) \qquad (4.15)$$

Using the silica activity calculations for orthopyroxene-undersaturated assemblages (see Appendix F), the experimental data from this study and the Andersen and Lindsley (1979) data are used to give the oxygen fugacity relative to FMQ as:

$$\Delta \log fO_2\ (FMQ) = 1.123 + \frac{1611}{T} - \frac{0.057P}{T} + 2\log(a_{SiO2})$$
$$+ 2\log(X_{hem}) - (\frac{2098}{T})\ (X_{ilm}X_{gk}) - (\frac{3876}{T})X_{esk}$$
$$+ (\frac{3410}{T})X_{hem} - 4\log(1 - X_{Mg}^{olv}) - (\frac{2826}{T})(X_{Mg}^{olv})^2 \qquad (4.16)$$

where the individual components are described above. The olivine-ilmenite + silica activity oxygen geobarometer is illustrated in Figure 4.19. The regression coefficient for the experimental data set of the olivine-ilmenite + silica activity oxygen geobarometer equals 0.985, and the calculated oxygen fugacities can be determined within one log unit of the experimental oxygen fugacities.

4.6 Results from the ilmenite- and spinel-based oxygen geobarometers and geothermometers

Finally, the ilmenite and spinel oxygen geobarometers are applied to several suites of mantle derived ilmenite and spinel xenocrysts sourced from kimberlites located in Africa, the Commonwealth of Independent States (CIS) and South Africa, and lamproites from Australia (spinel only) (Figures 4.20 and 4.21). Xenocryst compositions are in part derived from the literature (e.g. Haggerty, 1979; Haggerty, 1991; Jaques *et al.*, 1986; Sobolev, 1977; Tompkins and Haggerty, 1985, among many), and are in part unpublished (Western Mining Corporation, unpubl. database).

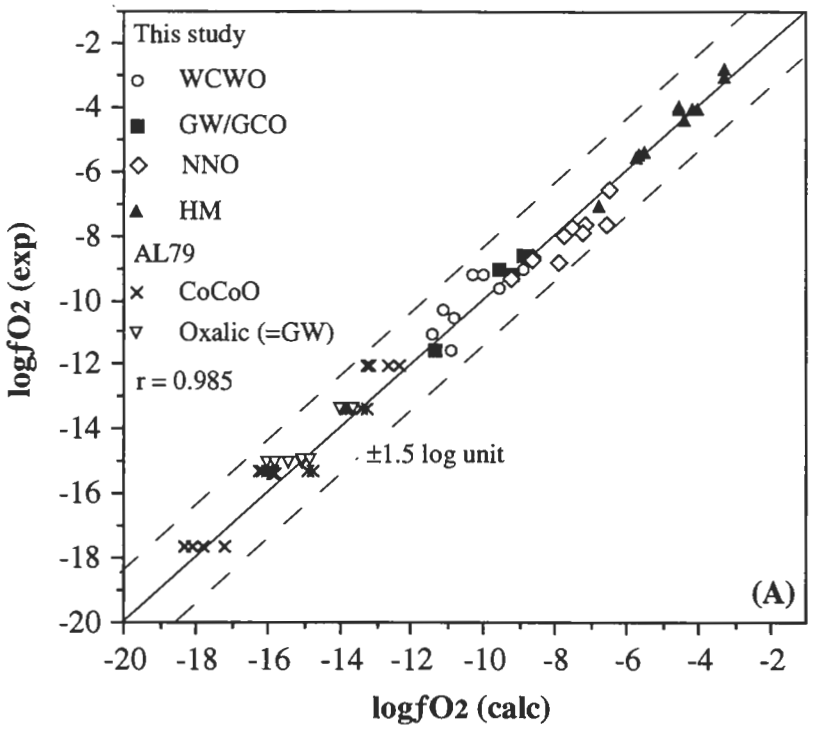

Figure 4.18: (A) Experimental oxygen fugacities against calculated oxygen fugacities, using the revised olivine-orthopyroxene-ilmenite oxygen geobarometer presented in this study, for experimental mineral pairs. The dashed lines indicate ± 1.0 log units. AL79 symbols indicate Andersen and Lindsley (1979) experimental data. The regression coefficient, r, equals 0.985 for the data set.

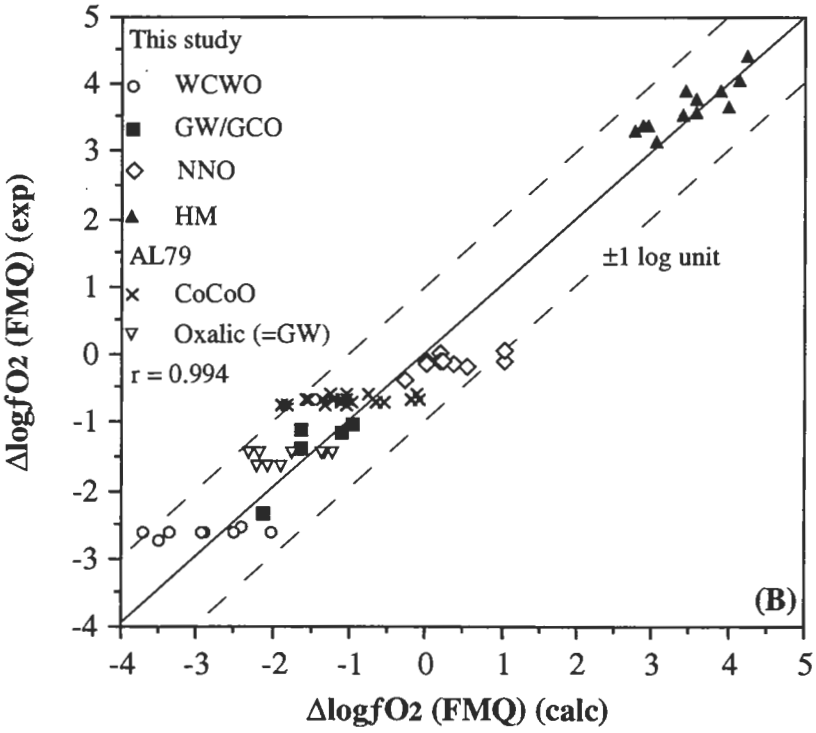

Figure 4.18: (B) Experimental oxygen fugacities against calculated oxygen fugacities (with reference to the fayalite-magnetite-quartz oxygen buffer), using the revised olivine-orthopyroxene-ilmenite oxygen geobarometer presented in this study, for experimental mineral pairs. The dashed lines indicate ± 1.0 log units. AL79 symbols indicate Andersen and Lindsley (1979) experimental data. The regression coefficient, r, equals 0.994 for the data set.

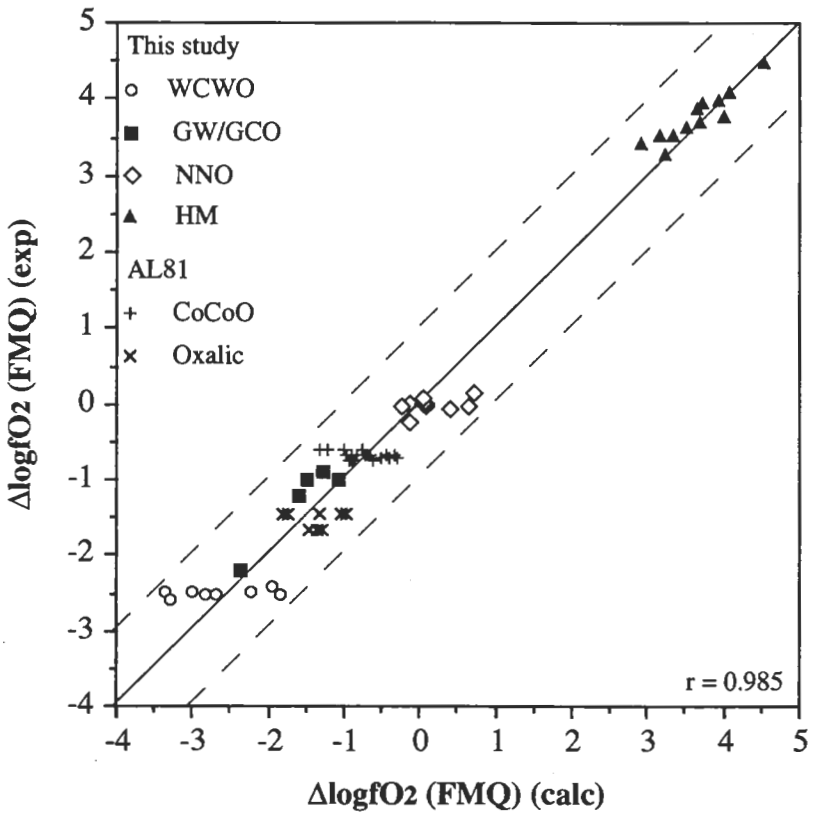

Figure 4.19: Experimental oxygen fugacities (with reference to the fayalite-magnetite-quartz oxygen buffer) against calculated oxygen fugacities, using the revised olivine-ilmenite + silica activity oxygen geobarometer presented in this study, for experimental mineral pairs. The dashed lines indicate ± 1.0 log units. AL81 symbols indicate Andersen and Lindsley (1981) experimental data. The regression coefficient, r, equals 0.985 for the data set.

Oxygen fugacity values for the xenocryst assemblages are calculated, using the relevant exchange geothermometers and oxygen geobarometers described above, assuming oxide equilibration with an Fo_{92} olivine composition. Since there is no method available with which to calculate pressures and temperatures of formation of ilmenite or spinel xenocrysts from routine microprobe analyses, a uniform pressure and temperature of formation of 50 kbar and 1100±100 °C respectively have been assumed for all the kimberlite and lamproite derived xenocrysts. $\ln K_d$ values for olivine-oxide pairs are determined from the assumed olivine composition and pressures and temperatures of formation using the olivine-oxide geothermometers. Values for a_{SiO2} are estimated according to Brey (1990), and calculated fO_2 values are determined from the olivine-oxide + silica activity oxygen geobarometers. It should be noted here that as the mineral analyses have been collected from the literature, there is a risk that, at least in the past, there has been little concern with the accurate determination of the Fe^{3+} content of ilmenites and spinels. Although more recent discussions have focussed on the precision and accuracy of the calculation of Fe^{3+} in spinel (e.g. Wood and Virgo, 1989; Wood, 1991) and ilmenite (e.g. Chapter 3 herein) from electron microprobe analyses, the lack of a detailed treatment of such analyses may introduce significant errors in the determination of the oxide redox ratio. Similarly, the determination of mineral stoichiometry in calculating Fe^{3+} has received little or no detailed attention in routine analytical work in older literature, and the lack of stoichiometry significantly alters the determination of the redox ratio in minerals such as ilmenite and spinel. However, it has been demonstrated in this study that mantle derived ilmenite and spinel xenocrysts originating from high pressure domains such as those used in this section are generally close to stoichiometric (e.g. Chapter 2 herein).

Ilmenite xenocryst compositions from Africa and South Africa cover a wide, apparently continuous, range of oxygen fugacities (Figure 4.20A and 4.20C). The majority of ilmenite compositions from these populations project at, or immediately above, the WM buffer, but compositions extend as low as the IW buffer and as high as oxygen fugacity conditions at FMQ+1.0 log units. The ilmenite xenocryst population from the CIS, although smaller in number than those from Africa and South Africa, shows a similar range in oxygen fugacities calculated at 50 kbar and 1100±100 °C, and projects primarily between the WM and FMQ buffers, but has a number of ilmenite compositions extending below the WM buffer towards the IW buffer (Figure 4.20B).

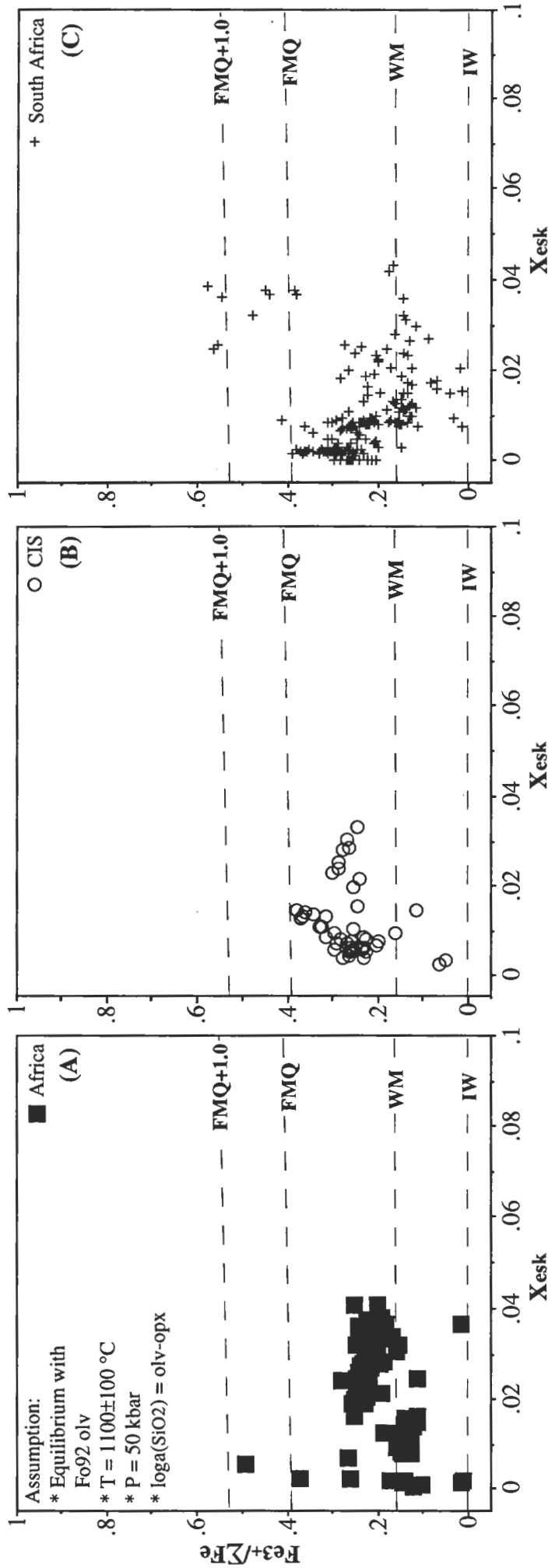

Figure 4.20: Application of the ilmenite-based oxygen geobarometer (this study) to ilmenite xenocrysts reported from (A) Africa, (B) the Commonwealth of Independent States (CIS), and (C) South Africa (compositional data are from Western Mining Corporation, unpubl. database) by plotting $Fe^{3+}/\Sigma Fe$ in ilmenite against the mole fraction of Cr_2O_3 (X_{esk}) in ilmenite. The following assumptions have been made in the calculation of the oxygen fugacity: ilmenite xenocrysts are in equilibrium with Fo_{92} olivine, pressure and temperature of equilibration are 50 kbar and 1100±100 °C respectively, and the silica activity is calculated using Brey (1990). IW, WM and FMQ represent the iron-wüstite, wüstite-magnetite and fayalite-magnetite-quartz oxygen buffers respectively. Ilmenite xenocrysts were sourced from kimberlites for (A), (B) and (C).

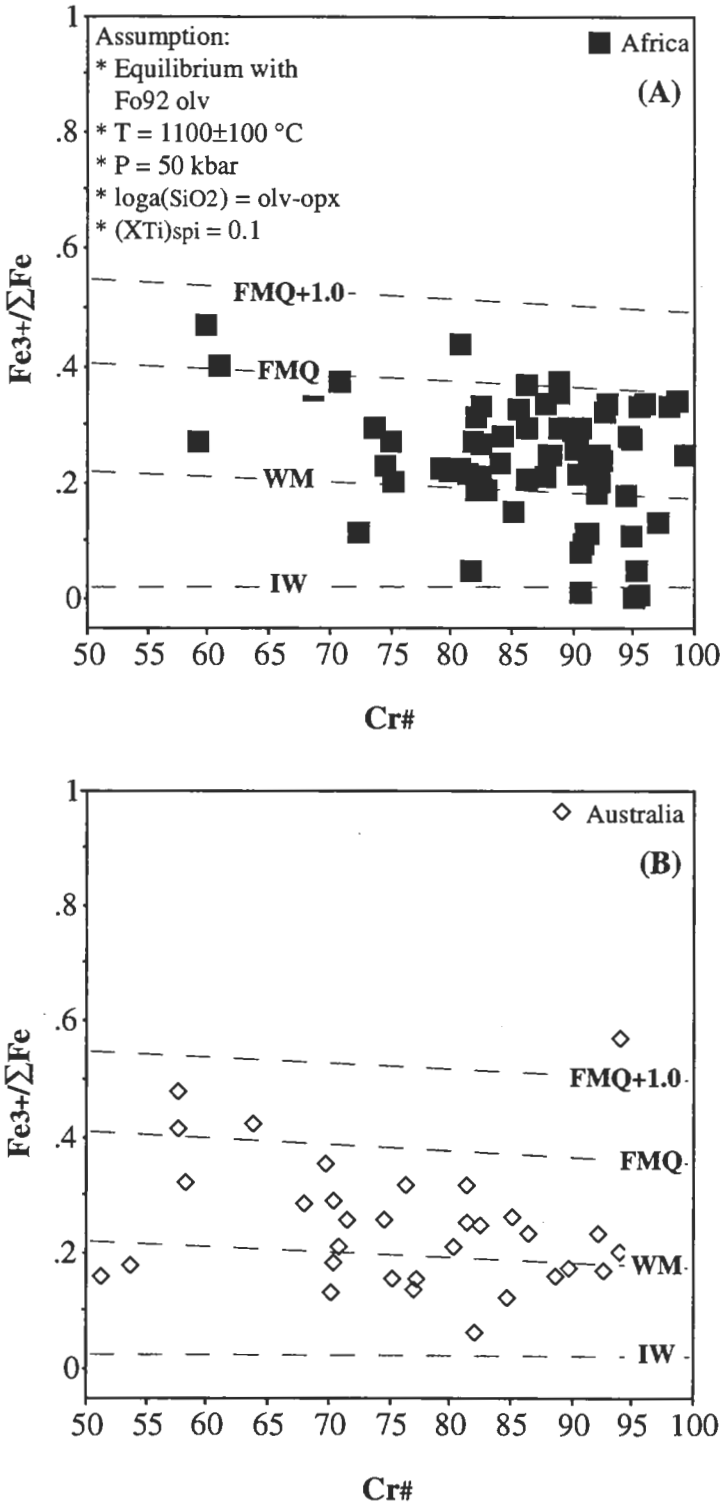

Figure 4.21: Application of the spinel-based oxygen geobarometer (this study) to spinel xenocrysts reported from (A) Africa, (B) Australia, (C) the Commonwealth of Independent States (CIS), and (D) South Africa (compositional data are from Western Mining Corporation, unpubl. database) by plotting $Fe^{3+}/\sum Fe$ in spinel against $Cr^{\#}$ in spinel. The following assumptions have been made in the calculation of the oxygen fugacity: spinel xenocrysts with $X_{Ti} = 0.1$ are in equilibrium with Fo_{92} olivine, pressure and temperature of equilibration are 50 kbar and 1100±100 °C respectively, and the silica activity is calculated using Brey (1990). IW, WM and FMQ represent the iron-wüstite, wüstite-magnetite and fayalite-magnetite-quartz oxygen buffers respectively. Spinel xenocrysts were sourced from kimberlites for (A), (C) and (D), and olivine lamproites for (B).

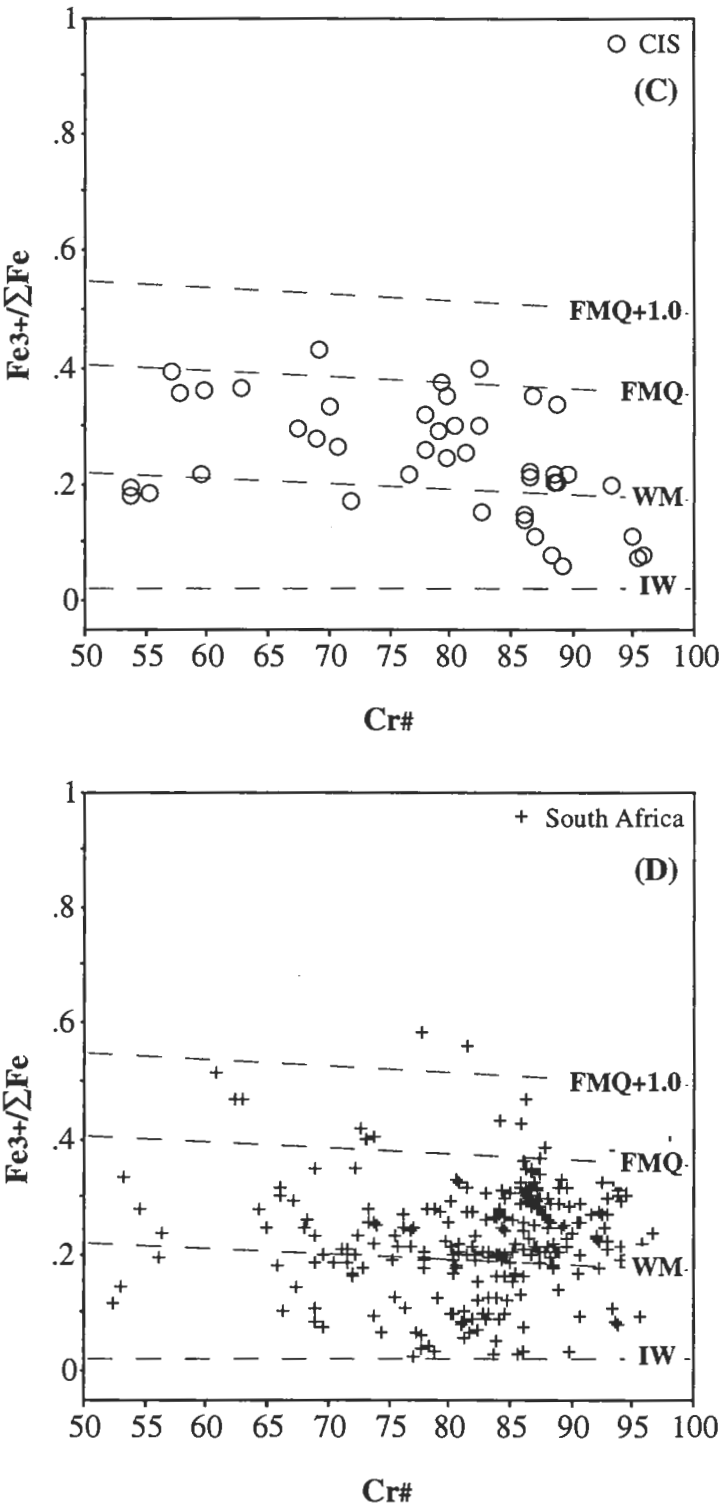

Figure 4.21: Continued.

A similar picture emerges from the spinel xenocrysts as shown in Figure 4.21. Oxygen fugacities determined at 50 kbar and 1100±100 °C from spinel compositions broadly range between the IW buffer and FMQ+1.0 log units, with the majority of the spinel samples projecting between the IW and FMQ buffers. It is interesting to note that for three populations, namely Africa, CIS and South Africa, a small number of high $Cr^{\#}$ ($\geq \approx 90$) spinel xenocrysts appear to indicate the most reducing conditions, with oxygen fugacity projections between IW and WM (Figure 4.21A, 4.21C and 4.21D). With decreasing $Cr^{\#}$, the remainder of these spinel populations 'cluster' at oxygen fugacity conditions between IW and FMQ. The interpretation that the high $Cr^{\#}$ spinels represent the most primitive compositions carries the connotation of a progressive increase in fO_2 with the formation of spinels with decreasing $Cr^{\#}$. For spinel xenocrysts from Australia, the general observation that the high $Cr^{\#}$ spinels indicate the most reducing conditions also holds. However, the trend for the Australian population towards lower $Cr^{\#}$ spinels which indicate more oxidized conditions appears to be more gradual (Figure 4.21B).

4.7 Conclusions

Experimental results published in this chapter have been used to constrain a four-component ilmenite regular solid solution model, with emphasis on the incorporation of Cr_2O_3 (eskolaite) in ilmenite. Ilmenites with elevated chromium contents were synthesized in the presence of olivine, orthopyroxene and spinel under mantle P-T conditions (1050 and 1200 °C and 17 to 35 kbar) and over a wide range in fO_2 (FMQ±4.0 log units). The experimental data were used to revise ilmenite-based exchange geothermometers and oxygen barometers with improved corrections for the eskolaite component in ilmenite. Coexisting spinels were used to improve existing spinel-based oxygen geobarometers and exchange geothermometers for high chromium ($Cr^{\#} > 90$) spinels. The experimental data were also used to model ilmenite- and spinel-based oxygen geobarometers for orthopyroxene-undersaturated assemblages by the introduction of a silica activity term.

Application of the improved ilmenite and spinel oxygen geobarometers presented in this study to a range of mantle-derived xenocryst assemblages reveals that the oxygen fugacity of the lithospheric upper mantle generally lies in the field bounded by the WM and FMQ buffers. This is broadly in agreement with oxygen fugacities calculated from ilmenite-bearing assemblages (e.g. Haggerty and Tompkins, 1983) and spinel-bearing assemblages (e.g. O'Neill and Wall, 1987). However, in contrast with this general observation, a consistent picture also emerges from both the ilmenite and spinel xenocryst populations

presented here which suggests that the mantle redox condition is, at least in part, more reduced, and projects as low as two log units below WM (e.g. Haggerty, 1990). Whether, as alleged for example by O'Neill and Wall (1987), those oxides which fall between IW and WM are the few exceptions and are probably artefacts caused by analytical error still remains to be determined. The major fluid species in the C-O-H system at oxygen fugacity conditions above WM is dominated by $CO_2 \pm H_2O$ (e.g. Taylor, 1985) where reduced carbon becomes unstable. However, at oxygen fugacity conditions below WM, CH_4 and H_2 will become the dominant fluid species and reduced carbon is stable (e.g. Taylor, 1985). Ilmenites and spinels which occur both as intergrowths with, and as inclusions in diamond, and which have redox ratios less than 0.1 (e.g. Sobolev, 1977), will compositionally project within the field bounded by IW and WM at 50 kbar and 1100±100 °C, which suggests that the mantle redox condition falls below the WM buffer. With this in mind, an issue that remains unanswered, but considered beyond the scope of this work, is whether the low oxidation state in the diamond-bearing lithosphere resulted from early redox melting between generally reduced lithosphere (e.g. Arculus, 1985) and oxidized recycled material (e.g. Wallace and Green, 1988), or whether it is the result of continuous degassing of reduced fluids from the asthenosphere (e.g. Green *et al.*, 1987; Taylor and Green, 1989; Green *et al.*, 1990).

CHAPTER 5

AN EXPERIMENTAL STUDY INTO THE SUBSTITUTION OF CHROMIUM, IRON AND WATER IN RUTILE AT HIGH TEMPERATURES AND PRESSURES - IMPLICATIONS FOR THE ROLE OF RUTILE AS AN INDICATOR OF THE WATER ACTIVITY IN THE EARTH'S MANTLE

5.1 Introduction

Rutile is a characteristic opaque mantle mineral found in eclogites (e.g. Smith and Dawson, 1975), kimberlites (e.g. Mitchell, 1979), the MARID suite of xenoliths from kimberlites (e.g. Dawson and Smith, 1977), zircon and LIMA-bearing nodules (e.g. Haggerty and Gurney, 1984), or as inclusions in diamonds (e.g. Meyer, 1987). A compositional characteristic of mantle-derived rutiles is the presence of moderate (1-2 wt.% Cr_2O_3) to high (8-12 wt% Cr_2O_3) amounts of chromium, iron (0.2-6.0 wt.% FeO_{total}), or niobium (with contents up to 21 wt.% Nb_2O_5, e.g. Haggerty, 1987). The nature of the structural cation substitution in anhydrous rutile has been documented by Hyde (1976).

A second important substitution into nominally 'anhydrous' rutile is water (e.g. Rossman and Smyth, 1990; Hammer and Beran, 1991). Water in mantle minerals is important because its presence can influence melting relations and phase transitions in mantle rocks. Although a hydrous component is more readily associated with minerals such as amphibole and phlogopite rather than rutile, structural hydroxyl groups in rutile were originally recognized based on a narrow double band near 3200-3300 cm^{-1} in the infrared (I.R.) absorption spectrum of synthetic crystals and attributed to an (OH) stretch mode (Soffer, 1961). Since that initial observation of (OH) in rutile, a number of authors have discussed the crystallographic nature of structural (OH) incorporated in synthetic rutile and its effect on electrical and optical properties (e.g. von Hippel *et al.*, 1962; Johnson *et al.*, 1968; Ohlsen and Shen, 1974; Andersson *et al.*, 1973, 1974). Beran and Zemann (1971) established the presence of (OH) in rutile from natural occurrences and suggested that (OH) dipoles on the O-site were oriented perpendicular to the plane of the three coordinating Ti-atoms. The first direct evidence for the location of H in rutile came from a neutron diffraction study of a Nb-Cr-Al-Fe-rich rutile crystal (1.86 wt.% Nb_2O_5, 1.16 wt.% Cr_2O_3, 0.68 wt.% Al_2O_3 and 0.67 wt.% FeO) with ~0.7 wt.% H_2O from the Roberts Victor kimberlite in South Africa (Swope *et al.*, 1992). In contrast with earlier

suggestions that the most energetically favourable position for H in synthetic rutile was in the ($^1/_2$00) site (Johnson *et al.*, 1968), the neutron diffraction study indicated that the H position in the natural rutile was much closer to ($^1/_2{}^1/_2$0).

Recently, Hammer and Beran (1991) presented I.R. spectra of rutiles of crustal origin. The concentration of (OH) groups was found to correlate with minor component concentrations in rutile, and there was some evidence that the environment of formation (e.g. metamorphic grade) influenced the (OH) incorporation with the greatest amounts of water detected in amphibolite facies rutiles. Rossman and Smyth (1990) documented I.R. spectra of Nb- and Cr-rich rutile from mantle eclogite xenoliths with intense absorption bands at 3300 and 3320 cm^{-1}. The rutile in the study of Rossman and Smyth (1990) contained substantially more (OH) (~0.7 wt.% H_2O) than an eclogitic rutile (0.08 wt.%) of Hammer and Beran (1991). Vlassopoulos *et al.* (1993) suggested that a combination of physicochemical environmental conditions (e.g. pressure, temperature and water activity, a_{H2O}) and the availability of substitutional cations could be responsible for variations in the (OH) contents of natural rutile. Vlassopoulos *et al.* (1993) examined rutiles derived from various mantle assemblages and concluded that mantle rutiles, like crustal rutiles, are typically hydrous, with the highest water concentration (0.8 wt.% H_2O) occurring in Nb- and Cr-rich rutile of metasomatic origin.

Despite many indirect observations that the substitution of water in rutile may be dependent on variables such as pressure, temperature and substitutional cations, no work has been done to establish possible links between H_2O concentrations and physicochemical conditions. The observations on iron and chromium substitution in rutile and their dependence on oxygen fugacity (for iron see Chapter 3 herein) have led to the use of high P-T experimental work and infra-red spectroscopy to confirm the presence of (OH) in synthetic rutiles. A series of high P-T experiments were performed with Cr-rich and Fe-rich TiO_2 compositions to test the effect of pressure, temperature and oxygen fugacity on the incorporation of water in rutile. The purpose of this chapter is: (i) to present experimental data of rutile assemblages, synthesized under controlled hydrous and anhydrous mantle P-T conditions in the presence (and absence) of trivalent and divalent cations; (ii) to introduce rutile as a possible geohygrometer, and (iii) to evaluate the role of rutile in recycling water from shallow to deep mantle conditions.

5.2 Experimental details

It should be noted that in the following sections, the term 'water' is loosely used to include all chemical forms of hydrogen. In this study, (OH) bound crystallographically in minerals is referred to as one form of 'water', and hydrogen, although occurring as (OH) in minerals and detected as such by infrared spectroscopy, is reported in terms of the charge-balanced oxide, H_2O.

5.2.1 Choice and preparation of experimental starting materials

Full details of the experimental starting mix preparation are described in Appendix A1. Five starting compositions, prepared from spectroscopically pure oxides, were used in this experimental study: pure TiO_2, $(TiO_2)_{0.9}$-$(Cr_2O_3)_{0.1}$, $(TiO_2)_{0.9}$-$(Fe_2O_3)_{0.1}$, $(TiO_2)_{0.9}$-$(Fe_3O_4)_{0.1}$ and $(TiO_2)_{0.9}$-$(FeO)_{0.1}$. One atmosphere data for the TiO_2-Cr_2O_3 system indicate that the $(TiO_2)_{0.9}$-$(Cr_2O_3)_{0.1}$ composition occurs as rutile + metastable $Ti_9Cr_2O_{21}$ at temperatures between 1200-1400 °C, and as metastable $Ti_9Cr_2O_{21}$ below ~1150 °C (e.g. Lee, 1970). At 1 atmosphere and 1100-1400 °C, the $(TiO_2)_{0.9}$-$(Fe_2O_3)_{0.1}$ composition is present as rutile + pseudobrookite (e.g. Lindsley, 1976a). Similarly, the $(TiO_2)_{0.9}$-$(Fe_3O_4)_{0.1}$ composition is present as $rutile_{ss}$ + $pseudobrookite_{ss}$ at 1400 °C and 1 atmosphere (e.g. MacChesney and Muan, 1959), and the $(TiO_2)_{0.9}$-$(FeO)_{0.1}$ composition also consists of rutile + pseudobrookite below ~1400 °C at 1 atm (e.g. Taylor, 1964).

The Cr_2O_3 and Fe_2O_3 compositions were initially selected to study the incorporation of trivalent cations and water into rutile as a function of pressure and temperature. Under the experimental conditions Cr_2O_3 was stable and Cr was present in the trivalent form. However, hematite requires relatively high oxygen fugacities ($fO_2 \geq$ HM) to be stable as a pure phase (e.g. Lindsley, 1991b). Under the experimental conditions employed here Fe_2O_3 was unstable and reduced to magnetite (see section 5.2.2). Thus, in order to avoid any internal redox reactions, the $(TiO_2)_{0.9}$-$(Fe_3O_4)_{0.1}$ mix prepared to control more accurately iron speciation and its substitution into rutile. The $(TiO_2)_{0.9}$-$(FeO)_{0.1}$ mix was used to investigate the incorporation of Fe and water into rutile as a function of oxygen fugacity at a constant temperature and pressure.

5.2.2 Experimental technique

All experiments were performed with a 0.5 inch (1.27 cm) piston-cylinder apparatus (e.g. Boyd and England, 1960) using techniques similar to those described by Green and Ringwood (1967). Run conditions varied from 1100 to 1400 °C at 20 kbar, and 1100 and 1300 °C at 5 kbar. Experiments using the TiO_2-Cr_2O_3 and TiO_2-Fe_3O_4 mixtures were carried out with single capsule, non-buffered assemblies (Appendix A4), whereas the

TiO_2-Fe_2O_3 mix experiments were performed with double capsule, buffered assemblies (Appendix A3). The 'buffer' material in these experiments, consisting of hematite in a nominally anhydrous environment, was used in an attempt to maintain all iron of the starting mix in the Fe^{3+} state. The observation that the hematite buffer was converted to magnetite on completion of the experiment indicated that reduction of the 'buffer' took place which would also have resulted in some ferric iron of the starting mix being reduced to Fe^{2+}. This reduction may have been caused by redox reaction with: (i) the graphite heater in the experimental assembly, or (ii) hydrogen generated by the dissociation of water in the inner starting mix capsule and diffusing through the capsule wall into the outer 'buffer' capsule. The experiments using the double capsule method with Fe_2O_3 in the outer capsule are referred to as HM-buffered. The single capsule runs with TiO_2-Fe_3O_4 starting material lie at an oxygen activity between WM and HM.

Experimental assemblages used outer sleeves of NaCl-pyrex as pressure media. Pressures with NaCl-sleeved assemblages in the 10-35 kbar range were estimated to have an accuracy of ±(1 % + 0.5) kbar (e.g. Mirwald *et al.*, 1975). Temperatures were monitored with $Pt/Pt_{90}Rh_{10}$ thermocouples and controlled to within ±10 °C of the desired values. Experiments were run for durations between 6 and 72 hours, with the run time depending on the temperature of the experiment.

The $(TiO_2)_{0.9}$-$(Cr_2O_3)_{0.1}$ mix experiments were undertaken under both hydrous and anhydrous conditions. For hydrous experiments pure H_2O was added to the sample (~5 to 10 wt.%). The TiO_2 and the Fe-rich TiO_2 experiments were performed under hydrous conditions only.

The $(TiO_2)_{0.9}$-$(FeO)_{0.1}$ mix experiments were conducted under hydrous conditions (~2.5 to 7 wt.% H_2O) at 1200 °C and 20 kbar using oxygen buffering techniques described in Appendix A3, and oxygen fucacity conditions for these experiments varied from IW to WM (see Appendix A3 for explanation of buffer abbreviations), corresponding to FMQ-4.0 to FMQ-1.0 log units. One $(TiO_2)_{0.9}$-$(FeO)_{0.1}$ mix experiment (T-4024) was conducted under nominally anhydrous, reducing (IW-~2.0 log units) conditions using an iron capsule.

5.2.3 Analytical details

Run products were optically examined under an immersion oil of accurately known refractive index (RI) to identify the mineral phases. Probe mounts of experimental run material were made using cold-set epoxy, and a high grade polish of the probe mounts was accomplished using successively finer grades of diamond polishing paste.

The mineral phases in the experimental runs were analysed at the University of Tasmania with a Cameca SX-50 electron probe microanalyser which was calibrated using natural mineral standards, and their concentrations were calculated from relative peak intensities using a PAP matrix correction procedure. Analytical conditions were 15 kV accelerating voltage, and a 20 nA beam current. A PET crystal was used for analysed Ti and Cr, and an LiF crystal was used to analyse Fe. The elements were analysed at 20 seconds on the peak and 10 seconds on the background. A detailed description of analytical procedures is given in Appendix B1.

Following the electron microprobe analyses, the polished sides of the probe mounts were attached to a glass slide (using superglue), and the mounts were cut and polished to between ~30-130 μm thickness to obtain a 'doubly-polished' section of the mineral grains. The resulting polished sections were removed from the glass slide using acetone, thus avoiding the need for spectra to be corrected by subtraction for the infrared effects of the glass and the mounting medium (c.f. Rossman and Smyth, 1990; Vlassopoulos *et al.*, 1993). Samples were dried at 120 °C for approximately two hours to remove any surface moisture, and samples were visually inspected to ensure that they were free of fluid inclusions. Fourier transform infrared (FTIR) absorption spectra of the experimental rutiles were obtained with a Brucker IFS 66 spectrometer connected to an optical microscope with a 40x objective lens, and equipped with an interactive operating system and software to perform a number of computing tasks (Appendix B3). Spectra acquisition on samples over the mid-I.R. region (4800-600 cm^{-1}) was obtained at a resolution of 4 cm^{-1}, and usually 128 scans on a sample and background were performed three to five times for each experimental run. A variable aperture attached to the optical microscope ensured that typical sample spot diameters ranged from 15 to 50 μm. The sample thickness of the areas where infrared spectra were taken was calculated to ±5 % from interference fringes generated by double reflection in samples (e.g. Osland, 1985 and Appendix B3).

The water contents of several experimental TiO_2-Cr_2O_3 and $(TiO_2)_{0.9}$-$(FeO)_{0.1}$ run products were determined using a Carlo Erba Elemental Analyser model EA 1108 with an accuracy of ±10 % (Appendix B5).

Powder X-ray diffraction (XRD) analyses (conducted at the Research School of Earth Sciences, ANU, Canberra) were used to confirm the mineralogy of several experimental phase assemblages for which analytical data had established compositional parameters.

5.3 Experimental results

5.3.1 Details of experimental results

Table 5.1 contains experimental details of all runs, including the mineral phases observed. Back-scattered electron images of a typical run product are presented in Figure 5.1.

The Cr-rich experiments showed a two-phase assembly consisting of abundant 'granular' rutile and smaller amounts of chromium oxide for all the subsolidus runs. One run (T-3918) was interpreted as having been performed under super-solidus conditions as deduced from the presence of a glass in the quench product. This experiment was not considered for any further investigations in this study. Rutiles were present as brown-orange to yellow pleochroic grains, whereas the chromium oxide was observed as emerald-green interstitial grains and inclusions in rutile. Optical examinations of the experimental run products suggested that the green chromium oxide was eskolaite. The grain size of rutile increased with increasing experimental temperature: at 1100 °C and 20 kbar the average length of rutile was estimated as 25-40 μm, whereas at 1400 °C and 20 kbar the average length was estimated at 75-100 μm. The modal amount of eskolaite in the run product decreased with increasing temperature from an estimated 5 % at 1100 °C to less than 3 % at 1400 °C. A powder X-ray diffraction analysis of experimental run products T-3917 and T-3919 identified ~98 modal % rutile, as well as a number of additional lines confirming the presence of eskolaite (Prof. D.H. Green, pers. comm.). Three Cr-rich experiments (T-3947, 3950 and 3953) were undertaken under anhydrous conditions. Run products from these experiments showed a 'welded' texture, and individual grain boundaries were difficult to detect. Rutile was present as brown-yellow weakly pleochroic grains and eskolaite was observed as small, dark green interstitial grains. The average grain size of rutile in the anhydrous runs was estimated at ~40-50 % of the grain size of rutiles in hydrous experiments synthesized under similar P-T conditions.

The Fe-rich experiments showed a two-phase assembly consisting of rutile and iron oxide, which was identified by electron microprobe analysis as ilmenite. Rutile from the Fe_2O_3-rich experiments was present as olive-green to brown pleochroic crystalline material, and ilmenite was observed in small modal amounts as a dark opaque phase displaying a weak response to an external magnetic field. For the Fe_3O_4-rich experiments, the run product consisted of light green to yellow-brown pleochroic rutile, and dark opaque interstitial ilmenite was present in small modal amounts. A powder X-ray diffraction analysis of experimental run products T-3922 (TiO_2-Fe_2O_3 starting mix) and

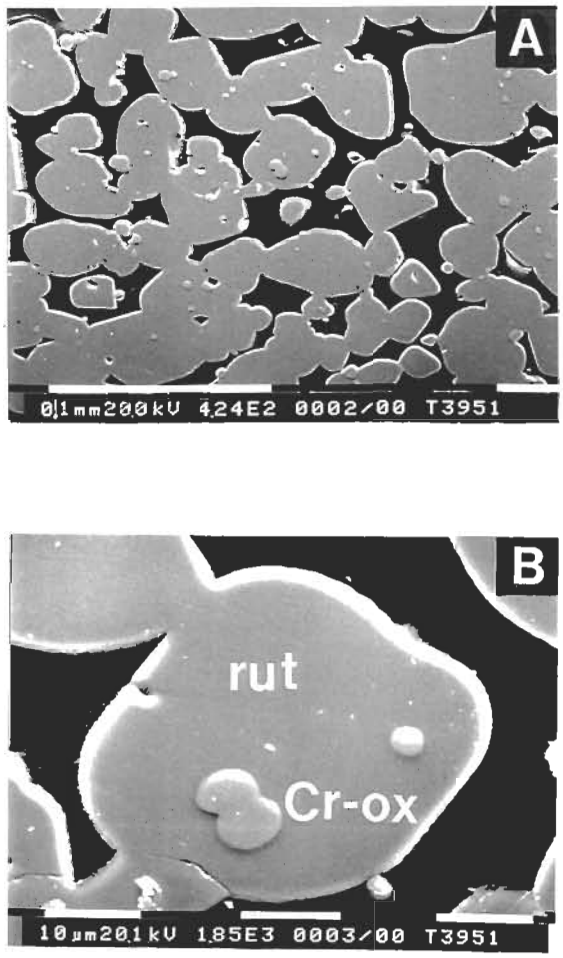

Figure 5.1: Back-scattered electron images of experimental products of $(TiO_2)_{0.9}$-$(Cr_2O_3)_{0.1}$ starting composition. (A) is experiment T-3951 (20 kbar, 1200 °C) showing large (~20-60 μm) rutile grains and small (~5-10 μm) chromium oxide grains. (B) is a magnified image of a dark grey rutile (rut) with three light grey chromium oxide (Cr-ox) inclusions. The white scale bar in (A) and (B) indicates 0.1 mm and 10 μm respectively.

Table 5.1: Details of Cr- and Fe-rich rutile experiments.

Run Number	Composition	H_2O (wt.%)	P (kbar)	T (°C)	Run time (hrs)	Phases	Comments
T-3916	$(TiO_2)_{0.9}$ - $(Cr_2O_3)_{0.1}$	9.9	20	1100	72	Rut+Cr-ox	
T-3917	$(TiO_2)_{0.9}$ - $(Cr_2O_3)_{0.1}$	10.0	20	1300	24	Rut+Cr-ox	
T-3918	$(TiO_2)_{0.9}$ - $(Cr_2O_3)_{0.1}$	5.2	5	1300	24	Rut+Cr-ox+Gl(?)	melting(?)
T-3919	$(TiO_2)_{0.9}$ - $(Cr_2O_3)_{0.1}$	5.3	5	1100	72	Rut+Cr-ox	
T-3951	$(TiO_2)_{0.9}$ - $(Cr_2O_3)_{0.1}$	10.9	20	1200	48	Rut+Cr-ox	
T-3954	$(TiO_2)_{0.9}$ - $(Cr_2O_3)_{0.1}$	5.8	20	1400	6	Rut+Cr-ox	
T-3973	$(TiO_2)_{0.9}$ - $(Cr_2O_3)_{0.1}$	10.6	20	1300	25	Rut+Cr-ox	repeat run
T-3947	$(TiO_2)_{0.9}$ - $(Cr_2O_3)_{0.1}$	(-)	20	1300	27	Rut+Cr-ox	
T-3950	$(TiO_2)_{0.9}$ - $(Cr_2O_3)_{0.1}$	(-)	20	1200	72	Rut+Cr-ox	
T-3953	$(TiO_2)_{0.9}$ - $(Cr_2O_3)_{0.1}$	(-)	20	1400	8	Rut+Cr-ox	
T-3933	TiO_2	9.8	20	1300	24	Rut	
T-3934	TiO_2	10.1	20	1100	72	Rut	
T-3920	$(TiO_2)_{0.9}$ - $(Fe_2O_3)_{0.1}$	10.0	20	1300	24	Rut+Ilm	
T-3921	$(TiO_2)_{0.9}$ - $(Fe_2O_3)_{0.1}$	9.7	20	1100	71	Rut+Ilm	
T-3922	$(TiO_2)_{0.9}$ - $(Fe_2O_3)_{0.1}$	5.3	5	1100	73	Rut+Ilm	
T-3932	$(TiO_2)_{0.9}$ - $(Fe_2O_3)_{0.1}$	10.0	20	1100	48	Rut+Ilm	repeat run
T-3925	$(TiO_2)_{0.9}$ - $(Fe_3O_4)_{0.1}$	10.0	5	1100	72	Rut+Ilm	
T-3926	$(TiO_2)_{0.9}$ - $(Fe_3O_4)_{0.1}$	5.1	20	1100	72	Rut+Ilm	
T-3927	$(TiO_2)_{0.9}$ - $(Fe_3O_4)_{0.1}$	9.5	20	1300	24	Rut+Ilm	
T-4022	$(TiO_2)_{0.9}$ - $(FeO)_{0.1}$	3.3	20	1200	24	Rut	IW buffer
T-4024	$(TiO_2)_{0.9}$ - $(FeO)_{0.1}$	(-)	20	1200	65	Rut+Ilm	Iron capsule
T-4026	$(TiO_2)_{0.9}$ - $(FeO)_{0.1}$	6.9	20	1200	24	Rut+Ilm	WCWO buffer
T-4028	$(TiO_2)_{0.9}$ - $(FeO)_{0.1}$	2.7	20	1200	24	Rut	WM buffer
T-4030	$(TiO_2)_{0.9}$ - $(FeO)_{0.1}$	7.3	20	1200	24	Rut+Ilm	GW buffer
T-4036	$(TiO_2)_{0.9}$ - $(FeO)_{0.1}$	2.4	20	1200	24	Rut+Ilm	WM buffer, repeat run
T-4037	$(TiO_2)_{0.9}$ - $(FeO)_{0.1}$	3.4	20	1200	24	Rut+Ilm	IW buffer, repeat run

Notes: Compositions are indicated as mol %. (-) indicates anhydrous experiments. Cr-ox indicates Ti-rich Cr_2O_3. T-3918 was not used in H_2O measurements. T-3973 was a repeat run for T-3917 to provide more run product for further study. T-3932 was a repeat run for T-3921. T-3950 and T-3953 were only analysed for cation contents. T-3936 was a repeat run for T-4028, and T-4037 was a repeat run for T-4022. Absence of ilmenite in T-4022 and T-4028 was interpreted as being due to Fe loss to the Pt capsule.

T-3925 (TiO_2-Fe_3O_4 starting mix) confirmed a rutile + ilmenite mineral phase assemblage in T-3925, and probable ilmenite in T-3922 as identified from very faint lines (Prof. D.H. Green, pers. comm.). Similarly, rutile from the FeO-rich experiments was observed as olive-green to yellow-brown pleochroic grains, and the coexisting ilmenite was present as interstitial and intergrown, opaque grains.

Two experiments were undertaken with the 100 % TiO_2 mix under hydrous conditions (T-3933 and T-3934). The run products showed large (~90-150 μm), slightly rounded, sapphire-blue rutiles. The grains were strongly pleochroic ranging from deep blue to yellow-brown.

5.3.2 Electron microprobe analyses

Electron microprobe analyses of mineral phases in the rutile experiments are presented in Table 5.2 and Table 5.3.

Chromium contents in rutiles synthesized under hydrous conditions increased with temperature and pressure. At 20 kbar, Cr_2O_3 ranges from 13.01 wt.% at 1100 °C to 15.34 wt.% at 1400 °C, whereas at 1100 °C the Cr_2O_3 content increases from 8.71 wt.% at 5 kbar to 13.01 wt.% at 20 kbar. Rutiles synthesized under nominally anhydrous conditions also showed chromium contents to increase with temperature: for the 20 kbar experiments, Cr_2O_3 contents increased from 14.64 wt.% at 1200 °C to 16.93 wt.% at 1400 °C. Recalculated as mol %, there is, within the accuracy of the analytical technique, little difference between the chromium contents of hydrous or anhydrous rutiles (Figure 5.2). One important difference between these rutiles lies in the analytical totals. Unless calculated water contents are included, the rutiles from the hydrous experiments show lower oxide totals (<99 wt.%) than the anhydrous rutiles (~100 wt.%).

Coexisting chromium oxide showed TiO_2 contents to increase with temperature and, to a smaller extent, with pressure. At 20 kbar, the chromium oxide contains 5.27 wt.% TiO_2 at 1100 °C and 6.54 wt.% at 1400 °C. At 1100 °C and 5 kbar the chromium oxide contains 5.12 wt.% TiO_2 whereas at 20 kbar the TiO_2 content is 5.27 wt.%. Under anhydrous conditions, TiO_2 contents of chromium oxide are similarly dependent on temperature, and at 20 kbar increases from 7.05 wt.% at 1200 °C to 7.65 wt.% at 1400 °C. Recalculated in terms of mol %, chromium oxides synthesized under hydrous conditions contain similar amounts of TiO_2 to anhydrous chromium oxides (Figure 5.2).

For the TiO_2-Fe_2O_3 and TiO_2-Fe_3O_4 experiments, analytical results of the rutiles are broadly similar to those of the chromium-rich experiments.

Table 5.2: Electron microprobe analyses of rutile experiments.

Run Number (P/T)	Rutile				Oxide		
	TiO_2 (wt. %)	Cr_2O_3 (wt. %)	H_2O_{calc} (wt. %)	Total (wt.%)	Cr_2O_3 (wt. %)	TiO_2 (wt. %)	Total (wt.%)
T-3916 (20/1100)	85.85 (0.12)	13.01 (0.04)	1.54	100.40	94.73 (0.54)	5.27 (0.32)	100.00
T-3917/3973 (20/1300)	84.11 (0.26)	14.36 (0.22)	1.70	100.17	93.70 (0.05)	6.04 (0.68)	99.74
T-3918 (5/1300)	91.41 (0.37)	7.47 (0.23)	0.89	99.77	(n.a.)	(n.a.)	
T-3919 (5/1100)	90.22 (0.39)	8.71 (0.09)	1.03	99.96	97.32 (0.26)	5.12 (0.47)	102.44
T-3951 (20/1200)	84.26 (0.31)	13.63 (0.10)	1.62	99.51	94.99 (0.35)	5.74 (0.57)	100.73
T-3954 (20/1400)	81.90 (0.27)	15.34 (0.14)	1.82	99.06	93.74 (0.49)	6.64 (0.58)	100.38
T-3947 (20/1300)	83.27 (0.38)	16.68 (0.49)	(anh)	99.95	94.42 (0.53)	7.45 (0.41)	101.87
T-3950 (20/1200)	85.32 (0.19)	14.64 (0.22)	(anh)	99.96	94.76 (0.88)	7.05 (0.78)	101.81
T-3953 (20/1400)	83.14 (0.41)	16.93 (0.33)	(anh)	100.07	94.63 (0.41)	7.65 (0.56)	102.29

Notes: Experiments T-3916 - T-3953 are TiO_2-Cr_2O_3 mix runs. Values in parentheses indicate standard deviations.

Table 5.2 continued: Electron microprobe analyses of rutile experiments.

Run Number (P/T)	TiO_2 (wt. %)	Fe_2O_3 (wt. %)	H_2O_{calc} (wt. %)	Total (wt.%)	FeO (wt. %)	Fe_2O_3 (wt. %)	TiO_2 (wt. %)	Total (wt.%)	$Fe^{3+}/\Sigma Fe$
T-3933 (20/1300)	98.43	(n.d.)	(-)	98.43	(n.d.)	(n.d.)	(n.d.)	(n.d.)	(n.d.)
	(0.11)								
T-3934 (20/1100)	98.48	(n.d.)	(-)	98.48	(n.d.)	(n.d.)	(n.d.)	(n.d.)	(n.d.)
	(0.34)								
T-3920 (20/1300)	90.43	8.38	0.85	99.66	34.30	29.20	38.17	101.67	0.434
	(0.25)	(0.05)			(0.26)	(0.22)	(0.68)		
T-3921 (20/1100)	89.69	8.87	0.90	99.46	19.79	56.54	22.01	98.34	0.720
	(0.18)	(0.15)			(0.10)	(0.28)	(0.43)		
T-3922 (5/1100)	94.11	4.86	0.49	99.46	37.50	22.40	41.74	101.64	0.350
	(0.20)	(0.09)			(0.19)	(0.13)	(0.20)		
T-3932 (20/1100)	88.62	8.78	0.89	98.29	18.66	59.47	20.75	98.88	0.741
	(0.25)	(0.08)			(0.13)	(0.42)	(0.60)		
T-3925 (5/1100)	97.44	3.13	0.32	100.89	41.82	12.47	46.51	100.80	0.212
	(0.09)	(0.02)			(0.10)	(0.03)	(0.13)		
T-3926 (20/1100)	95.26	5.13	0.52	100.91	38.32	19.49	42.62	100.43	0.314
	(0.24)	(0.07)			(0.10)	(0.05)	(0.17)		
T-3927 (20/1300)	94.97	5.17	0.52	100.66	40.31	14.76	44.83	99.90	0.248
	(0.30)	(0.11)			(0.55)	(0.20)	(0.94)		

Notes: Experiments T-3933 & 3934 are TiO_2 mix runs; T-3920-3922 & 3932 are TiO_2-Fe_2O_3 mix runs; T-3925-3927 are TiO_2-Fe_3O_4 mix runs. Further experimental details are shown in Table 5.1. Values in parentheses represent standard deviations. (n.a.) indicates not analysed; (anh) indicates an anhydrous experiment; (-) indicates not calculated from mineral stoichiometry and (n.d.) indicates mineral phase not detected. Fe_2O_3 contents of rutiles are recalculated from FeO. H_2O (wt. %) is calculated using the assumption that all water in rutile is contained as CrO(OH) or, where linked to Fe_2O_3, as FeO(OH).

Table 5.3: Electron microprobe analyses of oxygen buffered rutile experiments at 20 kbar and 1200 °C using the TiO_2-FeO starting mix.

	Rutile			Oxide						
Run Number (buffer)	TiO_2 (wt. %)	Fe_2O_3 (wt. %)	Total (wt.%)	FeO (wt. %)	Fe_2O_3 (wt. %)	TiO_2 (wt. %)	Ti_2O_3 (wt. %)	Total (wt.%)	$Fe^{3+}/\sum Fe$	$Ti^{3+}/\sum Ti$
T-4022 (IW)	97.58 (0.44)	1.88 (0.07)	99.46	(n.d.)	(n.d.)	(n.d.)	(n.d.)	(n.d.)	(n.d.)	(n.d.)
T-4024 (IW)	99.35 (0.49)	0.14 (0.07)	99.49	43.74 (0.25)	(-)	48.64 (0.16)	8.69 (0.04)	101.07	(-)	0.165
T-4026 (WCWO)	97.83 (0.50)	1.87 (0.09)	99.70	46.86 (0.48)	(-)	52.11 (0.40)	1.85 (0.02)	100.82	(-)	0.038
T-4028 (WM)	96.26 (0.79)	3.07 (0.27)	99.33	(n.d.)	(n.d.)	(n.d.)	(n.d.)	(n.d.)	(n.d.)	(n.d.)
T-4030 (GW)	97.53 (0.84)	2.00 (0.08)	99.53	47.78 (0.03)	0.19 (0.01)	53.13 (0.14)	(-)	101.10	0.004	(-)
T-4036 (WM)	97.50 (0.44)	2.20 (0.11)	99.70	47.28 (0.17)	1.38 (0.02)	52.58 (0.15)	(-)	101.24	0.026	(-)
T-4037 (IW)	99.72 (0.53)	0.30 (0.03)	100.02	42.18 (0.33)	(-)	46.91 (0.29)	11.41 (0.08)	100.50	(-)	0.213

Notes: Experimental details are shown in Table 5.1. Fe_2O_3 contents of rutiles are recalculated from FeO. Values in parentheses represent standard deviations. (n.d.) indicates mineral phase not detected and (-) indicates not calculated from mineral stoichiometry.

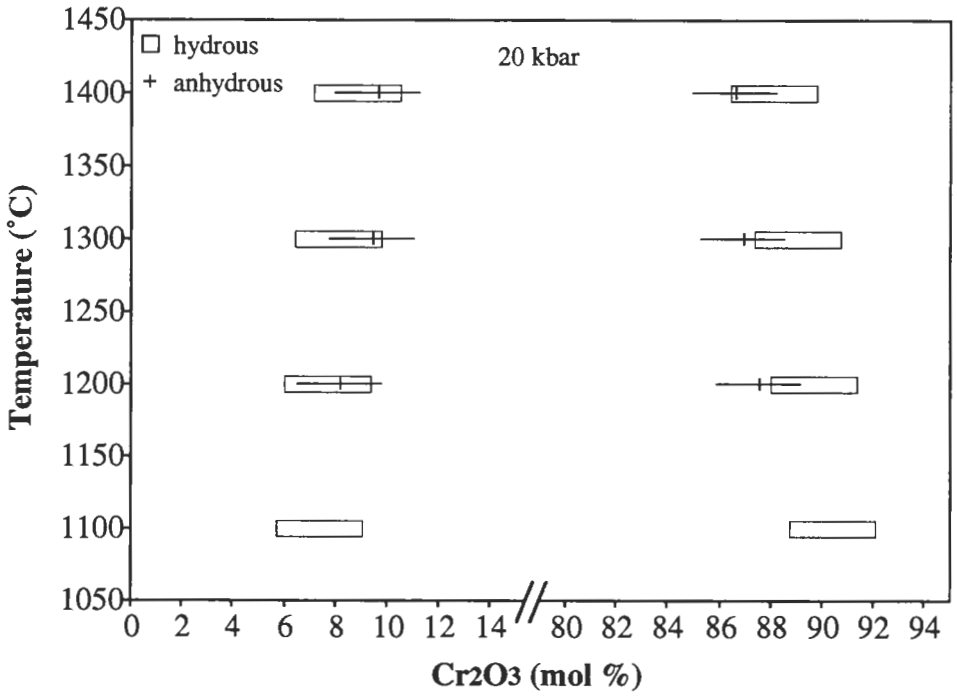

Figure 5.2: The Cr_2O_3 content of experimental rutiles (expressed as mol %) at 20 kbar for temperatures from 1100 to 1400 °C. Results are shown for hydrous and nominally anhydrous experiments. The width of the symbols denotes the standard deviation in the Cr_2O_3 content of the rutiles.

The iron content of rutiles, expressed as Fe_2O_3, increases with increasing pressure: at 1100 °C, rutiles synthesized from the TiO_2-Fe_2O_3-H_2O mix at 5 kbar contain 4.86 wt.% and at 20 kbar contain 8.87 wt.% Fe expressed as Fe_2O_3. There is no obvious temperature effect on Fe_2O_3 content. For example, rutiles synthesized at 1300 °C and 20 kbar contain 8.38 wt.% Fe expressed as Fe_2O_3. As noted previously, these experiments are considered to be buffered on fO_2 at the HM buffer.

The effect of oxidation state is an important factor in the substitution of cations into the rutile structure. For example, the iron content of rutiles synthesized from the TiO_2-Fe_3O_4-H_2O mix is lower than that in rutiles synthesized under similar P-T conditions from the TiO_2-Fe_2O_3-H_2O mix. At 1100 °C and 5 kbar, rutiles contain 3.13 wt.% Fe expressed as Fe_2O_3, whereas at 20 kbar at the same temperature the rutiles contain 5.13 wt.% Fe expressed as Fe_2O_3. At 20 kbar and 1300 °C, rutiles in the TiO_2-Fe_3O_4-H_2O system contain 5.17 wt.% Fe expressed as Fe_2O_3.

The redox ratio, $Fe^{3+}/\sum Fe$, calculated from electron microprobe analyses assuming mineral stoichiometry (see Chapter 2 herein), of coexisting ilmenites ranges from 0.72-0.74 for the TiO_2-Fe_2O_3 experiments and 0.21-0.31 for the TiO_2-Fe_3O_4 experiments. However, two TiO_2-Fe_2O_3 experiments (T-3920 and T-3922) have ilmenites with lower redox ratios at 0.43 and 0.35 respectively, which may reflect a response to the reduction of the hematite 'buffer' to magnetite. The effects of such reduction processes appear to be less pronounced in the mineral chemistry of coexisting rutiles (Table 5.2), although it should be noted that rutiles synthesized from the TiO_2-Fe_2O_3 mix at 1300 °C and 20 kbar have approximately 0.5 wt.% Fe_2O_3 less than rutiles synthesized at 1100 °C and 20 kbar. This is in contrast with the data from the TiO_2-Cr_2O_3 experiments where rutiles synthesized at higher temperatures contain more Cr_2O_3 than rutiles synthesized at lower temperatures at the same pressures (Figure 5.2).

Analytical data from the $(TiO_2)_{0.9}$-$(FeO)_{0.1}$ controlled oxygen buffer experiments confirm a positive correlation between increasing oxygen fugacity and cation substitution into the rutile structure (Figure 5.3A). Rutiles synthesized at 20 kbar and 1200 °C under hydrous and IW buffer conditions contain 0.30 wt.% Fe_2O_3 (T-4037), whereas rutiles synthezised at the same P,T conditions but under nominally anhydrous, reducing conditions using the iron capsule (T-4024) contain 0.14 wt.% Fe_2O_3. Rutiles synthesized at 20 kbar and 1200 °C under WCWO (T-4026), GW (T-4030) and WM (T-4036) buffer conditions contain 1.87 wt.%, 2.00 wt.% and 2.20 wt.% Fe_2O_3 respectively. Two initial experiments (T-4022 and T-4028) were also conducted at 20 kbar and 1200 °C under IW and WM conditions respectively.

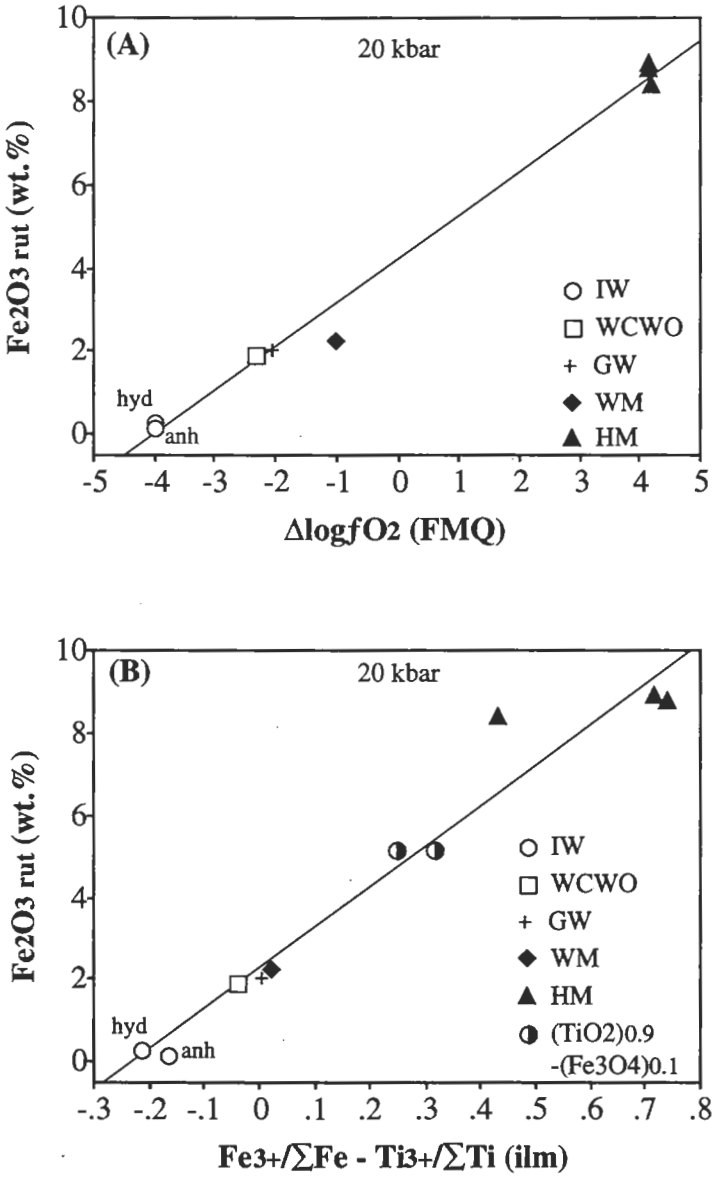

Figure 5.3: The iron content (expressed as Fe_2O_3 in wt.%) of experimental rutiles synthesized under controlled oxygen fugacity conditions at 20 kbar. (A) Fe_2O_3 rut (wt.%) against $\Delta\log fO_2$ (FMQ) of the experiment, showing a line of best fit. The regression coefficient of the line of best fit equals 0.99. 'hyd' indicates results for the IW experiment undertaken under hydrous conditions, and 'anh' indicates results for the anhydrous IW experiment. (B) Fe_2O_3 rut (wt.%) against the ilmenite redox value, $Fe^{3+}/\Sigma Fe$ - $Ti^{3+}/\Sigma Ti$ (ilm) for coexisting rutile-ilmenite mineral pairs. This diagram includes analytical data from the single capsule, unbuffered TiO_2-Fe_3O_4 experiments, indicating that these experiments approached oxidation conditions between WM and HM. The regression coefficient of the line of best fit as shown is 0.95.

In these experiments, however, the run product consisted of rutile only. The absence of coexisting ilmenite is believed to be the consequence of iron loss from the starting mix to the surrounding Pt metal capsule, with an ensuing increase in the oxygen activity. As a result of the 'internal' redox reaction, rutiles in these two runs have significantly higher iron contents than rutiles from equivalent buffer experiments where ilmenite was a co-product, with 1.88 wt.% Fe_2O_3 for T-4022 (cf. 0.30 wt.%) and 3.07 wt.% Fe_2O_3 for T-4028 (cf. 2.20 wt.%).

Ilmenites coexisting with rutiles synthesized from the $(TiO_2)_{0.9}$-$(FeO)_{0.1}$ starting mix under GW (T-4030) and WM (T-4036) oxidation conditions contain 0.19 and 1.38 wt.% Fe_2O_3 respectively, with redox ratios, $Fe^{3+}/\sum Fe$, of 0.004 and 0.026. Ilmenites from reduced experiments with oxygen fugacities below WCWO buffer conditions (T-4024, T-4026 and T-4037) have high analytical oxide totals, and from low cation totals appear non-stoichiometric unless Ti_2O_3 is calculated. Assuming that all iron in these reduced ilmenites is present as Fe^{2+}, titanium is present as Ti^{3+} and Ti^{4+}, and the ilmenites are stoichiometric with two cations per three anions, the Ti_2O_3 contents calculated are 8.69 wt.%, 1.85 wt.% and 11.41 wt.% for T-4024, T-4026 and T-4037 respectively (Table 5.3). The $Ti^{3+}/\sum Ti$ ratio for these reduced ilmenites ranges from 0.213 (T-4037) to 0.038 (T-4026).

The oxidation effect on the substitution of cations into the rutile structure is further illustrated by a positive correlation between the iron content of experimental rutile and the resultant redox value, $Fe^{3+}/\sum Fe$ - $Ti^{3+}/\sum Ti$, of coexisting ilmenite (Figure 5.3B). It can be seen that the total iron content of experimental rutile (expressed as Fe_2O_3) increases linearly with an increasing ilmenite redox value, from 0.30 wt.% Fe_2O_3 at a calculated redox value of -0.21 for IW conditions, to 8.87 wt.% Fe_2O_3 at a calculated redox value of 0.72 at HM conditions. These observations suggest that the measure of total iron substitution into the rutile structure is strongly dependent on oxygen fugacity conditions and the valency state of iron. With increasing oxygen fugacity, iron in rutile will increasingly manifest itself as Fe^{3+}, and the rutile redox ratio, $Fe^{3+}/\sum Fe$, will thus increase.

5.3.3 I.R. spectroscopy of synthetic rutiles

The positions and relative intensities (in terms of integrated absorbance) of the absorption bands of the experimental rutiles in the mid I.R.-region infrared spectroscopy are given in Table 5.4, and representative spectra are shown in Figure 5.4.

Table 5.4: IR absorption in experimental rutile in the 3250 cm^{-1} region.

Run Number	(a) υ_{OH} (cm^{-1})	(b) t (μm)	(c) abs (cm^{-2})	(d) abs/t ($x10^4$ cm^{-3})	(e) $H_2O_{calc(i)}$ (wt.%)	(f) $H_2O_{calc(ii)}$ (wt.%)	(g) H_2O_{meas} (wt.%)
T-3916	3239	128 (2)	413.3 (15.6)	3.23	2.09 (0.06)	0.91 (0.03)	1.15
T-3917 / 73	3244	65 (3)	305.3 (17.9)	4.70	3.03 (0.17)	1.31 (0.07)	1.42
T-3919	3246	116 (2)	188.7 (35.6)	1.63	1.05 (0.18)	0.45 (0.08)	0.84
T-3951	3237	39 (7)	147.3 (12.4)	3.78	2.48 (0.35)	1.07 (0.15)	1.31
T-3954	3235	37 (5)	189.6 (29.3)	5.12	3.26 (0.18)	1.41 (0.08)	1.71
T-3947	(n.d)	(n.d)	(n.d)	(-)	(-)	(-)	(-)
T-3953	(-)	(-)	(-)	(-)	(-)	(-)	0.00
T-3933	(n.d)	(n.d)	(n.d)	(-)	(-)	(-)	(-)
T-3934	(n.d)	(n.d)	(n.d)	(-)	(-)	(-)	(-)
T-3920	3250	78 (6)	183.6 (1.0)	2.35	1.53 (0.12)	0.66 (0.05)	(-)
T-3921	3250	66 (3)	127.4 (11.8)	1.93	1.25 (0.11)	0.54 (0.05)	(-)
T-3922	3250	54 (4)	65.0 (9.1)	1.20	0.77 (0.06)	0.33 (0.03)	(-)
T-3932	3250	40 (3)	72.0 (14.2)	1.80	1.18 (0.27)	0.51 (0.12)	(-)
T-3925	3255	40 (5)	17.4 (4.8)	0.44	0.28 (0.06)	0.12 (0.03)	(-)
T-3926	3255	76 (1)	53.8 (10.0)	0.71	0.46 (0.08)	0.20 (0.04)	(-)
T-3927	3253	77 (6)	69.0 (10.0)	0.90	0.59 (0.13)	0.26 (0.05)	(-)
T-4022	3281	41 (3)	35.9 (7.0)	0.88	0.57 (0.09)	0.25 (0.04)	0.53
T-4024	(n.d)	(n.d)	(n.d)	(-)	(-)	(-)	0.00
T-4026	(n.d)	(n.d)	(n.d)	(-)	(-)	(-)	0.00
T-4028	3281	45 (3)	41.1 (6.6)	0.91	0.58 (0.08)	0.25 (0.03)	0.52
T-4030	3279	27 (2)	17.4 (2.3)	0.64	0.42 (0.06)	0.18 (0.03)	0.39
T-4036	3281	45 (3)	30.3 (4.1)	0.67	0.44 (0.06)	0.19 (0.02)	(-)
T-4037	(n.d)	(n.d)	(n.d)	(-)	(-)	(-)	0.00

Notes: Experimental details are shown in Table 5.1. Values in parentheses represent standard deviations. (-) indicates not analysed and (n.d.) indicates not detected. υ_{OH} (cm^{-1}) is position of OH peak; t (μm) is sample thickness; abs (cm^{-2}) is integrated absorbance; abs/t ($x10^4$ cm^{-3}) is the ratio of absorbance to sample thickness as a measure of water content; $H_2O_{calc(i)}$ is the water content calculated from I.R. absorption using the integral molar extinction coefficient (ε^* = 6540 L mol^{-1} cm^{-1}) of Hammer (1988); $H_2O_{calc(ii)}$ is the water content calculated from I.R. absorption using a value of ε^* = 15100 L mol^{-1} cm^{-1} of Johnson et al. (1973); H_2O_{meas} is the water content determined by elemental analyses (see text for explanation).

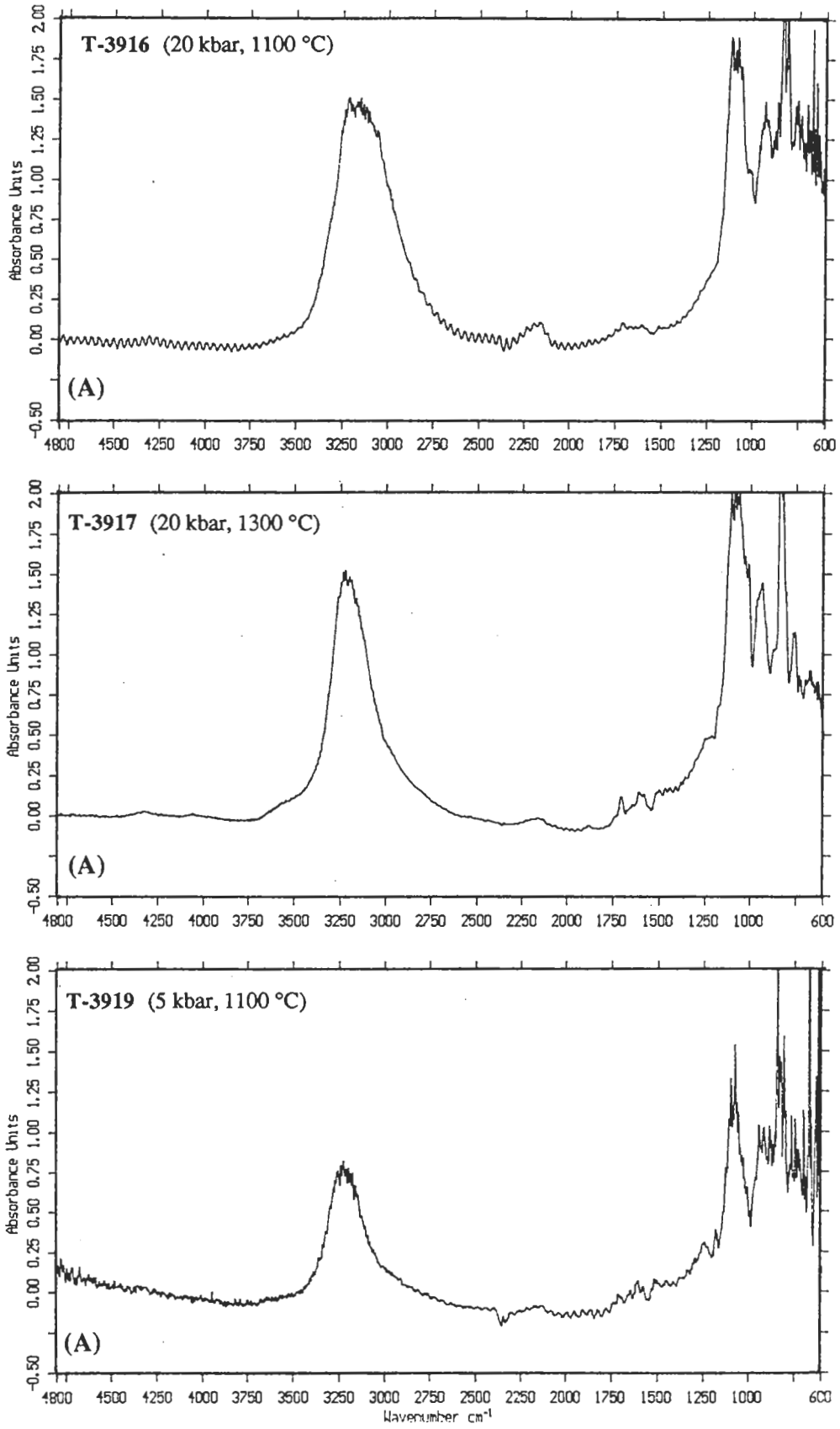

Figure 5.4: I.R. absorption spectra of experimental rutiles. See Table 5.1 for experimental details. (A) Cr-bearing rutiles synthesized in the TiO_2-Cr_2O_3 system under water saturated conditions.

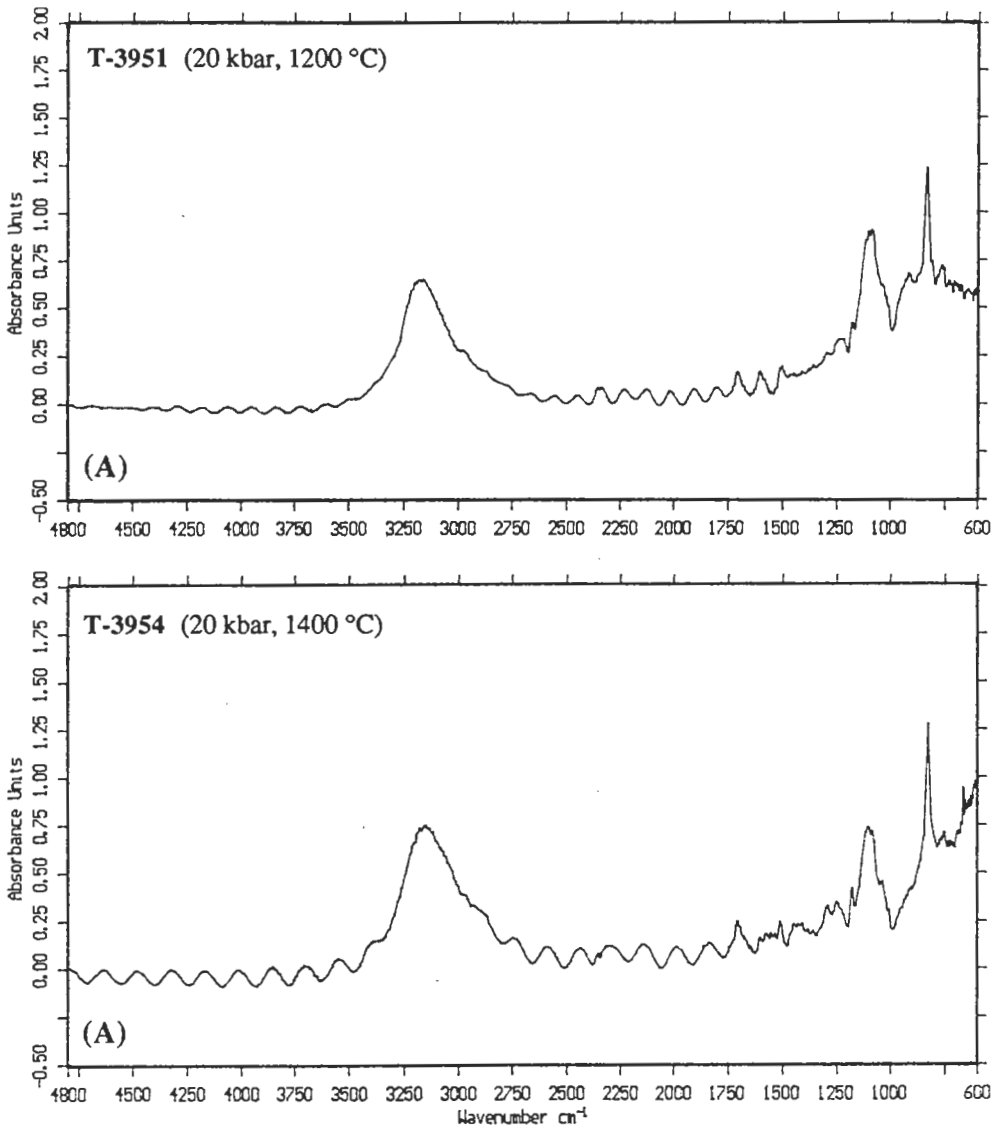
T-3951 (20 kbar, 1200 °C)
(A)
T-3954 (20 kbar, 1400 °C)
(A)
Absorbance Units
Wavenumber cm-1
4800 4500 4250 4000 3750 3500 3250 3000 2750 2500 2250 2000 1750 1500 1250 1000 600
-0.50 0.00 0.25 0.50 0.75 1.00 1.25 1.50 1.75 2.00

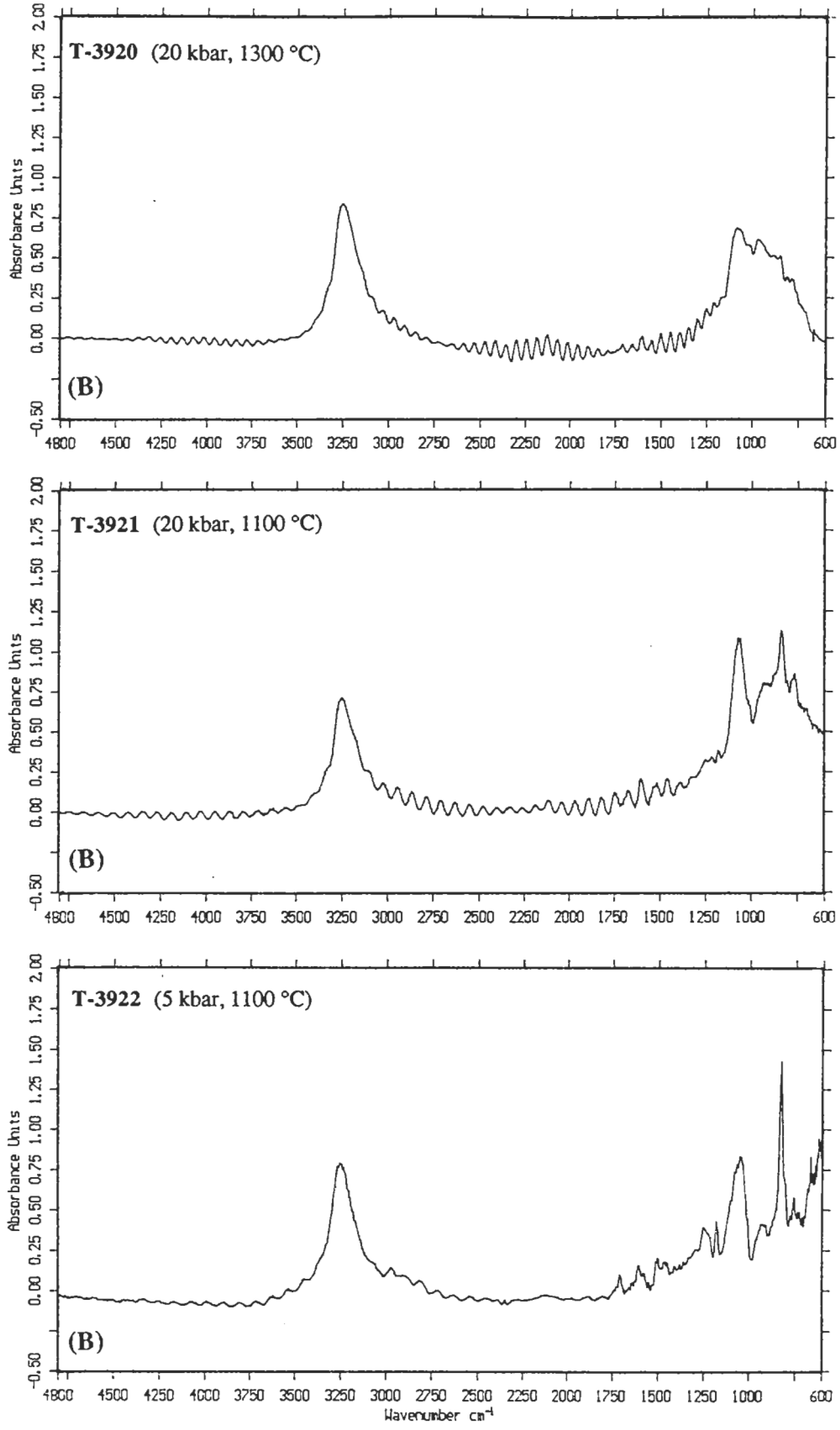

Figure 5.4: Continued. (B) Fe-bearing rutiles synthesized in the TiO_2-Fe_2O_3 system under water saturated conditions.

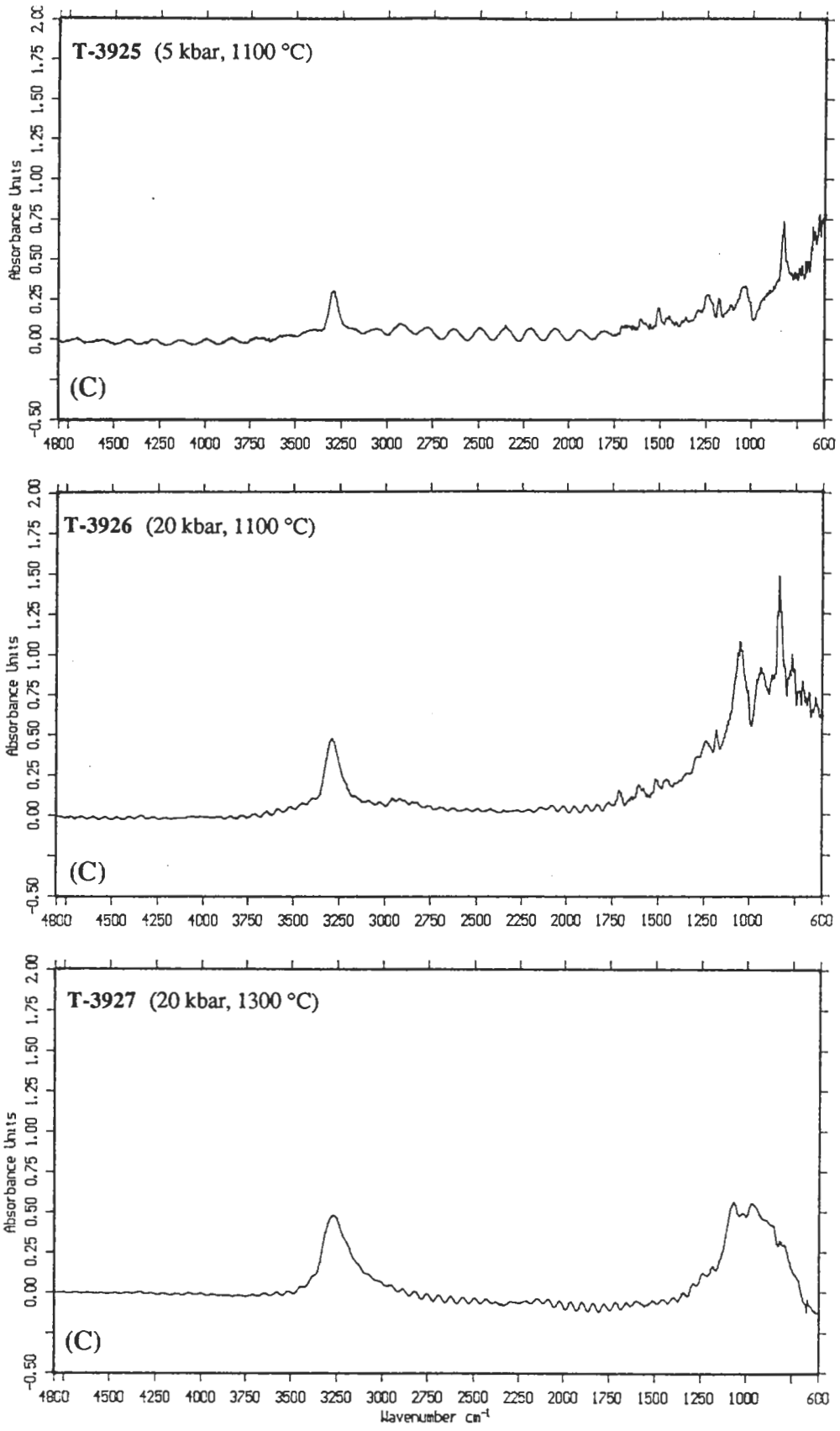

Figure 5.4: Continued. (C) Fe-bearing rutiles synthesized in the TiO_2-Fe_3O_4 system under water saturated conditions.

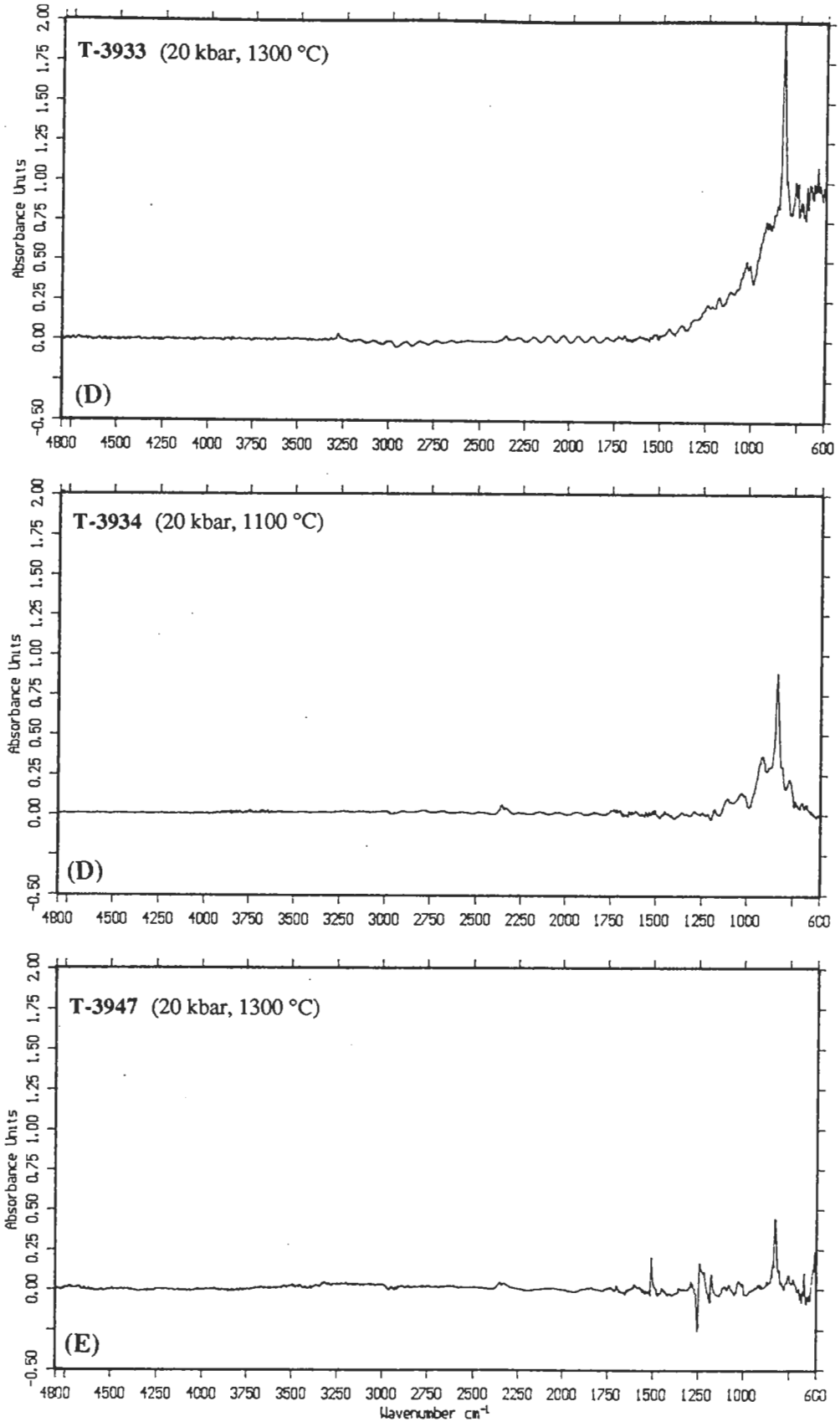

Figure 5.4: Continued. (D) Rutiles synthesized in the TiO_2 system under water saturated conditions. (E) Cr-bearing rutile synthesized in the TiO_2-Cr_2O_3 system under nominally anhydrous conditions.

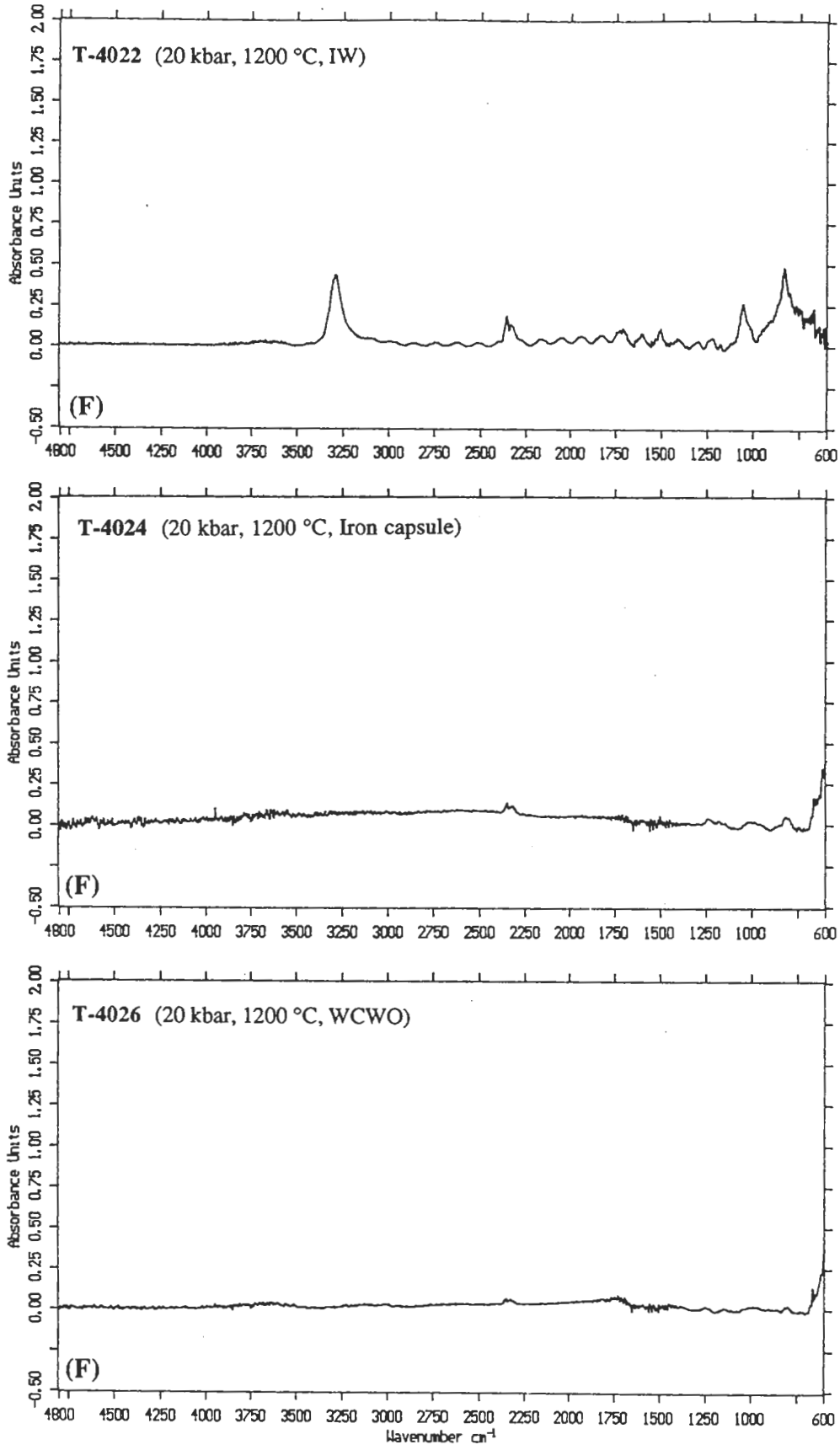

Figure 5.4: Continued. (F) Rutiles synthesized in the TiO_2-FeO system under controlled oxygen buffer conditions. See the text for explanation.

Note: where observed, the small I.R. peak at 2300 cm^{-1} is due to atmospheric CO_2.

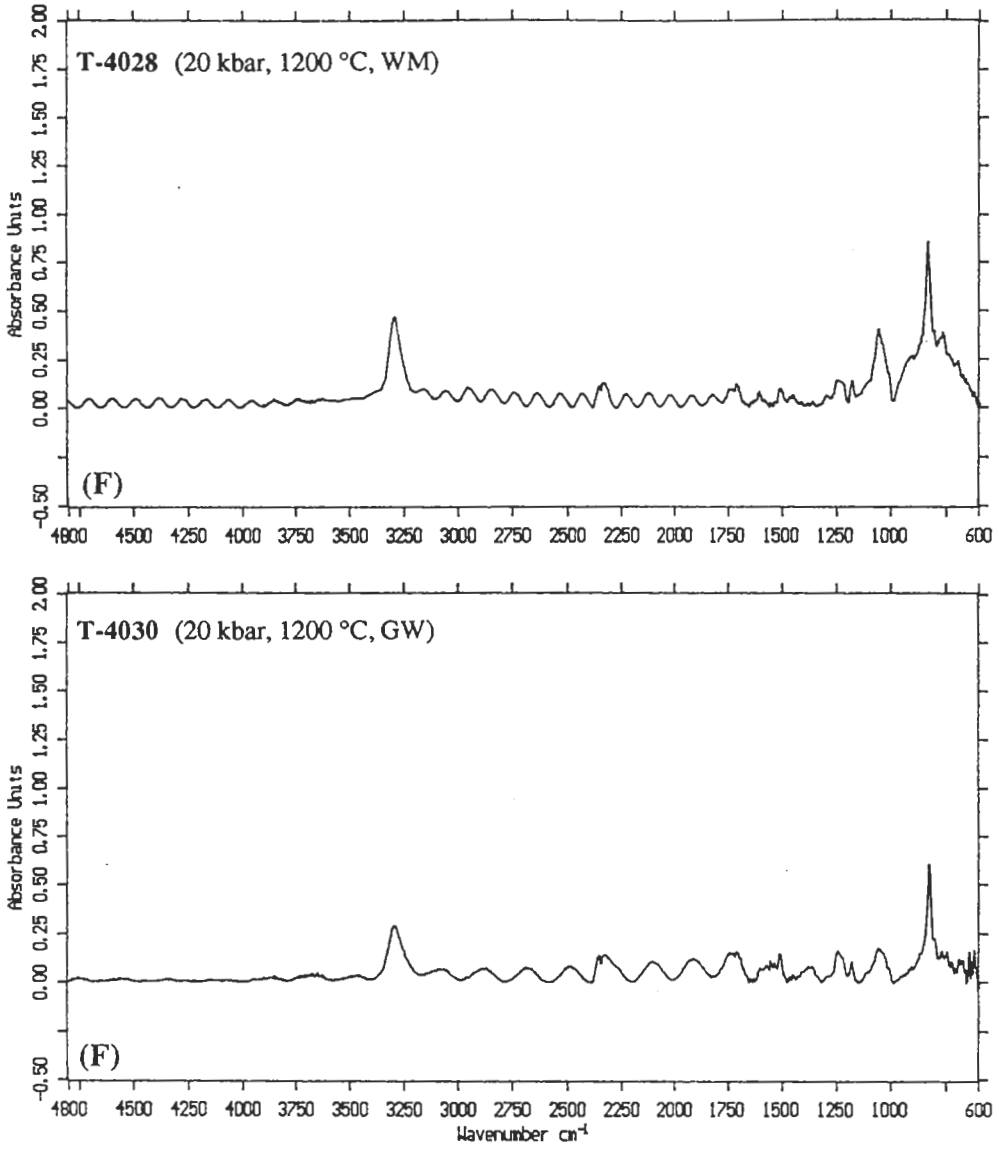
T-4028 (20 kbar, 1200 °C, WM)
(F)
T-4030 (20 kbar, 1200 °C, GW)
(F)
Absorbance Units
2.00
1.75
1.50
1.25
1.00
0.75
0.50
0.25
0.00
-0.50
4800 4500 4250 4000 3750 3500 3250 3000 2750 2500 2250 2000 1750 1500 1250 1000 600
Wavenumber cm-1

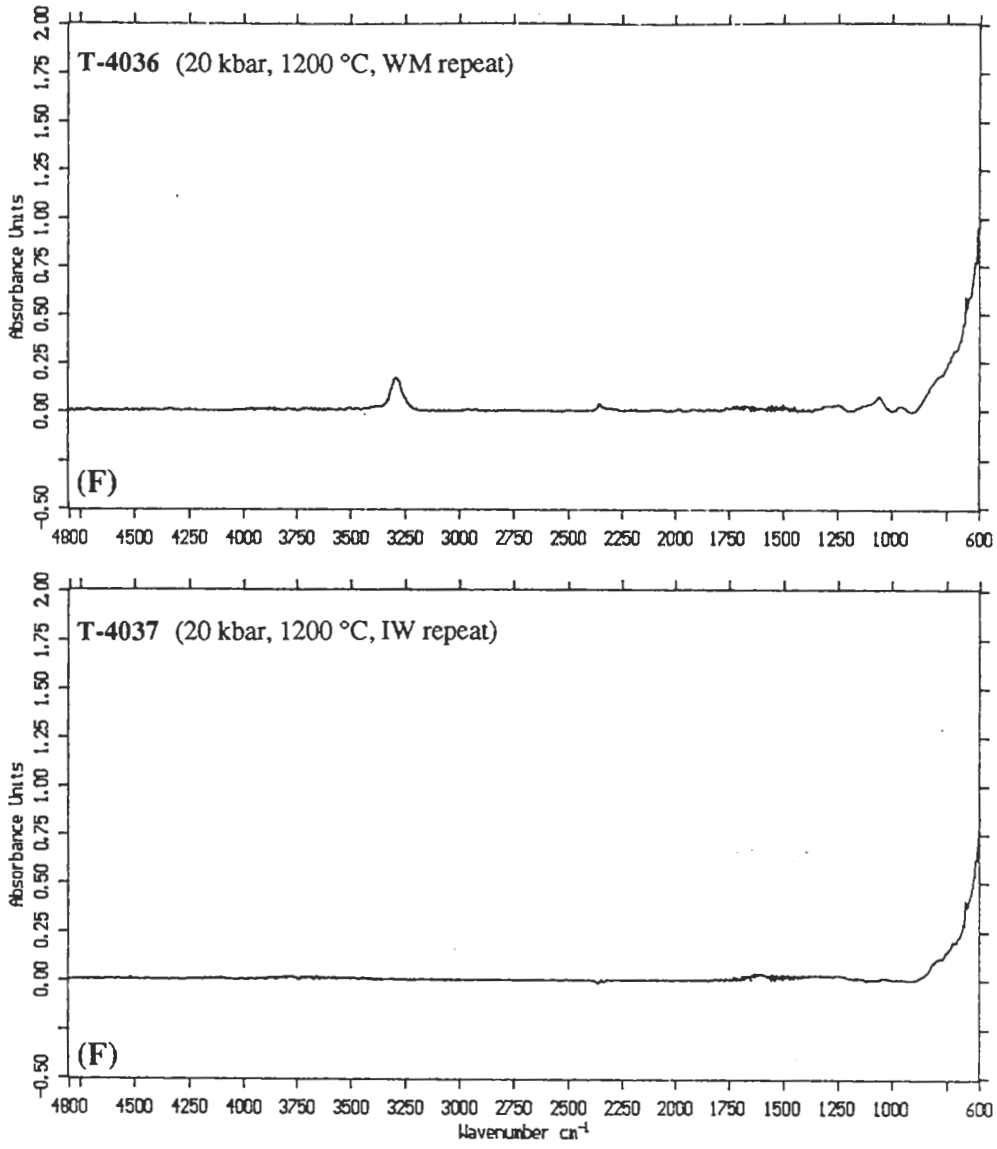
T-4036 (20 kbar, 1200 °C, WM repeat)
(F)
T-4037 (20 kbar, 1200 °C, IW repeat)
(F)
Absorbance Units
-0.50
0.00
0.25
0.50
0.75
1.00
1.25
1.50
1.75
2.00
4800
4500
4250
4000
3750
3500
3250
3000
2750
2500
2250
2000
1750
1500
1250
1000
600
Wavenumber cm-1

The chromium-bearing rutiles synthesized from the TiO_2-Cr_2O_3-H_2O mix typically show a single, broad band with the peak at ~3240 cm^{-1} assigned to simple symmetric and asymmetric O-H stretching. The ratio of integrated absorbance/sample thickness (abs/t) as a measure of H_2O content (Table 5.4 - column (d)) increases with increasing pressure and temperature. In some spectra a weak band at ~1650 cm^{-1} can be observed and has previously been interpreted as being due to a H-O-H bending frequency (e.g. Gadsden, 1975). In the fingerprint region (<1500 cm^{-1}) a distinctive single sharp band at ~1070 cm^{-1} is assigned to M-O-H (where M indicates a metal cation) bending (e.g. Gadsden, 1975). Additional sharp but relatively weak bands in this area can be assigned to either a hydroxyl bending or stretching frequency, or a M-O stretching frequency (e.g. Gadsden, 1975).

The iron-bearing rutiles show similar I.R. spectra to those of the Cr-rich rutiles. Rutiles synthesized from the TiO_2-Fe_2O_3-H_2O mix show a single, broad band with the peak at ~3250 cm^{-1}, whereas rutiles from the TiO_2-Fe_3O_4-H_2O system show single, sharp bands with a peak at ~3255 cm^{-1}. Weak bands assigned to bending and/or weak stretching frequencies are also occasionally discernible around ~1650 cm^{-1}, and in the finger print region. The bands recorded by the iron-rich rutiles have abs/t ratios that correlate positively with pressure, temperature and cation content (i.e. FeO_{total}). However, the I.R. bands from rutiles in the TiO_2-Fe_3O_4-H_2O system have much smaller abs/t ratios than rutiles from equivalent P-T experiments in the TiO_2-Fe_2O_3-H_2O system.

Infrared spectra of the oxygen buffered TiO_2-FeO experiments show similar absorptions to the spectra of the other Fe-bearing and Cr-bearing rutiles. Where detected, the rutiles from the TiO_2-FeO starting mix show a single band at ~3280 cm^{-1}. Some of the stronger I.R. responses also show a weak band at ~1650 cm^{-1} (H-O-H bending frequency) and ~1070 cm^{-1} (M-O-H bending frequency). At constant P-T conditions (20 kbar, 1200 °C), the abs/t ratio of experimental rutiles synthesized under controlled oxygen buffer conditions show an increase with increasing oxygen fucacity (Table 5.4 - column (d)). Rutiles synthesized under oxygen fugacities below WCWO buffer conditions showed no evidence of I.R. absorption bands due to O-H stretching and bending, and rutiles from the nominally anhydrous, experiment using the iron capsule (T-4024) also failed to indicate any O-H group I.R. spectroscopic response. Aside from a flat I.R. spectrum over the 4800 - 1500 cm^{-1} range, these rutiles only show weak bands in the fingerprint region, which may be assigned to M-O stretching.

The pronounced I.R. absorption bands due to O-H stretching (~3250 cm^{-1}) and bending (~1070 cm^{-1}) observed in the chromium- and iron-bearing TiO_2-H_2O systems are not

observed in rutiles from the nominally anhydrous TiO_2-Cr_2O_3 system (T-3947) or in rutiles from the hydrous TiO_2 system (T-3933 and T-3934). Rather, these rutile spectra show flat I.R. response over the 4800 - 1500 cm^{-1} range, and several weak bands in the fingerprint region, which may be assigned to M-O stretching.

5.3.4 Determination of H_2O concentrations in rutile from I.R. measurements and elemental analyses

The concentration of water in rutile can be determined from I.R. measurements using a modified Beer-Lambert law according to:

$$c = 18.02 \times abs / (\rho \times t \times \varepsilon^*) \qquad (5.1)$$

where c is the concentration in weight fraction, abs is the integrated absorbance (in cm^{-1}), ρ is the density (in g L^{-1}), t is the sample thickness (in cm) and ε^* is the integrated molar absorptivity (in L mol^{-1} cm^{-2}). This approach has been used previously in studies of H_2O in rutile (e.g. Johnson *et al.*, 1973; Hammer and Beran, 1991; Vlassopoulos *et al.*, 1993). Johnson *et al.* (1973) determined a value of ε^* = 15100 (± 500) L mol^{-1} cm^{-2} from D-H exchange experiments on synthetic rutile. On the other hand, Hammer (1988) determined ε^* = 6540 (±20%) L mol^{-1} cm^{-2} for natural rutile samples using moisture evolution analysis, with H_2O contents ranging from 0.04-0.2 wt.%. Vlassopoulos *et al.* (1993) were unable to explain the large disparity in the two values of ε^*, but selected the value of Hammer (1988) because it was based on natural samples with (OH) absorbances similar to their own study, determined from the actual amount of H_2O released from rutile on thermal decomposition, and more in keeping with ε^* values determined for other minerals (e.g. Rossman, 1988). In this study, H_2O contents of Cr-bearing and Fe-bearing rutiles have been calculated using both values (Table 5.4 - columns (e) and (f)).

The water contents of experimental Cr-rich rutiles determined by elemental analysis are shown in Table 5.4 - column (g), and varies from 0.84 wt.% for rutiles synthesized at 5 kbar and 1100 °C to 1.71 wt.% for rutiles synthesized at 20 kbar and 1400 °C. It can be seen that the elemental analyses are a closer match with the water contents calculated using equation (5.1) and the ε^* value of Johnson *et al.* (1973) than to those calculated using the ε^* value of Hammer (1988). Figure 5.5 shows the H_2O content, determined by elemental analysis, of the Cr-rich rutiles, synthesized at 20 kbar, as a function of the abs/t ratio for the ~3240 cm^{-1} (OH) stretching band. The slope of a simple linear regression line (forced through origin) as shown in Figure 5.5 (3.324E-5) can be used to calculate an integrated molar absorptivity of 12760 (±600) L mol^{-1} cm^{-2} (assuming a rutile density of 4250 g L^{-1}).

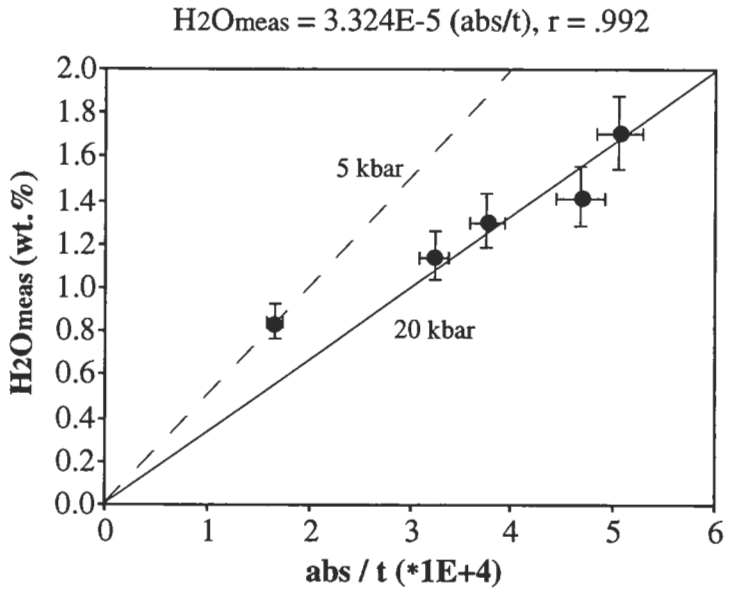

Figure 5.5: The H_2O content of experimental Cr-bearing rutiles shown as a function of abs / t (where abs is the integrated absorbance in cm^{-1} and t is the sample thickness in cm) for 5 and 20 kbar experiments. The H_2O content is determined by elemental analysis for hydrogen. The limited data at 5 kbar suggests that ε^* may depend strongly on the rutile composition (i.e. Cr_2O_3 content). See text for an explanation of the determination of the integrated molar absorptivity from this linear relationship.

Although constrained by only one actual point (in addition to the assumption that the line passes through origin), it is tentatively suggested that for the 5 kbar experiment the slope of the simple linear regression line is larger, and the integrated molar absorptivity will be smaller. From the limited data the value of ε^* for the 5 kbar experiment is calculated as 7900 (±400) L mol^{-1} cm^{-2}.

Elemental analyses were also undertaken to determine the water contents of several Fe-rich rutiles synthesized from the TiO_2-FeO mix under controlled oxygen buffer conditions (Table 5.4 - column (g)). The water content of these rutiles, as measured by elemental analysis, varied from 0.53 wt.% for rutiles from T-4022 (IW conditions, where rutile was observed as a single mineral phase in the run product, see section 5.3.2) to 0.39 wt.% for rutiles synthesized under GW conditions (T-4030). In contrast with the Cr-rich rutiles, it appears from the limited data that the elemental analyses of these Fe-bearing rutiles are more closely matched with water contents calculated using equation (5.1) and the ε^* value of Hammer (1988) than to those calculated using the ε^* value of Johnson *et al.* (1973). Using a similar approach to that described for Cr-rich rutiles, a value for the integrated molar absorptivity can be determined from the abs/t ratio and the measured water content. The slope of a simple linear regression line (forced through origin and the three data points) gives a value of 6.158E-5, which, assuming a rutile density of 4250 g L^{-1}, gives an integrated molar absorptivity, ε^*, for the Fe-bearing rutiles of 6900 (±1400) L mol^{-1} cm^{-2}.

The variable nature, as demonstrated above, of the integrated molar absorptivity as a function of composition, intensive variables (pressure and temperature) and possibly also mineral grain orientation to I.R. beam interaction (e.g. Vlassopoulos *et al.*, 1993) indicates that considerable care should be taken when calculating water contents of rutiles directly from I.R. absorption spectra. Although this particular aspect of I.R. spectroscopy does not constitute a major part of this experimental study, it has identified one possible reason for the large difference between the documented ε^* values of Johnson *et al.* (1973) and Hammer (1988).

5.4 Discussion of results

5.4.1 Incorporation of H and cations into rutile

Using polarization I.R. spectroscopy of water-bearing rutiles, and observing a systematic shift in the O-H vibrational band to lower wavenumbers relative to the isolated (OH) stretch (~3735 cm^{-1}), the study of Vlassopoulos *et al.* (1993) concluded that H in the rutiles under investigation was present as protons bonded to structural O, rather than

interstitial (OH), in the ($^1/_2\,^1/_2 0$) site. The polarization of the (OH) vibration precluded the existence of fluid inclusion or interstitial water in any of their samples. A neutron diffraction study by Swope *et al.* (1992) also found that the H position in hydrogen-bearing rutile was closer to ($^1/_2\,^1/_2 0$) than any other site. Although the polarization I.R. option was not available on the Brucker IFS 66 spectrometer used in this study, and therefore the strong, broad absorption band at 3250 cm^{-1} may not automatically be assigned to a structural O-H bond, the strong sharp band at ~1070 cm^{-1} is very distinctive of a structural M-O-H bending frequency (e.g. Gadsden, 1975). The small band at ~1650 cm^{-1} in I.R. spectra from some experimental rutiles does not preclude the presence of minor amounts of interstitial water, but its relative size to the strong band at ~1070 cm^{-1} would suggest that H is primarily present in a structural M-O-H bond. The shift in the O-H vibrational band to lower wavenumbers observed in the experimental rutiles in this study are consistent with those reported by Vlassopoulos *et al.* (1993) and thus consistent with the suggestion that the ($^1/_2\,^1/_2 0$) site is the most likely location for H in the experimental rutiles. Slightly larger downshifts for Cr-rich rutiles compared with Fe-rich rutiles suggest that O-H bonds in the Cr-rich rutiles are marginally stronger.

Several authors have reported small satellite peaks in natural rutiles in addition to major bands at ~3100-3400 cm^{-1} (e.g. Johnson *et al.*, 1968; Rossman and Smyth, 1990; Hammer and Beran, 1991). Hammer and Beran (1991) regarded these satellite peaks as an indication of rutile crystallization at high temperature because they were observed in rutiles from high temperature metamorphic assemblages. However, in view of high temperature experimental results from this study where no such 'secondary' bands are observed, the suggestion by Vlassopoulos *et al.* (1993) that such satellite peaks are due to minor element-associated (OH), appears to be a more likely explanation.

The experimental work in this study has shown that rutile can accommodate significant amounts of Cr and Fe in solid solution. Under nominally anhydrous conditions, the experimental rutiles contained increasing amounts of Cr and Fe with increasing temperature and pressure. The nature of the defect solution through the introduction of trivalent impurities (i.e. $[TiO_2]\cdot[CrO_{1.5}\square]$, where $\square$ represents an anion site vacancy) induces the formation of oriented planar defects resulting in crystallographic shear (CS) structures, and the trivalent cations selectively occupy planes in rutile crystallographically similar to those in hematite (e.g. Hyde, 1976; Waychunas, 1991). The introduction of H (or water) into the rutile structure appears to be intimately coupled with the Cr^{3+} and Fe^{3+} contents of the experimental rutiles. In assessing H incorporation, constraints on the valence states of the minor components in rutile are required. Chavenas *et al.* (1973) synthesized CrOOH and FeOOH with a modified rutile structure. ESR spectra to study

the oxidation states of Cr and Fe in rutile found predominantly Cr^{3+} and Fe^{3+} (e.g. Ohlsen and Shen, 1974; Ishida *et al.*, 1990).

Consistent with these earlier studies, oxygen buffered experiments in this study have shown a strong linear increase in total iron contents of rutiles with increasing oxygen fugacity and increasing redox ratios, $Fe^{3+}/\sum Fe$, of coexisting ilmenites. In addition, rutiles synthesized from the TiO_2-Fe_2O_3 starting mix at HM buffered conditions contain more total iron than rutiles synthesized at the same P-T conditions from the TiO_2-Fe_3O_4 starting mix. It seems reasonable therefore to invoke trivalent cation substitution in normal Ti sites with increasing oxygen fugacity conditions. Furthermore, where water is detected in cation-bearing rutiles, a link between the OH group and trivalent cations (e.g. MOOH, where M denotes a trivalent cation) may be indicated.

Analytical data from this study show that the water content of experimental rutile increases as a function of the increasing 'redox' value, $Fe^{3+}/\sum Fe$ - $Ti^{3+}/\sum Ti$, ratio of coexisting ilmenite, and therefore as a function of increasing oxygen fugacity (Figure 5.6). Also, the water content of rutile is significantly lower where rutile is synthesized in the presence of Fe_3O_4 than in rutiles which is synthesized in the presence of Fe_2O_3. The observations that with increasing oxygen fugacity (i) the total amount of iron in rutile increases, and (ii), where synthesized under hydrous conditions, the water content of those rutiles also increases, strongly supports a link between ferric iron and water in the form of an OH group. In following with the crystallographic and mineralogical study of Chavenas *et al.* (1973), the presence of an FeOOH component in rutile is proposed by this experimental study. Likewise, for the Cr-rich experiments, the presence of a CrOOH component in rutile appears plausible.

In summary therefore, experimental results from this study appear to indicate two processes that are involved when considering trivalent cation substitution in the rutile structure. Firstly, under anhydrous conditions, trivalent cations such as Cr^{3+} and Fe^{3+} can enter the rutile structure without H^+, thus invoking crystal defect structures. Secondly, trivalent cations can also enter rutile in the presence of water; in this case no defect structures arise from the cation substitution, but interstitial H^+ is detected in the rutile structure. The experimental results indicate that H^+ cannot enter the rutile structure without the presence of a trivalent cation such as Cr^{3+} or Fe^{3+}.

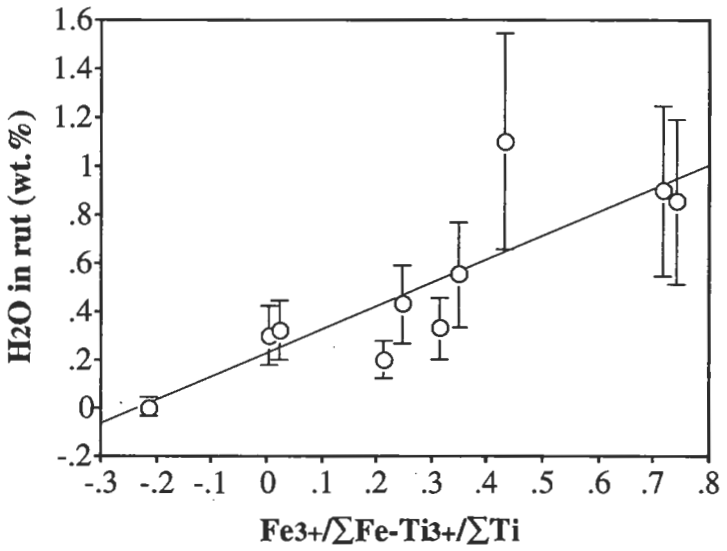

Figure 5.6: H_2O (wt.%) content of rutile against the 'redox' value, $Fe^{3+}/\Sigma Fe - Ti^{3+}/\Sigma Ti$, of coexisting ilmenite from the TiO_2-Fe_2O_3, TiO_2-Fe_3O_4 and TiO_2-FeO experiments. The water content is determined from I.R. absorption spectroscopy. The bars indicate maximum and minimum water contents, depending on the selected value of the integrated molar absorptivity, ε*, and the actual data points are an average value.

The degree of H^+ incorporation into rutile is strongly dependent on temperature. Figure 5.7 shows the ratio of H_2O_{meas}/H_2O_{calc} as a function of temperature for Cr-rich rutiles, synthesized at 20 kbar under water-saturated conditions (where H_2O_{calc} is the water content calculated assuming that all Cr_2O_3 analysed is present as CrOOH, and H_2O_{meas} is the water content measured by elemental analysis). The linear relationship indicates that with increasing temperature Cr_2O_3 is increasingly present as CrOOH. Using this relationship it is suggested that, under the experimental conditions, H^+ substitution into rutile is complete at ~1525 °C, and at this upper limit all Cr is present as CrOOH with defect structures (i.e. $[TiO_2]\cdot[CrO_{1.5}\square]$) no longer present.

5.4.2 Rutile as a possible geohygrometer

The observation that rutile can be a significant host to structural water as a function of temperature, pressure and cation composition suggests that the mineral may be used as an indicator of water activity, a_{H2O}. The following discussion is pertinent to the Cr-rich TiO_2-H_2O experiments in an attempt to illustrate how rutile can be employed as a geohygrometer. The Cr-rich experimental data were selected over the Fe-rich experimental data for several reasons. For the Cr-bearing rutiles synthesized in this study, it can be assumed that all Cr is present as Cr^{3+}. Thus, assuming the presence of CrOOH, water in these rutiles can be assigned to such a component, and its activity, a_{CrOOH}, can be calculated. For the Fe-rich experimental data however, the procedure to obtain a_{FeOOH} is more complex. It can not be assumed that iron is present solely as Fe^{3+} under the experimental conditions of this study. Certainly, under HM conditions the redox ratio of rutile, $Fe^{3+}/\sum Fe$, will be at or close to unity, but under IW conditions the ratio is zero. For oxygen fugacity conditions intermediate to these two oxygen buffer conditions, the rutile redox ratio is difficult to determine, and can not be assumed to be the same as $Fe^{3+}/\sum Fe$ of coexisting ilmenite because of likely differences in ferric and ferrous iron partitioning coefficients for the two mineral phases.

One method for estimating the ferric iron content in rutile is by way of the water (or OH) content using I.R. spectroscopy. However, as already pointed out, an accurate determination of the water content of rutile by I.R. spectroscopy is potentially flawed if the value of the integrated molar absorptivity, ε^*, is poorly constrained, and as discussed in section 5.3.3, ε^* appears dependent on the composition of rutile. Thus, for the redox ratio of rutile to be determined, the integrated molar absorptivity needs to be accurately known, and a systematic experimental and analytical approach to constrain the ε^* value is recommended. However, as such an investigation falls outside the scope of this study, the emphasis is on the Cr-rich rutile experiments as an illustration of the potential of rutile as a geohygrometer.

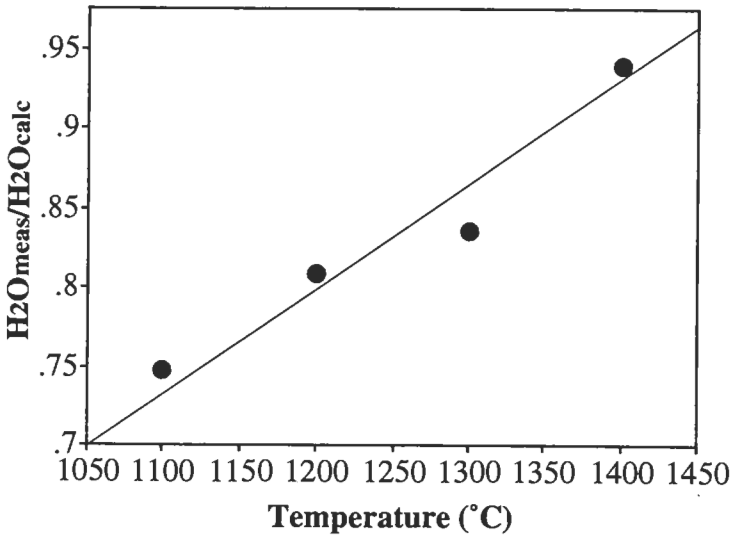

Figure 5.7: The ratio H_2O_{meas} / H_2O_{calc} for experimental Cr-bearing rutiles as a function of temperature. H_2O_{meas} is determined by elemental analysis. H_2O_{calc} is calculated from the Cr_2O_3 content of rutiles assuming that all Cr is present as CrOOH.

For rutile to be used as an indicator of a_{H2O}, it is necessary to formulate a thermodynamic model based on observations such as H contents, minor cation contents taking into account electroneutrality constraints and physical conditions (e.g. Vlassopoulos *et al.*, 1993). A relevant reaction to describe rutile as a geohygrometer can be written as:

$$Cr_2O_3 \text{ (Cr-ox)} + H_2O \text{ (fluid)} = 2 \text{ CrOOH (rut)} \quad (5.2)$$

which can be expressed as:

$$\Delta G = \Delta H - T\Delta S + P\Delta V_s + RT\ln\frac{(a_{CrOOH})^2_{rut}}{a_{H2O}} \quad (5.3)$$

where $(a_{CrOOH})_{rut}$ represents the activity of CrOOH in rutile, and a_{H2O} is the activity of water. Thus, equation (5.3) can be rewritten as:

$$\ln a_{H2O} = \Delta H/RT - \Delta S/R + P\Delta V_s/RT + 2\ln(a_{CrOOH})_{rut} \quad (5.4)$$

where R is the gas constant. The use of experimental data where the water activity, pressure, temperature and the CrOOH activity are well constrained will enable the determination of values for ΔH, ΔS and ΔV for the equilibrium reaction in (5.2) by means of a linear least-squares method. Thus, assuming ideal site mixing for CrOOH in rutile, and assigning all measured OH to the CrOOH species in a coupled substitution of Cr for Ti and OH for O, it is possible to use the experimental data and solve equation (5.4) for the Cr-rich TiO_2-H_2O experiments to obtain a semi-quantitative rutile geohygrometer:

$$\log a_{H2O} = 3097.5/T + 0.0847 - 0.0240\ P/T + 2\log(X_{CrOOH})_{rut} \quad (5.5)$$

Applying equation (5.5) to two documented hydrous, chromium-rich rutile (+ coexisting ilmenite) bearing xenoliths from the Jagersfontein kimberlite (JAG83-30 and JAG85-2, Vlassopoulos *et al.*, 1993), assuming a source pressure of 30 kbar and a temperature of 1150 °C, and assuming that equation (5.5) can be used as a broad estimate with an $(X_{MOOH})_{rut}$ term (where M denotes trivalent cations such as Al, V, Cr and Fe), results in calculated water activity ($\log a_{H2O}$) values of -0.48 (1σ of 0.14) and -1.30 respectively. This agrees well with the qualitative observation that for sample JAG80-30 the H content closely matches the calculated charge deficiency per formula unit, which requires a relatively high f_{H2O} value, whereas for sample JAG85-2 the H content is significantly less than required for charge balance, indicating a relatively low f_{H2O} (Vlassopoulos *et al.*, 1993).

It should be noted that, as not all the experiments were undertaken at a_{H2O} = 1.0, the data presented in this study is by no means complete and could be significantly improved. Particular attention can be given to the thermodynamic parameters, and improvements may be made to the level of confidence that can be attached to them. A more elaborate treatment will require multi-component experiments to be undertaken under constraints of, for example, the C-H-O fluid system, where a_{H2O} (generally <1.0) can be calculated as a function of temperature, pressure and oxygen fugacity (e.g. Taylor, 1985).

For example, one TiO_2-FeO oxygen buffer experiment was conducted under WCWO oxygen fugacity conditions (FMQ-2.30 log units) at 20 kbar and 1200 °C (T-4026). For this experiment with a_{H2O} ~0.6-0.7 (e.g. Taylor and Foley, 1989), the total iron content of rutile is 1.87 wt.% Fe_2O_3, and water is not detected in the rutile phase. This compares with the TiO_2-FeO experiment (T-4030) conducted at the same P-T conditions using the GW oxygen buffer (FMQ-2.06 log units), where the rutile contains 2.00 wt.% Fe_2O_3 and, depending on the value of ε^*, ~0.2-0.4 wt.% H_2O. Ilmenite coexisting with rutile in the experimental product of T-4026 shows no ferric iron and a small Ti^{3+} content, whereas ilmenite coexisting with rutile in T-4030 has minor ferric iron ($Fe^{3+}/\sum Fe$ ~0.004).

A possible explanation for these observations is that rutile synthesized under WCWO conditions contains iron in the +2 valency state and the absence of the FeOOH substitution is indicated by the lack of any water in the rutile structure. On the other hand, rutiles synthesized under GW conditions contain some ferric iron, possibly coexisting with the presence of water in the rutile structure, and coexisting ilmenite also contains Fe_2O_3 in very small amounts. It should be noted here that the amount of water detected in the rutiles synthesized under GW conditions will calculate an $Fe^{3+}/\sum Fe$ value approximating unity, which appears to be very high in comparison with that of the coexisting ilmenites. This anomaly may be related to problems already described above regarding the determination of ε^*, although the elemental analysis of the rutiles confirms the amount of water determined by I.R. spectroscopy.

Nevertheless it can be seen that minor element speciation, in terms of valency states, is controlled by oxygen fucacity, and a systematic experimental study will allow for a quantitative assessment of the effect of trivalent cations (versus divalent and pentavalent, e.g. Vlassopoulos *et al.*, 1993) on the incorporation of water into the rutile structure. Although such a detailed study is beyond the scope of this work, the experimental data presented here can be used to make some qualitative remarks regarding the use of rutile as a potential water activity indicator. Figure 5.8A shows the water content of rutile as a function of the Cr cation content in rutile for various temperatures and pressures at a_{H2O} = 1.0.

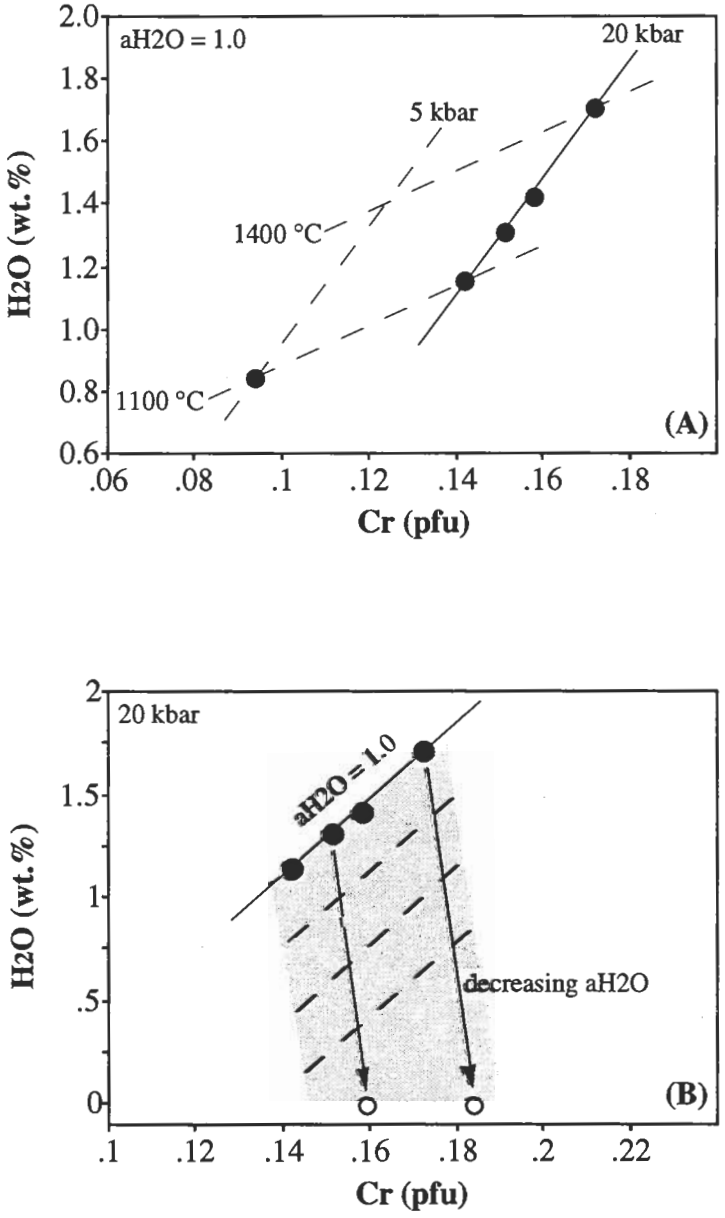

Figure 5.8: The water content of Cr-bearing rutiles (expressed as H_2O in wt.%) as a function of Cr cations in rutiles (per formula unit). (A) The H_2O content versus Cr for experiments at a_{H2O} = 1.0 for known temperatures and pressures. Solid lines indicate experimental results, dashed lines indicate exptrapolated results. (B) The H_2O content versus Cr at 20 kbar and a_{H2O} = 1.0, and extrapolated to lower a_{H2O}. Open circles represent data from nominally anhydrous experiments (i.e. a_{H2O} = 0).

From the illustration it can be seen that an isothermal-isobaric grid can be constructed over rutile compositions with known water and minor cation contents at a fixed water activity. The diagram shows an increasing water content, linked to the minor cation content, with increasing temperature and pressure. The effect of oxygen fugacity has not been illustrated in this diagram because it was not pertinent to the Cr-rich experiments. However, it can be seen from the Fe-rich experiments that for a fixed P-T-a_{H2O}, the amount of water substituted into rutile will decrease with decreasing oxygen fugacity and, by inference increasing divalent cation contents.

Figure 5.8B attempts to show diagrammatically how the water content of the experimental rutiles may decrease with a decreasing water activity at constant pressure and oxygen fugacity, the diagram being consistent with the observation that the experimental rutiles contain significant amounts of chromium at a zero a_{H2O}. The two illustrations in Figure 5.8 highlight the complicated nature behind the use of rutile as a geohygrometer. The water activity of a rutile-bearing assemblage can be estimated if independent estimates can be made of the temperature, pressure and cation speciation (dependent on oxygen fugacity), and if the thermodynamic parameters in equation (5.4) are known.

Finally, in applying the geohygrometer to natural rutile-bearing assemblages, potential problems may arise when a position of mineral equilibration can not be established, which can become a significant factor when the difference in rate of diffusion through rutile of H versus minor cations is considered (e.g. Vlassopoulos *et al.*, 1993). In addition, the experimental results presented here have shown that saturation with respect to the CrOOH component reaches an upper limit to both the H and Cr concentrations in rutile only at very high temperatures (>1500 °C at 20 kbar). Thus, knowledge of a kinetic relationship between the water content and physical parameters, particularly at lower temperatures, may be also be important in establishing the potential use of rutile as an indicator of water activity.

5.4.3 A possible role for rutile in recycling water in the Earth's mantle

The substitution of single (OH) groups for O anions in nominally anhydrous mantle minerals was initially suggested as a potential mechanism important for water storage in the mantle (Martin and Donnay, 1972). Bell and Rossman (1992) summarized the current state of knowledge regarding water storage in 'anhydrous' minerals. The importance of any mantle mineral in terms of the water budget of the mantle depends on its ability to accommodate water and its a abundance in the mantle. According to the study of Bell and Rossman (1992) of the most abundant natural mantle minerals, pyroxenes are the most hydrous, containing as much as 500 ppm H_2O by weight, followed by garnets and olivines

which contain up to 50 ppm. Other, less common minerals with an affinity for water, include β-Mg_2SiO_4 (e.g. McMillan *et al.*, 1991) and stishovite (Pawley *et al.*, 1993). As discussed above, rutile has been widely reported as an accessory mineral with a strong affinity for (OH).

This study proposes that rutile can contain significant amounts of water. In fact, under the experimental conditions of this study, synthetic rutiles can contain as much as 1.71 wt.% H_2O, and this figure far exceeds any values for the water content of nominally anhydrous minerals reported in the literature. Although its modal abundance in mantle assemblages is usually less than 1 %, the experimental data suggest that rutile must still be considered as a potentially important storage mineral for water. Especially on a local scale, in regions of rutile-dominated assemblages (e.g. the rutile-bearing nodules from Jagersfontein, Orapa and other localities) this affinity for water may be significant in controlling small scale magmatic processes. For example, Haggerty (1987) interpreted the origin of some Nb- and Cr-rich rutile in upper mantle xenoliths as products of metasomatism by a fluid phase or melt rich in hydrous incompatible elements.

Moreover, in a subduction environment where oceanic crust transforms to eclogite in response to increasing pressure, and hydrous minerals such as amphibole, chlorite, phlogopite and serpentine undergo dehydration reactions, rutile may, in addition to the more abundant clinopyroxene (e.g. Bell and Rossman, 1992), become an important storage mineral for water. With increasing pressure and temperature, rutile would incorporate increasing amounts of water, a feature which may also be applicable to other nominally anhydrous minerals. Thus, deep subduction of such assemblages may allow transport of water into the mantle. Pods of eclogite situated in peridotitic mantle could encounter relatively reduced regimes, resulting in the liberation of water and local areas of comparatively high water concentrations might form, thus perhaps contributing to small degrees of mantle melting.

The high affinity for (OH) by the experimental rutiles also suggests that its structural isomorph, stishovite, may be similarly hydrous and act as a potential H reservoir in the mantle, particularly coupled with Al-Si substitution (c.f. Pawley *et al.*, 1993). In a subduction zone the gradual breakdown of 'hydrous' pyroxene and the onset of stishovite crystallization in the basaltic portion of the descending slab (e.g. Irifune and Ringwood, 1987) could result in some of the released water being incorporated in the crystallizing stishovite, as well as coexisting garnet. The water content of stishovite may, like the experimental rutiles, increase with increasing pressure and temperature. In the transition zone garnet exsolves perovskite and gradually disappears (e.g. Irifune and Ringwood,

1987) leaving stishovite as a likely candidate for continued water storage, and the transportation of water into the lower mantle.

REFERENCES CITED

Aines R.D. and Rossman, G.R. (1984). The water content of mantle garnets. Geology 12: 720-723.

Andersen, D.J. and Lindsley, D.H. (1979). The olivine-ilmenite thermometer. Proc. 10th Lunar Planet. Sci. Conf.: 493-507.

Andersen, D.J. and Lindsley, D.H. (1981). A valid Margules formulation for an asymmetric ternary solution: revision of the olivine-ilmenite thermometer, with applications. Geochim. Cosmochim. Acta 45: 847-853.

Andersen, D.J. and Lindsley, D.H. (1988). Internally consistent solution models for Fe-Mg-Mn-Ti oxides: Fe-Ti oxides. Am. Min. 73: 714-726.

Andersson, P-O., Kollberg, E.L. and Jelenski, A. (1973). Extra EPR spectra of iron-doped rutile. Phys. Rev. B8: 4956-4965.

Andersson, P-O., Kollberg, E.L. and Jelenski, A. (1974). Charge compensation in iron-doped rutile. J. Phys. C: Sol. State Phys. 7: 1868-1880.

Aragon, R. and McCallister, R.H. (1982). Phase and point defect equilibria in the titanomagnetite solid solution. Phys. Chem. Min. 8: 112-120.

Arculus, R.J. (1985). Oxidation state of the mantle: past and present. Ann. Rev. Earth Planet. Sci. 13: 75-95.

Atkinson, W.J. (1989). Diamond exploration philosophy, practice, and promises: a review. In: Ross, J. (ed), Kimberlites and Related Rocks, Vol. 2. Geol. Soc. Aust. Inc. Spec. Publ. No. 14: 1075-1107.

Babich, Yu. V., Green, D.H. and Sobolev, N.V. (1992). Iron solubility in rutile of harzburgite assemblage (Mg-Fe-Ti-Si-O system). Int. Min. Assoc., 2nd Int. Symposium. Thermodynamics of natural processes. United Inst. Geol. Geoph. and Mineral., Russ. Acad. Sci., Abstr.: 8.

Ballhaus, C. (1993). Redox states of lithospheric and asthenospheric upper mantle. Contrib. Mineral. Petrol. 114: 331-348.

Ballhaus, C., Berry, R.F. and Green, D.H. (1990). Oxygen fugacity controls in the Earth's upper mantle. Nature 348: 437-440.

Ballhaus, C., Berry, R.F. and Green, D.H. (1991). High pressure experimental calibration of the olivine-orthopyroxene-spinel oxygen geobarometer: implications for the oxidation state of the upper mantle. Contrib. Mineral. Petrol. 107: 27-40.

Bell, D.R. and Rossman, G.R. (1992). The distribution of hydroxyl in garnets from the subcontinental mantle of southern Africa. Contrib. Mineral. Petrol. 111: 161-178.

Beran A. and Zemann, J. (1971). Measurement of the infrared-pleochroism in minerals. XI. The pleochroism of the OH-stretching frequency in rutile, anatase, brookite, and cassiterite. Tscher. Min. Mitt. 15: 71-80.

Bishop, F.C. (1977). The distribution of Fe^{2+} and Mg between pyroxene and ilmenite intergrowths from kimberlites. 2nd Int. Kimb. Conf., extended abstracts.

Bishop, F.C. (1979). Mg-Fe^{2+} partitioning between olivine and ilmenite (abstract). EOS Trans. Am. Geophys. Union 60: 420.

Bishop, F.C. (1980). The distribution of Fe^{2+} and Mg between coexisting ilmenite and pyroxene with applications to geothermochemistry. Am. J. Sci. 280: 46-77.

Bohlen, S.R. and Boettcher, A.L. (1981). Experimental investigations and geological applications of orthopyroxene geobarometry. Am. Min. 66: 951-964.

Bowles, J.F.W. (1988). Definition and range of composition of naturally occurring minerals with the pseudobrookite structure. Am. Min. 73: 1377-1383.

Boyd, F.R. (1971). Ensatite-ilmenite and diopside-ilmenite intergrowths from the Monastery Mine. Carneg. Inst. Wash. Yr. Bk. 70: 134-138.

Boyd, F.R. and England, J.L. (1960). Apparatus for phase-equilibrium measurements at pressures up to 50 kilobars and temperatures up to 1750 °C. J. Geophys. Res. 65: 741-748.

Boyd, F.R. and Nixon, P.H. (1973). Origin of the ilmenite-silicate nodules in kimberlites from Lesotho and South Africa. In: Nixon, P.H. (ed), Lesotho Kimberlites. Lesotho National Development Corporation, Maseru: 254-268.

Brey, G.P. (1990). Geothermometry for lherzolites: experiments from 10 to 60 kbar, new thermobarometers, and application to natural rocks. Unpubl. Habilitation Thesis, University of Mainz, Germany.

Bryndzia, L.T. and Wood, B.J. (1990). Oxygen thermobarometry of abyssal spinel peridotites: the redox state and C-O-H volatile composition of the Earth's suboceanic mantle. Am. J. Sci. 290: 1093-1116.

Bunch, T.E. and Keil, K. (1971). Chromite and ilmenite in non-chondritic meteorites. Am. Min. 56: 146-157.

Canil, D., ONeill, H. St. C., Pearson, D.G., Rudnick, R.L., McDonough, W.F. and Carswell, D.A. (1994). Ferric iron in peridotites and mantle oxidation states. Earth Planet. Sci. Lett. 123: 205-220.

Carmichael, I.S.E. (1991). The redox states of basic and silicic magmas: a reflection of their source regions? Contrib. Mineral. Petrol. 106: 129-141.

Carswell, D.A. and Gibb, F.G.F. (1987). Garnet lherzolite xenoliths in the kimberlites of northern Lesotho: revised P-T equilibration conditions and upper mantle palaeogeotherm. Contrib. Mineral. Petrol. 97: 473-487.

Cawthorn, R.G. and Biggar, G.M. (1993). Crystallization of titaniferous chromite, magnesian ilmenite and armalcolite in tholeiitic suites in the Karoo Igneous Province. Contrib. Mineral. Petrol. 114: 221-235.

Chavenas, J., Joubert, J.C., Capponi, J.J. and Marézio, M. (1973). Synthèse de nouvelles phases denses d'oxyhydroxydes $M^{3+}OOH$ des métaux de la première série de transition, en milieu hydrothermal à trés haute pression. J. Sol. State Chem. 6: 1-15.

Chou, I.M. (1978). Calibration of oxygen buffers at elevated P and T using the hydrogen fugacity sensor. Am. Min. 63: 690-703.

Connolly, J.A.D. (1990). Multivariable phase diagrams; an algorithm based on generalized thermodynamics. J. Sci. 290: 666-718.

Dawson, J.B. and Smith, J.V. (1977). The MARID (mica-amphibole-rutile-ilmenite-diopside) suite of xenoliths in kimberlites. Geochim. Cosmochim. Acta, 41: 309-323.

Dawson, J.B. and Stephens, W.E. (1975). Statistical analysis of garnets from kimberlites and associated xenoliths. J. Geol. 83, 589-607.

Dyar, M.D., McGuire, A.V. and Ziegler, R.D. (1989). Redox equilibria and crystal chemistry of coexisting minerals from spinel lherzolite mantle xenoliths. Am. Min. 74: 969-980.

Edwards, D., Rock, N.M.S., Taylor, W.R., Griffin, B.J. and Ramsay, R.R. (1992). Mineralogy and petrology of the Aries diamondiferous kimberlite pipe, Central Kimberley Block, Western Australia. J. Petrol. 33: 1157-1191.

Eggler, D.H. (1983). Upper mantle oxidation state: evidence from olivine-orthopyroxene-ilmenite assemblages. Geophys. Res. Lett. 10: 365-368.

Eggler, D.H. and Baker, D.R. (1982). Reduced volatiles in the system C-O-H: implications to mantle melting, fluid formation and diamond genesis. In: Akimoto, S. and Manghani, M.H. (eds), High pressure reearch in geophysiscs. Centre Acad. Publ., Tokyo: 237-250.

Eggler, D.H. and McCallum, M.E. (1976). A geotherm from megacrysts in the Sloan kimberlite pipes, Colorado. Carn. Inst. Wash. Yr. Bk. 75: 538-541.

Eggler, D.H., McCallum, M.E. and Smith, C.B. (1979). Megacryst assemblages in kimberlites from Northern Colorado and Southern Wyoming: petrology, geothermometry-barometry and a real distribution. In: Boyd, F.R. and Meyer, H.O.A. (eds), The mantle sample: Inclusions in kimberlites and other volcanics. Proc. 2nd Int. Kimb. Conf. Vol. 2: 213-226.

El Goresy, A., Ramdohr, P., Medenbach, O. and Bernhardt, H.-J. (1974). Taurus-Littrow TiO_2-rich basalts: opaque mineralogy and geochemistry. Proc. 5th Lunar Sci. Conf.: 627.

Eugster, H.P. and Wones, D.R. (1962). Stability relations of the ferruginous biotite, annite. J. Petrol. 3: 82.

Finger, L.W. (1972). The uncertainty of the calculated ferric iron content of a microprobe analysis. Carn. Inst. Wash. Yr. Bk. 71: 600-603.

Fischer, G.W. and Medaris, L.G. (1969). Cell dimensions and x-ray determination curves for synthetic Mg-Fe olivines. Am. Min. 54: 741-753.

Ford, C.E., Russel, D.G., Groven, J.A. and Fisk, M.R. (1983). Distribution coefficients of Mg^{2+}, Fe^{2+}, Ca^{2+} and Mn^{2+} between olivine and melt. J. Petrol. 24: 256-265.

Gadsden, J.A. (1975). Infrared spectra of minerals and related inorganic compounds. Butterworths & Co. (Publ.) Ltd., England.

Gaspar, J.C. and Wyllie, P.J. (1983). Ilmenite (high Mg, Mn, Nb) in the carbonatites from the Jacupiranga Complex. Am. Min. 68: 960-971.

Ghiorso, M.S. (1990). Thermodynamic properties of hematite-ilmenite-geikielite solid solutions. Contrib. Mineral. Petrol. 104: 645-667.

Ghiorso, M.S. and Sack, R.O. (1991). Fe-Ti oxide geothermometry: thermodynamic formulation and the estimation of intensive variables in silicic magmas. Contrib. Mineral. Petrol. 108: 485-510.

Green, D.H. and Ringwood, A.E. (1967). The genesis of basaltic magmas. Contrib. Mineral. Petrol. 15: 103-190.

Green, D.H. and Sobolev, N.V. (1975). Coexisting garnets and ilmenites synthesized at high pressures from pyrolite and olivine basanite and their significance for kimberlite assemblages. Contrib. Mineral. Petrol. 50: 217-229.

Green, D.H., Falloon, T.J. and Taylor, W.R. (1987). Mantle-derived magmas - roles of variable source peridotite and variable C-O-H fluid compositions. In: Mysen, B.O. (ed), Magmatic processes: physico-chemical principles. Geochem. Soc. Penn State Univ.: 139-154.

Green, D.H., Taylor, W.R. and Foley, S.F. (1990). The Earth's upper mantle as a source for volatiles. In: Herbert, H.K. (ed.), Proceedings of the conference on stable isotopes and fluid processes in mineralization. Publ. Geol. Dept. Ext. Serv., University of Western Australia, 23: 17-34.

Griffin, W.L., Gurney, J.J. and Ryan, C.G. (1992). Variation in trapping temperatures and trace elements in peridotite-suite inclusions from African diamonds: evidence for two inclusion suites, and implications for lithosphere stratigraphy. Contrib. Mineral. Petrol., 110: 1-5.

Gurney, J.J. (1989). Diamonds. In: Ross, J. (ed), Kimberlites and Related Rocks, Vol. 2. Geol. Soc. Aust. Inc. Spec. Publ. No. 14: 935-965.

Gurney, J.J., Jakob, W.R.O. and Dawson, J.B. (1979). Megacrysts from the Monastery Kimberlite pipe, South Africa. In: Boyd, F.R. and Meyer, H.O.A. (eds), The mantle sample: Inclusions in kimberlites and other volcanics. Proc. 2nd Int. Kimb. Conf. Vol. 2: 227-243.

Gurney, J.J., Moore, R.O., Otter, M.L., Kirkley, M.B., Hops, J.J. and McCandless, T.E. (1991). Southern African kimberlites and their xenoliths. In: Kampunzu, A.B. and Lubala, R.T. (eds), Magmatism in extensional structural settings. The Phanerozoic African plate. Springer -Verlag, Berlin: 495-536.

Haggerty, S.E. (1975). The chemistry and genesis of opaque minerals in kimberlites. Phys. Chem. Earth 9: 295-307.

Haggerty, S.E. (1979). Spinels in high pressure regimes. In: Boyd, F.R. and Meyer, H.O.A. (eds), The mantle sample: Inclusions in kimberlites and other volcanics. Proc. 2nd Int. Kimb. Conf. Vol. 2: 183-196.

Haggerty, S.E. (1986). Diamond genesis in a multiply-constrained model. Nature 320: 34-39.

Haggerty, S.E. (1987). Metasomatic mineral titanates in upper mantle xenoliths. In: Nixon, P.H. (ed), Mantle xenoliths. J. Wiley & Sons, New York: 671-690.

Haggerty, S.E. (1989). Mantle metasomes and the kinship between carbonatites and kimberlites. In: Bell, K. (ed), Carbonatites, Genesis and Evolution. Unwin Hyman, London: 546-560.

Haggerty, S.E. (1990). Redox state of the contitnental lithosphere. In: Menzies, M.A. (ed), Continental mantle. Clarendon, Oxford: 87-109.

Haggerty, S.E. (1991). Oxide mineralogy of the upper mantle. In: Lindsley, D.H. (ed), Oxide minerals: petrologic and magnetic significance. Min. Soc. Am. Rev. Min. 25: 355-416.

Haggerty, S.E., Boyd, F.R., Bell, P.M., Finger, L.W. and Bryan, W.B. (1970). Opaque minerals and olivine in lavas and breccias from Mare Tranquillitatis. Proc. Apollo 11th Lunar Sci. Conf., Geochim. Cosmochim. Acta, Suppl. 1, 1: 513-558.

Haggerty, S.E. and Gurney, J.J. (1984). Zircon-bearing nodules from the upper mantle (abstract). EOS Trans. Am. Geophys. Union 65: 301.

Haggerty, S.E., Hardie, R.B. and McMahon, R.M. (1979). The mineral chemistry of ilmenite nodule associations from the Monastery diatreme. In: Boyd, F.R. and Meyer, H.O.A. (eds), The mantle sample: Inclusions in kimberlites and other volcanics. Proc. 2nd Int. Kimb. Conf. Vol. 2: 249-256.

Haggerty, S.E., Moore, A.E. and Erlank, A.J. (1985). Macrocryst Fe-Ti oxides in olivine melilitites from Namaqualand-Bushmanland, South Africa. Contrib. Mineral. Petrol. 91: 163-170.

Haggerty S.E. and Tompkins, L.A. (1983). Redox state of the Earth's upper mantle from kimberlitic ilmenites. Nature 303: 295-300.

Haggerty S.E. and Tompkins, L.A. (1984). Subsolidus reactions in kimberlitic ilmenites: exsolution, reduction and the redox state of the mantle. In: Kornprobst, J. (ed), Kimberlites I: Kimberlites and related rocks. Proc. 3rd Int. Kimb. Conf. Vol. 1: 335-357.

Hammer V.M.F. (1988). Quantitative IR-spectroscopic determination of structural OH-groups in natural rutiles of various occurrences. Z. Kristallogr. 185: 631.

Hammer V.M.F. and Beran, A. (1991). Variations in the OH concentrations of rutiles from different geological environments. Min. Petrol. 45: 1-9.

Harte, B. (1977). Rock nomenclature with particular relation to deformation and recrystallisation textures in olivine-bearing xenoliths. J. Geol. 8: 279-288.

Hemingway, B.S. (1990). Thermodynamic properties for bunsenite, NiO, magnetite, Fe_3O_4, and hematite, Fe_2O_3, with comments on selected oxygen buffer reactions. Am. Min. 75: 781-790.

Holland, T.J.B. and Powell, R. (1990). An enlarged and updated internally consistent thermodynamic dataset with uncertainties and correlations: the system K_2O-Na_2O-CaO-MgO-MnO-FeO-Fe_2O_3-Al_2O_3-TiO_2-SiO_2-C-H_2-O_2. J. Metam. Geol. 8: 89-124.

Huebner, J.S. (1971). Buffering techniques for hydrostatic systems at elevated pressures. In: Ulmer, G.C. (ed), Research techniques for high pressures and high temperatures. Springer, Berlin Heidelberg New York: 123-177.

Huebner J.S. and Sato, M. (1970). The oxygen fugacity-temperature relationships of manganese and nickel oxide buffers. Am. Min. 55: 934-952.

Hyde, B.G. (1976). Rutile: Planar defects and derived structures. In: Wenk, H.-R. (ed), Electron m icroscopy in mineralogy. Springer Verlag, New York: 310-318.

Hynes, A. and Gee, R.D. (1986). Geologic setting and petrochemistry of the Naracoota Volcanics, Capricorn Orogen, Western Australia. Precambrian Res. 31: 107-132.

Irifune, T. and Ringwood, A.E. (1987). Phase transformations in a harzburgite composition to 26 GPa; implications for dynamical behaviour of the subducting slab. Earth Planet. Sci. Lett. 86: 365-376.

Ishida, S., Hayashi, M., Fujimura, Y. and Fujiyoshi, K. (1990). Spectroscopic study of the chemical state and coloration of chromium in rutile. J. Am. Cer. Soc. 73: 3351-3355.

Jamieson, H.E. and Roeder, P.L. (1984). The distribution of Mg and Fe^{2+} between olivine and spinel at 1300 °C. Am. Min. 69: 283-291.

Jaques, A.L., Lewis, J.D. and Smith, C.B. (1986). The kimberlites and lamproites of Western Australia. Geol. Surv. Western Australia Bull. 132.

Jarosewich, E., Nelen, J.A. and Norber, J.A. (1980). Reference samples for electron microprobe analysis. Geostand. Newslett. 4: 43-47.

Johnson, O.W., Ohlsen, W.D. and Kingsbury, P.I. (1968). Defects in rutile. III. Optical and electrical properties of impurities and charge carriers. Phys. Rev. 175: 1102-1109.

Johnson, O.W., DeFord, J. and Shaner, J.W. (1973). Experimental technique for the precise determination of H and D concentrations in rutile (TiO_2). J. Appl. Phys. 44: 3008-3012.

Jones, A.P., Smith, J.V. and Dawson, J.B. (1982). Mantle metasomatism in 14 veined peridotites from Bultfontein Mine, South Africa. J. Geol. 90: 435-453.

Kamperman, M., Taylor, W.R., Hamilton, R. and Jablonski, W. (1993). Major and trace element discrimination of magnesiochromites from boninitic and diamond-related sources. In: 1993 General Assembly of the International Association of Volcanology and Chemistry of the Earth's Interior (IAVCEI) Abstr.: 55.

Katsura, T. and Muan, A. (1964). Experimental study of equilibria in the system FeO-Fe_2O_3-Cr_2O_3 at 1300 °C. Trans. Am. Inst. Minning Metal. Engr. 230: 77-84.

Kress, V.C. and Carmichael, I.S.E. (1988). Stoichiometry of the iron oxidation reaction in silicate melts. Am. Min. 73: 1267-1274.

Leblanc, M., Dautria, J. and Girod, M. (1982). Magnesian ilmenite xenoliths in a basanite from Tahalra, Ahaggar (Southern Algeria). Contrib. Mineral. Petrol. 79: 347-354.

Lee, C.W. (1970). Titania-chromium oxide compositions and their phase conditions. Ber. Deut. Keram. Ges. 47: 169-175.

Lindsley, D.H. (1976a). Experimental studies of oxide minerals. In: Rumble III, D. (ed), Oxide minerals. Min. Soc. Am. Rev. Min. 3: L61-L88.

Lindsley, D.H. (1976b). The crystal chemistry of oxide minerals as exemplified by the Fe-Ti oxides. In: Rumble III, D. (ed), Oxide minerals. Min. Soc. Am. Rev. Min. 3: L1-L52.

Lindsley, D.H. (1978). Magnetite-ilmenite equilibria: solution models including MgO and MnO (abstract). EOS Trans. Am. Geophys. Union 59: 395.

Lindsley, D.H. (1991a). Oxide minerals: petrologic and magnetic significance. Min. Soc. Am. Rev. Min. 25.

Lindsley, D.H. (1991b). Experimental studies of oxide minerals. In: Lindsley, D.H. (ed), Oxide minerals: petrologic and magnetic significance. Min. Soc. Am. Rev. Min. 25: 69-106.

Lucas, H., Muggeridge, M.T. and McConchie, D.M. (1989). Iron in kimberlitic ilmenites and chromium spinels: a survey of analytical techniques. In: Ross, J. (ed), Kimberlites and Related Rocks, Vol. 1. Geol. Soc. Aust. Inc. Spec. Publ. No. 14: 311-320.

MacChesney, J.B. and Muan, A. (1959). Studies in the system iron oxide-titanium dioxide. Am. Min. 44: 926-945.

Martin, R.F. and Donnay, G. (1972). Hydroxyl in the mantle. Am. Min. 57: 554-570.

Matsui, Y. and Nishizawa, O. (1974). Iron(II)-magnesium exchange equilibrium between olivine and calcium-free pyroxene over a temperature range 800 °C to 1300 °C. Bull. Soc. Fr. Mineral. Christallogr. 97: 122-130.

Mattioli, G.S. and Wood, B.J. (1988). Magnetite activity across the $MgAl_2O_4$-Fe_3O_4 spinel join, with application to thermobarometric estimates of upper mantle oxygen fugacity. Contrib. Mineral. Petrol. 98: 148-162.

Mattioli, G.S., Baker, M.B., Rutter, H.J. and Stolper, E.M. (1989). Upper mantle oxygen fugacity and its relationship to metasomatism. J. Geol. 97: 521-536.

McGuire, A.V., Dyar, M.D. and Ward, K.A. (1989). Neglected Fe^{3+}/Fe^{2+} ratios - A study of Fe^{3+} content of megacrysts from alkali basalts. Geol. 17: 687-690.

McGuire, A.V., Francis, C.A. and Dyar, M.D. (1992). Mineral standards for electron microprobe analysis of oxygen. Am. Min. 77: 1087-1091.

McMillan P.F., Akaogi, M., Sato, R.K., Poe, B. and Foley, J. (1991). Hydroxyl groups in β-Mg_2SiO_4. Am. Min. 76: 354-360.

McMillan, P.F., Smyth, J.R. and Akaogi, M. (1987). OH in beta-Mg_2SiO_4 (abstract). EOS Trans. Am. Geophys. Union 68: 1470.

Menzies, M.A. (1990). Archaean, Proterozoic, and Phanerozoic lithospheres. In: Menzies, M.A. (ed), Continental mantle. Clarendon, Oxford: 67-86.

Meyer, H.O.A. (1987). Inclusions in diamond. In: Nixon, P.H. (ed), Mantle xenoliths. John Wiley & Sons, Chichester, England: 501-522.

Meyer, H.O.A. and McCallum, M.E. (1986). Mineral inclusions in diamonds from the Sloan Kimberlite, Colorado. J. Geol., 94: 600-612.

Meyer, H.O.A. and Svisero, D.P. (1975). Mineral inclusions in Brazilian diamonds. Phys. Chem. Earth, 9: 785-795.

Mirwald, P.W., Getting, I.C. and Kennedy, G.C. (1975). Low-friction cell for piston-cylinder high-pressure apparatus. J. Geophys. Res. 80: 1519-1525.

Mitchell, R.H. (1973). Magnesian ilmenite and its role in kimberlite petrogenesis. J. Geol. 81: 301-311.

Mitchell, R.H. (1977). Geochemistry of magnesian ilmenites from kimberlites in South Africa and Lesotho. Lithos 10: 29-37.

Mitchell, R.H. (1979). Mineralogy of the Tunraq kimberlite, Somerset Island, N.W.T., Canada. In: Boyd, F.R. and Meyer, H.O.A. (eds), Kimberlites, diatremes, and diamonds: their geology, petrology, and geochemistry. Proc. 2nd Int. Kimb. Conf. Vol. 1: 161-171.

Mitchell, R.H. (1986). Kimberlites. Mineralogy, Geochemistry, and Petrology. Plenum Press, New York and London.

Moore, A.E. (1987). A model for the origin of ilmenite in kimberlite and diamond: implications for the genesis of the discrete nodule (megacryst) suite. Contrib. Mineral. Petrol. 95: 245-253.

Murad, E and Johnston, J.K. (1987). Iron oxides and oxyhydroxides. In: G.J. Long (ed), Mössbauer spectroscopy applied to inorganic chemistry, Vol. 2, Plenum Press New York: 507-528.

Nell, J. and Wood, B.J. (1991). High-temperature electrical measurements and thermodynamic properties of Fe_3O_4-$FeCr_2O_4$-$MgCr_2O_4$-$FeAl_2O_4$ spinels. Am. Min. 76: 405-426.

Nixon, P.H. (1987). Mantle xenoliths. J. Wiley & Sons, Chichester, England.

Nixon, P.H. and Boyd, F.R. (1979). Garnet-bearing lherzolites and discrete nodule suites from the Malaita alnöite, Solomon Islands, S.W. Pacific, and their bearing on oceanic mantle composition and geotherm. In: Boyd, F.R. and Meyer, H.O.A. (eds), The mantle sample: Inclusions in kimberlites and other volcanics. Proc. 2nd Int. Kimb. Conf. Vol. 2: 400-423.

Novak, G.A. and Coville, A.A. (1989). A practical interactive least squares cell-parameter program using an electronic spreadsheet and a personal computer. Am. Min. 74: 488-490.

O'Neill, H.St.C. (1987a). The quartz-fayalite-iron and quartz-fayalite-magnetite equilibria and the free energies of formation of fayalite (Fe_2SiO_4) and magnetite (Fe_3O_4). Am. Min. 72: 67-75.

O'Neill, H.St.C. (1987b). The free energies of formation of NiO, CoO, Ni_2SiO_4. Am. Min. 72: 280-291.

O'Neill, H.St.C. (1988). Systems Fe-O and Cu-O: thermodynamic data for the equilibria Fe-"FeO", Fe-Fe_3O_4, "FeO"-Fe_3O_4, Fe_3O_4-Fe_2O_3, Cu-Cu_2O, and Cu_2O-CuO from emf measurements. Am. Min. 73: 470-486.

O'Neill, H.St.C. and Navrotsky, A. (1984). Cation distribution and thermodynamic properties of binary spinel solid solutions. Am. Min. 69: 733-753.

O'Neill, H.St.C. and Wall, V.J. (1987). The olivine-orthopyroxene-spinel oxygen geobarometer, the nickel precipitation curve, and the oxygen fugacity of the Earth's upper mantle. J. Petrol. 28: 1169-1191.

O'Neill, H.St.C. and Wood, B.J. (1979). An experimental study of Fe-Mg partitioning between garnet and olivine and its calibration as a geothermometer. Contrib. Mineral. Petrol. 70: 59-70.

Ohlsen, W.D. and Shen, L.N. (1974). Hyperfine structures of Fe^{3+} ions in rutile (TiO_2). J. Phys. Soc. Japan 37: 1467.

Osland, R.C.J. (1985). Principles and practices of infrared spectroscopy. Pye Unicam Ltd., Cambridge, England.

Parfenoff, A. (1982). Une mineral traceur pour la prospection alluvionaire: L'ilmenite. Relations entre ilmenites magnesieanes, basaltes alcalins, kimberlites et diamant. BRGM. Doc. Bur. Rech. Geol. Minieres, No. 37.

Pasteris, J.D. (1980). The significance of groundmass ilmenite and megacryst ilmenite in kimberlites. Contrib. Mineral. Petrol. 75: 315-325.

Pattison, D.R.M. (1994). Are reversed Fe-Mg exchange and solid solution experiments really reversed? Am. Min. 79: 938-950.

Pawley A.R., McMillan, P.F. and Holloway, J.R. (1993). Hydrogen in stishovite, with implications for mantle water content. Science 261: 1024-1026.

Pearce, N.J.G. (1990). Zirconium and niobium-bearing ilmenites from the Igaliko dyke swarm, South Greenland. Min. Mag. 54: 585-588.

Peck, D.C. (1990). The platinum-group element geochemistry and petrogenesis of the Heazlewood River Mafic/Ultramafic Complex, Tasmania. Unpubl. PhD Thesis, University of Melbourne, Australia.

Pickney, L. and Lindsley, D.H. (1976). Effects of magnesium on iron-titanium oxides (abstract). Geol. Soc. Am. Abstr. Progr. 8: 1051.

Pouchou, J.L. and Pichoir, F. (1991) Quantitative analysis of homogeneous or stratified microvolumes applying the model "PAP". In K.F.J. Heinrich and D.E. Newbury (eds), Electron probe quantitation. Plenum Press, New York: 31-75.

Pownceby, M.I. and O'Neill, H. St. C. (1995). Thermodynamic data from redox reactions at high temperatures. IV. Calibration of the Re-ReO2 oxygen buffer from EMF and NiO + Ni-Pd redox sensor measurements. Contrib. Mineral. Petrol. 118: 130-137.

Ramsay, R.R. (1992). The geochemistry of diamond indicator minerals. Unpubl. PhD Thesis, University of Western Australia, Australia.

Rock, N.M.S. (1989). Kimberlites as varieties of lamprophyres: implications for geological mapping, petrological research and mineral exploration. In: Ross, J. (ed), Kimberlites and Related Rocks, Vol. 1. Geol. Soc. Aust. Inc. Spec. Publ. No. 14: 46-59.

Rossman, G.R. (1988). Vibrational spectroscopy of hydrous components. In: Hawthorne, F.C. (ed), Spectroscopic methods in mineralogy and geology. Min. Soc. Am. Rev. Min. 18: 183-206.

Rossman, G.R. and Smyth, J.R. (1990). Hydroxyl contents of accessory minerals in mantle eclogites and related rocks. Am. Min. 75: 775-780.

Rumble III, D. (1976). Oxide minerals. Min. Soc. Am. Rev. Min. 3.

Sack, R.O. and Ghiorso, M.S. (1991). Chromian spinels as petrogenetic indicators: thermodynamics and petrological applications. Am. Min. 76: 827-847.

Schulze, D.J. (1984). Cr-poor megacrysts from the Hamilton Branch kimberlite, Elliot County, Kentucky. In: Boyd, F.R. and Meyer, H.O.A. (eds), The mantle sample: Inclusions in kimberlites and other volcanics. Proc. 2nd Int. Kimb. Conf. Vol. 2: 97-108.

Shee, S.R. (1984). The oxide minerals of the Wesselton Mine Kimberlite, Kimberley, South Africa. In: Kornprobst, J. (ed), Kimberlites I: Kimberlites and related rocks. Proc. 3rd Int. Kimb. Conf. Vol. 1: 59-73.

Sigurdsson, I.A., Kamenetsky, V.S., Crawford, A.J., Eggins, S.M. and Zlobin, S.K. (1993). Primitive island arc and oceanic lavas from the Hunter Ridge-Hunter Fracture Zone. Evidence from glass, olivine and spinel compositions. Min. Petrol. 47: 149-169.

Smith, J.V. and Dawson, J.B. (1975). Chemistry of Ti-poor spinels, ilmenites and rutiles from peridotite and eclogite xenoliths. Phys. Chem. Earth 9: 309-322.

Smyth, J.R. (1987). β-Mg_2SiO_4: A potential host for water in the mantle? Am. Min. 72: 1050-1055.

Sobolev, N.V. (1977). Deep-seated inclusions in kimberlites and the problem of the composition of the upper mantle. Am. Geophys. Union Washington D.C.

Sobolev, A.V. and Danyushevsky, L.V. (1994). Petrology and geochemistry of boninites from the north termination of the Tonga Trench: constraints on the generation conditions of primary high-Ca boninite magmas. J. Petrol. 35: 1183-1211.

Soffer, B.H. (1961). Studies of the optical and infrared absorption spectra of rutile crystals. J. Chem. Phys. 35: 940-945.

Spear, F.S. (1993). Metamorphic phase equilibria and pressure-temperature-time paths. Min. Soc. Am. Monograph.

Sweeney, R.J., Thompson, A.B. and Ulmer, P. (1993). Phase relations of a natural MARID composition and implications for MARID genesis, lithospheric melting and mantle metasomatism. Contrib. Mineral. Petrol. 115: 225-241.

Swope, R.J., Smyth, J.R. and Larson, A.C. (1992). Crystal chemistry of hydrogen in rutile of mantle origin (abstract). EOS Trans. Am. Geophys. Union 73: 651.

Taylor, R.W. (1964). Phase equilibria in the system FeO-Fe_2O_3-TiO_2 at 1300 °C. Am. Min. 49: 1016-1030.

Taylor, W.R. (1985). The role of C-O-H fluids in upper mantle processes - a theoretical, experimental and spectroscopic study. Unpubl. PhD Thesis, University of Tasmania, Australia.

Taylor, W.R. and Foley, S.F. (1989). Improved oxygen-buffering techniques for C-O-H fluid saturated experiments at high pressure. J. Geophys. Res. 94: 4146-4158.

Taylor, W.R. and Green, D.H. (1987). The petrogenetic role of methane: effects on liquidus phase relations and the solubility mechanism of reduced C-H volatiles. In: Mysen, B.O. (ed), Magmatic Processes: Physico-chemical Principles. The Geochem. Soc. Spec. Publ. No. 1: 121-138.

Taylor, W.R. and Green, D.H. (1989). The role of reduced C-O-H fluids in mantle partial melting. In: Ross, J. (ed), Kimberlites and Related Rocks, Vol. 1. Geol. Soc. Aust. Inc. Spec. Publ. No. 14: 592-602.

Taylor, W.R. and Green, D.H. (1991). Mineral chemistry of silicate and oxide phases from fertile peridotite equilibrated with a C-O-H fluid phase - a low fO_2 data set for the evaluation of mineral barometers, thermometers and oxygen sensors. In 5th Int. Kimb. Conf., Ext. Abstr.: 417.

Tompkins, L.A. and Haggerty, S.E. (1985). Groundmass oxide minerals in the Koidu kimberlite dikes, Sierra Leone, West Africa. Contrib. Mineral. Petrol. 91: 245-263.

Virgo, D., Luth, R.W., Moats, M.A. and Ulmer, G.C. (1988). Constraints on the oxidation state of the mantle: an electochemical and ^{57}Fe Mössbauer study of mantle-derived ilmenites. Geochim. Cosmochim. Acta. 52: 1781-1794.

Vlassopoulos, D., Rossman, G.R. and Haggerty, S.E. (1993). Coupled substitution of H and minor elements in rutile and the implications of high OH contents in Nb- and Cr-rich rutile from the upper mantle. Am. Min. 78: 1181-1191.

von Hippel A., Kalnajs, J. and Westphal, W.B. (1962). Protons, dipoles and charge carriers in rutile. J. Phys. Chem. Solids 23: 779-799.

von Seckendorff, V. and O'Neill, H. St. C. (1993). An experimental study of Fe-Mg partitioning between olivine and orthopyroxene at 1173, 1273 and 1423 K and 1.6 GPa. Contrib. Mineral. Petrol. 113: 196-207.

Wallace, M.E. and Green, D.H. (1988). An experimental determination of primary carbonatite magma composition. Nature 332: 349-352.

Waychunas, G.A. (1991). Crystal chemistry of oxides and oxyhydroxides. In: Lindsley, D.H. (ed), Oxide minerals: petrologic and magnetic significance. Min. Soc. Am. Rev. Min. 25: 11-68.

Wechsler, B.A. (1977). Cation distribution and high-temperature crystal chemistry of armalcolite. Am Min. 62: 913-920.

Wiser, N.M. and Wood, B.J. (1991). Experimental determination of activities in Fe-Mg olivine at 1400 K. Contrib. Mineral. Petrol. 108: 146-153.

Woermann, E., Hirschberg, A. and Lamprecht, A. (1970). Das System Hämatit-Ilmenit-Geikielith unter hohen Temperaturen und hohen Drucken. Fortsch. Mineral. 47: 79-80.

Wood, B.J. (1990). An experimental test of the spinel peridotite oxygen barometer. J. Geophys. Res. 95: 15845-15851.

Wood, B.J. (1991). Oxygen barometry of spinel peridotites. In: Lindsley, D.H. (ed), Oxide minerals: petrologic and magnetic significance. Min. Soc. Am. Rev. Min. 25: 417-431.

Wood, B.J., Nell, J. and Woodland, A.B. (1991). Macroscopic and microscopic thermodynamic properties of oxides. In: Lindsley, D.H. (ed), Oxide minerals: petrologic and magnetic significance. Min. Soc. Am. Rev. Min. 25: 265-302.

Wood, B.J., Bryndzia, L.T. and Johnson, K.E. (1990). Mantle oxidation state and its relationship to tectonic environment and fluid speciation. Science 248: 337-345.

Wood, B.J. and Virgo, D. (1989). Upper mantle oxidation state: Ferric ion contents of lherzolite spinels by ^{57}Fe Mössbauer spectroscopy and resultant oxygen fugacities. Geochim. Cosmochim. Acta 53: 1277-1291.

APPENDIX A

EXPERIMENTAL DETAILS

A1 Preparation of starting mixes for experimental studies
A2 High pressure-temperature experimental equipment
A3 Oxygen-buffered experiments
A4 Non-buffered experiments
A5 Sample preparation

APPENDIX A

EXPERIMENTAL DETAILS

A1 Preparation of starting mixes for experimental studies

All starting mixes used in the experimental work were prepared from analytical reagent (99-99.9 % purity) or, where analytical reagent was unavailable, laboratory reagent (generally less than 99 % purity) metal oxides. Reagents were weighed and mixed together by grinding to dryness under acetone in an agate pestle and mortar for approximately one hour to achieve homogeneity and a sufficiently small particle size. Mixes were oven dried at 120 °C before being pressed into pellets. The pellets were weighed and fired at 950 °C for 12 hours and cooled to room temperature. Following this the pellets were weighed again and ground under acetone with added fayalite to ensure that all the required iron was present as Fe^{2+} (SiO_2 in fayalite was allowed for in the original mix preparation). The final product was ground under acetone to dryness for approximately one hour and oven dried at 120 °C. All starting mixes were stored in a desiccator.

A2 High pressure-temperature experimental equipment

High pressure-temperature experiments were performed with a 0.5 inch (1.27 cm) piston-cylinder apparatus (e.g. Boyd and England, 1960) using techniques similar to those described by Green and Ringwood (1967), with outer sleeves of NaCl, NaCl-pyrex, talc and talc-pyrex. Pressures with NaCl-sleeved assemblages in the 10-35 kbar range were estimated to have an accuracy of ±(1 % + 0.5) kbar (Mirwald *et al.* 1975). A pressure correction of -10 % of the nominal load pressure was applied to experimental runs using talc sleeves. Temperatures were monitored during the experimental runs with $Pt/Pt_{90}Rh_{10}$ thermocouples and regulated with a Eurotherm Model 818P programmable temperature controller to within ±2 °C of the preset value. When allowance is made for thermal gradients within the high pressure cell as well, the recorded temperatures are within ±10 °C of the desired values. Experiments were run for durations between 6 and 176 hours, with the run time depending on the temperature of the experiment and, where employed, the buffering capacity of the oxygen buffer components.

A3 Oxygen-buffered experiments

The controlled oxygen fugacity experiments used the double capsule technique of Huebner (1971) with oxygen buffering being achieved through both welded and open inner sample

capsules (Figure A1). The oxygen buffers used in the experiments were iron-wüstite (IW), WC-WO_2-graphite (WCWO), wüstite-magnetite (WM), Ni-NiO (NNO), and Fe_2O_3-Fe_3O_4 (HM). The chemical equations describing the oxygen equilibria for these buffers are given in Table A1.

Table A1: Chemical equilibria for the oxygen buffers used in this work.

IW	$2\ Fe_xO = 2x\ Fe + O_2$
WCWO	$WO_2 + C = WC + O_2$
WM	$^{2x}/_{(4x-3)}\ Fe_3O_4 = {}^{6}/_{(4x-3)}\ Fe_xO + O_2$
EMOG	$MgSiO_3 + MgCO_3 = Mg_2SiO_4 + C + O_2$
FMQ	$2\ Fe_3O_4 + 3\ SiO_2 = 3\ Fe_2SiO_4 + O_2$
NNO	$2\ NiO = 2\ Ni + O_2$
HM	$6\ Fe_2O_3 = 4\ Fe_3O_4 + O_2$

Notes: The EMOG buffer (enstatite-magnesite-forsterite-graphite) of Eggler and Baker (1982) has been used in places as a comparison to illustrate some of the experimental and natural analytical data.

The equations for calculating oxygen fugacity values (fO_2) for experimental conditions at known pressures and temperatures are given in Table A2. Where values for fO_2 in this thesis are reported with reference to the fayalite-magnetite-quartz (FMQ) buffer, they are quoted as $\Delta \log fO_2$ (FMQ) log units.

Table A2: Equilibrium equations for calculation of log fO_2 values for some common oxygen buffers from pressure and temperature data.

Buffer	Equilibrium Equation	Reference
IW	14.07 - 28784/T - 2.04logT + 53P/T + 0.003P	O'Neill, 1987a
WCWO	14.33 - 29105/T - 1.56logT + 66P/T	Taylor and Foley, 1989
WM	-3.43 - 30392/T + 4.66logT + 84.1P/T - $1E^{-3}$P	O'Neill, 1987a
EMOG	7.83 - 23781/T + 53.5P/T - $8E^{-4}$P	Eggler and Baker, 1982
FMQ	82.75 + 0.00484T - 30681/T - 24.45logT +94P/T - 0.002P	O'Neill, 1987a
NNO	12.78 - 25073/T - 1.1logT + 45P/T + 0.0025P	O'Neill, 1987b
HM	14.91 - 26184/T + 20P/T - 0.005P	Hemingway, 1990

Notes: Pressures are in kbars and temperatures are in °K. Pressure corrections are from standard molar volume and thermal expansion data. The Hemingway (1990) equilibrium equation for the HM oxygen buffer requires a correction for unit activity of magnetite (e.g. O'Neill, 1988; O'Neill, pers. comm.).

The fugacity values of the oxygen buffer experiments using the double capsule technique are fixed by equilibration of fluid with the solid phases that make up the buffer. Oxygen fugacities are maintained at a near constant value while the mineral phases under investigation react and equilibrate according to the physical conditions (P,T, fO_2) for the

Figure A1: (A) Schematic diagram (not to scale) of the double-capsule assemblies used in oxygen-buffered experiments. Both assembly types described below use a 5.56 mm ($^{7}/_{32}$") internal diameter graphite heater, fitted with boron nitride inserts to surround the outer metal capsule and admit the thermocouple to the assembly. (B) The experimental sample mix is contained in an inner (3.0 mm O.D.) capsule of graphite (e.g. IW and WCWO buffers) or San Carlos olivine (e.g. NNO buffer), and isolated from the buffer mixture by close-fitting lids and discs. The fluid source is water (or stearic acid in case of the WCWO buffer). An outer Pt or $Ag_{50}Pd_{50}$ capsule is sealed by arc-welding. (C) For experiments employing the HM and WM buffers, the experimental sample mix is contained in an inner metal capsule (2.3 mm O.D.) which is enclosed (within the buffer mixture) in an outer Pt or $Ag_{50}Pd_{50}$ capsule. Both capsules are sealed by arc-welding. The fluid source is water.

Note: For single capsule, unbuffered hydrous experiments (not shown) a 3.97 mm ($^{5}/_{32}$") internal diameter graphite heater is used, with boron nitride inserts. For dry experiments (not shown) a 3.18 mm ($^{1}/_{8}$") internal diameter graphite heater is used, with Al_2O_3 capsule surrounds and mullite/fired pyrophyllite spacers as inserts.

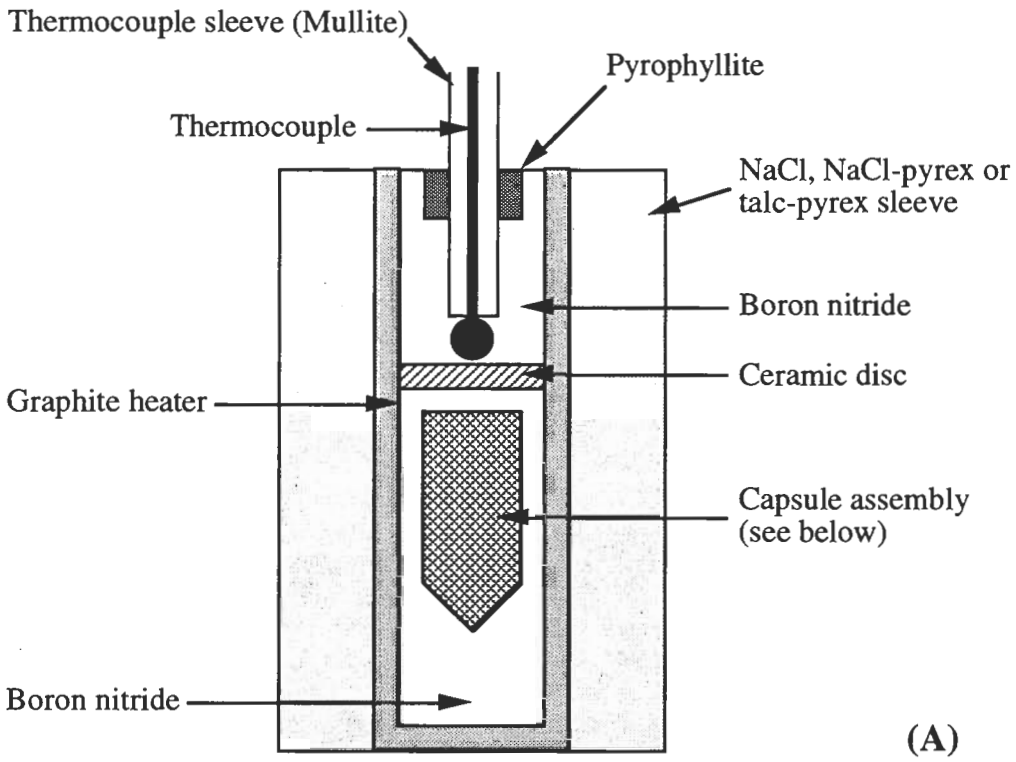
Thermocouple sleeve (Mullite)
Pyrophyllite
Thermocouple
NaCl, NaCl-pyrex or talc-pyrex sleeve
Boron nitride
Ceramic disc
Graphite heater
Capsule assembly (see below)
Boron nitride
(A)

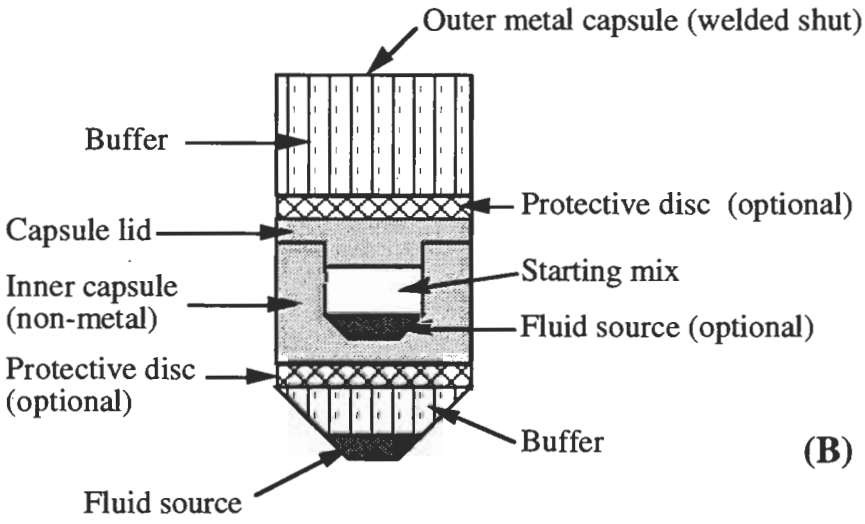
Outer metal capsule (welded shut)
Buffer
Protective disc (optional)
Capsule lid
Starting mix
Inner capsule (non-metal)
Fluid source (optional)
Protective disc (optional)
Buffer
Fluid source
(B)

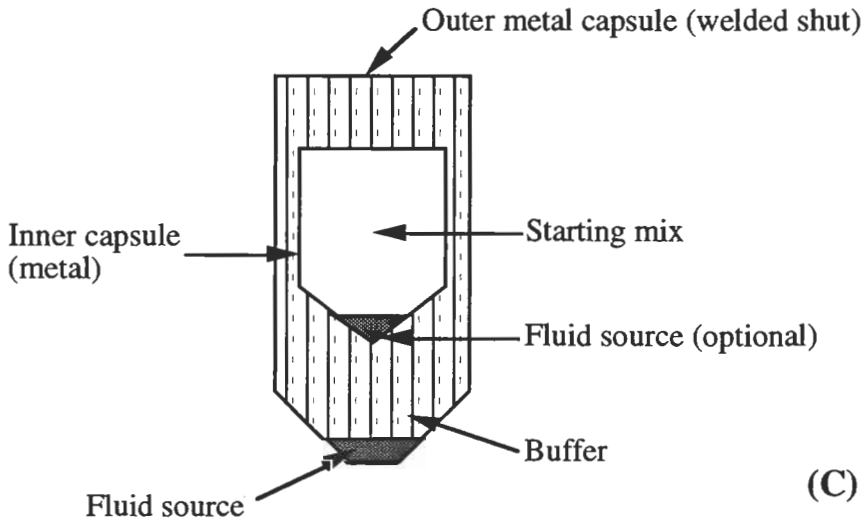
Outer metal capsule (welded shut)
Inner capsule (metal)
Starting mix
Fluid source (optional)
Buffer
Fluid source
(C)

sample mix was contained in olivine capsule cylinders (height 4 mm, outer diameter 3 mm, inner diameter 2 mm) and covered by olivine powder and an olivine lid. This inner capsule assembly was sealed in an outer Pt or $Ag_{50}Pd_{50}$ capsule. The use of protective olivine lids prevented any contamination of the sample mix by the buffer components. The buffer mix consisted of Ni-NiO made up in a 1:5 mol ratio. The fluid was pure H_2O added by microsyringe to the buffer (~1 µl) and sample (~0.5 µl). The use of olivine capsules in this buffer assembly has some advantages over more conventional double capsule techniques. Redox equilibria are achieved very rapidly because the fluid equilibrates directly with the buffer and the sample and, as a result, run times are shorter (~25-40 % of conventional double capsule run times). Iron loss to the capsule has been eliminated and sample contamination was not encountered. However, due to the high a_{H2O} of the system, small degrees of melting of the sample mix may be encountered in higher temperature experimental runs (e.g. Ballhaus *et al.*, 1991).

Experiments conducted with the WM oxygen buffer used $Ag_{50}Pd_{50}$ or $Ag_{75}Pd_{25}$ inner capsules, and $Ag_{50}Pd_{50}$ or Pt outer capsules. The use of the metal alloy inner capsules minimises iron loss from the sample mix. The sample mix was contained in the welded inner metal capsule together with ~3 wt.% H_2O. This inner assembly was placed in the outer capsule and surrounded by a mix of wüstite:magnetite (made up in a 9:1 mol ratio) containing ~2-3 wt.% H_2O, and the outer capsule was sealed. Buffering was achieved by the thermal decomposition of H_2O and the exchange of H_2 between buffer and sample through the inner semi-permeable metal capsule walls.

The highest oxygen fugacities were generated with the use of the HM buffer. As for the WM experiments, a double metal-capsule technique was also used for this buffer as non-metal capsules are no longer stable. The sample mix was contained in a $Ag_{50}Pd_{50}$ or $Ag_{75}Pd_{25}$ welded inner metal capsule together with ~3 wt.% H_2O. The inner assembly was placed in a $Ag_{50}Pd_{50}$ or Pt outer capsule and surrounded by a mix of hematite:magnetite (made up in a 9:1 mol ratio) containing ~2 wt.% H_2O, and the outer capsule was sealed. Oxygen buffering was achieved by the thermal decomposition of H_2O and the exchange of H_2 between buffer and sample through the inner semi-permeable metal capsule walls. The hematite:magnetite ratio progressively decreased with time but exhaustion of the buffer was never visibly observed.

Some oxygen buffer experiments were conducted under graphite-water (GW) or graphite-CO_2-CO (GCO) conditions. These 'furnace-buffers' do not act like an oxygen buffer sensu stricto but rather define a fixed point on the system C-O-H-graphite saturation curve in P-T-fO_2 space (e.g. Taylor, 1985). For these GW and GCO 'buffer' experiments, sample mix and a fluid source (~0.5-1.5 µl H_2O) were contained in an inner graphite capsule enclosed in a welded Pt or $Ag_{50}Pd_{50}$ capsule. Graphite powder was used to surround the inner

duration of the experiment. The requirements of oxygen buffering are: (i) the capsule material does not react with the buffer components or the sample mix; (ii) the buffer components do not infiltrate the sample mix as a result of high element mobility under fluid rich conditions, and (iii) iron loss from the sample mix is avoided. To achieve these requirements protective lids (metal, silicate or graphite) were inserted between the buffer component and the inner capsule where these capsules were open (e.g. graphite and olivine capsules). The use of non-metal capsules also avoided Fe loss from the sample mix. At very high oxygen fugacity conditions where the non-metal capsules are chemically unstable, $Ag_{50}Pd_{50}$ or $Ag_{75}Pd_{25}$ welded inner metal capsules were used to minimise Fe loss. The relatively large oxygen fugacity 'gap' between the NNO and HM buffers was attempted to be bridged by the use of the $Mn_{1-x}O$-Mn_3O_4 buffer (e.g. Huebner and Sato, 1970). However, this buffer proved unsuitable on account of Mn mobility in this buffer system. Manganese-rich ilmenites were detected in mineral systems that equilibrated from Mn-free chemical starting mixes. Pownceby and O'Neill (1995) documented a low temperature (850–1250 °K) Re-ReO_2 oxygen buffer which bridges the oxygen fugacity gap between the NNO and HM buffers. However, the low temperature operating range of this buffer render it inappropriate for higher temperature experiments in this study.

Experiments with the IW buffer were carried out in inner graphite capsules enclosed in a welded outer Pt or $Ag_{50}Pd_{50}$ capsule. The buffer was separated from the inner graphite capsule by Pt protective lids. The volatile component of the buffer was generated by the addition of ~5 wt.% stearic acid ($C_{18}H_{36}O_2$, octadecanoic acid, m.p. 71.2 °C). The thermal decomposition of stearic acid under IW fO_2 conditions generates a fluid predominantly consisting of CH_4>>H_2O. Several anhydrous experiments were also conducted under IW oxygen fugacity conditions. In these experiments the starting mix was contained in an iron capsule, which was enclosed in a graphite heater, with Al_2O_3 capsule surrounds.

Experiments with the WCWO buffer used a technique modified from that described by Taylor and Foley (1989). The sample was contained in an inner graphite capsule and sealed in a welded outer $Ag_{50}Pd_{50}$ or Pt capsule. The inner capsule was isolated from the buffer mix by graphite protective lids. In some early experiments W was detected in synthetic rutile products and the subsequent use of protective lids was found to diminish such sample contamination. The buffer consisted of a mix of W-WO_3-C made up in a 29:1:70 mol ratio. Stearic acid (~3–5 wt.%) was added to the buffer material and the equilibrium fluid generated under WCWO conditions was CH_4-H_2O (Taylor and Green, 1987b).

Oxygen fugacity conditions around FMQ are generated by the use of the NNO buffer. At these buffer conditions, graphite capsules are no longer stable and, with low $Fe^{3+}/\sum Fe$ ratios, the use of metal capsules with accompanying iron loss is considered less than ideal. Instead, experiments were carried out in capsules made of San Carlos Olivine (Fo_{90}). The

graphite capsule and a small amount of H_2O (~0.5 µl) was added to provide part of the volatile component. The exact position in P-T-fO_2 space was determined by analysing the composition of the resultant experimental C-O-H fluid phase using a capsule piercing technique and mass spectrometry (see Appendix B6). The experimental log fO_2 value was calculated from the end-member equations according to the composition of the fluids. The GCO and GW 'buffers' are given by the following equations applicable over the range 5-50 kbar, 800-1700 °K:

$$\log fO_2 = a + b\ln T + c/T + d(P/T) + e(P/T)^2$$

	a	b	c	d	e
GCO	2.0815	2.5754×10^{-1}	-21060	0.17112	-7.4268×10^{-4}
GW	5.0186	-6.5844×10^{-2}	-22674	0.12858	-6.6384×10^{-4}

with P in bars and T in °K (Taylor, 1985).

A4 Non-buffered experiments

The rutile-cation-water experiments (Chapter 5) were carried out using single capsule, non-buffered, hydrous and dry experimental assemblies, as well as oxygen buffered double capsule assemblies. For the dry runs, the sample mix was placed in a small diameter (2.3 mm outer diameter) welded Pt capsule; for the hydrous runs sample mix and H_2O (5-10 wt.%) were placed in a small diameter (2.3 mm outer diameter) welded Pt, $Ag_{50}Pd_{50}$ or $Ag_{75}Pd_{25}$ capsule. The metal capsules were contained in graphite heaters and NaCl, NaCl-pyrex, talc and talc-pyrex assemblies were used as pressure media. The experimental technique and equipment have been described in detail in Appendix A2.

A5 Sample preparation

Experimental run products were removed from capsule containers and some material was optically inspected under an immersion oil of accurately known refractive index (RI) to identify mineral phases and to ensure that buffer exhaustion had not occurred. Probe mounts of experimental run products and mineral grain concentrates under investigation were made using cold-set epoxy. Great care was taken to obtain a high quality polish, using successively finer grades of diamond polishing paste. Rock samples were studied as polished thin sections of 30 µm thickness. Mineral samples and experimental run products studied by FTIR (see Appendix B4) were prepared as doubly polished sections of 30-100 µm thickness.

APPENDIX B

ANALYTICAL DETAILS

B1 Electron probe microanalysis (EPMA) - major element analyses
B2 Scanning electron microscopy (SEM)
B3 Fourier transform infrared spectroscopy (FTIR)
B4 X-ray diffraction spectrometry (XRD)
B5 Elemental analysis
B6 Mass spectrometry
B7 Mössbauer spectroscopy

APPENDIX B

ANALYTICAL DETAILS

B1 Electron probe microanalysis (EPMA) - major element analyses

Oxide mineral concentrates, mineral phases in thin sections, and all mineral phases in experimental runs were analysed at the Central Science Laboratory, University of Tasmania, using a Cameca SX-50 electron probe microanalyser (EPMA) equipped with one inclined and two vertical wavelength-dispersive spectrometers (WDS) with a total of eight analyzing crystals.
Two multi-purpose analytical labels were designed to analyse the major element cation content of minerals. A 'silicate' label was programmed specifically to analyse silicate minerals, and elements included in the label were calibrated on primary silicate and oxide mineral standards of known composition (Table B1). A separate 'oxide' label was programmed to analyse oxide minerals and included the same elements as the silicate label but with calibrations mainly performed on primary oxide standards of known compositions (Table B1).

Analyses were performed at 15 kV accelerating voltage, a beam current of 20 nA, and a focussed beam diameter varying from 1 to 10 μm, generally at a 20,000x magnification. All elements were analysed at 20 seconds on the peak and 10 seconds on the background. Concentrations were calculated from relative peak intensities using the PAP matrix correction procedure incorporated in the Cameca software.

The analytical labels were checked before and after each EPMA session using appropriate primary and secondary standards. Data corrections were made by adjusting the analytical results when a systematic shift or standard drift occurred between two adjacent sets of standard analyses. A list of primary and secondary standard compositions used for analytical work is presented in Table B2.

The Mg-rich ilmenite secondary standard from the Monastery kimberlite (South Africa) was also analysed at the Electron Microscopy Centre, University of Western Australia. The mineral was analysed using a JEOL 6400 scanning electron microscope using a Link EDS system. Analytical conditions were 15 kV accelerating voltage, a beam current of 3 nA, and a 60 seconds count time. Mineral X-ray data were corrected using standard correction procedures of N. Ware.

Table B2: Analytical details of primary and secondary silicate and oxide standards.

	Primary Mineral Standards		Secondary Mineral Standards				
	USNM 111312 Mg-olivine	USNM 117075 chromite	Olivine	Rutile	Ilmenite (Cameca)	Ilmenite (JEOL)	Chromite
SiO_2	40.81		40.48				0.07
TiO_2				98.97	48.69 (0.23)	48.93 (0.21)	
Al_2O_3		9.92	0.11		0.33 (0.04)	0.36 (0.05)	3.26
Cr_2O_3		60.50	0.17	0.06	0.68 (0.05)	0.72 (0.06)	66.50
Fe_2O_3		3.45			12.44 (0.27)	12.25 (0.23)	3.84
FeO		9.93			28.48 (0.22)	28.54 (0.19)	11.74
FeO_{total}	9.55	13.04	10.21	0.29	39.68 (0.25)	39.57 (0.21)	15.19
MnO	0.14	0.11	0.12		0.21 (0.06)	0.30 (0.06)	
MgO	49.42	15.20	47.75		8.42 (0.12)	8.50 (0.12)	13.30
CaO			0.20				
ZnO							0.09
NiO	0.37		0.47		0.08 (0.04)		0.11
Total	100.29	99.12	99.51	99.32	99.34	99.61	98.52
$Fe^{3+}/\sum Fe$ (calculated)		0.238			0.282 (0.03)	0.279 (0.03)	0.228
$Fe^{3+}/\sum Fe$ (Mössbauer)				0.420 (0.05)	0.300 (0.05)	0.300 (0.05)	

Notes: Major element analyses are reported in wt.%. Values in brackets represent standard deviations. Primary standards are quoted from Jarosewich et al. (1980). The olivine secondary standard is from a Hawaiian picrite, the rutile secondary standard is from a quartz vein in an eclogite from Czechoslovakia, the ilmenite secondary standard is a xenocryst from the Monastery kimberlite, South Africa, and the spinel secondary standard is from a boninite from the Heazlewood ultramafic complex, western Tasmania. Secondary standards' major element values were calculated from multiple EPMA analyses (n = 20+) conducted on the Cameca SX-50 electron microprobe at Melbourne University and the University of Tasmania. The ilmenite secondary standard was also analysed on the JEOL 6400 scanning electron microprobe at the University of Western Australia. The $Fe^{3+}/\sum Fe$ (Mössbauer) ratios were determined by Mössbauer spectroscopy at the School of Mathematical and Physical Sciences at Murdoch University, Western Australia.

Table B1: Analytical labels used for analysing major elements in silicate and oxide minerals.

Silicate Label			
Element	Crystal	Mineral Standard	Detection Limit
Mg K_α	TAP	USNM 111312 Mg-olivine	0.060 wt.%
Al K_α	TAP	USNM 657S synthetic corundum	0.015 wt.%
Si K_α	TAP	USNM R17701 quartz	0.020 wt.%
Ti K_α	PET	Astimex MIMN 25-53 rutile	0.045 wt.%
Cr K_α	PET	USNM 117075 chromite	0.065 wt.%
Mn K_α	LiF	Astimex MIMN 25-53 rhodonite	0.090 wt.%
Fe K_α	LiF	USNM 85276 fayalite	0.070 wt.%
Ni K_α	LiF	Astimex MIMN 25-53 nickelsilicide	0.085 wt.%
Zn K_α	LiF	USNM 111989 gahnite	0.170 wt.%

Oxide Label			
Element	Crystal	Mineral Standard	Detection Limit
Mg K_α	TAP	USNM 117075 chromite	0.045 wt.%
Al K_α	TAP	USNM 111989 gahnite	0.015 wt.%
Si K_α	TAP	USNM R17701 quartz	0.020 wt.%
Ti K_α	PET	Astimex MIMN 25-53 rutile	0.050 wt.%
Cr K_α	PET	USNM 117075 chromite	0.085 wt.%
Mn K_α	LiF	Astimex MIMN 25-53 rhodonite	0.120 wt.%
Fe K_α	LiF	USNM 96189 ilmenite	0.090 wt.%
Ni K_α	LiF	Astimex MIMN 25-53 nickelsilicide	0.100 wt.%
Zn K_α	LiF	USNM 111989 gahnite	0.215 wt.%

Notes: Detection limits are calculated according to counting times, background counts, standard compositions and physical conditions of analytical labels.

B2 Scanning electron microscopy (SEM)

All scanning electron microscopy was conducted using a Phillips 505 Scanning Electron Microscope at the Central Science Laboratory University of Tasmania. An accelerating voltage of 20 or 25 kV was used. SEM was used to examine mineral textures, and in photography of back scattered electron images of experimental run products.

B3 Fourier transform infrared spectroscopy (FTIR)

The water content of natural and experimental rutiles was investigated by Fourier transform infrared spectroscopy using a Digilab model FTS-20E spectrometer (up to December 1993) and a Brucker IFS 66 spectrometer (after January 1994). Both spectrometers were connected to an optical microscope with a 40x objective lens, and were equipped with an interactive operating system and software to perform a number of tasks including automatic scaling, smoothing, spectrum subtraction and peak integration.

Spectra acquisition of samples over the mid-IR region (4000–400 cm^{-1}) was obtained at a resolution of 4 cm^{-1} and usually 128 scans on a sample and background were performed per analysis. A variable aperture attached to the optical microscope ensured that typical sample spot diameters ranged from 15 to 50 μm.

Sample thickness was calculated from interference fringes generated by double reflection in samples (Figure B1, e.g. Osland, 1985). Interference fringes are generated when sample sides are parallel, and the fringes can be observed over most of the wavelength range. The intervals over which the fringes occurred were checked over several parts of the wavelength range in order to ensure that a consistent thickness of a sample was calculated. Thickness calculations were estimated with an accuracy of ±5 %.

B4 X-ray diffraction spectrometry (XRD)

Some experimental run products were analysed by X-ray diffraction at the Department of Mineral Resources of Tasmania using an automated Philips X-ray diffractometer system consisting of a generator (model PW 1729), a goniometer (model PW 1050), a PW 1710 printing recorder and microprocessor, a graphite monochromator (model PW 1752), a sample spinner and a sealed, gas filled, proportional detector (model PW 1711). The electron beam was generated by a nickel-filtered copper radiation X-ray tube operating at 40 kV and 30 nA.

The samples were calibrated against an internal natural quartz standard. The qualitative mineralogy was determined by manual search-match methods. The six strongest peaks on iron-titanium oxides were used for cell dimension refinement, using the Excel templates of Novak and Coville (1989). X-ray diffraction data was interpreted by Mr. R. Bottrill of the Department of Mineral Resources of Tasmania.

B5 Elemental analysis

Experimental rutiles (see Chapter 5 herein) were analysed for their water content using a Carlo Erba Elemental Analyser model EA 1108 at the Central Science Laboratory University of Tasmania. Equipment set up was in standard run mode. Samples selected for analysis were dried at 120 °C in a conventional oven. Samples were then weighed to 0.1 μg in a pre-weighed silver cup, crimped and crushed. Analyses were made at 1000 °C using flash combustion of sample and container under pure oxygen conditions. Acetanilide ($C_6H_5NHCOCH_3$, m.p. 114 °C) with 6.67 wt.% H was used as a standard before, during and after analyses of the unknown samples and the elemental contents of

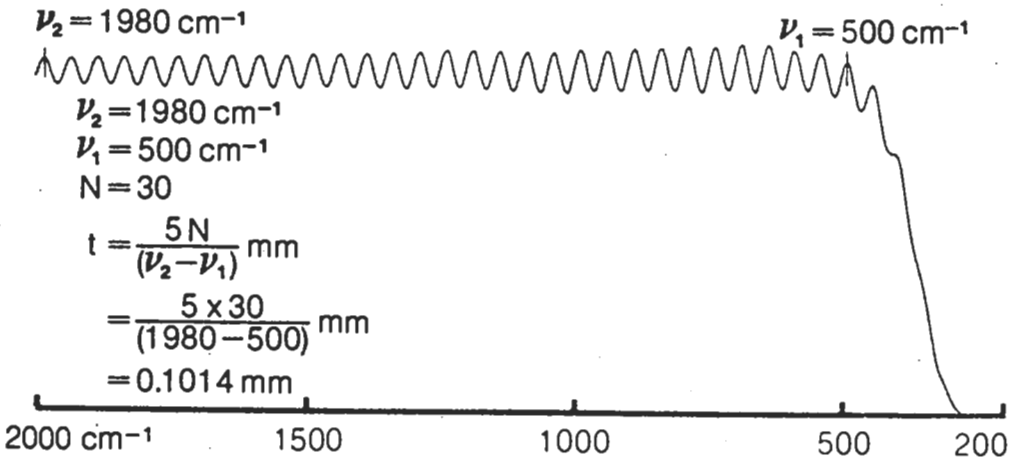

Figure B1: Calculated example for the determination of sample thickness from I.R. interference fringes generated by double reflection (from Osland, 1985). Thickness calculations are determined with an accuracy of ±5 %.

samples were calculated by peak integration. The elemental analyses were determined with an accuracy of ±10 %.

B6 Mass spectrometry

The nature of C-H-O buffer volatiles in some experimental run products was studied at the Central Science Laboratory University of Tasmania by mass spectrometry using a capsule piercing technique.

Capsules were pierced using a modified regulating valve (Whitey #SS-1VS6, stainless steel) with a redesigned stem tip fashioned into a hardened needle point (e.g. Taylor, 1985). The capsule piercing device was directly coupled to the mass spectrometry ion source via fixed silica tubing. The entire capsule piercing assembly and tubing was heated in an HP 5890 GC oven to 110 °C and gases were released under vacuum (~10^{-7} torr) into the ion source of the mass spectrometer. A VG-micromass 7070 double focussing mass spectrometer was used up to 1993. A Kratos Concept ISQ double focussing mass spectrometer was used from 1993 onwards. With the VG-micromass 7070 instrument mass spectra were obtained by multiple scans of ~2 sec duration over the mass/charge (m/z) range 10-70. With the Kratos Concept ISQ instrument mass spectra were measured by accurate mass scans of 1 sec/decade over the range 10-70 m/z. Evacuation and heating of the entire assembly for ~1 hour was deemed necessary to obtain low background levels, particularly with H_2O adsorption on graphite and metal capsule surfaces. The total ion current was monitored during the piercing procedure and both background and sample spectra were recorded at various sensitivities. Methane, CO_2 and any other C-based gases were released quickly but water was released more slowly due to adsorption on the capsule surfaces. Mass spectra were collected for ~40 min until the H_2O level had returned to the background levels obtained prior to capsule piercing. Mass spectra were interpreted by Dr. W.R. Taylor.

B7 Mössbauer spectroscopy

Mössbauer spectroscopy of some oxide minerals was performed and interpreted by Dr. T. St. Pierre of the School of Mathematical and Physical Sciences at Murdoch University. Samples were prepared at the University of Tasmania.

Mineral concentrate samples selected for Mössbauer study were coarse crushed between layers of calico material in a large steel pestle and mortar and then pulverized to powder in an agate ring mill. The powders were cleaned of silicate impurities in ~10 % HF acid and

rinsed with distiled water. At the Mössbauer laboratory, samples were diluted by mixing with fine sucrose powder. A sample with an Fe density equal to 10 μg Fe cm^{-2} was prepared for spectroscopy work.

The Fe^{2+}/Fe^{3+} ratio for a sample was determined using Mössbauer spectroscopy in transmission mode at room temperature. Mössbauer spectra were recorded using a 1024 channel analyser in constant acceleration mode with a symmetric double ramp waveform and were subsequently folded to eliminate the parabolic background. A 20 mCi ^{57}Co in a rhodium matrix source was used. The velocity scale was calibrated with reference to the spectrum of an α-iron foil at room temperature with the centre of the six line pattern taken as zero velocity.

The resulting Mössbauer spectra were fitted with Lorentzian peaks using the model of Dyar *et al.* (1989). The standard error on values obtained by using this model is ± 3-5 % (Dr. St. Pierre, pers. comm.).

APPENDIX C

ELECTRON PROBE MICROANALYSES FOR OXYGEN

C1 Diamond-indicator spinels
C2 Spinel inclusions in olivine from primitive subduction related magmas
C3 Spinels from metamorphosed volcanics
C4 Mg-rich ilmenite xenocrysts from kimberlites

Appendix C1

No.	1	2	3	4	5	6	7	8	9	10
Sample	Argyle	Argyle	Argyle	Argyle	Argyle	Aries	Aries	Aries	Aries	Aries
Grain No.	B1	B2	B3	B4	B5	5	6	8	9	11
Type	Lmp	Lmp	Lmp	Lmp	Lmp	Kmb	Kmb	Kmb	Kmb	Kmb
Si	0.04	0.03	0.04	0.05	0.04	0.02	0.01	0.02	0.01	0.02
Ti	0.02	0.02	0.02	0.02	0.02	0.02	0.03	0.00	0.19	0.23
Al	1.68	2.27	2.24	2.30	2.27	6.17	6.52	4.89	5.38	5.99
Cr	47.88	46.88	46.87	46.89	46.51	41.75	41.12	43.74	42.71	40.65
V	0.10	0.08	0.09	0.09	0.09	0.12	0.13	0.10	0.13	0.12
Fe	10.41	10.55	10.82	10.54	10.71	10.42	10.56	10.94	10.31	11.52
Mg	7.38	7.38	7.37	7.32	7.37	7.78	7.78	7.25	7.39	7.29
Mn	0.18	0.22	0.20	0.23	0.26	0.22	0.19	0.20	0.17	0.26
Ni	0.07	0.05	0.03	0.03	0.06	0.07	0.03	0.08	0.06	0.06
Zn	0.01	0.03	0.08	0.06	0.07	0.11	0.08	0.11	0.08	0.07
O	31.89	31.69	32.04	32.06	31.48	33.44	32.54	32.53	33.01	32.77
Total	99.66	99.21	99.81	99.59	98.87	100.12	98.98	99.86	99.45	98.52
Ocalculated	31.62	31.72	31.80	31.72	31.65	33.06	33.10	32.62	32.61	32.53
ΔO	0.28	-0.04	0.24	0.34	-0.18	0.38	-0.56	-0.09	0.40	0.24
Σcations	2.999	3.001	3.003	2.999	3.004	2.997	2.998	2.994	2.987	3.000
Omin	31.62	31.72	31.77	31.72	31.61	33.06	33.10	32.62	32.61	32.53
Omax	33.11	33.23	33.32	33.23	33.14	34.55	34.61	34.19	34.09	34.18
FeO (real)	10.91	13.58	11.50	10.50	13.78	9.99	13.59	14.08	9.69	12.64
Fe2O3 (real)	2.75	0.00	2.69	3.40	0.00	3.80	0.00	0.00	3.97	2.42

Appendix C1

No.	11	12	13	14	15	16	17	18	19
Sample	Aries	Aries	Aries	Roberts Victor	Roberts Victor	Roberts Victor	Roberts Victor	Roberts Victor	Roberts Victor
Grain No.	12	13	14	008	104	301	303	402	406
Type	Kmb	Kmb	Kmb	Kmb	Kmb	Kmb	Kmb	Kmb	Kmb
Si	0.05	0.02	0.02	0.01	0.01	0.01	0.01	0.05	0.03
Ti	0.14	0.03	0.08	0.20	0.03	0.09	0.14	0.18	0.11
Al	3.41	5.81	4.86	4.81	5.17	5.48	5.07	3.14	4.38
Cr	45.71	42.20	43.81	41.16	41.99	41.72	42.37	43.69	44.15
V	0.16	0.12	0.11	0.12	0.11	0.10	0.12	0.07	0.20
Fe	9.77	10.63	10.34	13.81	11.53	10.92	11.86	12.69	10.54
Mg	7.25	7.63	6.73	6.83	7.97	8.40	7.92	7.90	7.93
Mn	0.22	0.22	0.23	0.31	0.22	0.29	0.28	0.28	0.24
Ni	0.04	0.06	0.07	0.02	0.05	0.07	0.05	0.13	0.06
Zn	0.09	0.10	0.15	0.08	0.15	0.05	0.07	0.05	0.04
O	31.94	32.59	32.62	32.08	32.81	32.98	32.36	32.28	32.79
Total	99.63	98.86	99.02	99.42	100.02	100.11	100.26	100.48	100.47
Ocalculated	32.02	32.91	32.19	32.26	32.93	33.24	33.14	32.51	32.85
ΔO	-0.08	-0.32	0.43	-0.18	-0.12	-0.26	-0.78	-0.23	-0.06
Σcations	2.983	2.997	2.976	3.020	3.019	3.019	3.018	3.035	3.004
Omin	32.02	32.91	32.19	32.04	32.72	33.02	32.95	32.14	32.81
Omax	33.42	34.44	33.67	34.02	34.37	34.59	34.65	33.96	34.32
FeO (real)	12.57	13.68	9.45	17.39	14.07	14.05	15.25	15.05	13.56
Fe2O3 (real)	0.00	0.00	4.28	0.41	0.85	0.00	0.00	1.42	0.00

Appendix C1

No.	20	21	22	23	24	25	26	27
Sample	Roberts Victor	Roberts Victor	Makganyene	Makganyene	Makganyene	Makganyene	Makganyene	Makganyene
Grain No.	408	410	002	004	006	103	105	208
Type	Kmb	Kmb	Kmb	Kmb	Kmb	Kmb	Kmb	Kmb
Si	0.03	0.04	0.01	0.03	0.05	0.03	0.03	0.03
Ti	0.04	0.16	0.07	0.27	0.13	0.65	0.22	0.25
Al	3.56	3.96	5.04	3.82	4.01	3.64	4.51	3.81
Cr	43.54	44.05	42.03	42.27	41.90	41.32	42.61	41.63
V	0.11	0.12	0.10	0.10	0.10	0.10	0.10	0.10
Fe	12.26	10.35	10.18	12.90	12.44	13.66	10.78	14.35
Mg	7.75	8.39	8.56	7.69	8.09	7.51	8.45	7.01
Mn	0.28	0.11	0.22	0.22	0.21	0.30	0.18	0.25
Ni	0.05	0.06	0.06	0.07	0.08	0.12	0.10	0.09
Zn	0.08	0.11	0.05	0.08	0.05	0.05	0.04	0.00
O	32.82	33.27	33.45	32.13	32.57	32.00	33.33	32.00
Total	100.53	100.62	99.76	99.58	99.63	99.37	100.35	99.53
Ocalculated	32.41	32.77	32.83	32.36	32.48	32.17	32.86	32.03
ΔO	0.41	0.50	0.62	-0.23	0.09	-0.17	0.47	-0.03
Σcations	3.028	3.014	3.019	3.031	3.037	3.034	3.020	3.034
Omin	32.11	32.62	32.63	32.03	32.08	31.81	32.64	31.68
Omax	33.87	34.11	34.08	33.88	33.87	33.77	34.19	33.74
FeO (real)	9.35	7.54	5.71	15.67	11.67	15.88	7.70	15.60
Fe2O3 (real)	7.15	6.41	8.21	1.03	4.82	1.88	6.85	3.18

Appendix C1

No.	28	29
Sample	Makganyene	Makganyene
Grain No.	209	307
Type	Kmb	Kmb
Si	0.04	0.01
Ti	0.34	0.19
Al	2.79	4.87
Cr	42.11	41.43
V	0.13	0.17
Fe	14.78	13.43
Mg	7.18	7.18
Mn	0.30	0.18
Ni	0.09	0.05
Zn	0.13	0.10
O	31.55	32.29
Total	99.44	99.91
Ocalculated	31.86	32.56
ΔO	-0.31	-0.27
Σcations	3.048	3.021
Omin	31.35	32.33
Omax	33.47	34.26
FeO (real)	17.22	17.28
Fe2O3 (real)	1.99	0.00

Appendix C2

No.	1	2	3	4	5	6	7	8	9	10
Sample No.	5-24 OL3A-SPC	5-24 OL3-SP	5-24 OL3A-SPA	5-24 OL3A-SPB	5-24 OL4-SPA	5-24 OL4-SPB	5-24 OL7-SP	5-24 OL8-SP	5-24 OL13-SP	5-24 OL13A-SP
Type	Bon	Bon	Bon	Bon	Bon	Bon	Bon	Bon	Bon	Bon
Si	0.03	0.03	0.03	0.03	0.04	0.05	0.05	0.03	0.04	0.03
Ti	0.06	0.07	0.05	0.07	0.05	0.04	0.05	0.05	0.04	0.05
Al	3.45	3.29	3.47	3.39	3.28	3.23	3.34	3.43	3.26	3.20
Cr	41.24	41.97	40.94	41.52	44.21	43.03	43.18	40.58	43.60	43.64
Fe	15.54	15.44	15.41	15.45	10.72	11.13	11.41	15.69	11.50	11.51
Mg	7.07	7.07	6.89	6.95	8.43	8.25	8.79	6.97	8.80	8.62
Mn	0.23	0.20	0.22	0.24	0.16	0.17	0.18	0.20	0.17	0.15
Ni	0.06	0.06	0.05	0.04	0.04	0.09	0.09	0.07	0.09	0.11
Zn	0.03	0.06	0.01	0.14	0.09	0.04	0.03	0.10	0.07	0.01
O	32.08	32.06	32.25	32.15	33.15	32.71	32.97	32.32	32.31	32.78
Total	99.79	100.26	99.33	99.98	100.17	98.73	100.10	99.43	99.88	100.10
Ocalculated	32.01	32.16	31.68	31.96	32.43	31.91	32.66	31.69	32.80	32.59
ΔO	0.07	-0.10	0.57	0.19	0.72	0.80	0.31	0.63	-0.49	0.19
Omin	31.42	31.60	31.14	31.42	32.15	31.56	32.18	31.07	32.32	32.16
Omax	33.65	33.81	33.34	33.64	33.68	33.15	33.82	33.32	33.97	33.80
FeO (st)	14.75	14.80	14.95	15.04	11.25	11.16	10.42	14.62	10.48	10.86
Fe2O3 (st)	5.83	5.63	5.42	5.38	2.83	3.51	4.74	6.19	4.79	4.38
Fe3+/∑Fe (st)	0.262	0.255	0.246	0.243	0.185	0.221	0.290	0.276	0.291	0.266
FeO (corr)	14.08	15.70	9.82	13.34	4.79	3.98	7.61	8.99	14.79	9.18
Fe2O3 (corr)	6.57	4.63	11.12	7.27	10.01	11.49	7.86	12.44	0.00	6.25
Fe3+/∑Fe (corr)	0.296	0.210	0.505	0.329	0.653	0.722	0.482	0.555	0.000	0.380
Fo	88.70	88.70	88.70	88.70	93.26	93.26	93.25	88.76	93.28	93.30

Appendix C2

No.	11	12	13	14	15	16	17	18	19	20	21
Sample No.	5-24	5-28	5-28	5-28	5-28	5-28	5-28	5-28	6-3	6-3	6-3
	OL27-SP	OL4A-SP	OL5-SPA	OL8-SP	OL9-SP	OL11-SP	OL19-SP	OL12-SP	SP55	OL64-SPB	OL64-SPA
Type	Bon	Bon	Bon	Bon	Bon	Bon	Bon	Bon	Bon	Bon	Bon
Si	0.03	0.05	0.02	0.03	0.04	0.03	0.03	0.02	0.03	0.02	0.02
Ti	0.02	0.05	0.10	0.05	0.04	0.05	0.05	0.02	0.13	0.22	0.18
Al	3.47	3.37	4.37	3.40	3.31	3.24	3.23	3.24	3.69	4.17	4.14
Cr	40.94	41.87	37.25	42.93	42.45	43.21	41.24	39.77	40.63	38.50	38.53
Fe	16.01	12.80	18.89	11.09	13.17	12.02	16.41	18.59	14.65	16.55	16.57
Mg	6.88	7.89	6.45	8.76	7.06	8.45	6.35	6.16	7.33	7.36	7.42
Mn	0.24	0.24	0.25	0.19	0.16	0.14	0.18	0.31	0.25	0.26	0.24
Ni	0.06	0.09	0.05	0.10	0.06	0.05	0.08	0.08	0.04	0.06	0.06
Zn	0.08	0.03	0.05	0.02	0.07	0.07	0.10	0.06	0.11	0.13	0.09
O	32.20	32.78	31.09	32.94	33.37	32.86	31.88	31.18	31.66	31.88	31.25
Total	99.93	99.17	98.52	99.51	99.72	100.12	99.55	99.44	98.52	99.14	98.50
Ocalculated	31.91	31.90	31.85	32.44	31.46	32.50	31.54	31.64	31.90	32.19	32.21
ΔO	0.29	0.88	-0.76	0.50	1.91	0.36	0.34	-0.46	-0.24	-0.31	-0.96
Omin	31.30	31.42	30.97	31.99	31.15	32.02	31.00	30.84	31.34	31.40	31.40
Omax	33.59	33.26	33.68	33.58	33.04	33.74	33.35	33.50	33.44	33.77	33.77
FeO (st)	15.07	12.19	16.40	10.24	14.19	11.15	16.30	16.76	13.86	14.16	14.02
Fe2O3 (st)	6.14	4.75	8.78	4.48	3.06	4.80	5.35	7.95	5.54	7.93	8.11
Fe3+/∑Fe (st)	0.268	0.260	0.325	0.282	0.163	0.279	0.228	0.299	0.265	0.335	0.342
FeO (corr)	12.49	4.29	23.23	5.72	0.00	7.93	13.24	20.85	15.97	16.98	21.32
Fe2O3 (corr)	9.01	13.53	1.19	9.51	18.83	8.37	8.75	3.41	3.20	4.80	0.00
Fe3+/∑Fe (corr)	0.394	0.740	0.044	0.600	1.000	0.487	0.373	0.128	0.153	0.203	0.000
Fo	88.62	91.38	87.02	93.44	91.55	92.88	89.24	86.19	0.00	89.28	89.28

Appendix C2

No.	22	23	24	25	26	27	28	29	30	31
Sample No.	6-3	6-3	7-18	115-4/H1	115-4/H1	115-4/H1	115-4/H1	115-4/H1	115-4/H1	115-4/H1
	OL79-SP	OL82-SP	OL33-SP	OL15B-SP	OL15E-SP	OL19-SPA	OL19-SPB	OL43A-SP	OL43B-SP	OL77A-SP-1
Type	Bon	Bon	Bon	Thol	Thol	Thol	Thol	Thol	Thol	Thol
Si	0.02	0.03	0.02	0.06	0.05	0.03	0.06	0.05	0.06	0.04
Ti	0.11	0.15	0.19	0.07	0.07	0.10	0.08	0.14	0.17	0.08
Al	3.74	3.67	3.62	5.85	5.20	5.57	6.01	6.54	7.29	5.49
Cr	41.73	39.63	39.69	36.39	38.29	36.89	35.56	34.07	32.81	36.45
Fe	12.51	15.71	15.98	16.50	15.97	16.57	16.71	18.51	18.71	16.96
Mg	8.43	7.51	7.35	7.16	7.35	7.04	7.24	6.92	7.11	7.06
Mn	0.18	0.22	0.28	0.18	0.28	0.20	0.24	0.29	0.22	0.19
Ni	0.09	0.07	0.06	0.13	0.09	0.08	0.06	0.03	0.06	0.08
Zn	0.05	0.05	0.09	0.04	0.03	0.05	0.18	0.06	0.07	0.00
O	31.85	31.68	31.31	32.35	32.62	33.14	31.97	31.93	32.24	32.85
Total	98.72	98.71	98.58	98.73	99.96	99.68	98.11	98.54	98.75	99.20
Ocalculated	32.49	32.01	32.00	32.40	32.65	32.29	32.38	32.58	32.92	32.19
ΔO	-0.64	-0.33	-0.69	-0.05	-0.03	0.85	-0.41	-0.65	-0.68	0.66
Omin	31.96	31.27	31.26	31.70	31.98	31.61	31.61	31.71	32.00	31.44
Omax	33.75	33.52	33.55	34.06	34.27	33.98	34.01	34.36	34.68	33.87
FeO (st)	11.32	13.61	13.93	14.95	14.60	15.20	14.60	15.94	15.84	15.10
Fe2O3 (st)	5.31	7.33	7.37	6.97	6.61	6.80	7.67	8.75	9.15	7.46
Fe3+/∑Fe (st)	0.297	0.326	0.323	0.296	0.289	0.287	0.321	0.331	0.342	0.308
FeO (corr)	16.10	16.55	20.13	15.39	14.83	7.56	18.28	21.79	21.91	9.16
Fe2O3 (corr)	0.00	4.06	0.48	6.48	6.36	15.29	3.58	2.25	2.40	14.06
Fe3+/∑Fe (corr)	0.000	0.181	0.021	0.275	0.278	0.645	0.150	0.085	0.090	0.580
Fo	92.08	89.71	90.26	88.97	89.44	89.04	89.04	87.35	87.68	88.55

Appendix C2

No.	32	33	34	35	36	37	38	39	40	41
Sample No.	115-4/H1 OL77A-SP-2	115-4/H1 OL77A-SP-3	115-4/H1 OL80-SP	115-4/H1 OL88-SP	115-4/H1 OL77C-SP	115-4/H1 OL77B-SP	115-4/H1 OL78-SP-1	115-4/H1 OL78-SP-2	115-4/H1 OL82-SP	115-4/H1 OL86-SP
Type	Thol	Thol	Thol	Thol	Thol	Thol	Thol	Thol	Thol	Thol
Si	0.04	0.04	0.04	0.05	0.02	0.02	0.04	0.02	0.05	0.04
Ti	0.05	0.04	0.13	0.05	0.07	0.06	0.17	0.17	0.11	0.08
Al	5.14	5.03	6.57	5.21	5.12	5.31	7.27	7.75	6.00	5.61
Cr	37.20	37.56	34.59	36.78	37.51	36.82	31.05	30.26	35.38	36.29
Fe	16.86	16.76	18.14	17.26	16.99	16.92	21.19	21.11	18.98	17.10
Mg	6.92	6.96	6.98	6.80	6.72	6.86	6.42	6.57	6.56	7.01
Mn	0.19	0.28	0.22	0.21	0.26	0.26	0.22	0.19	0.25	0.22
Ni	0.06	0.04	0.07	0.05	0.03	0.11	0.07	0.09	0.06	0.06
Zn	0.05	0.01	0.09	0.06	0.02	0.03	0.06	0.05	0.17	0.07
O	32.85	32.85	32.67	32.64	na	na	na	na	na	na
Total	99.36	99.56	99.49	99.10	66.74	66.40	66.50	66.20	67.55	66.48
Ocalculated	32.05	32.12	32.72	32.00	32.04	32.04	32.50	32.63	32.57	32.25
ΔO	0.80	0.73	-0.05	0.64	na	na	na	na	na	na
Omin	31.34	31.41	31.88	31.26	na	na	na	na	na	na
Omax	33.75	33.81	34.48	33.73	na	na	na	na	na	na
FeO (st)	15.27	15.17	15.85	15.57	15.81	15.26	17.39	17.07	16.86	15.22
Fe2O3 (st)	7.13	7.10	8.32	7.38	6.72	7.23	10.97	11.21	8.40	7.54
Fe3+/∑Fe (st)	0.296	0.296	0.321	0.299	0.277	0.299	0.362	0.371	0.310	0.308
FeO (corr)	8.09	8.58	16.26	9.78						
Fe2O3 (corr)	15.11	14.43	7.87	13.82						
Fe3+/∑Fe (corr)	0.627	0.602	0.303	0.560						
Fo	88.55	88.55	88.00	88.21	88.29	88.40	85.06	85.06	87.90	88.49

Appendix C3

No.	1	2	3	4	5	6	7	8	9	10
Locality	Peak Hill	Peak Hill	Peak Hill	Peak Hill	Peak Hill	Peak Hill	Peak Hill	Peak Hill	Heazlewood	Heazlewood
Grain No.	507	405	202	304	204	806	708	203	1	2
Si	0.04	0.01	0.03	0.02	0.03	0.03	0.04	0.03	0.03	0.03
Ti	0.01	0.09	0.07	0.01	0.02	0.01	0.05	0.02	0.02	0.02
Al	1.46	2.76	1.69	1.67	1.54	1.46	1.79	1.85	3.20	3.32
Cr	48.31	42.00	47.73	47.40	46.76	47.39	44.72	45.89	42.13	42.40
V	0.01	0.01	0.01	0.01	0.01	0.01	0.01	0.01	0.04	0.04
Fe	9.39	19.20	8.16	9.87	11.49	10.67	14.91	12.29	17.54	17.40
Mg	7.08	2.05	7.52	6.50	5.66	5.52	3.46	5.20	5.38	5.35
Mn	0.53	1.41	0.90	0.99	0.81	1.04	0.83	0.60	0.19	0.27
Ni	0.12	0.01	0.10	0.06	0.05	0.10	0.05	0.00	0.05	0.08
Zn	0.06	0.56	0.43	0.27	0.36	0.77	0.95	1.37	0.10	0.04
O	33.04	31.33	33.37	33.06	32.76	32.88	32.07	33.33	31.26	31.61
Total	100.04	99.42	99.99	99.84	99.48	99.87	98.87	100.57	99.93	100.55
Ocalculated	31.25	29.36	31.34	30.91	30.40	30.47	29.39	30.37	31.41	31.55
ΔO	1.79	1.97	2.03	2.15	2.36	2.41	2.68	2.96	-0.15	0.07
Σcations	2.988	3.002	2.992	2.989	2.989	2.982	2.985	2.994	3.038	3.034
Omin	31.25	29.36	31.34	30.91	30.40	30.47	29.39	30.37	31.01	31.19
Omax	32.59	32.11	32.50	32.33	32.04	32.00	31.53	32.13	33.52	33.69
FeO (st)	12.08	24.57	10.50	12.69	14.78	13.73	19.19	15.81	19.03	19.22
Fe2O3 (st)									3.93	3.51
Fe3+/ΣFe (st)									0.157	0.141
FeO (real)		7.00							20.38	18.60
Fe2O3 (real)	13.43	19.67	11.66	14.11	16.42	15.26	21.32	17.57	2.43	4.20
Fe3+/ΣFe (real)		0.717							0.097	0.169

Appendix C3

No.	11	12	13	14	15	16
Locality	Heazlewood	Heazlewood	Heazlewood	Heazlewood	Heazlewood	Heazlewood
Grain No.	3	4	5	6	8	11
Si	0.02	0.03	0.04	0.02	0.03	0.03
Ti	0.02	0.02	0.02	0.02	0.02	0.02
Al	3.28	3.24	3.19	3.19	3.21	2.94
Cr	42.76	43.06	42.93	42.75	42.59	41.89
V	0.04	0.04	0.04	0.04	0.04	0.04
Fe	16.98	16.93	17.02	16.81	17.16	18.39
Mg	5.29	5.25	5.24	5.31	5.23	5.03
Mn	0.26	0.21	0.26	0.25	0.28	0.21
Ni	0.05	0.05	0.04	0.05	0.02	0.00
Zn	0.06	0.07	0.08	0.08	0.05	0.08
O	31.37	31.90	31.99	32.37	32.41	32.11
Total	100.12	100.80	100.85	100.87	101.04	100.74
Ocalculated	31.44	31.47	31.43	31.32	31.34	31.10
ΔO	-0.07	0.42	0.56	1.05	1.07	1.01
Σcations	3.027	3.024	3.026	3.027	3.029	3.042
Omin	31.15	31.22	31.16	31.03	31.03	30.67
Omax	33.59	33.64	33.59	33.44	33.49	33.31
FeO (st)	19.29	19.51	19.45	19.09	19.36	19.80
Fe2O3 (st)	2.84	2.53	2.73	2.82	3.02	4.29
Fe3+/∑Fe (st)	0.117	0.104	0.112	0.117	0.123	0.163
FeO (real)	19.96	15.70	14.39	9.65	9.72	10.73
Fe2O3 (real)	2.09	6.76	8.35	13.31	13.73	14.38
Fe3+/∑Fe (real)	0.086	0.279	0.343	0.554	0.560	0.547

Appendix C4

No.	1	2	3	4	5	6	7	8	9	10	11	12
Locality	Monastery	Monastery	Monastery	Monastery	Nouzees	Nouzees	Nouzees	Nouzees	Orapa	Orapa	Orapa	Orapa
Grain No.	201	202	207	304	401	409	410	505	602	609	702	706
Si	0.05	0.00	0.00	0.00	0.00	0.01	0.00	0.01	0.03	0.01	0.01	0.00
Ti	29.82	32.32	31.64	29.90	32.17	32.17	32.22	31.27	30.51	28.79	29.89	29.70
Al	0.41	0.10	0.11	0.00	0.00	0.01	0.02	0.00	0.32	0.00	0.09	0.00
Cr	0.24	0.52	0.62	0.62	0.67	0.77	1.13	0.88	0.07	1.81	1.77	2.15
Fe	29.00	24.52	25.56	31.01	24.78	24.61	24.47	26.78	26.80	30.62	25.75	29.16
Mg	6.13	7.24	7.01	4.57	7.18	7.17	7.27	6.39	7.03	4.44	7.30	5.02
Mn	0.18	0.20	0.25	0.28	0.22	0.30	0.25	0.34	0.22	0.24	0.25	0.26
Ni	0.14	0.06	0.06	0.09	0.08	0.10	0.09	0.06	0.03	0.08	0.03	0.09
Zn	0.04	0.03	0.03	0.03	0.00	0.00	0.04	0.00	0.04	0.00	0.00	0.03
O	33.53	34.34	33.87	32.88	33.96	33.96	34.49	33.82	33.67	32.93	34.05	33.29
Total	99.54	99.33	99.13	99.36	99.06	99.08	99.97	99.55	98.72	98.92	99.14	99.69
Ocalculated	34.12	34.33	34.28	33.26	34.29	34.31	34.53	34.07	34.20	32.95	34.27	33.51
ΔO	-0.59	0.01	-0.42	-0.39	-0.33	-0.35	-0.04	-0.24	-0.53	-0.02	-0.22	-0.23
Fe3+/∑Fe (st)	0.295	0.153	0.200	0.227	0.164	0.161	0.163	0.201	0.284	0.247	0.308	0.221
Fe3+/∑Fe (real)	0.153	0.156	0.087	0.139	0.070	0.060	0.150	0.136	0.144	0.243	0.247	0.166
	(0.161)	(0.196)	(0.186)	(0.149)	(0.192)	(0.193)	(0.197)	(0.177)	(0.175)	(0.150)	(0.184)	(0.160)
Mg#	40.80	44.48	44.06	30.46	44.33	44.37	44.91	40.69	45.69	30.66	48.49	33.67

Appendix C4

No.	13	14	15	16
Locality	Rietfontein	Rietfontein	Rietfontein	Rietfontein
Grain No.	807	809	901	905
Si	0.00	0.00	0.01	0.02
Ti	32.10	19.62	28.44	29.93
Al	0.01	0.02	0.20	0.31
Cr	2.06	1.63	0.19	0.03
Fe	23.06	44.68	32.38	30.12
Mg	7.42	1.87	4.69	5.64
Mn	0.30	0.07	0.17	0.20
Ni	0.19	0.08	0.02	0.03
Zn	0.01	0.10	0.02	0.05
O	34.23	31.69	32.79	33.44
Total	99.40	99.75	98.91	99.75
Ocalculated	34.50	31.74	33.16	33.92
ΔO	-0.27	-0.05	-0.37	-0.48
Fe3+/∑Fe (st)	0.138	0.589	0.315	0.279
Fe3+/∑Fe (real)	0.059	0.581	0.235	0.166
	(0.206)	(0.098)	(0.142)	(0.155)
Mg#	46.16	18.97	32.68	37.38

APPENDIX D

REPRESENTATIVE ELECTRON PROBE MICROANALYSES OF MINERAL PHASES FROM SiO_2 - TiO_2 - FeO - MgO EXPERIMENTAL RUNS

D1.1 YVB-1 olivine
D1.2 YVB-1 orthopyroxene
D1.3 YVB-1 ilmenite
D1.4 YVB-1 rutile
D1.5 YVB-1 armalcolite
D2.1 MAK-2 olivine
D2.2 MAK-2 ilmenite
D2.3 MAK-2 rutile
D2.4 MAK-2 armalcolite

Appendix D1.1

Experiment	T-3329	T-3350	T-3357	T-3366	T-3377	T-3386	T-3398	T-3399	T-3409
T (°C)	1100	1100	1100	1100	1100	1000	1200	900	1050
P (kbar)	30	30	25	25	15	25	35	25	25
Buffer	WCWO	GW/GCO	GW/GCO	HM	NNO	HM	NNO	HM	NNO
log$fO2$	-10.32	-8.74	-9.04	-4.11	-8.40	-5.51	-6.57	-7.15	-8.69
Δlog$fO2$ (FMQ)	-2.65	-1.07	-1.03	3.90	0.27	3.80	-0.32	3.67	-0.06
	(n=3)	(n=3)	(n=3)	(n=4)	(n=3)	(n=5)	(n=3)	(n=4)	(n=3)
SiO2	39.33	39.69	39.44	40.89	40.21	40.78	40.16	41.71	39.94
TiO2	0.65	0.51	0.59	0.48	0.41	0.48	0.49	0.46	0.57
FeO	14.18	11.94	13.18	5.15	10.45	5.51	10.89	5.54	11.36
MnO							0.13		
MgO	45.42	48.04	46.17	53.14	48.92	52.29	47.93	53.06	47.49
NiO					0.15		0.15		
Total	99.58	100.19	99.38	99.67	100.15	99.06	99.76	100.76	99.36
Mg#	85.1	87.8	86.2	94.8	89.3	94.4	88.7	94.5	88.2
Si	0.988 (0.008)	0.982 (0.006)	0.988 (0.008)	0.985 (0.008)	0.988 (0.007)	0.990 (0.017)	0.993 (0.019)	0.994 (0.032)	0.992 (0.003)
Ti	0.012 (0.006)	0.010 (0.001)	0.011 (0.001)	0.009 (0.004)	0.008 (0.001)	0.009 (0.003)	0.009 (0.001)	0.008 (0.003)	0.011 (0.005)
Fe	0.298 (0.003)	0.247 (0.005)	0.276 (0.006)	0.104 (0.003)	0.215 (0.015)	0.112 (0.005)	0.225 (0.020)	0.110 (0.007)	0.236 (0.004)
Mn							0.003 (0.001)		
Mg	1.701 (0.010)	1.771 (0.006)	1.725 (0.008)	1.908 (0.009)	1.791 (0.011)	1.891 (0.018)	1.766 (0.023)	1.885 (0.032)	1.758 (0.005)
Ni					0.003 (0.002)		0.003 (0.002)		
Sum	3.000	3.009	3.000	3.006	3.004	3.002	2.998	2.998	2.997

Appendix D1.1

Experiment	T-3410	T-3412	T-3419	T-3431	T-3436	T-3437	T-3445	T-3450
T (°C)	1100	1100	1000	1000	1100	1000	1050	1000
P (kbar)	15	35	35	25	35	25	30	15
Buffer	NNO	HM	HM	NNO	GW/GCO	GW/GCO	GW/GCO	HM
log$f$O2	-8.40	-4.01	-5.40	-9.39	-8.64	-11.57	-9.23	-5.61
Δlog$f$O2 (FMQ)	0.27	3.33	3.19	-0.08	-1.30	-2.26	-0.94	4.41
	(n=3)	(n=4)	(n=5)	(n=3)	(n=3)	(n=3)	(n=3)	(n=5)
SiO2	39.72	41.47	41.27	39.83	39.06	39.53	39.37	41.40
TiO2	0.50	0.44	0.39	0.44	0.54	0.60	0.65	0.44
FeO	12.37	5.70	5.17	11.38	12.73	12.06	11.68	4.98
MnO				0.10			0.00	
MgO	46.70	52.66	53.25	47.39	46.98	47.25	47.80	53.18
NiO				0.13				
Total	99.29	100.27	100.07	99.26	99.31	99.44	99.51	99.99
Mg#	87.1	94.3	94.8	88.1	86.8	87.5	87.9	95.0
Si	0.992 (0.004)	0.994 (0.017)	0.990 (0.016)	0.992 (0.002)	0.979 (0.007)	0.985 (0.004)	0.980 (0.008)	0.992 (0.008)
Ti	0.009 (0.004)	0.008 (0.003)	0.007 (0.002)	0.008 (0.003)	0.010 (0.000)	0.011 (0.003)	0.012 (0.002)	0.008 (0.004)
Fe	0.258 (0.009)	0.114 (0.003)	0.104 (0.003)	0.237 (0.002)	0.267 (0.010)	0.251 (0.003)	0.243 (0.006)	0.100 (0.003)
Mn				0.002 (0.000)				
Mg	1.739 (0.007)	1.882 (0.017)	1.903 (0.016)	1.759 (0.003)	1.755 (0.009)	1.755 (0.005)	1.773 (0.009)	1.900 (0.009)
Ni				0.003 (0.001)				
Sum	2.998	2.998	3.003	3.000	3.011	3.003	3.008	3.000

Appendix D1.2

Experiment	T-3329	T-3350	T-3357	T-3366	T-3377	T-3386	T-3398	T-3399	T-3409
T (°C)	1100	1100	1100	1100		1000	1200	900	1050
P (kbar)	30	30	25	25		25	35	25	25
Buffer	WCWO	GW/GCO	GW/GCO	HM		HM	NNO	HM	NNO
log$fO2$	-10.32	-8.74	-9.04	-4.11		-5.51	-6.57	-7.15	-8.69
Δlog$fO2$ (FMQ)	-2.65	-1.07	-1.03	3.90		3.80	-0.32	3.67	-0.06
	(n=3)	(n=4)	(n=3)	(n=3)		(n=5)	(n=4)	(n=4)	(n=4)
SiO2	56.65	56.37	56.54	57.88		57.47	56.92	58.52	56.92
TiO2	0.83	0.75	0.80	0.63		0.63	0.69	0.49	0.75
Al2O3	0.12	0.12	0.12	0.07		0.11	0.04	0.09	0.09
FeO	8.52	7.66	8.57	3.74		4.11	7.46	4.00	7.53
MgO	33.24	35.22	34.15	37.47		37.20	34.25	37.60	33.54
Total	99.36	100.12	100.18	99.79		99.53	99.36	100.70	98.83
Mg#	87.4	89.1	87.7	94.7		94.2	89.1	94.4	88.8
Si	1.983 (0.024)	1.955 (0.035)	1.966 (0.012)	1.975 (0.017)		1.971 (0.031)	1.983 (0.025)	1.980 (0.018)	1.992 (0.020)
Ti	0.022 (0.003)	0.019 (0.003)	0.021 (0.001)	0.016 (0.003)		0.016 (0.006)	0.018 (0.012)	0.012 (0.002)	0.020 (0.010)
Al	0.005 (0.000)	0.005 (0.001)	0.005 (0.000)	0.003 (0.000)		0.004 (0.002)	0.002 (0.001)	0.004 (0.001)	0.004 (0.001)
Fe	0.249 (0.006)	0.222 (0.020)	0.249 (0.008)	0.107 (0.011)		0.118 (0.027)	0.217 (0.014)	0.113 (0.007)	0.221 (0.024)
Mg	1.734 (0.015)	1.821 (0.049)	1.770 (0.009)	1.906 (0.014)		1.902 (0.024)	1.778 (0.019)	1.896 (0.012)	1.750 (0.017)
Sum	3.993	4.023	4.011	4.007		4.012	3.998	4.006	3.986

Appendix D1.2

Experiment	T-3410	T-3412	T-3419	T-3431	T-3436	T-3437	T-3445	T-3450
T (°C)		1100	1000	1000	1100	1000	1050	1000
P (kbar)		35	35	25	35	25	30	15
Buffer		HM	HM	NNO	GW/GCO	GW/GCO	GW/GCO	HM
log$fO2$		-4.01	-5.40	-9.39	-8.64	-11.57	-9.23	-5.61
Δlog$fO2$ (FMQ)		3.33	3.19	-0.08	-1.30	-2.26	-0.94	4.41
		(n=4)	(n=3)	(n=3)	(n=3)	(n=4)	(n=3)	(n=5)
SiO2		57.82	57.88	57.27	56.40	56.85	55.91	58.53
TiO2		0.58	0.49	0.80	0.78	0.65	0.79	0.65
Al2O3		0.07	0.06	0.18	0.08	0.14	0.09	0.07
FeO		4.19	3.44	7.39	8.04	7.62	8.01	3.38
MgO		37.14	37.44	33.81	34.80	34.65	34.22	37.66
Total		99.79	99.30	99.45	100.10	99.90	99.02	100.28
Mg#		94.1	95.1	89.1	88.5	89.0	88.4	95.2
Si		1.977 (0.031)	1.981 (0.014)	1.990 (0.022)	1.959 (0.016)	1.972 (0.009)	1.963 (0.009)	1.983 (0.016)
Ti		0.015 (0.002)	0.013 (0.003)	0.021 (0.021)	0.020 (0.002)	0.017 (0.002)	0.021 (0.007)	0.016 (0.004)
Al		0.003 (0.001)	0.002 (0.001)	0.007 (0.001)	0.003 (0.001)	0.006 (0.001)	0.004 (0.002)	0.003 (0.001)
Fe		0.120 (0.022)	0.098 (0.003)	0.215 (0.013)	0.234 (0.006)	0.221 (0.005)	0.235 (0.005)	0.096 (0.002)
Mg		1.893 (0.026)	1.910 (0.011)	1.751 (0.020)	1.802 (0.011)	1.792 (0.009)	1.791 (0.007)	1.901 (0.012)
Sum		4.007	4.005	3.985	4.019	4.008	4.014	3.999

Appendix D1.3

Experiment	T-3329	T-3350	T-3357	T-3366	T-3377	T-3386	T-3398	T-3399	T-3409
T (°C)	1100	1100	1100	1100	1100	1000	1200	900	1050
P (kbar)	30	30	25	25	15	25	35	25	25
Buffer	WCWO	GW/GCO	GW/GCO	HM	NNO	HM	NNO	HM	NNO
log$fO2$	-10.32	-8.74	-9.04	-4.11	-8.40	-5.51	-6.57	-7.15	-8.69
Δlog$fO2$ (FMQ)	-2.65	-1.07	-1.03	3.90	0.27	3.80	-0.32	3.67	-0.06
	(n=9)	(n=6)	(n=3)	(n=5)	(n=6)	(n=5)	(n=5)	(n=3)	(n=6)
SiO2	0.10	0.06	0.05	0.08	0.05	0.12	0.07	0.23	0.11
TiO2	57.42	55.96	57.24	34.83	54.24	33.02	53.59	28.38	53.59
Al2O3								0.08	
Cr2O3							0.91		
Fe2O3	0.30	3.06	1.77	39.15	7.08	41.73	7.79	49.88	6.30
FeO	27.40	25.17	26.73	12.76	21.32	13.69	20.91	13.61	24.71
MnO							0.24		
MgO	13.66	14.15	13.92	10.47	15.43	9.06	15.10	6.84	13.24
NiO							0.21		
Total	98.88	98.41	99.71	97.30	98.13	97.62	98.82	99.02	97.95
Mg#	47.1	50.0	48.1	59.4	56.3	54.1	56.3	47.2	48.9
Si	0.002 (0.001)	0.001 (0.000)	0.001 (0.001)	0.002 (0.001)	0.001 (0.001)	0.003 (0.002)	0.002 (0.001)	0.006 (0.008)	0.002 (0.002)
Ti	0.996 (0.018)	0.972 (0.009)	0.984 (0.005)	0.639 (0.009)	0.938 (0.007)	0.611 (0.005)	0.923 (0.010)	0.529 (0.009)	0.942 (0.043)
Al								0.002 (0.001)	
Cr							0.017 (0.005)		
Fe3+	0.005 (0.003)	0.053 (0.018)	0.030 (0.011)	0.718 (0.018)	0.122 (0.015)	0.772 (0.011)	0.134 (0.020)	0.929 (0.024)	0.111 (0.046)
Fe2+	0.528 (0.013)	0.486 (0.011)	0.511 (0.004)	0.260 (0.010)	0.410 (0.007)	0.282 (0.006)	0.401 (0.010)	0.282 (0.012)	0.483 (0.041)
Mn							0.005 (0.001)		
Mg	0.469 (0.023)	0.487 (0.006)	0.474 (0.004)	0.381 (0.006)	0.529 (0.006)	0.332 (0.004)	0.516 (0.006)	0.252 (0.005)	0.461 (0.041)
Ni							0.004 (0.002)		
Sum	2.000	2.000	2.000	2.000	2.000	2.000	2.000	2.000	2.000
Fe3+/$\sum$Fe	0.009 (0.005)	0.099 (0.027)	0.056 (0.018)	0.734 (0.003)	0.230 (0.017)	0.733 (0.001)	0.251 (0.023)	0.767 (0.003)	0.186 (0.043)
Ilm (mol %)	52.8	48.6	51.1	26.0	41.0	28.2	40.7	28.2	48.3
Geik (mol %)	46.9	48.7	47.4	38.1	52.9	33.2	52.4	25.3	46.1
Hem (mol %)	0.3	2.7	1.5	35.9	6.1	38.6	6.8	46.5	5.5

Appendix D1.3

Experiment	T-3410	T-3412	T-3419	T-3431	T-3436	T-3437	T-3445	T-3450
T (°C)	1100	1100	1000	1000	1100	1000	1050	1000
P (kbar)	15	35	35	25	35	25	30	15
Buffer	NNO	HM	HM	NNO	GW/GCO	GW/GCO	GW/GCO	HM
log$fO2$	-8.40	-4.01	-5.40	-9.39	-8.64	-11.57	-9.23	-5.61
Δlog$fO2$ (FMQ)	0.27	3.33	3.19	-0.08	-1.30	-2.26	-0.94	4.41
	(n=5)	(n=6)	(n=4)	(n=8)	(n=7)	(n=3)	(n=1)	(n=5)
SiO2	0.15	0.09	0.07	0.09	0.10	0.19	0.59	0.06
TiO2	54.77	35.99	32.59	54.34	56.29	57.77	56.90	31.35
Al2O3								0.06
Cr2O3								
Fe2O3	5.35	36.65	42.56	6.19	2.69	0.65	2.77	45.35
FeO	24.13	14.58	13.83	24.54	25.12	26.84	23.19	11.78
MnO				0.19				
MgO	14.19	10.04	8.73	13.60	14.37	14.22	16.09	9.25
NiO								
Total	98.59	97.36	97.78	98.95	98.57	99.68	99.54	97.85
Mg#	51.2	55.1	52.9	49.7	50.5	48.6	55.3	58.3
Si	0.003 (0.004)	0.002 (0.002)	0.002 (0.001)	0.002 (0.002)	0.002 (0.001)	0.004 (0.009)	0.013	0.001 (0.001)
Ti	0.950 (0.011)	0.661 (0.008)	0.604 (0.006)	0.944 (0.019)	0.974 (0.011)	0.990 (0.009)	0.963	0.579 (0.004)
Al								0.002 (0.000)
Cr								
Fe3+	0.093 (0.024)	0.673 (0.016)	0.789 (0.012)	0.108 (0.039)	0.047 (0.022)	0.011 (0.026)	0.047	0.837 (0.008)
Fe2+	0.466 (0.012)	0.298 (0.008)	0.285 (0.008)	0.474 (0.015)	0.484 (0.012)	0.511 (0.005)	0.437	0.242 (0.005)
Mn				0.004 (0.001)				
Mg	0.488 (0.010)	0.366 (0.006)	0.321 (0.006)	0.468 (0.016)	0.493 (0.009)	0.483 (0.007)	0.540	0.339 (0.003)
Ni								
Sum	2.000	2.000	2.000	2.000	2.000	2.000	2.000	2.000
Fe3+/$\sum$Fe	0.166 (0.030)	0.693 (0.001)	0.735 (0.002)	0.185 (0.045)	0.088 (0.034)	0.021 (0.045)	0.097	0.776 (0.002)
Ilm (mol %)	46.6	29.8	28.5	47.6	48.4	51.1	43.7	24.2
Geik (mol %)	48.8	36.6	32.1	47.0	49.3	48.3	54.0	33.9
Hem (mol %)	4.6	33.7	39.4	5.4	2.3	0.6	2.3	41.9

Appendix D1.4

Experiment	T-3329	T-3350	T-3357	T-3366	T-3377	T-3386	T-3398	T-3399	T-3409
T (°C)	1100	1100	1100	1100	1100	1000	1200	900	1050
P (kbar)	30	30	25	25	15	25	35	25	25
Buffer	WCWO	GW/GCO	GW/GCO	HM	NNO	HM	NNO	HM	NNO
log$f$O2	-10.32	-8.74	-9.04	-4.11	-8.40	-5.51	-6.57	-7.15	-8.69
Δlog$f$O2 (FMQ)	-2.65	-1.07	-1.03	3.90	0.27	3.80	-0.32	3.67	-0.06
	(n=9)	(n=3)	(n=3)	(n=5)	(n=7)	(n=7)	(n=8)	(n=5)	(n=5)
SiO2	0.05	0.06	0.23	0.06	0.03	0.07	0.07	0.08	0.10
TiO2	96.35	95.65	96.23	89.59	92.92	91.02	91.77	92.62	92.65
Cr2O3					0.13		0.67		0.17
FeO	1.33	2.15	2.00	6.19	3.55	6.07	4.45	5.51	4.17
MgO	0.34	0.22	0.45	0.32	0.33	0.22	0.58	0.12	0.33
Total	98.07	98.08	98.91	96.17	96.95	97.39	97.54	98.33	97.42
Si	0.001 (0.001)	0.001 (0.001)	0.003 (0.000)	0.001 (0.000)	0.000 (0.001)	0.001 (0.000)	0.001 (0.001)	0.001 (0.001)	0.001 (0.001)
Ti	0.988 (0.004)	0.985 (0.001)	0.981 (0.003)	0.959 (0.005)	0.975 (0.004)	0.961 (0.003)	0.962 (0.004)	0.966 (0.003)	0.970 (0.018)
Cr					0.001 (0.001)		0.007 (0.003)		0.002 (0.001)
Fe	0.015 (0.003)	0.025 (0.000)	0.023 (0.000)	0.074 (0.005)	0.041 (0.004)	0.071 (0.003)	0.052 (0.002)	0.064 (0.003)	0.049 (0.011)
Mg	0.007 (0.002)	0.004 (0.001)	0.009 (0.003)	0.007 (0.003)	0.007 (0.002)	0.005 (0.001)	0.012 (0.002)	0.002 (0.001)	0.007 (0.015)
Sum	1.011	1.015	1.016	1.040	1.025	1.038	1.034	1.033	1.028

Appendix D1.4

Experiment	T-3410	T-3412	T-3419	T-3431	T-3436	T-3437	T-3445	T-3450
T (°C)	1100	1100	1000	1000	1100	1000	1050	1000
P (kbar)	15	35	35	25	35	25	30	15
Buffer	NNO	HM	HM	NNO	GW/GCO	GW/GCO	GW/GCO	HM
log$fO2$	-8.40	-4.01	-5.40	-9.39	-8.64	-11.57	-9.23	-5.61
Δlog$fO2$ (FMQ)	0.27	3.33	3.19	-0.08	-1.30	-2.26	-0.94	4.41
	(n=5)	(n=6)	(n=6)	(n=9)	(n=4)	(n=4)	(n=4)	(n=7)
SiO2	0.06	0.08	0.07	0.15	0.08	0.16	0.05	0.07
TiO2	94.84	90.04	89.68	94.22	95.96	96.15	97.16	91.83
Cr2O3				0.19				
FeO	3.13	6.40	6.91	3.77	2.28	1.54	1.85	5.12
MgO	0.25	0.32	0.29	0.24	0.50	0.35	0.41	0.13
Total	98.28	96.85	96.94	98.57	98.82	98.21	99.47	97.15
Si	0.001 (0.000)	0.001 (0.001)	0.001 (0.000)	0.002 (0.001)	0.001 (0.000)	0.002 (0.003)	0.001 (0.000)	0.001 (0.001)
Ti	0.979 (0.002)	0.958 (0.003)	0.955 (0.001)	0.972 (0.003)	0.981 (0.007)	0.985 (0.004)	0.985 (0.002)	0.968 (0.002)
Cr				0.002 (0.002)				
Fe	0.036 (0.002)	0.076 (0.002)	0.082 (0.001)	0.043 (0.003)	0.026 (0.007)	0.018 (0.001)	0.021 (0.002)	0.060 (0.002)
Mg	0.005 (0.000)	0.007 (0.002)	0.006 (0.001)	0.005 (0.001)	0.010 (0.002)	0.007 (0.002)	0.008 (0.001)	0.003
Sum	1.020	1.041	1.044	1.025	1.018	1.012	1.015	1.031

Appendix D1.5

Experiment	T-3329	T-3350	T-3357	T-3366	T-3377	T-3386	T-3398	T-3399	T-3409
T (°C)	1100								
P (kbar)	30								
Buffer	WCWO								
log$f$O2	-10.32								
Δlog$f$O2 (FMQ)	-2.65								
	(n=1)								
SiO2	0.06								
TiO2	75.20								
FeO	14.82								
MgO	7.02								
Total	97.11								
Mg#	45.8								
Si	0.003								
Ti	2.078								
Fe	0.456								
Mg	0.385								
Sum	2.920								

Appendix D1.5

Experiment	T-3410	T-3412	T-3419	T-3431	T-3436	T-3437	T-3445	T-3450
T (°C)								
P (kbar)								
Buffer								
log$f$O2								
Δlog$f$O2 (FMQ)								
SiO2								
TiO2								
FeO								
MgO								
Total								
Mg#								
Si								
Ti								
Fe								
Mg								
Sum								

Appendix D2.1

Experiment	T-3525	T-3535	T-3547	T-3596	T-3665	T-3705	T-3708
T (°C)	1150	1125	1150	1150	1100	1050	1050
P (kbar)	25	28	35	32	30	20	20
Buffer	NNO	WCWO	WCWO	WCWO	HM	NNO	HM
log$fO2$	-7.46	-10.07	-9.42	-9.56	-2.87	-8.88	-4.83
Δlog$fO2$ (FMQ)	-0.04	-2.56	-2.64	-2.59	3.69	0.10	4.15
	(n=5)	(n=5)	(n=5)	(n=5)	(n=4)	(n=3)	(n=3)
SiO2	40.02	39.80	40.37	40.26	40.95	40.65	41.33
TiO2	0.34	0.38	0.42	0.39	0.31	0.36	0.30
FeO	7.07	7.11	7.15	7.67	4.02	7.63	3.90
MgO	51.89	51.53	52.13	51.06	53.37	51.03	53.99
NiO	0.27						
Total	99.59	98.82	100.07	99.39	98.66	99.67	99.51
Mg#	92.9	92.8	92.9	92.2	95.9	92.3	96.1
Si	0.976 (0.006)	0.977 (0.008)	0.978 (0.012)	0.984 (0.012)	0.991 (0.016)	0.990 (0.006)	0.991 (0.005)
Ti	0.006 (0.003)	0.007 (0.002)	0.008 (0.002)	0.007 (0.005)	0.006 (0.002)	0.007 (0.003)	0.005 (0.001)
Fe	0.144 (0.006)	0.146 (0.007)	0.145 (0.006)	0.157 (0.012)	0.081 (0.003)	0.155 (0.006)	0.078 (0.003)
Mg	1.886 (0.007)	1.886 (0.009)	1.883 (0.013)	1.860 (0.015)	1.925 (0.016)	1.852 (0.008)	1.929 (0.006)
Ni	0.005 (0.002)						
Sum	3.018	3.016	3.014	3.009	3.003	3.004	3.004

Appendix D2.2

Experiment	T-3525	T-3535	T-3547	T-3596	T-3665	T-3705	T-3708
T (°C)	1150	1125	1150	1150	1100	1050	1050
P (kbar)	25	28	35	32	30	20	20
Buffer	NNO	WCWO	WCWO	WCWO	HM	NNO	HM
log$fO2$	-7.46	-10.07	-9.42	-9.56	-2.87	-8.88	-4.83
Δlog$fO2$ (FMQ)	-0.04	-2.56	-2.64	-2.59	3.69	0.10	4.15
	(n=7)	(n=5)	(n=5)	(n=4)	(n=8)	(n=7)	(n=5)
SiO2	0.03	0.07	0.09	0.15	0.05	0.08	0.04
TiO2	58.17	59.75	59.94	59.65	38.48	56.36	39.35
Al2O3					0.22	0.18	0.22
Cr2O3	0.31						
Fe2O3	3.85	0.84	0.88	1.08	34.22	4.19	32.61
FeO	16.82	17.02	17.21	17.73	11.76	17.79	12.04
MnO	0.27						
MgO	19.59	20.64	20.65	20.25	12.85	18.51	13.13
NiO	0.36						
Total	99.40	98.33	98.77	98.86	97.58	97.11	97.39
Mg#	67.5	68.4	68.1	67.1	66.1	65.0	66.0
Si	0.001 (0.001)	0.002 (0.001)	0.002 (0.001)	0.003 (0.001)	0.001 (0.001)	0.002 (0.001)	0.001 (0.000)
Ti	0.965 (0.008)	0.991 (0.008)	0.991 (0.009)	0.988 (0.013)	0.689 (0.015)	0.960 (0.005)	0.704 (0.037)
Al					0.006 (0.001)	0.005 (0.000)	0.006 (0.002)
Cr	0.005 (0.001)						
Fe3+	0.064 (0.016)	0.014 (0.017)	0.015 (0.018)	0.018 (0.027)	0.613 (0.030)	0.071 (0.011)	0.584 (0.074)
Fe2+	0.310 (0.009)	0.314 (0.007)	0.316 (0.009)	0.326 (0.018)	0.234 (0.017)	0.337 (0.007)	0.240 (0.054)
Mn	0.005 (0.001)						
Mg	0.644 (0.006)	0.679 (0.010)	0.676 (0.008)	0.665 (0.012)	0.456 (0.016)	0.625 (0.004)	0.466 (0.046)
Ni	0.006 (0.002)						
Sum	2.000	2.000	2.000	2.000	2.000	2.000	2.000
Fe3+/ΣFe	0.171 (0.029)	0.042 (0.044)	0.044 (0.047)	0.052 (0.062)	0.724 (0.004)	0.175 (0.018)	0.709 (0.017)
Ilm (mol %)	31.5	31.4	31.6	32.6	23.5	33.8	24.0
Geik (mol %)	65.3	67.9	67.6	66.5	45.8	62.6	46.7
Hem (mol %)	3.2	0.7	0.7	0.9	30.7	3.6	29.3

Appendix D2.3

Experiment	T-3525	T-3535	T-3547	T-3596	T-3665	T-3705	T-3708
T (°C)	1150	1125	1150	1150	1100	1050	1050
P (kbar)	25	28	35	32	30	20	20
Buffer	NNO	WCWO	WCWO	WCWO	HM	NNO	HM
log$fO2$	-7.46	-10.07	-9.42	-9.56	-2.87	-8.88	-4.83
Δlog$fO2$ (FMQ)	-0.04	-2.56	-2.64	-2.59	3.69	0.10	4.15
	(n=7)	(n=7)	(n=5)	(n=8)	(n=5)	(n=8)	(n=7)
SiO2	0.02	0.04	0.08	0.13	0.07	0.08	0.03
TiO2	94.47	95.39	96.28	95.18	89.01	93.74	91.02
Al2O3						0.08	
Cr2O3	0.75					0.10	
FeO	2.70	1.26	1.36	1.71	6.34	2.61	5.51
MgO	0.50	0.58	0.82	0.69	0.41	0.38	0.27
Total	98.45	97.27	98.54	97.72	95.84	97.00	96.84
Si	0.000 (0.000)	0.001 (0.001)	0.001 (0.000)	0.002 (0.001)	0.001 (0.002)	0.001 (0.001)	0.000 (0.001)
Ti	0.973 (0.003)	0.986 (0.002)	0.983 (0.001)	0.981 (0.004)	0.957 (0.003)	0.978 (0.003)	0.964 (0.004)
Al						0.001 (0.001)	
Cr	0.008 (0.001)					0.001 (0.001)	
Fe	0.031 (0.003)	0.015 (0.001)	0.015 (0.001)	0.020 (0.002)	0.076 (0.002)	0.030 (0.001)	0.065 (0.004)
Mg	0.010 (0.001)	0.012 (0.001)	0.017 (0.001)	0.014 (0.004)	0.009 (0.002)	0.008 (0.002)	0.006 (0.001)
Sum	1.023	1.013	1.016	1.017	1.042	1.020	1.035

Appendix D2.4

Experiment	T-3525	T-3535	T-3547	T-3596	T-3665	T-3705	T-3708
T (°C)		1125		1150			
P (kbar)		28		32			
Buffer		WCWO		WCWO			
log$fO2$		-10.07		-9.56			
Δlog$fO2$ (FMQ)		-2.56		-2.59			
		(n=1)		(n=1)			
SiO2		0.06		0.07			
TiO2		68.16		71.75			
FeO		13.33		14.60			
MgO		16.29		14.91			
Total		97.83		101.33			
Mg#		68.5		64.5			
Si		0.002		0.003			
Ti		1.857		1.894			
Fe		0.404		0.429			
Mg		0.880		0.780			
Sum		3.142		3.105			

APPENDIX E

REPRESENTATIVE ELECTRON PROBE MICROANALYSES (EPMA) OF MINERAL PHASES FROM SiO_2 - TiO_2 ± Al_2O_3 - Cr_2O_3 - FeO - MgO - K_2O ± NiO ± ZnO EXPERIMENTAL RUNS

E1.1 MAK-6 olivine
E1.2 MAK-6 orthopyroxene
E1.3 MAK-6 ilmenite
E1.4 MAK-6 spinel
E1.5 MAK-6 rutile
E2.1 MAK-7 olivine
E2.2 MAK-7 orthopyroxene
E2.3 MAK-7 ilmenite
E2.4 MAK-7 spinel
E2.5 MAK-7 rutile
E2.6 MAK-7 phlogopite
E3.1 MAK-8 olivine
E3.2 MAK-8 orthopyroxene
E3.3 MAK-8 ilmenite
E3.4 MAK-8 spinel
E3.5 MAK-8 rutile
E3.6 MAK-8 phlogopite

Appendix E1.1

Experiment	T-3740	T-3743	T-3770	T-3808	T-3813	T-3834	T-3840	T-3841
T (°C)	1150	1050	1200	1200	1100	1100	1200	1100
P (kbar)	30	20	35	30	25	30	35	25
Buffer	WCWO	WCWO	HM	WCWO	NNO	HM	IW	IW
log$fO2$	-9.65	-11.54	-2.83	-9.03	-8.05	-4.06	-10.57	-12.26
Δlog$fO2$ (FMQ)	-2.55	-2.56	3.42	-2.47	-0.05	3.61	-4.32	-4.25
	(n=5)	(n=4)	(n=5)	(n=6)	(n=4)	(n=5)	(n=6)	(n=5)
SiO2	39.09	38.91	41.02	39.20	39.64	40.40	38.77	38.83
TiO2	0.19	0.22	0.16	0.20	0.20	0.14	0.26	0.24
Cr2O3	0.53	0.51	0.33	0.55	0.39	0.34	0.72	0.72
FeO	15.19	15.54	5.61	15.32	11.35	4.96	16.41	16.18
MnO					0.15			
MgO	44.45	43.84	52.34	44.37	46.86	51.48	43.51	43.46
NiO	0.52	0.52	0.67	0.45	0.38	0.62	0.31	0.36
ZnO	0.22	0.27	0.35	0.26		0.32	0.21	0.25
Total	100.18	99.80	100.48	100.34	98.96	98.26	100.20	100.03
Mg#	83.9	83.4	94.3	83.8	88.0	94.9	82.5	82.7
Si	0.986 (0.007)	0.987 (0.007)	0.987 (0.018)	0.987 (0.022)	0.992 (0.013)	0.991 (0.010)	0.983 (0.018)	0.985 (0.012)
Ti	0.004 (0.001)	0.004 (0.001)	0.003 (0.001)	0.004 (0.001)	0.004 (0.002)	0.003 (0.001)	0.005 (0.002)	0.004 (0.005)
Cr	0.010 (0.003)	0.010 (0.004)	0.006 (0.002)	0.011 (0.004)	0.008 (0.005)	0.007 (0.003)	0.014 (0.010)	0.014 (0.008)
Fe	0.320 (0.008)	0.330 (0.011)	0.113 (0.005)	0.323 (0.011)	0.238 (0.004)	0.102 (0.005)	0.348 (0.016)	0.343 (0.009)
Mn					0.003 (0.001)			
Mg	1.671 (0.008)	1.657 (0.010)	1.878 (0.018)	1.665 (0.020)	1.748 (0.014)	1.883 (0.012)	1.644 (0.020)	1.644 (0.015)
Ni	0.010 (0.001)	0.011 (0.002)	0.013 (0.001)	0.009 (0.002)	0.008 (0.001)	0.012 (0.001)	0.006 (0.002)	0.007 (0.008)
Zn	0.004 (0.001)	0.005 (0.001)	0.006 (0.001)	0.005 (0.002)		0.006 (0.002)	0.004 (0.001)	0.005 (0.002)
Sum	3.005	3.004	3.007	3.004	3.000	3.003	3.005	3.003

Appendix E1.1

Experiment	T-3864	T-3937
T (°C)	1050	1100
P (kbar)	22	28
Buffer	NNO	NNO
log$fO2$	-8.80	-7.95
Δlog$fO2$ (FMQ)	0.04	-0.14
	(n=5)	(n=5)
SiO2	39.51	40.20
TiO2	0.17	0.15
Cr2O3	0.32	0.33
FeO	11.38	11.00
MnO		0.12
MgO	47.36	48.27
NiO	0.33	0.35
ZnO	0.04	
Total	99.11	100.42
Mg#	88.1	88.7
Si	0.987 (0.007)	0.989 (0.007)
Ti	0.003 (0.003)	0.003 (0.000)
Cr	0.006 (0.008)	0.006 (0.001)
Fe	0.238 (0.007)	0.226 (0.007)
Mn		0.003 (0.003)
Mg	1.764 (0.009)	1.771 (0.008)
Ni	0.007 (0.003)	0.007 (0.002)
Zn	0.001 (0.003)	
Sum	3.006	3.005

Appendix E1.2

Experiment	T-3740	T-3743	T-3770	T-3808	T-3813	T-3834	T-3840	T-3841
T (°C)	1150	1050	1200	1200	1100	1100	1200	1100
P (kbar)	30	20	35	30	25	30	35	25
Buffer	WCWO	WCWO	HM	WCWO	NNO	HM	IW	IW
log$f$O2	-9.65	-11.54	-2.83	-9.03	-8.05	-4.06	-10.57	-12.26
Δlog$f$O2 (FMQ)	-2.55	-2.56	3.42	-2.47	-0.05	3.61	-4.32	-4.25
	(n=5)	(n=4)	(n=5)	(n=6)	(n=4)	(n=5)	(n=6)	(n=5)
SiO2	55.99	55.90	57.71	56.52	56.11	56.58	56.18	56.08
TiO2	0.51	0.45	0.28	0.44	0.47	0.27	0.42	0.48
Al2O3					0.08			
Cr2O3	0.60	0.52	0.42	0.48	0.47	0.52	0.56	0.72
FeO	9.02	9.34	3.73	9.35	8.01	3.52	10.52	9.53
MgO	33.34	33.09	37.25	33.47	33.25	36.46	32.51	32.85
NiO	0.19	0.17	0.20	0.15	0.15	0.28	0.15	0.15
Total	99.65	99.46	99.60	100.41	98.54	97.63	100.33	99.82
Mg#	86.8	86.3	94.7	86.5	88.1	94.9	84.6	86.0
Si	1.966 (0.012)	1.969 (0.013)	1.977 (0.028)	1.970 (0.012)	1.980 (0.020)	1.977 (0.018)	1.971 (0.046)	1.970 (0.021)
Ti	0.014 (0.002)	0.012 (0.002)	0.007 (0.001)	0.012 (0.004)	0.013 (0.003)	0.007 (0.003)	0.011 (0.004)	0.013 (0.003)
Al					0.003 (0.001)			
Cr	0.017 (0.006)	0.014 (0.007)	0.011 (0.001)	0.013 (0.002)	0.013 (0.007)	0.014 (0.005)	0.016 (0.003)	0.020 (0.006)
Fe	0.265 (0.005)	0.275 (0.010)	0.107 (0.006)	0.273 (0.008)	0.236 (0.015)	0.103 (0.006)	0.309 (0.032)	0.280 (0.011)
Mg	1.745 (0.012)	1.737 (0.016)	1.902 (0.019)	1.739 (0.012)	1.749 (0.018)	1.899 (0.020)	1.700 (0.040)	1.720 (0.024)
Ni	0.005 (0.002)	0.005 (0.001)	0.006 (0.004)	0.004 (0.002)	0.004 (0.002)	0.008 (0.002)	0.004 (0.003)	0.004 (0.002)
Sum	4.012	4.012	4.010	4.011	3.999	4.009	4.010	4.007

Appendix E1.2

Experiment	T-3864	T-3937
T (°C)	1050	1100
P (kbar)	22	28
Buffer	NNO	NNO
log$fO2$	-8.80	-7.95
Δlog$fO2$ (FMQ)	0.04	-0.14
	(n=4)	(n=5)
SiO2	56.34	57.88
TiO2	0.42	0.38
Al2O3	0.11	0.07
Cr2O3	0.41	0.37
FeO	7.38	7.60
MgO	34.08	34.11
NiO	0.12	0.11
Total	98.87	100.51
Mg#	89.2	88.9
Si	1.976 (0.027)	1.994 (0.020)
Ti	0.011 (0.001)	0.010 (0.002)
Al	0.005 (0.004)	0.003 (0.000)
Cr	0.011 (0.004)	0.010 (0.003)
Fe	0.216 (0.014)	0.219 (0.009)
Mg	1.782 (0.023)	1.751 (0.014)
Ni	0.003 (0.000)	0.003 (0.001)
Sum	4.005	3.990

Appendix E1.3

Experiment	T-3740	T-3743	T-3770	T-3808	T-3813	T-3834	T-3840	T-3841
T (°C)	1150	1050	1200	1200	1100	1100	1200	1100
P (kbar)	30	20	35	30	25	30	35	25
Buffer	WCWO	WCWO	HM	WCWO	NNO	HM	IW	IW
log$fO2$	-9.65	-11.54	-2.83	-9.03	-8.05	-4.06	-10.57	-12.26
Δlog$fO2$ (FMQ)	-2.55	-2.56	3.42	-2.47	-0.05	3.61	-4.32	-4.25
	(n=5)	(n=4)	(n=6)	(n=10)	(n=4)	(n=5)	(n=5)	(n=3)
SiO2	0.10	0.08	0.17	0.08	0.27	0.12	0.09	0.12
TiO2	50.09	52.59	18.22	50.46	46.86	18.26	51.08	51.97
Cr2O3	10.72	6.00	25.38	10.84	10.57	22.94	10.56	8.12
Fe2O3	1.29	1.22	40.81	1.59	7.80	41.10		
FeO	25.35	26.66	5.61	25.83	21.47	6.08	25.79	26.77
MnO					0.18			
MgO	10.91	11.43	5.97	10.72	11.49	5.70	10.45	10.93
NiO	0.37	0.36	0.35	0.35	0.33	0.34	0.27	0.30
ZnO				0.22			0.22	0.26
Total	98.82	98.34	96.52	100.09	98.97	94.55	98.45	98.47
Mg#	43.4	43.3	65.5	42.5	48.8	62.6	41.9	42.1
Si	0.002 (0.001)	0.002 (0.000)	0.004 (0.005)	0.002 (0.000)	0.006 (0.006)	0.003 (0.003)	0.002 (0.001)	0.003 (0.003)
Ti	0.887 (0.005)	0.931 (0.010)	0.349 (0.004)	0.884 (0.006)	0.827 (0.006)	0.358 (0.008)	0.910 (0.015)	0.923 (0.010)
Cr	0.200 (0.004)	0.112 (0.005)	0.511 (0.009)	0.200 (0.004)	0.196 (0.003)	0.473 (0.013)	0.198 (0.014)	0.152 (0.004)
Fe3+	0.023 (0.012)	0.022 (0.021)	0.782 (0.016)	0.028 (0.013)	0.138 (0.016)	0.805 (0.022)		
Fe2+	0.499 (0.006)	0.525 (0.012)	0.120 (0.007)	0.503 (0.004)	0.421 (0.005)	0.132 (0.014)	0.509 (0.019)	0.528 (0.005)
Mn					0.004 (0.000)			
Mg	0.383 (0.005)	0.401 (0.010)	0.227 (0.004)	0.372 (0.005)	0.402 (0.007)	0.221 (0.006)	0.369 (0.012)	0.384 (0.007)
Ni	0.007 (0.001)	0.007 (0.002)	0.007 (0.003)	0.007 (0.001)	0.006 (0.002)	0.007 (0.001)	0.005 (0.002)	0.006 (0.001)
Zn				0.004 (0.001)			0.004 (0.004)	0.005 (0.002)
Sum	2.000	2.000	2.000	2.000	2.000	2.000	1.998	2.000
Fe3+/$\sum$Fe	0.044 (0.020)	0.040 (0.035)	0.867 (0.004)	0.052 (0.022)	0.246 (0.019)	0.859 (0.009)	0.000 (0.000)	0.000 (0.000)
Ilm (mol %)	50.3	52.9	12.0	50.9	42.6	13.3	52.1	53.4
Geik (mol %)	38.6	40.4	22.8	37.6	40.6	22.3	37.8	38.9
Hem (mol %)	1.1	1.1	39.4	1.4	6.9	40.6	0.0	0.0
Esk (mol %)	10.0	5.6	25.7	10.1	9.9	23.8	10.1	7.7

Appendix E1.3

Experiment	T-3864	T-3937
T (°C)	1050	1100
P (kbar)	22	28
Buffer	NNO	NNO
log$fO2$	-8.80	-7.95
Δlog$fO2$ (FMQ)	0.04	-0.14
	(n=5)	(n=5)
SiO2	0.10	0.10
TiO2	48.97	44.71
Cr2O3	8.10	10.62
Fe2O3	6.89	11.10
FeO	22.34	21.02
MnO	0.21	0.19
MgO	11.97	10.59
NiO	0.29	0.24
ZnO		
Total	98.88	98.57
Mg#	48.8	47.3
Si	0.002 (0.001)	0.002 (0.003)
Ti	0.862 (0.007)	0.799 (0.007)
Cr	0.150 (0.003)	0.200 (0.008)
Fe3+	0.121 (0.014)	0.198 (0.017)
Fe2+	0.437 (0.005)	0.418 (0.006)
Mn	0.004 (0.002)	0.004 (0.002)
Mg	0.417 (0.005)	0.375 (0.007)
Ni	0.006 (0.002)	0.005 (0.001)
Zn		
Sum	2.000	2.000
Fe3+/$\sum$Fe	0.217 (0.017)	0.322 (0.015)
Ilm (mol %)	44.2	42.1
Geik (mol %)	42.2	37.8
Hem (mol %)	6.1	10.0
Esk (mol %)	7.6	10.1

Appendix E1.4

Experiment	T-3740	T-3743	T-3770	T-3808	T-3813	T-3834	T-3840	T-3841
T (°C)	1150	1050		1200	1100		1200	1100
P (kbar)	30	20		30	25		35	25
Buffer	WCWO	WCWO		WCWO	NNO		IW	IW
log$fO2$	-9.65	-11.54		-9.03	-8.05		-10.57	-12.26
Δlog$fO2$ (FMQ)	-2.55	-2.56		-2.47	-0.05		-4.32	-4.25
	(n=7)	(n=6)		(n=6)	(n=3)		(n=5)	(n=8)
SiO2	0.15	0.32		0.23	0.16		0.42	0.39
TiO2	8.83	7.82		9.06	5.27		10.71	8.81
Al2O3		0.05		0.04	0.84		0.40	0.09
Cr2O3	51.29	52.26		50.91	51.27		45.48	51.41
Fe2O3	2.43	1.91		2.28	8.63		0.97	0.67
FeO	24.14	24.29		24.49	20.10		26.93	25.09
MnO					0.22			
MgO	9.02	8.24		9.08	9.79		8.15	8.48
NiO	0.33	0.31		0.24	0.22		0.20	0.19
ZnO	1.18	1.31		1.18	0.66		0.98	1.20
Total	97.36	96.52		97.51	97.17		94.24	96.33
Mg#	40.0	37.7		39.8	46.5		35.0	37.6
Si	0.005 (0.004)	0.012 (0.007)		0.008 (0.003)	0.006 (0.001)		0.016 (0.015)	0.014 (0.007)
Ti	0.237 (0.007)	0.213 (0.007)		0.243 (0.003)	0.141 (0.012)		0.298 (0.048)	0.240 (0.012)
Al		0.002 (0.001)		0.002 (0.001)	0.035 (0.002)		0.017 (0.008)	0.004 (0.001)
Cr	1.449 (0.019)	1.497 (0.018)		1.435 (0.012)	1.441 (0.019)		1.329 (0.097)	1.470 (0.025)
Fe3+	0.065 (0.018)	0.052 (0.019)		0.061 (0.015)	0.231 (0.022)		0.027 (0.117)	0.018 (0.027)
Fe2+	0.722 (0.015)	0.736 (0.015)		0.730 (0.011)	0.598 (0.013)		0.832 (0.118)	0.759 (0.022)
Mn					0.007 (0.004)			
Mg	0.480 (0.011)	0.445 (0.009)		0.483 (0.016)	0.519 (0.014)		0.449 (0.065)	0.457 (0.013)
Ni	0.009 (0.004)	0.009 (0.003)		0.007 (0.002)	0.006 (0.002)		0.006 (0.005)	0.005 (0.003)
Zn	0.031 (0.003)	0.035 (0.003)		0.031 (0.003)	0.017 (0.002)		0.027 (0.003)	0.032 (0.003)
Sum	3.000	3.000		3.000	3.000		3.000	3.000
Fe3+/∑Fe	0.083 (0.018)	0.066 (0.021)		0.077 (0.016)	0.279 (0.014)		0.031 (0.100)	0.024 (0.031)
Cr#	100.0	99.9		99.9	97.6		98.7	99.8
Fe3#	4.3	3.4		4.1	13.5		2.0	1.2

Appendix E1.4

Experiment	T-3864	T-3937
T (°C)	1050	1100
P (kbar)	22	28
Buffer	NNO	NNO
log$fO2$	-8.80	-7.95
Δlog$fO2$ (FMQ)	0.04	-0.14
	(n=6)	(n=5)
SiO2	0.39	0.08
TiO2	5.54	4.62
Al2O3	0.66	0.88
Cr2O3	48.53	50.58
Fe2O3	8.81	11.25
FeO	20.17	19.22
MnO	0.26	0.31
MgO	9.58	10.14
NiO	0.21	0.21
ZnO	0.63	0.31
Total	94.80	97.61
Mg#	45.8	48.5
Si	0.014 (0.011)	0.003 (0.002)
Ti	0.152 (0.023)	0.123 (0.012)
Al	0.028 (0.009)	0.037 (0.004)
Cr	1.398 (0.122)	1.413 (0.028)
Fe3+	0.241 (0.098)	0.299 (0.029)
Fe2+	0.615 (0.115)	0.568 (0.030)
Mn	0.008 (0.004)	0.009 (0.002)
Mg	0.520 (0.046)	0.534 (0.014)
Ni	0.006 (0.002)	0.006 (0.003)
Zn	0.017 (0.008)	0.008 (0.008)
Sum	3.000	3.000
Fe3+/ΣFe	0.282 (0.035)	0.345 (0.010)
Cr#	98.0	97.5
Fe3#	14.5	17.1

Appendix E1.5

Experiment	T-3740	T-3743	T-3770	T-3808	T-3813	T-3834	T-3840	T-3841
T (°C)					1100			
P (kbar)					25			
Buffer					NNO			
log$fO2$					-8.05			
Δlog$fO2$ (FMQ)					-0.05			
					(n=4)			
SiO2					0.09			
TiO2					88.56			
Cr2O3					6.99			
FeO					2.10			
MgO					0.16			
Total					97.89			
Si					0.001 (0.001)			
Ti					0.927 (0.003)			
Cr					0.077 (0.001)			
Fe					0.024 (0.002)			
Mg					0.003 (0.000)			
Sum					1.033			

Appendix E1.5

Experiment	T-3864	T-3937
T (°C)		
P (kbar)		
Buffer		
log$fO2$		
Δlog$fO2$ (FMQ)		
SiO2		
TiO2		
Cr2O3		
FeO		
MgO		
Total		
Si		
Ti		
Cr		
Fe		
Mg		
Sum		

Appendix E2.1

Experiment	T-3855	T-3858	T-3862	T-3863	T-3872	T-3879	T-3913	T-3944
T (°C)	1050	1050	1100	1150	1200	1175	1100	1125
P (kbar)	20	20	25	30	35	32	25	26
Buffer	NNO	IW	WCWO	IW	HM	WCWO	HM	NNO
log$fO2$	-8.88	-13.19	-10.56	-11.38	-2.83	-9.24	-4.11	-7.71
Δlog$fO2$ (FMQ)	0.10	-4.22	-2.56	-4.29	3.42	-2.54	3.90	-0.07
	(n=5)	(n=7)	(n=5)	(n=5)	(n=3)	(n=4)	(n=5)	(n=7)
SiO2	39.81	38.47	38.93	38.93	41.36	38.91	41.10	40.77
TiO2	0.18	0.29	0.28	0.35	0.30	0.32	0.23	0.20
Cr2O3	0.38	0.53	0.63	0.51	0.45	0.58	0.31	0.27
FeO	10.77	15.38	15.43	14.31	5.79	15.42	4.78	9.41
MnO								0.16
MgO	48.35	43.85	44.52	45.63	52.75	44.27	53.01	49.59
NiO	0.16							0.29
Total	99.65	98.52	99.79	99.73	100.64	99.49	99.43	100.68
Mg#	88.9	83.6	83.7	85.0	94.2	83.7	95.2	90.4
Si	0.986 (0.008)	0.985 (0.008)	0.984 (0.016)	0.980 (0.009)	0.990 (0.013)	0.986 (0.008)	0.991 (0.031)	0.993 (0.022)
Ti	0.003 (0.004)	0.006 (0.002)	0.005 (0.003)	0.007 (0.003)	0.005 (0.009)	0.006 (0.003)	0.004 (0.003)	0.004 (0.004)
Cr	0.007 (0.005)	0.011 (0.007)	0.013 (0.010)	0.010 (0.002)	0.009 (0.011)	0.012 (0.003)	0.006 (0.004)	0.005 (0.004)
Fe	0.223 (0.004)	0.329 (0.009)	0.326 (0.006)	0.301 (0.009)	0.116 (0.007)	0.327 (0.005)	0.096 (0.005)	0.192 (0.017)
Mn								0.003 (0.002)
Mg	1.784 (0.009)	1.674 (0.010)	1.677 (0.016)	1.711 (0.011)	1.881 (0.016)	1.672 (0.010)	1.905 (0.030)	1.799 (0.026)
Ni	0.003 (0.001)							0.006 (0.003)
Sum	3.007	3.004	3.005	3.009	3.001	3.002	3.002	3.001

Appendix E2.2

Experiment	T-3855	T-3858	T-3862	T-3863	T-3872	T-3879	T-3913	T-3944
T (°C)	1050	1050	1100	1150	1200	1175	1100	1125
P (kbar)	20	20	25	30	35	32	25	26
Buffer	NNO	IW	WCWO	IW	HM	WCWO	HM	NNO
log$fO2$	-8.88	-13.19	-10.56	-11.38	-2.83	-9.24	-4.11	-7.71
Δlog$fO2$ (FMQ)	0.10	-4.22	-2.56	-4.29	3.42	-2.54	3.90	-0.07
	(n=6)	(n=8)	(n=5)	(n=5)	(n=5)	(n=4)	(n=5)	(n=2)
SiO2	55.29	54.63	56.18	55.86	57.45	55.90	57.31	57.54
TiO2	0.55	0.53	0.51	0.50	0.39	0.51	0.34	0.55
Al2O3	0.29	0.16	0.08	0.20	0.34	0.19	0.33	0.29
Cr2O3	0.65	0.69	0.57	0.67	0.57	0.69	0.54	0.43
FeO	7.85	9.30	9.28	9.07	4.17	9.17	3.53	7.41
MgO	34.20	32.94	33.21	33.21	36.77	32.97	37.79	33.98
Total	98.83	98.25	99.84	99.51	99.69	99.43	99.85	100.21
Mg#	88.6	86.3	86.4	86.7	94.0	86.5	95.0	89.1
Si	1.949 (0.060)	1.951 (0.042)	1.969 (0.024)	1.963 (0.023)	1.969 (0.031)	1.967 (0.015)	1.958 (0.017)	1.987 (0.032)
Ti	0.015 (0.003)	0.014 (0.006)	0.013 (0.001)	0.013 (0.002)	0.010 (0.009)	0.014 (0.002)	0.009 (0.004)	0.014 (0.004)
Al	0.012 (0.004)	0.007 (0.007)	0.003 (0.001)	0.008 (0.003)	0.014 (0.003)	0.008 (0.002)	0.013 (0.003)	0.012 (0.004)
Cr	0.018 (0.009)	0.020 (0.009)	0.016 (0.002)	0.019 (0.003)	0.015 (0.013)	0.019 (0.007)	0.015 (0.006)	0.012 (0.000)
Fe	0.231 (0.012)	0.278 (0.013)	0.272 (0.011)	0.267 (0.019)	0.120 (0.018)	0.270 (0.004)	0.101 (0.009)	0.214 (0.017)
Mg	1.797 (0.068)	1.753 (0.044)	1.735 (0.019)	1.740 (0.023)	1.878 (0.032)	1.729 (0.013)	1.924 (0.016)	1.749 (0.023)
Sum	4.022	4.022	4.008	4.010	4.006	4.006	4.019	3.987

Appendix E2.3

Experiment	T-3855	T-3858	T-3862	T-3863	T-3872	T-3879	T-3913	T-3944
T (°C)	1050	1050	1100	1150	1200	1175	1100	1125
P (kbar)	20	20	25	30	35	32	25	26
Buffer	NNO	IW	WCWO	IW	HM	WCWO	HM	NNO
log$fO2$	-8.88	-13.19	-10.56	-11.38	-2.83	-9.24	-4.11	-7.71
Δlog$fO2$ (FMQ)	0.10	-4.22	-2.56	-4.29	3.42	-2.54	3.90	-0.07
	(n=5)	(n=5)	(n=4)	(n=6)	(n=7)	(n=4)	(n=5)	(n=5)
SiO2	0.05	0.11	0.13	0.08	0.07	0.08	0.07	0.04
TiO2	45.91	53.53	52.38	51.74	19.95	50.04	20.40	44.40
Al2O3					0.52	0.22	0.57	
Cr2O3	9.46	6.37	8.17	11.44	24.52	11.63	22.00	13.02
Fe2O3	10.55		0.61		40.26	0.64	40.93	10.28
FeO	20.49	27.79	26.63	24.47	6.14	26.19	6.23	18.76
MnO								0.21
MgO	11.63	11.44	11.58	11.45	6.67	10.61	6.85	11.71
NiO	0.12							0.13
Total	98.21	99.24	99.49	99.17	98.14	99.40	97.04	98.56
Mg#	50.3	42.3	43.7	45.5	65.9	41.9	66.2	52.7
Si	0.001 (0.001)	0.003 (0.007)	0.003 (0.006)	0.002 (0.001)	0.002 (0.001)	0.002 (0.001)	0.002 (0.001)	0.001 (0.000)
Ti	0.817 (0.010)	0.939 (0.011)	0.916 (0.007)	0.904 (0.010)	0.373 (0.007)	0.882 (0.008)	0.385 (0.004)	0.787 (0.009)
Al					0.015 (0.001)	0.006 (0.001)	0.017 (0.001)	
Cr	0.177 (0.006)	0.118 (0.004)	0.150 (0.004)	0.212 (0.009)	0.482 (0.009)	0.215 (0.004)	0.437 (0.006)	0.242 (0.006)
Fe3+	0.188 (0.020)		0.011 (0.018)		0.753 (0.018)	0.011 (0.017)	0.773 (0.011)	0.182 (0.019)
Fe2+	0.405 (0.006)	0.542 (0.009)	0.518 (0.006)	0.476 (0.008)	0.128 (0.010)	0.513 (0.007)	0.131 (0.009)	0.370 (0.010)
Mn								0.004 (0.002)
Mg	0.410 (0.007)	0.398 (0.010)	0.401 (0.007)	0.397 (0.008)	0.247 (0.007)	0.370 (0.006)	0.256 (0.008)	0.411 (0.007)
Ni	0.002 (0.002)							0.003 (0.001)
Sum	2.000	2.000	2.000	1.990	2.000	1.998	2.000	2.000
Fe3+/$\sum$Fe	0.316 (0.019)	0.000 (0.000)	0.020 (0.032)	0.000 (0.000)	0.855 (0.006)	0.021 (0.030)	0.855 (0.007)	0.330 (0.017)
Ilm (mol %)	40.6	54.3	51.8	48.6	12.9	51.5	13.2	37.2
Geik (mol %)	41.1	39.8	40.1	40.6	24.9	37.2	25.8	41.4
Hem (mol %)	9.4	0.0	0.5	0.0	37.9	0.6	39.0	9.2
Esk (mol %)	8.9	5.9	7.5	10.8	24.3	10.8	22.0	12.2

Appendix E2.4

Experiment	T-3855	T-3858	T-3862	T-3863	T-3872	T-3879	T-3913	T-3944
T (°C)	1050	1050	1100	1150		1175		1125
P (kbar)	20	20	25	30		32		26
Buffer	NNO	IW	WCWO	IW		WCWO		NNO
log$fO2$	-8.88	-13.19	-10.56	-11.38		-9.24		-7.71
Δlog$fO2$ (FMQ)	0.10	-4.22	-2.56	-4.29		-2.54		-0.07
	(n=7)	(n=7)	(n=7)	(n=7)		(n=6)		(n=5)
SiO2	0.13	0.17	0.56	0.11		0.32		0.11
TiO2	5.54	7.44	8.17	8.77		8.52		5.41
Al2O3	1.81	0.91	1.54	1.37		1.85		1.30
Cr2O3	46.92	53.87	51.19	53.28		50.59		50.38
Fe2O3	12.21	0.49	1.64	0.56		1.13		10.00
FeO	19.95	25.13	25.02	24.28		24.81		16.85
MnO	0.17							0.29
MgO	10.67	8.40	9.55	10.20		9.53		12.23
NiO	0.09							0.30
Total	97.49	96.40	97.66	98.56		96.74		96.88
Mg#	48.8	37.3	40.5	42.8		40.6		56.4
Si	0.005 (0.004)	0.006 (0.004)	0.020 (0.015)	0.004 (0.005)		0.011 (0.009)		0.004 (0.001)
Ti	0.146 (0.019)	0.201 (0.014)	0.216 (0.008)	0.229 (0.006)		0.227 (0.007)		0.142 (0.011)
Al	0.075 (0.006)	0.038 (0.003)	0.064 (0.004)	0.056 (0.002)		0.077 (0.019)		0.054 (0.003)
Cr	1.301 (0.049)	1.533 (0.028)	1.422 (0.026)	1.463 (0.018)		1.417 (0.016)		1.392 (0.023)
Fe3+	0.322 (0.049)	0.013 (0.031)	0.043 (0.034)	0.015 (0.022)		0.030 (0.020)		0.263 (0.023)
Fe2+	0.585 (0.039)	0.757 (0.028)	0.735 (0.020)	0.705 (0.013)		0.735 (0.012)		0.492 (0.021)
Mn	0.005 (0.001)							0.009 (0.002)
Mg	0.558 (0.042)	0.451 (0.020)	0.500 (0.031)	0.528 (0.023)		0.503 (0.008)		0.637 (0.010)
Ni	0.003 (0.004)							0.008 (0.001)
Sum	3.000	3.000	3.000	3.000		3.000		3.000
Fe3+/∑Fe	0.355 (0.018)	0.017 (0.037)	0.056 (0.038)	0.020 (0.028)		0.039 (0.023)		0.348 (0.009)
Cr#	94.6	97.6	95.7	96.3		94.8		96.3
Fe3#	19.0	0.8	2.8	0.9		2.0		15.4

Appendix E2.5

Experiment	T-3855	T-3858	T-3862	T-3863	T-3872	T-3879	T-3913	T-3944
T (°C)								1125
P (kbar)								26
Buffer								NNO
log$fO2$								-7.71
Δlog$fO2$ (FMQ)								-0.07
								(n=5)
SiO2								0.05
TiO2								87.17
Cr2O3								7.51
FeO								2.34
MgO								0.21
Total								97.29
Si								0.001 (0.000)
Ti								0.921 (0.001)
Cr								0.083 (0.001)
Fe								0.028 (0.001)
Mg								0.004 (0.000)
Sum								1.037

Appendix E2.6

Experiment	T-3855	T-3858	T-3862	T-3863	T-3872	T-3879	T-3913	T-3944
T (°C)		1050						
P (kbar)		20						
Buffer		IW						
log$fO2$		-13.19						
Δlog$fO2$ (FMQ)		-4.22						
		(n=6)						
SiO2		40.92						
TiO2		5.84						
Al2O3		9.61						
Cr2O3		1.97						
FeO		6.19						
MgO		19.77						
K2O		8.97						
Total		93.26						
Mg#		85.1						
Si		5.990 (0.036)						
Ti		0.643 (0.012)						
Al		1.656 (0.055)						
Cr		0.228 (0.021)						
Fe		0.758 (0.038)						
Mg		4.314 (0.027)						
K		1.676 (0.046)						
Sum		15.264						

Appendix E3.1

Experiment	T-3880	T-3897	T-3901	T-3903	T-3909	T-3910	T-3911	T-3912
T (°C)	1075	1175	1025	1125	1125	1075	1175	1145
P (kbar)	22	32	17	27	25	22	32	25
Buffer	WCWO	WCWO	IW	NNO	NNO	HM	HM	IW
log$fO2$	-11.07	-9.24	-13.71	-7.68	-7.75	-4.47	-3.13	-11.65
Δlog$fO2$ (FMQ)	-2.55	-2.54	-4.18	-0.10	-0.04	4.05	3.56	-4.17
	(n=4)	(n=4)	(n=5)	(n=4)	(n=4)	(n=6)	(n=4)	(n=5)
SiO2	39.00	38.76	39.05	40.28	40.06	41.13	40.72	40.04
TiO2	0.29	0.23	0.26	0.18	0.12	0.32	0.14	0.28
Al2O3								
Cr2O3	0.45	0.53	0.37	0.23	0.23	0.37	0.23	0.55
FeO	14.39	15.23	14.75	9.89	10.54	4.73	5.07	15.40
MnO								
MgO	44.14	44.19	44.56	48.52	48.03	53.56	53.60	44.60
NiO								
Total	98.28	98.94	98.98	99.10	98.98	100.11	99.78	100.87
Mg#	84.5	83.8	84.3	89.7	89.0	95.3	95.0	83.8
Si	0.995 (0.008)	0.987 (0.005)	0.991 (0.006)	0.997 (0.004)	0.996 (0.011)	0.985 (0.024)	0.981 (0.010)	0.998 (0.008)
Ti	0.006 (0.001)	0.004 (0.001)	0.005 (0.004)	0.003 (0.002)	0.002 (0.002)	0.006 (0.004)	0.003 (0.000)	0.005 (0.004)
Al								
Cr	0.009 (0.005)	0.011 (0.002)	0.007 (0.003)	0.004 (0.001)	0.005 (0.003)	0.007 (0.004)	0.004 (0.001)	0.011 (0.003)
Fe	0.307 (0.012)	0.324 (0.003)	0.313 (0.004)	0.205 (0.004)	0.219 (0.004)	0.095 (0.008)	0.102 (0.002)	0.321 (0.006)
Mn								
Mg	1.678 (0.011)	1.677 (0.006)	1.685 (0.007)	1.789 (0.005)	1.779 (0.012)	1.912 (0.025)	1.924 (0.009)	1.657 (0.011)
Ni								
Sum	2.995	3.003	3.001	2.998	3.000	3.005	3.014	2.991

Appendix E3.2

Experiment	T-3880	T-3897	T-3901	T-3903	T-3909	T-3910	T-3911	T-3912
T (°C)	1075	1175	1025	1125	1125	1075	1175	1145
P (kbar)	22	32	17	27	25	22	32	25
Buffer	WCWO	WCWO	IW	NNO	NNO	HM	HM	IW
log$f$O2	-11.07	-9.24	-13.71	-7.68	-7.75	-4.47	-3.13	-11.65
Δlog$f$O2 (FMQ)	-2.55	-2.54	-4.18	-0.10	-0.04	4.05	3.56	-4.17
	(n=5)	(n=5)	(n=9)	(n=4)	(n=1)	(n=5)	(n=5)	(n=7)
SiO2	55.95	55.70	55.89	56.33	53.10	56.90	56.60	56.97
TiO2	0.56	0.54	0.46	0.51	0.84	0.38	0.41	0.62
Al2O3	0.11	0.25	0.07	0.51	0.36	0.59	0.74	0.72
Cr2O3	0.62	0.68	0.60	0.56	0.51	0.59	0.63	0.93
FeO	9.01	9.00	9.14	7.30	7.84	3.57	3.84	9.08
MgO	32.80	32.84	32.44	33.65	34.73	37.58	37.35	32.87
NiO								
Total	99.05	99.00	98.59	98.86	97.38	99.61	99.56	101.19
Mg#	86.6	86.7	86.4	89.1	88.8	94.9	94.5	86.6
Si	1.974 (0.024)	1.967 (0.014)	1.981 (0.018)	1.974 (0.031)	1.907	1.950 (0.026)	1.943 (0.019)	1.966 (0.019)
Ti	0.015 (0.001)	0.014 (0.003)	0.012 (0.002)	0.013 (0.005)	0.023	0.010 (0.002)	0.010 (0.006)	0.016 (0.003)
Al	0.005 (0.002)	0.010 (0.001)	0.003 (0.001)	0.021 (0.011)	0.015	0.024 (0.013)	0.030 (0.007)	0.029 (0.006)
Cr	0.017 (0.007)	0.019 (0.003)	0.017 (0.009)	0.016 (0.008)	0.015	0.016 (0.004)	0.017 (0.003)	0.025 (0.004)
Fe	0.266 (0.015)	0.266 (0.006)	0.271 (0.011)	0.214 (0.022)	0.236	0.102 (0.008)	0.110 (0.010)	0.262 (0.005)
Mg	1.724 (0.019)	1.728 (0.017)	1.714 (0.017)	1.757 (0.028)	1.859	1.919 (0.024)	1.911 (0.020)	1.691 (0.014)
Ni								
Sum	4.001	4.004	3.997	3.995	4.055	4.021	4.023	3.990

Appendix E3.3

Experiment	T-3880	T-3897	T-3901	T-3903	T-3909	T-3910	T-3911	T-3912
T (°C)	1075	1175	1025	1125	1125	1075	1175	1145
P (kbar)	22	32	17	27	25	22	32	25
Buffer	WCWO	WCWO	IW	NNO	NNO	HM	HM	IW
log$fO2$	-11.07	-9.24	-13.71	-7.68	-7.75	-4.47	-3.13	-11.65
Δlog$fO2$ (FMQ)	-2.55	-2.54	-4.18	-0.10	-0.04	4.05	3.56	-4.17
	(n=6)	(n=5)	(n=5)	(n=4)	(n=3)	(n=5)	(n=5)	(n=7)
SiO2	0.04	0.08	0.05	0.10	0.07	0.07	0.07	0.20
TiO2	53.00	49.97	53.63	45.45	48.17	21.37	21.70	51.38
Al2O3		0.11		0.09	0.12	0.80	1.12	0.28
Cr2O3	6.39	11.66	5.09	11.54	9.68	21.48	22.26	10.02
Fe2O3	0.39	0.40		6.91	6.48	39.95	39.12	
FeO	27.12	25.60	26.91	19.69	21.47	6.68	6.75	25.48
MnO								
MgO	11.55	10.90	11.86	11.96	12.30	7.08	7.21	11.33
NiO								
Total	98.49	98.72	97.55	95.74	98.30	97.43	98.22	98.70
Mg#	43.2	43.1	44.0	52.0	50.5	65.4	65.6	44.2
Si	0.001 (0.001)	0.002 (0.000)	0.001 (0.001)	0.003 (0.002)	0.002 (0.001)	0.002 (0.001)	0.002 (0.001)	0.005 (0.003)
Ti	0.936 (0.006)	0.885 (0.007)	0.954 (0.006)	0.824 (0.010)	0.850 (0.006)	0.401 (0.004)	0.402 (0.009)	0.906 (0.014)
Al		0.003 (0.001)		0.003 (0.001)	0.003 (0.001)	0.023 (0.001)	0.032 (0.001)	0.008 (0.007)
Cr	0.119 (0.003)	0.217 (0.003)	0.095 (0.002)	0.220 (0.004)	0.180 (0.004)	0.423 (0.005)	0.434 (0.016)	0.186 (0.005)
Fe3+	0.007 (0.013)	0.007 (0.015)		0.125 (0.022)	0.114 (0.013)	0.749 (0.010)	0.725 (0.024)	
Fe2+	0.533 (0.008)	0.504 (0.006)	0.532 (0.004)	0.397 (0.012)	0.421 (0.006)	0.139 (0.006)	0.139 (0.012)	0.498 (0.011)
Mn								
Mg	0.404 (0.004)	0.382 (0.004)	0.418 (0.007)	0.429 (0.011)	0.430 (0.009)	0.263 (0.009)	0.265 (0.007)	0.396 (0.017)
Ni								
Sum	2.000	2.000	2.000	2.000	2.000	2.000	2.000	1.998
Fe3+/ΣFe	0.013 (0.022)	0.014 (0.028)	0.000 (0.000)	0.240 (0.024)	0.214 (0.016)	0.843 (0.004)	0.839 (0.007)	0.000 (0.000)
Ilm (mol %)	53.3	50.5	53.3	39.7	42.2	14.1	14.1	50.5
Geik (mol %)	40.4	38.3	41.9	43.0	43.1	26.6	26.9	40.1
Hem (mol %)	0.3	0.4	0.0	6.3	5.7	37.9	36.9	0.0
Esk (mol %)	5.9	10.9	4.8	11.0	9.0	21.4	22.1	9.4

Appendix E3.4

Experiment	T-3880	T-3897	T-3901	T-3903	T-3909	T-3910	T-3911	T-3912
T (°C)	1075	1175	1025	1125	1125			1145
P (kbar)	22	32	17	27	25			25
Buffer	WCWO	WCWO	IW	NNO	NNO			IW
log$fO2$	-11.07	-9.24	-13.71	-7.68	-7.75			-11.65
Δlog$fO2$ (FMQ)	-2.55	-2.54	-4.18	-0.10	-0.04			-4.17
	(n=5)	(n=4)	(n=6)	(n=4)	(n=3)			(n=5)
SiO2	0.31	0.19	0.40	0.14	0.17			0.23
TiO2	7.30	8.65	6.85	5.09	5.93			9.99
Al2O3	1.29	1.97	1.55	2.30	2.44			3.29
Cr2O3	51.17	49.17	50.40	51.29	48.55			47.51
Fe2O3	1.40	1.41	1.02	7.58	8.67			0.67
FeO	23.56	23.75	23.07	16.13	19.61			25.21
MnO					0.19			
MgO	9.00	9.82	8.74	12.70	11.04			10.32
NiO					0.16			
Total	94.02	94.95	92.04	95.23	96.77			97.21
Mg#	40.5	42.4	40.3	58.4	50.1			42.2
Si	0.011 (0.004)	0.007 (0.006)	0.015 (0.010)	0.005 (0.003)	0.006 (0.002)			0.008 (0.007)
Ti	0.201 (0.009)	0.234 (0.009)	0.193 (0.008)	0.135 (0.006)	0.156 (0.004)			0.262 (0.009)
Al	0.056 (0.004)	0.084 (0.006)	0.068 (0.007)	0.095 (0.009)	0.101 (0.004)			0.135 (0.008)
Cr	1.481 (0.019)	1.398 (0.016)	1.488 (0.028)	1.425 (0.011)	1.346 (0.008)			1.308 (0.015)
Fe3+	0.038 (0.020)	0.038 (0.018)	0.029 (0.027)	0.200 (0.012)	0.229 (0.011)			0.017 (0.022)
Fe2+	0.721 (0.013)	0.714 (0.013)	0.721 (0.025)	0.474 (0.006)	0.575 (0.008)			0.734 (0.009)
Mn					0.006 (0.002)			
Mg	0.491 (0.017)	0.526 (0.009)	0.487 (0.015)	0.665 (0.006)	0.577 (0.009)			0.536 (0.021)
Ni					0.005 (0.002)			
Sum	3.000	3.000	3.000	3.000	3.000			3.000
Fe3+/$\sum$Fe	0.051 (0.024)	0.051 (0.021)	0.038 (0.032)	0.297 (0.009)	0.285 (0.007)			0.023 (0.027)
Cr#	96.4	94.4	95.6	93.7	93.0			90.6
Fe3#	2.4	2.5	1.8	11.6	13.7			1.2

Appendix E3.5

Experiment	T-3880	T-3897	T-3901	T-3903	T-3909	T-3910	T-3911	T-3912
T (°C)				1125	1125			
P (kbar)				27	25			
Buffer				NNO	NNO			
log$fO2$				-7.68	-7.75			
Δlog$fO2$ (FMQ)				-0.10	-0.04			
				(n=4)	(n=2)			
SiO2				0.08	0.07			
TiO2				85.01	87.39			
Cr2O3				7.87	7.34			
FeO				1.89	1.98			
MgO				0.22	0.20			
Total				95.06	96.98			
Si				0.001 (0.001)	0.001 (0.000)			
Ti				0.918 (0.002)	0.924 (0.001)			
Cr				0.089 (0.002)	0.082 (0.000)			
Fe				0.023 (0.000)	0.023 (0.001)			
Mg				0.005 (0.000)	0.004 (0.001)			
Sum				1.036	1.034			

Appendix E3.6

Experiment	T-3880	T-3897	T-3901	T-3903	T-3909	T-3910	T-3911	T-3912
T (°C)			1025					
P (kbar)			17					
Buffer			IW					
log$fO2$			-13.71					
Δlog$fO2$ (FMQ)			-4.18					
			(n=5)					
SiO2			41.85					
TiO2			4.42					
Al2O3			10.63					
Cr2O3			1.58					
FeO			5.80					
MgO			21.55					
K2O			8.62					
Total			94.45					
Mg#			86.9					
Si			5.999 (0.033)					
Ti			0.477 (0.016)					
Al			1.795 (0.015)					
Cr			0.179 (0.006)					
Fe			0.695 (0.024)					
Mg			4.605 (0.039)					
K			1.576 (0.031)					
Sum			15.326					

APPENDIX F

SILICA ACTIVITY VERSION

F1 Silica activity calculation

F2 Estimation of the $(X_{en})^{opx}$ term

APPENDIX F

SILICA ACTIVITY VERSION

F1 Silica activity calculation

For the reaction:

$$2MgSi_{0.5}O_2 + SiO_2 = Mg_2Si_2O_6$$

The silica activity term is derived as follows:

$$\ln(a_{SiO2})^{opx\text{-}olv} = {}^{-36.1}/_{T} - 0.38 - 0.02*({}^{P}/_{T})$$
$$+ 2\ln(X_{en})^{opx} - 2\ln(X_{fo})^{olv} - ({}^{3254}/_{T})*(1-X_{fo})^2$$

and:

$$\log(a_{SiO2})^{opx\text{-}olv} = {}^{-15.68}/_{T} - 0.165 - 0.0087*({}^{P}/_{T})$$
$$+ 2\log(X_{en})^{opx} - 2\log(X_{fo})^{olv} - ({}^{1413}/_{T})*(1-X_{fo})^2$$

where ideal two-site mixing in orthopyroxene is assumed, and the thermodynamic terms are derived from Holland and Powell (1990). The olivine W_G value is from a best fit of the semi-empirical O_2 sensor equations for ilmenite and spinel derived in Chapter 4. The value here is higher than that determined for the olivine-ilmenite Fe-Mg exchange geothermometer because it also corrects for enstatite activity and differences between the X_{en} and X_{fo} relationship in the experiments of this experimental study and that of Brey (1990). However, the W_G value is still within the range of those reported for olivine.

F2 Estimation of the $(X_{en})^{opx}$ term

For orthopyroxene, the $(X_{en})^{opx}$ term can be estimated from orthopyroxene undersaturated olivine-bearing assemblages according to Brey (1990):

$$(X_{en})^{opx} = A*e^{ß}/(1 + A*e^{ß})$$

where: $ß = 134/T - 0.078 + 0.0027*(P/T)$

and: $A = X_{fo}/(1-X_{fo})$

"That is the worst of erudition - that the next scholar sucks the few drops of honey that you have accumulated, sets right your blunders, and you are superseded."

A.C. Benson,
From a College Window